Optical Modeling of Superconducting Nanowire Single Photon Detectors

Optical Modeling of Superconducting Nanowire Single Photon Detectors

A DISSERTATION PRESENTED
BY
KRISTEN ANN SUNTER
TO
THE SCHOOL OF ENGINEERING AND APPLIED SCIENCE

IN PARTIAL FULFILLMENT OF THE REQUIREMENTS
FOR THE DEGREE OF
DOCTOR OF PHILOSOPHY
IN THE SUBJECT OF
APPLIED PHYSICS

HARVARD UNIVERSITY
CAMBRIDGE, MASSACHUSETTS
SEPTEMBER 2014

Thesis advisor: Professor Karl K. Berggren Kristen Ann Sunter

Optical Modeling of Superconducting Nanowire Single Photon Detectors

Abstract

Superconducting nanowire single photon detectors (SNSPDs) can detect single photons or low levels of infrared light in applications that require high speed and low timing jitter, such as integrated circuit analysis. Most applications also require a high device detection efficiency (DDE), but the DDE of SNSPDs is limited by many factors. A good optical design with an integrated optical cavity and dielectric layers can increase the absorptance of 1550-nm light in the active area to over 90%. Therefore, optical modeling using the transfer matrix method was used to guide the design and fabrication of high-efficiency detectors with a measured DDE of over 70%. In addition, finite element analysis was used to simulate the effect of adding different types of optical antennas to SNSPD designs to increase their active area without compromising their speed, and the fabrication of antennas integrated with nanowires achieved sub-10 nm gaps between features.

Thin films of niobium nitride, the starting material of the SNSPDs, were investigated using several techniques for thin film characterization, including x-ray diffraction, Auger electron spectroscopy and x-ray photoelectron spectroscopy. Optical setups based on reflectometry and transmittometry were built to determine the film thickness more accurately than deposition time for optical modeling and to provide feedback on the deposition conditions. The optical setups are able to provide reproducible and precise thickness measurements to within 0.1 nm.

Contents

Listing of figures

Acknowledgments

The research in this thesis would never have been possible without help from the many people who were kind enough to share their knowledge, skills and time with me. Professor Karl Berggren welcomed me into his group three years ago and gave me clear research advice and direction that helped me grow as both a researcher and a collaborator in scientific projects. The members of my thesis committee at Harvard, Professors Bob Westervelt, Marko Loncar and Vinny Monaharan, provided support as I developed my thesis topic and navigated the requirements at Harvard, especially my co-adviser Professor Westervelt. At MIT, Professor Rajeev Ram let us use his probe station for most of the device testing that is reported here, and Professor Hank Smith shared his expertise in nanofabrication.

I am greatly indebted to the technical staff at MIT and Harvard for their help, in particular, Jim Daley and Mark Mondol. In addition to their general helpfulness, Jim did all of the gold evaporation required for the fabrication of devices, and Mark trained me on the Elionix and SEM. The technical and research staff at the Center for Materials Science and Engineering (CMSE) at MIT trained me and provided assistance with instruments to characterize thin films: Dr. Scott Speakman trained me on the high-resolution x-ray diffractometer and helped me gather the data in Chapter 3, Libby Shaw provided training and guidance with the Auger electron spectroscopy and x-ray photoelectron spectroscopy, and Tim McClure discussed thin film characterization techniques with me. In the Research Laboratory of Electronics, Dr. Gale Petrich provided some variable-angle spectroscopic ellipsometry data, and Dr. Euclid Moon provided much training and assistance with atomic force microscopy. Bob Bicchieri and Bernard Alamariu at the Microsystems Technology Laboratory at MIT grew the nitride and oxide films on silicon used as substrates in device fabrication. In addition, I'd like to acknowledge the training and help I've received from the technical staff at the Center for Nanoscale Systems at Harvard University over the years.

Funding for this research was provided by the Intelligence Advanced Research Projects Activity (IARPA/AFRL), and I'd like to thank the researchers at DCG Systems, IBM and PhotonSpot who worked on this project, in particular Dr. Euan Ramsay at DCG, Dr. Franco Stellari and Dr. Andrea Bahgat Shehata at IBM and Dr. Vikas Anant at PhotonSpot for technical discussions.

The members of the Berggren group at MIT provided a great amount of help and support, especially those who work with SNSPDs. Faraz Najafi helped me settle into the group at the start of my time here, and his training and assistance with device characterization and design have been invaluable. Andrew Dane deposited most of the films used by the group and gave me excellent feedback

on the reflectometer and transmittometer. Qingyuan Zhao solved many problems related to fabrication using the Elionix, and he provided the first device to test whether I could fabricate optical cavities and predict their performance. I've had many fruitful technical discussions with Adam McCaughn, Yujia Yang, Francesco Bellei and Dr. Francesco Marsili, and I'm grateful to Hasan Korre, Lars Schonenberg, Domenico De Fazio and Dr. Yachin Ivry for their work on NbN film deposition, which contributed to the group's knowledge. The TEM measurements reported in Chapter 3 were performed by Dr. Chung-Soo Kim, and David Meyer trained me on the ellipsometer, which I used in preliminary investigations of HSQ and NbN films. Dr. Richie Hobbs provided helpful suggestions to address the some fabrication issues, which are detailed in Chapter 1.

I've been fortunate to work with talented undergraduate researchers. Chris Lang made the visible reflectometer much more user friendly, summer student Bethel Tarekegne found an important error in one of my COMSOL simulations, and Melissa Hunt worked on an earlier version of the IR transmittometer. I'd also like to thank the administrative assistants Mauro Bortolussi and Dorothy Fleischer.

Finally, I would like to thank my friends for their support over the years, especially Dr. Malima Wolf, who first encouraged me to find an adviser at MIT, and Alex Khripin, who was interested in the technical details of my work and asked good questions even though it was outside his area of expertise. I love my family, especially my three younger sisters who have all graduated with advanced degrees in engineering and medicine, and I couldn't be more proud of them :)

0

Introduction

This thesis describes several designs to enhance the performance of a type of single-photon detector composed of a nanowire, or several nanowires in parallel, of superconducting material. Superconducting nanowire single photon detectors (SNSPDs) are particularly relevant for applications where single photons or low levels of light must be detected with low timing jitter, such as circuit analysis[1,2], quantum key distribution[3,4,5,6,7] and IR telescopy[8]. SNSPDs typically have a low dark count rate (that is, the rate of false detection events in the absence of photons)[9], low timing jitter[10,11,12], and

a short recovery time when composed of niobium nitride[13]. They have a high detection efficiency in the visible and near infrared wavelength regions, with reported detection efficiencies of over 90% for detectors based on amorphous WSi[14] and NbN detectors with integrated optical cavities[15].

SNSPDs do not have the capability to resolve photon number on their own[10,16], and they must be operated at liquid helium temperatures because they are based on low critical temperature superconductors. Nevertheless, their low timing jitter[17] is substantially better than competing technologies in the near infrared for applications where timing is critical[18,19]. They can be integrated with optical components such as waveguides[20] and optical fibers[21,22].

0.1 Superconducting Nanowire Single Photon Detectors (SNSPDs)

SNSPDs are composed of nanowires that have widths between 30 nm[23] and 100 nm and a thickness of several nanometers[24]. Figure 1 shows an example of the geometry of a typical device. The active area of the device is defined by laying the nanowire in a boustrophedonic, or meander, pattern. The absorptance of the device depends in part on the fill factor, which is the ratio of the nanowire width to the pitch of the meander pattern. The active area can be increased by either decreasing the fill factor while maintaining the same nanowire length or increasing the nanowire length. The lower the fill factor, the lower the absorptance of the material, and thus the lower the detection efficiency per area. However, the longer the nanowire, the greater the kinetic inductance of the detector, which limits the reset time of the detector because it increases the time necessary to restart the current flow after a detection event[13]. Therefore, the design of a device for a particular application requires considering the tradeoffs between device properties.

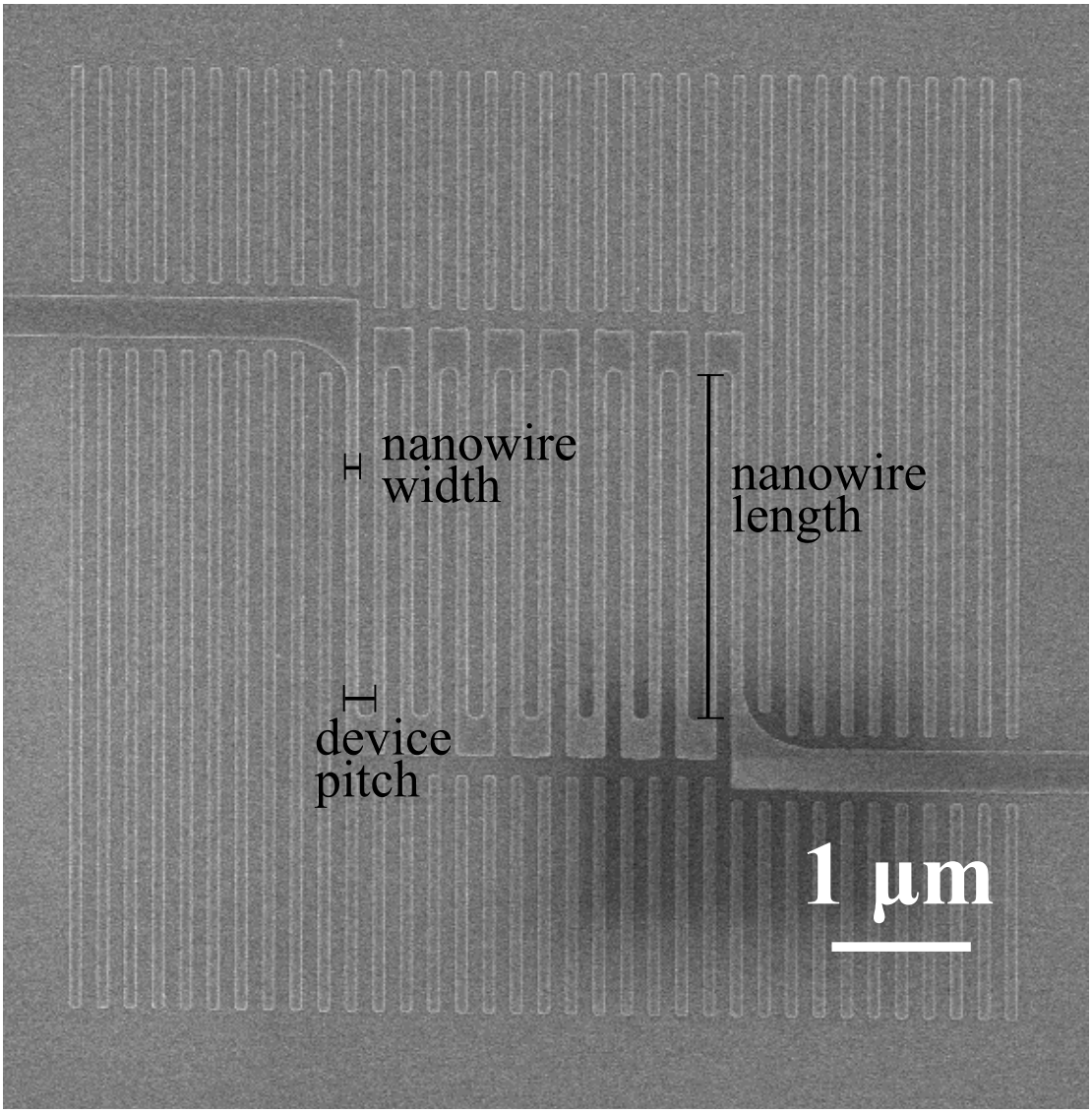

Figure 1: This is a very small active area (approximately $2.5\,\mu\mathrm{m} \times 2\,\mu\mathrm{m}$) device to show the different features of a meander pattern. The fill factor is the ratio of the nanowire width to the device pitch. The inner curves of the turns are rounded to prevent current crowding, which is discussed below. The length of the device is the sum of the lengths of the nanowires, excluding the turns, which are much wider and shorter than the nanowires and so do not contribute significantly to the device resistance. The image shows a darkened area on the bottom right of the device due to charging of the sample when viewed at a higher magnification.

0.2 Theory of Operation of SNSPDs

According to the hot spot model of operation [25], an incident photon is absorbed by the superconducting nanowire, which breaks the Cooper pairs responsible for superconductivity and causes a normal (non-superconducting) region to form. If there is a super current running through the nanowire, it is diverted from the resistive normal region into the superconducting metal surrounding the normal region. The current density thus increases in the superconducting regions surrounding the hot spot, and, if it increases above the critical current, these regions are also driven normal. The hot spot eventually grows across the entire nanowire, which leads to a resistive barrier and the generation of a voltage difference along the nanowire that can be detected as the current is redirected into a parallel readout line at 50 Ω. The hot spot initially grows quickly due to Joule heating [26]. Then, as the current in the device is shunted into the parallel line, it decreases, which in turn decreases the Joule heating and allows the detector to be cooled and switched to the superconducting state. This electrothermal feedback limits the recovery time of the device and thus the maximum count rate, along with the kinetic inductance [13].

The electrothermal model of SNSPD operation [26] seems to fit the observed experimental evidence, but the microscopic mechanism of photon absorption is still unclear [27,28]. The hot spot model gives an intuitive explanation for the decreased sensitivity of SNSPDs in the infrared because IR photons carry less energy [29], but it neglects the excess quasi-particles in the regions surrounding the hot spot [27]. It may be the case that photon absorption leads to the formation of a normal metal region, but photon absorption may also induce a detection event by reducing the effective depairing critical current to a level below the bias current [30,31] or decreasing the critical current for vortex crossings [32]. Magnetic vortexes crossing into the nanowire have already been proposed as the mechanism for intrinsic dark counts [33,34], which increase rapidly as the bias current approaches the switching current.

0.2.1 Good Device Design

Despite uncertainty about the microscopic mechanism of detection, several properties of SNSPDs have been correlated with good detector performance. A good device will be free of constrictions, which are sections of the nanowire where the critical current is reduced, thus limiting the bias current that can be applied before the constricted section of the nanowire switches[35]. If the applied bias current is limited by current crowding in the constricted sections, it will be too far below the switching current of the non-constricted sections along the nanowire, and those sections will not be as sensitive to photons and will not contribute to the device detection efficiency. The best devices will have uniform nanowires and adiabatic turns in the meander pattern that do not induce vortex tunneling into the device[36,37].

Good devices will also have a high optical absorptance because the device detection efficiency (DDE) is a product of the optical absorptance and the intrinsic detection efficiency[38]. Optical modeling is used in Chapter 4 to determine the ideal NbN thickness and the design of the optical cavity to increase the light that is absorbed in the nanowire.

Narrow lines are typically more sensitive to lower energy photons[29], and thus for detection in the infrared, devices composed of narrower lines (as long as the fill factor of the device is equal) will have a higher intrinsic detection efficiency. The devices reported in this thesis were fabricated with nanowire line widths down to 60 nm as a compromise between making the nanowires as narrow as possible and the reproducible and reliable fabrication of large area detectors, but devices with linewidths down to 30 nm[23] have been successfully tested.

Another important property of SNSPD devices is the critical current, or switching current, I_{sw}. A higher switching current allows the device to be operated at a higher bias current, which leads to a faster instrument response function. When the device switches to normal and the bias current is redirected into the parallel readout line, a higher bias current will lead to a higher voltage pulse

because the parallel readout line has a resistance of 50 Ω. A higher voltage pulse gives a higher signal to noise ratio, and a higher SNR leads to a lower jitter[17]. Therefore, devices with higher switching currents will have lower jitter and are better in applications where timing jitter is critical.

In general, the specific properties of devices and the tradeoffs favored depend on the specific application for which the detector is being built. The detectors fabricated for this thesis were designed for use in a circuit analysis tool built by IBM and DCG Systems. The spot size in their instrument is 9 μm in diameter, which required large area devices with active areas of at least this size. The jitter and low dark counts were also important factors that guided the device design, eventually leading to the use of the superconducting nanowire avalanche photodetector (SNAP) geometry, as described in Section 1.4.

0.3 Overview

Chapter 1 describes the fabrication and testing of SNSPDs, as well as a new detector design. The fabrication process described here is followed by several members of the Berggren group and has been refined by many people over several years. Solutions to some commonly encountered problems, including adhesion and write fracturing, have also been found over the years and are included for future reference. The testing protocols followed are also based on techniques described previously, but this thesis attempts to quantify the quality of devices by assigning them a "constriction factor". In this way, high quality devices can be sorted from lower quality devices on a chip before time-consuming testing and the fabrication of additional structures, such as optical cavities and antennas. One such constriction factor is the ratio of the effective widths according to the switching current and the resistance. The effective width of a device is calculated by comparing the device to an ideal device with the same nominal geometry and assigning it an "effective" cross-sectional geometry based on its actual resistance or switching current. Figure 2 shows that the constriction factor

based on the ratio of the effective widths of a device correlates with the device detection efficiency.

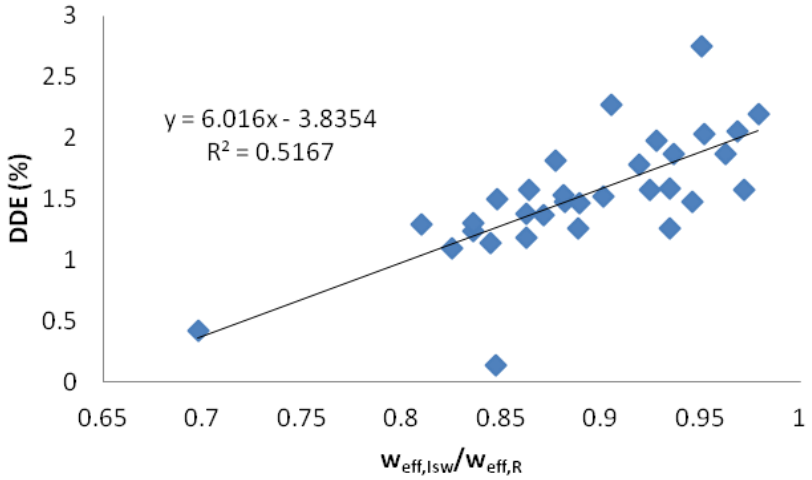

Figure 2: Device detection efficiency (DDE) versus the ratio of the effective widths for devices on a single chip. The device detection efficiency increases as the effective width ratio increases, and thus the effective width ratio can provide a measure of the quality of a device during the screening process.

This chapter also presents a new design for a device with multiple nanowires in parallel in each section of the meander pattern, which is known as a SNAP, as shown in Figure 3. The new design is more condensed than the previous one, which gives it a higher fill factor and thus a greater amount of NbN in the active layer of the device. The greater amount of material leads to a higher absorptance of light and thus a higher device detection efficiency. The new design for a 4-SNAP, with four nanowires in parallel in each section, had a device detection efficiency that was greater than that of the old design by almost a factor of 1.5 on average.

Chapter 2 explores the material properties of the NbN thin film that is the starting material for device fabrication. NbN films were characterized with x-ray diffraction (XRD), Auger electron spectroscopy (AES) and x-ray photoelectron spectroscopy (XPS). The XRD results showed that the films were epitaxial to MgO substrates but were strained and had a high defect concentration. The AES and XPS results gave some insight into the chemistry of the films, in particular whether they contained oxygen, which might degrade the superconductor properties. For example, Figure 4

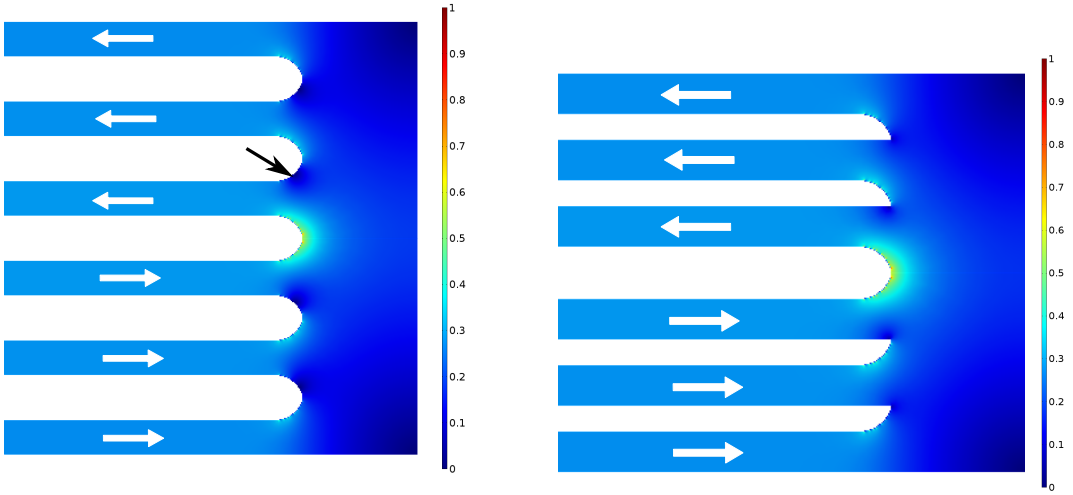

(a) 4-SNAP **(b)** c4-SNAP

Figure 3: (a) Normalized current density in one turn of a 3-SNAP pattern according to finite element analysis. The black arrow indicates an area where the current density is zero. The current flow is as indicated by the white arrows. The bright area in the middle of the turn is due to current crowding because the turn is slightly tighter than the optimal curve. The somewhat bright areas along the edges of the other turns are an artifact of the size of the steps in the model. (b) Normalized current density in one turn of a condensed 3-SNAP (c3-SNAP) pattern. The current crowding seen in the middle of the turn is as in the case of the 3-SNAP.

shows the niobium peak with depth into a film, which changes shape as it transitions from an oxynitride environment to the nitride. These results showed that the films had an oxide on the surface, but no oxygen within the bulk of the film.

A non-destructive and fast method to measure the thickness of the films is presented in Chapter 3. Two optical setups were built to measure the transmittance of light through the films at different wavelengths, and the results show good agreement with other methods, such as x-ray reflectometry and transmission electron microscopy (TEM). Figure 5 shows a schematic of the infrared reflectometer. The transmittance of the film can then be matched with the calculated transmittance for a certain thickness, given the refractive index of NbN. This method is simple and more reliable than using the deposition time of a film as a proxy for the thickness.

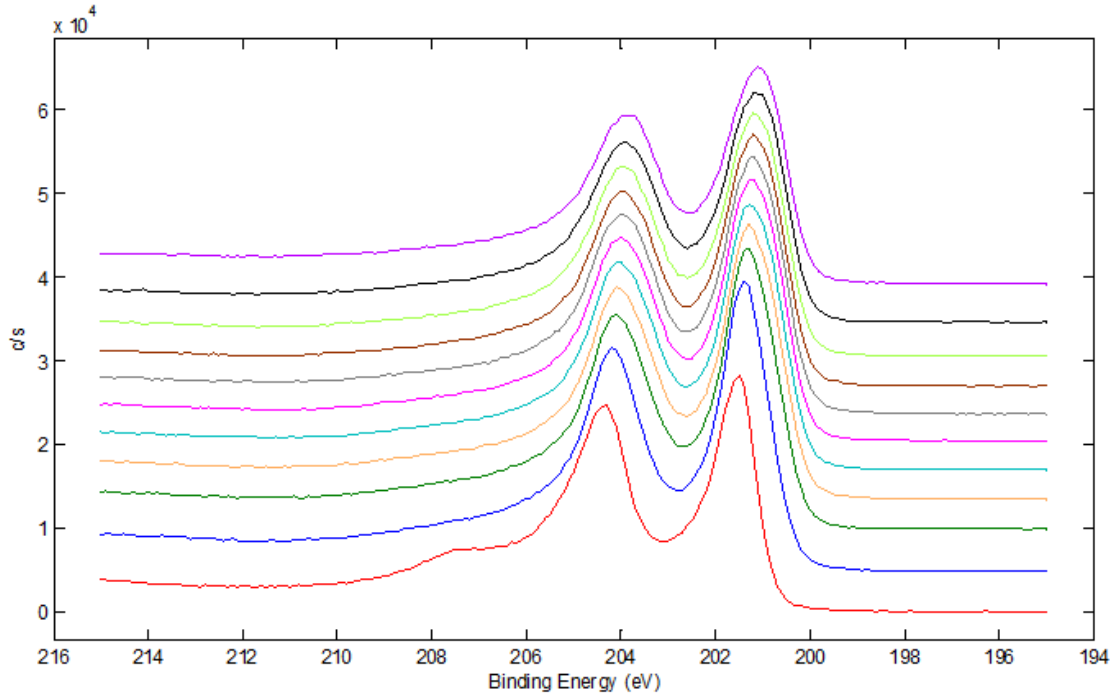

Figure 4: XPS results for the niobium peak of a thin film of NbN on MgO measured between 1-min sputtering intervals. There is a change in the shape of the peak with depth near the surface, indicating a change in the bonding of the niobium atoms from oxide and oxynitride to nitride within the bulk of the film. There is no change in the peak shape near the substrate, however (top lines), which indicates that there is no niobium oxide layer between the NbN and the substrate.

Chapter 4 further develops the calculations of the optical properties of devices. The transfer matrix method is used to model both sides of a substrate that is thicker than the coherence length of the incident light, and thus this method can give the transmittance, reflectance and total absorptance of a device, as well as the absorptance within the NbN device layer, which can be modeled using an effective index of refraction by assuming that the polarization of the incident light is parallel to the nanowires. One surprising result was the effect that an anti-reflection coating (ARC) has on the absorptance in NbN when a device is back-illuminated through the substrate with a light source that has a coherence length longer than the thickness of the substrate. As Figure 6 shows, the lack of an ARC can lead to a higher absorptance than that obtained with an ARC when the NbN device also

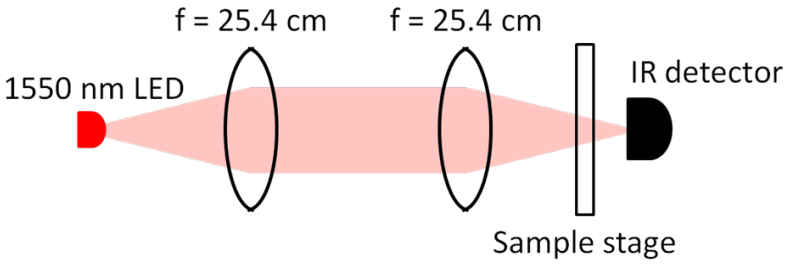

(a) IR transmittometer schematic

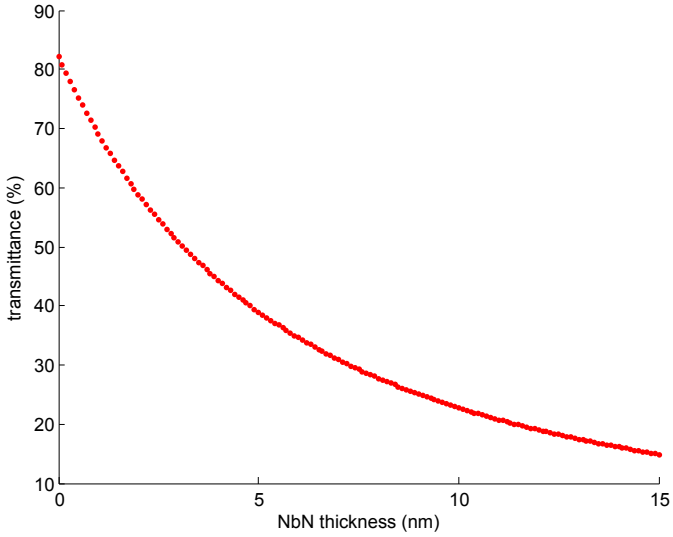

(b) sample transmittance plot

(c) photograph of the IR transmittometer

Figure 5: (a) Schematic of the infrared transmittometer showing the basic optical components. (b) Transmittance versus NbN thickness for an NbN film grown on silicon nitride on silicon. In this case, the NbN film is on the side of the chip that is facing the detector. The thickness of a sample can be determined by measuring the transmittance and then reading the thickness from this plot. (c) Photograph of the IR reflectometer.

includes an integrated optical cavity, depending on the thickness of the substrate. This result clearly demonstrates why an incoherent light source is necessary for testing. Other results in this chapter give the absorptances expected for different device geometries and show how different substrates and optical cavities can enhance the absorptance and thus the device detection efficiency. Then, Chapter 5 gives some experimental confirmation of these calculations.

Chapter 6 approaches the problem of increasing the amount of light detected by SNSPDs in a

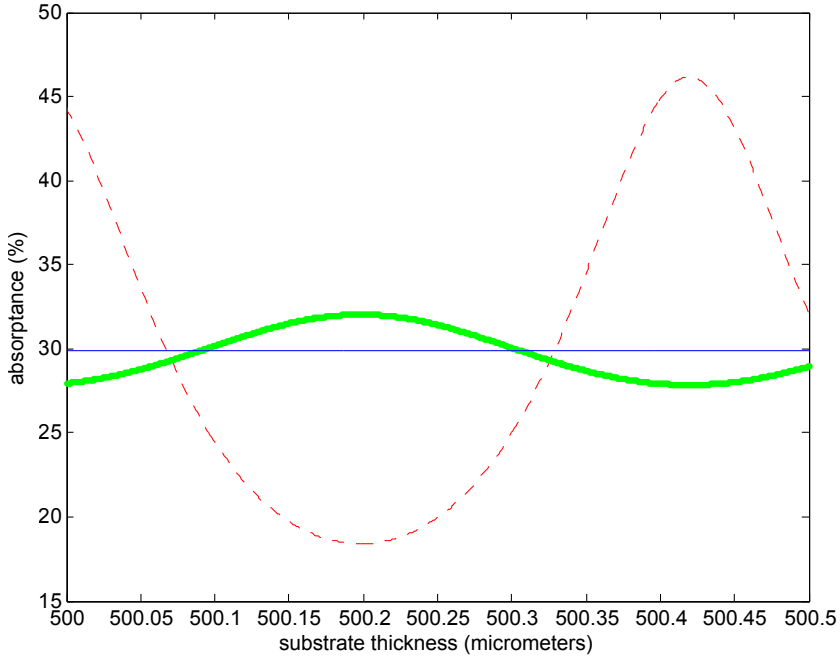

Figure 6: Absorptance in NbN versus substrate thickness with a perfect ARC ($n \approx 1.32$) (thin blue line), an imperfect ARC composed of HSQ ($n = 1.38$) (thick green line) and no ARC (dashed red line). The substrate is sapphire ($n = 1.75$), and the fill factor of the 4-nm-thick NbN layer is 40%. The optical cavity on top of the NbN device is composed of a quarter-wavelength layer of HSQ and gold. Without an ARC, the absorptance varies by a factor of 2.5 over a range of substrate thicknesses of only 200 nm, which is far less than the typical thickness tolerance of our substrates. Even an imperfect ARC can help or hinder the absorptance compared to the case of a perfect ARC.

different way. Instead of adding optical cavities or other dielectric layers to increase the absorptance in the NbN layer, the incident light is collected from a larger area using optical nanoantennas. Several antenna designs are discussed, and two stand out as promising for different applications. The double-threaded dual Vivaldi antenna, shown in Figure 7, can enhance the absorptance of a low-fill-factor SNSPD by a factor fo 3.62, and thus it may provide a way to produce high-speed large-area devices that still have a high device detection efficiency. A figure of merit presented in a previous paper shows that this device is comparable to detectors currently being fabricated. A log-period antenna design that surrounds a small active area device was also simulated, as shown in Figure 8. In this case, the antenna collects light from a much larger area and focuses it onto a small detector, which both

increases the effective area of the detector and increases its sensitivity to long-wavelength photons. The use of coplanar antennas with SNSPDs has not yet been reported, and it could provide a way to produce large-area detectors and detectors that are sensitive to light in the mid-infrared wavelength range.

Finally, Chapter 7 gives the outlook and conclusions of this thesis. It describes the advances in the design of SNSPDs made by my contributions, particularly methods to increase the device detection efficiency without sacrificing speed. It also provides some directions for future work to improve the accuracy of the optical measurements of film thickness and to optimize and fabricate the optical nanoatennas.

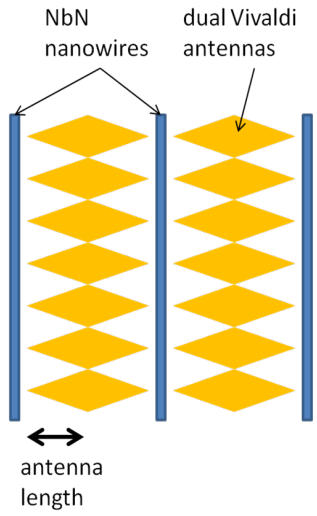

(a) double-threaded dual Vivaldi antenna design

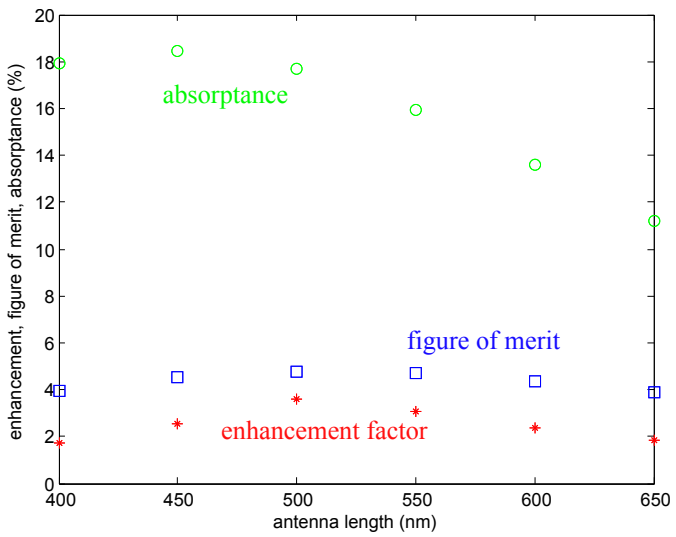

(b) enhancement factor, FOM and DDE vs. $L_{\text{double Vivaldi}}$

Figure 7: (a) Geometry for the "double-threaded" dual Vivaldi antenna. (b) Enhancement factor, figure of merit and device detection efficiency versus length of the double-threaded dual Vivaldi antenna. The enhancement factor is the ratio of the absorptance with and without the antenna present, the figure of merit is discussed in Chapter 6, and the device detection efficiency is assumed to be equal to the Joule heating in the nanowire.

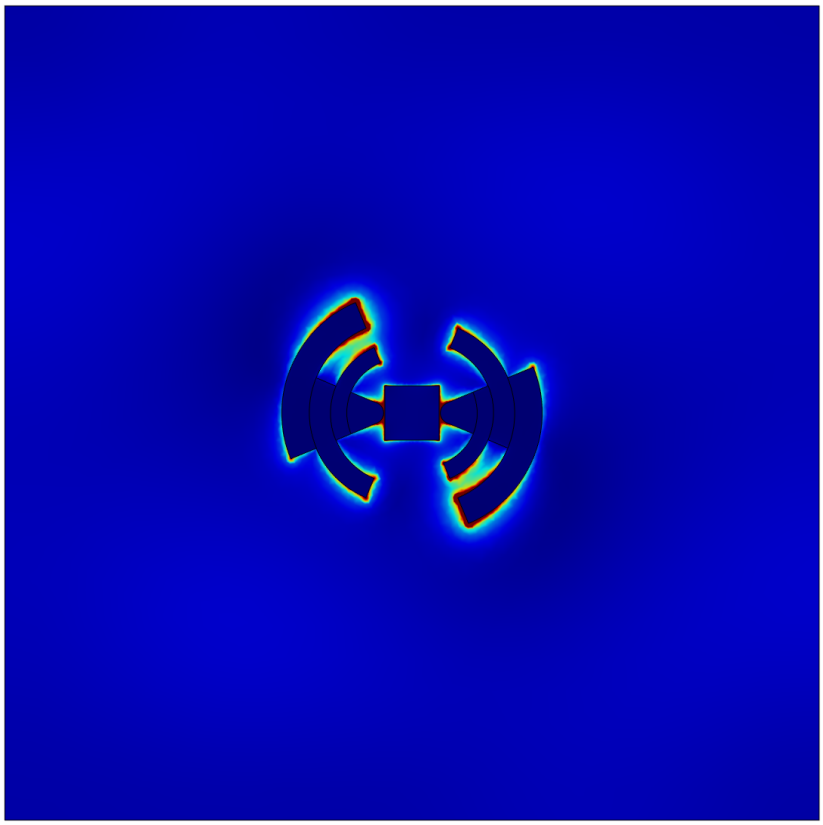

Figure 8: Electric field intensity surrounding the gold log-periodic antenna and NbN patch (square in the center of the image) for incident light at a wavelength of 5 μm. The color range is from 0 (dark blue) to 10 V/m (red). The log-periodic antenna is composed of arcs that function similarly to dipole antennas and contribute to the overall response of the antenna to incident light.

1

Fabrication of SNSPDs

The process developed to fabricate the devices based on the optical designs in this thesis is described below. Solutions to several problems that are commonly encountered during fabrication are also given for future reference. Then, the characterization method we use to screen for high-performance devices is outlined, which includes a method to quantify the amount of "constriction" in a device and thus the device quality. Finally, a new type of device design, the condensed 4-SNAP, is presented, which provides an example of how finite element modeling and experimental results can be

used to optimize the design of devices with high detection efficiencies.

1.1 Fabrication Process For a Device Without An Optical Cavity

Figure 1.1 shows the process of fabricating a typical device. First, a thin (approximately 4-nm-thick) NbN film is sputter coated onto a substrate, which is typically a 1 cm × 1 cm chip. The growth of this film and its material characteristics is described in more detail in Chapter 2.

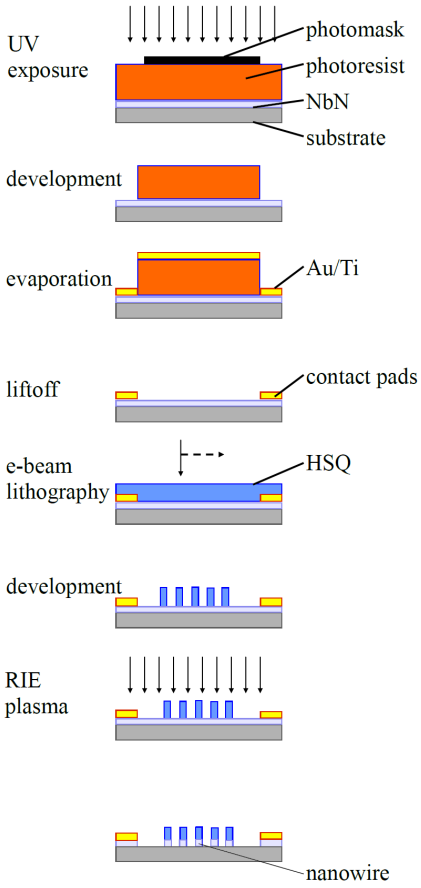

Figure 1.1: Schematic of the steps in the fabrication process of SNSPDs from a starting material. The gold contact pads are defined through photolithography with ultraviolet light. Then, electron beam lithography is used to define the pattern of the device in HSQ, which is a negative tone resist. After the HSQ is developed, reactive ion etching removes the NbN film that is not covered by HSQ, leaving the patterned NbN device.

There are two main classes of substrates: those that are transparent in the visible and those based on silicon. Magnesium oxide and sapphire (purchased from MTI Corporation) have been used in the past because their lattice constants are close to that of NbN. These substrates are transparent to visible light, and thus the NbN film thickness could be measured using a visible reflectometer (see Chapter 3). However, the substrate height is measured in the Elionix e-beam writing tool using a visible laser, and the reflection from transparent substrates is often not strong enough for the tool to determine the height correctly. Therefore, writing devices on MgO and sapphire requires an extra step, described below in Section 1.2.3.

The substrates based on silicon are not transparent in the visible, and the thickness of NbN films on silicon must be measured with an infrared transmittometer (see Chapter 3). The advantage of silicon-based substrates is the inclusion of silicon dioxide or silicon nitride layers that can act as anti-reflection coatings on the back side of the chip and as an optical cavity between the silicon and the device to enhance optical performance. Double sided silicon wafers with thermally grown silicon dioxide on both sides are obtained commercially from Silicon Valley Microelectronics. The silicon nitride is grown on silicon substrates via by Bob Bicchieri, and the thermal oxide is grown by Bernard Alamariu, both in the Microwave Technology Laboratory (MTL) at MIT[39].

After growth and characterization of the NbN film, gold pads for electrical contact of the the devices are fabricated via a liftoff process. Typically, a layer of photoresist (Shipley S1813) is spin coated onto the substrate (5.5 krpm for 60 s) and baked at 110 °C for 90 s, and then the pattern is exposed using a mask and a source of UV radiation with a power of 2750 $\mu W/cm^2$ for 22 s (for a total dose of 60 mJ/cm^2). The photoresist is developed in CD-26, a dilute solution of tetramethyl ammonium hydroxide (TMAH), for 15 s and then rinsed in a stream of deionized water for 1 min before drying with compressed nitrogen. A sticking layer of titanium (10 nm) and a layer of gold (15 nm) are evaporated on the chip. The photoresist is then lifted off by squirting acetone, methanol and isopropyl alcohol (IPA) for several seconds. Sometimes soaking in acetone for several minutes or sonication in

acetone is required before the photoresist can be lifted off by squirting with acetone, methanol and IPA.

The gold pads can also be fabricated via a bilayer liftoff process that was adapted by Faraz Najafi from the suggestions provided by the manufacturer[40]. In this case, a layer of polymethylglutarimide (PMGI) is spin coated at 4 krpm and 2 krpm/s acceleration and baked at 90 °C for 2 min. It is followed by a layer of S1813, which is spin coated at 5.5 krpm and 1 krpm/s acceleration and baked at 90 °C for 2 min. The same UV source is used, but the exposure time is only 11 s, which corresponds to a dose of approximately 30 mJ/cm^2. The pattern is developed in CD-26 for 24 s and rinsed in deionized water for 60 s. The titanium and gold are evaporated as described above. The liftoff is performed by squirting with acetone to remove the S1813 and then sonicating in CD-26 for 1 min to remove the PMGI. CD-26 contains TMAH, which is ultimately damaging to NbN. However, it is a dilute solution, and, in other methods of device fabrication, sonication in CD-26 is used to remove the oxide layer on the NbN to promote HSQ adhesion.

NbN oxidizes when exposed to air, so the liftoff process is typically not performed until right before the electron-beam writing step. After liftoff, a layer of hydrosesquisiloxane (HSQ) is spin coated at 5 krpm and an acceleration of 10 krpm/s. It is also helpful to first spin coat a dummy sample of silicon and check the HSQ thickness on the dummy sample using an ellipsometer. With a given index of refraction of 1.38 for 632 nm light, the HSQ layer should be 54 nm thick.

The HSQ must be patterned in the e-beam writer shortly after spin coating and is typically done within half an hour, though it is not clear how long the time frame between spinning and writing can be before the HSQ ages and the device quality suffers. It probably depends somewhat on environmental factors, such as the relative humidity because any exposure to water can cause the HSQ to begin to gel.

The electron beam writing is performed with an Elionix F-125 at an accelerating voltage of 125 kV. The overall pattern to be written is placed using two registration marks. The pattern for an individ-

ual device is typically divided into the device active area and the leads to the gold pads. The device active area is written with a 200 pA current using a 1.25-nm spacing (240,000 dots in a write field of 300 μm × 300 μm). The exposure time per dot is typically around 0.36 μs (which corresponds to a dose of 4608 $\mu C/cm^2$), but every write includes a range of exposure times to take into account the varying sensitivity of HSQ as it ages. The electrical leads are written using a 2 nA current with a dot exposure time of 0.24 μs (a dose of 30720 $\mu C/cm^2$), and every other dot is skipped to further reduce the total dose and decrease the write time.

Once removed from vacuum, the HSQ is developed in TMAH (25%) at a temperature of 25–30 °C for 1.5 min by placing the chip face up in a beaker of TMAH that is warmed in a water bath. Higher temperatures seem to produce better contrast in the HSQ pattern, which has been founded previously [41]. During the first 30 s of development, a pipette is used to blow bubbles from the surface. After development in TMAH, the chip is rinsed in deionized water from a faucet for 1 min and blown dry under nitrogen flow. At this point, it is helpful to view the pattern under SEM to check for adhesion problems and to measure the thickness of the lines produced by different doses.

The pattern in the HSQ is transferred to the NbN by reactive ion etching in tetrafluoromethane (CF_4) gas at a radiofrequency power of 50 W for 2:40 (min:s). Thicker films might require longer etching times, but it is typical to slightly over etch the devices anyway to ensure that there is not a thin film of NbN left between the nanowires. It is important not to etch for too long because the HSQ mask is also etched; in fact, a previous report suggests that 7 nm of HSQ are etched for every 1 nm of NbN [42].

This process produces devices without an integrated optical cavity on top; details of the fabrication of an optical cavity are given in Chapter 5. Below are some common problems with device fabrication and their solutions.

1.2 Common Fabrication Problems

Some typical problems encountered in the fabrication of SNSPDs are described below. Issues such as adhesion and write fracturing may not destroy a device if they are not severe, but they might lead to constrictions[43] and reduce the device quality and the yield of the chip. Solutions to these problems that have been found by members of this group are included for future reference.

1.2.1 Adhesion of HSQ

Occasionally, the HSQ pattern lifts off as well during HSQ development, as shown in Figure 1.2, and, in extreme cases, the devices can be destroyed or disappear entirely. A lack of adhesion is hypothesized to be due to exposing the NbN to air (as when storing them on a shelf in the laboratory or in a nitrogen box with a leak) because a niobium oxide develops. The HSQ developer can then attack both the unexposed HSQ and the native oxide underneath the HSQ that has been exposed, leading to poor adhesion of the written HSQ features[44]. To solve this problem, do not perform liftoff for the gold pads until shortly before spinning on the HSQ to minimize the exposure of the NbN film to air. Alternatively, the NbN film can be dipped in a solution containing TMAH before spinning on HSQ because niobium pentaoxide is soluble in strong bases[45].

The design of the device also seems to affect the adhesion of HSQ. For example, in Figure 1.3, note that the adhesion issues tend to occur where the lead meets the device at a right angle. Perhaps some stress in the film develops during the writing process and is released in the development process, which leads to poor adhesion. Devices that are designed such that the lead connects to the write pattern in a straight line do not have this issue; designs with multiple nanowires in parallel also seem to be robust (as discussed in Section 1.4).

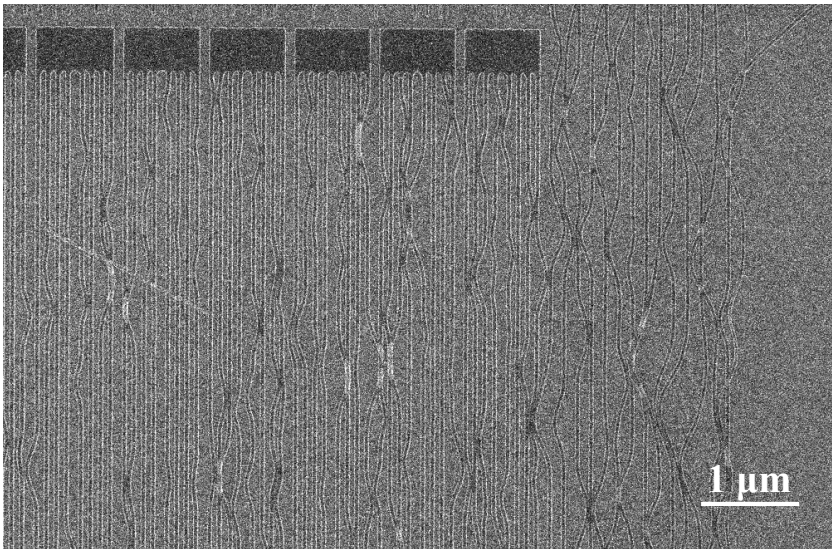

Figure 1.2: SEM image showing that the HSQ lines detached from the film surface during HSQ development. This adhesion problem is likely due to oxidation of the NbN surface before the HSQ was spun on. Then, the TMAH used to develop the HSQ also attacked niobium pentoxide beneath the HSQ.

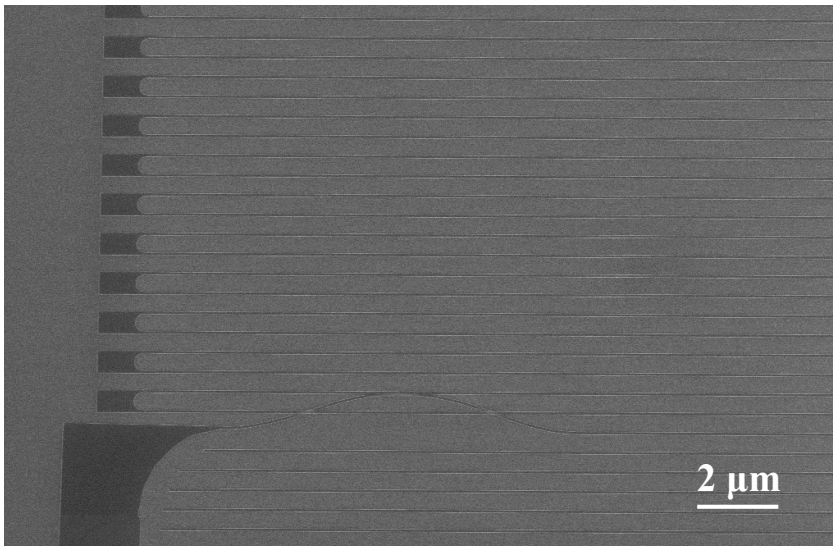

Figure 1.3: The HSQ line that is connected to the larger electrical lead did not adhere well to the film surface during HSQ development. However, the other lines of the device pattern do not seem to have detached from the surface. It is possible that strain developed in the HSQ film during the e-beam writing process, which caused the nanowire to lift off of the surface during development.

1.2.2 Write Fracturing

Figure 1.4 shows an example of write fracturing. When write fracturing leads to a gap between features, such as a gap between nanowires and the turns in the meander pattern as shown here, the NbN underneath the gap can be damaged or removed during the RIE step, leading to an open circuit. The Elionix software does not necessarily write the device from left to right (which would be appropriate for vertical nanowires) or top to bottom (appropriate for horizontal nanowires), but sometimes writes one section and then goes back later to write another. Because alignment is not perfect and varies slightly over the course of the e-beam writing process, the sections written later might not match with the sections previously written. Therefore, it is important to change the Elionix files (specifically the .cc files) to force them to write from left to write (or top to bottom for horizontal nanowires). This change can be made with a MATLAB script written by Qingyuan Zhao, which is provided in Appendix A.

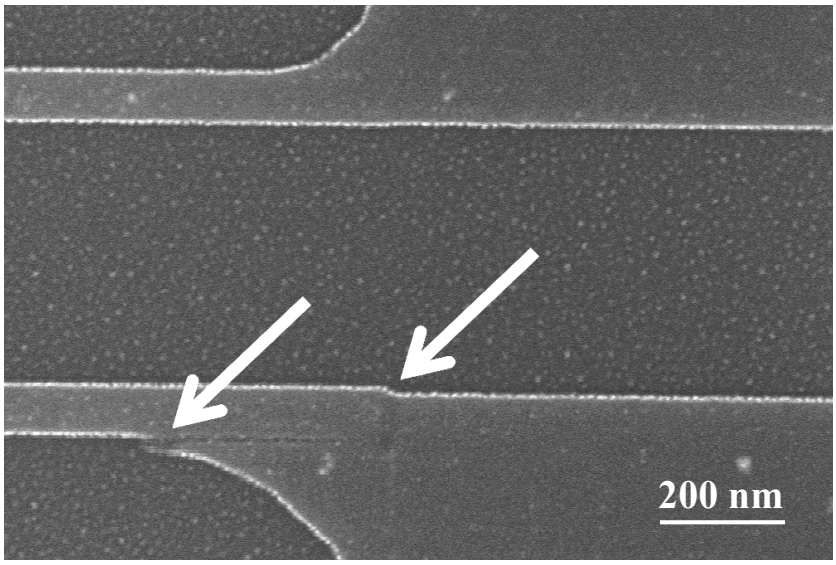

Figure 1.4: The white arrows show defects in the HSQ pattern due to the slight misalignment between the nanowire and the turn in the meander pattern due to write fracturing. An extreme mismatch can lead to an open circuit, but even a small defect in the nanowire can lead to current crowding and thus poor device performance.

1.2.3 Height Sensor Malfunctions With Transparent Substrates

As mentioned above, transparent substrates with only a thin layer of NbN do not reflect enough light for the Elionix height sensor to function correctly. In the worst case, the Elionix software will default to the height given in the "Set Options" dialogue, and the beam will be severely out of focus for most if not all of the devices. This problem is less damaging if optical cavities or other large features are written, however.

In this case, the Elionix software must be given a map of the height of the chip, which can be approximated as a tilted plane. First, measure the height of three points on the chip that are covered with gold (typically near the edges) with the height sensor. Then, calculate the height of the surface of the entire chip by approximating the chip as a flat plane. This procedure can be performed with a MATLAB script written by Qingyuan Zhao, which will produce a .csv file that can be input to the Elionix program. This script can be found in Appendix A.

1.3 Characterization of Detectors

The detectors are characterized after fabrication in the probe station setup that has been described elsewhere [46,13], which has a moveable RF probe connected to room temperature electronics outside the probe station through a coaxial cable and a vacuum feedthrough. The probe can contact each device on the chip in turn, and thus the chip can be rapidly screened. The room temperature resistances are measured first, and then the chip is cooled to approximately 3 K to measure the switching currents of the devices. The device detection efficiencies (DDE) of the most promising detectors are then tested by flood illuminating the device from an optical fiber inserted into the probe station with 1550-nm light from a pulsed picosecond laser that is attenuated to the single-photon level. The polarization of the light is adjusted to maximize the detected signal.

To measure the DDE, first, the bias current is ramped up to the switching current, and the num-

ber of voltage peaks above a certain threshold (typically 150 mV) in the readout line is measured. This procedure is first done with no light incident on the device to determine the dark count rate. Because the chip is exposed to 40 K radiation from the shield and any radiation that leaks into the chamber through the fiber, the dark count rate includes both stray photons and the intrinsic dark counts of the device. Then, the device is flood illuminated with the 1550-nm pulsed picosecond laser, which forms a spot size of several millimeters on the chip, and the bias current is ramped again while measuring the number of voltage spikes. The device detection efficiency calculated depends on the area of the device because the light is not focused to a spot on the device. The light that is incident on the chip but not on the device under test is not considered when determining the device detection efficiency, although it would need to be considered if we were characterizing the system detection efficiency of the probe station.

In general, it is assumed that constrictions, such as caused by line edge roughness due to poor lithography, will lower the switching current. Poor device quality across the chip will lead to large variations in the switching current among nominally similar devices because of the statistical distribution of constrictions. Thus, the next section describes how devices are screened to select only the best for DDE measurements.

1.3.1 Screening Devices

Due to the long electron-beam writing time required to fabricate optical cavities (2 hr for a chip with 225 devices), the devices on chips are screened first by measuring the room-temperature resistance and the switching current. The best devices are then further screened in terms of the device detection efficiency, and, if the DDE is high enough, optical cavities are added to boost the DDE by more than a factor of 2 or 3 depending on the specific device geometry. The room-temperature resistance is measured with a multimeter. Low variation (less than 5%) between devices of a similar geometry on a chip is generally a good sign. A high variation, or several devices that are open, gener-

ally indicates a problem with the fabrication of the chips, for example, poor liftoff of the gold pads leading to poor connection between the gold pads and the NbN leads.

The switching current is the bias current at which the devices switch from superconducting to normal phase as the current is ramped up. The slew rate in our setup is very slow (pn the order of microamps per second, depending on the step size), which leads to some noise in the results as dark counts cause the devices to switch at lower currents, but a better setup that can measure both the switching current and the retrapping current (the current at which the devices switch from normal to superconducting as the bias is ramped down) can give a histogram of the switching currents measured. A constricted device will have a switching current determined by the narrowest regions, material defects or areas with local current crowding. It is assumed that the constricted regions do not affect the resistance much because they are very short in length.

The devices are initially screened by plotting the inverse of the switching current versus the resistance. The best devices will have a relatively high switching current for their resistance (and a relatively low inverse of the switching current) because they will not be constricted. A chip with a consistent quality will have data points that lie along a line. Figure 1.5 shows a plot for a chip labeled SPE223, whic has several promising devices.

Another way to characterize devices is in terms of their "effective widths". Given the sheet resistance of a film, the expected resistance of a device with a given length and width can be calculated. The effective width according to resistance ($w_{\mathrm{eff,R}}$) is the width calculated with the length (l), sheet resistance (R_S) and measured resistance (R) of the device:

$$w_{\mathrm{eff,R}} = \frac{l}{R/R_S} \tag{1.1}$$

The sheet resistance, however, changes during fabrication, so the sheet resistance to use is not that measured before fabrication but that calculated by measuring the resistance of wide test lines and

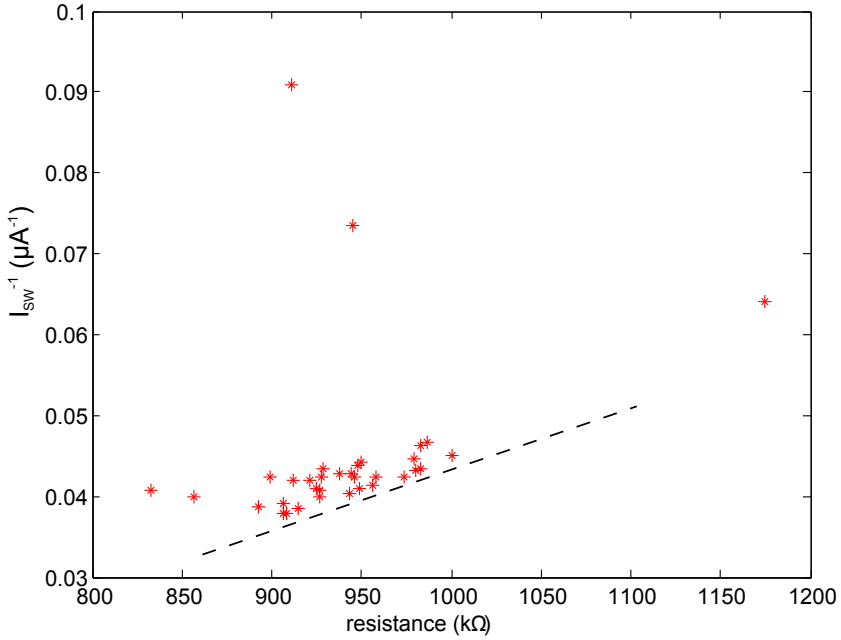

Figure 1.5: Inverse of the switching current versus resistance for devices on a single chip (SPE223). The dashed line is a guide for the eyes. The best devices will have a low inverse of the switching current for their resistance. This chip has many promising devices that form a clear linear trend, along with some outliers that will probably show poor performance.

dividing by their number of squares to get the resistance per square (the units of sheet resistance).

The effective width according to the switching current ($w_{\text{eff},I_{\text{sw}}}$) can be calculated as

$$w_{\text{eff},I_{\text{sw}}} = \frac{I_{\text{sw}}}{\max(I_{\text{sw}}/w)} \tag{1.2}$$

where $\max(I_{\text{sw}}/w)$ refers to the maximum switching current to width ratio of the devices on the chip. This equation essentially normalizes the widths of the devices by the best device on the chip, which is assumed to have the nominal thickness, rather than giving an absolute value for the effective width that can be compared across devices.

The effective widths can be plotted against each other, as shown in Figure 1.6, which will give the same results for "good" devices as Figure 1.5 above because Figure 1.6 is essentially plotting I_{sw} versus

R but with different prefactors. The ratio of the effective widths ($w_{\text{eff},I_{\text{sw}}}/w_{\text{eff,R}}$) offers a quantitative value for the constriction factor and gives an intuitive sense of the amount of narrowing in the device due to constrictions. For example, the best device on the chip will have an effective width according to I_{sw} equal to the nominal width of the devices, and devices that have more constrictions will have a narrower effective width. The difference between the best device and the worst on a chip in terms of I_{sw} can be large, with the worst devices having an effective width according to I_{sw} of 0 if they are resistive even with no applied current. The effective width according to resistance shows much less variation across chips (generally within 5%), and the variation that is present is likely due to the variation in the actual width of devices that were written with different doses.

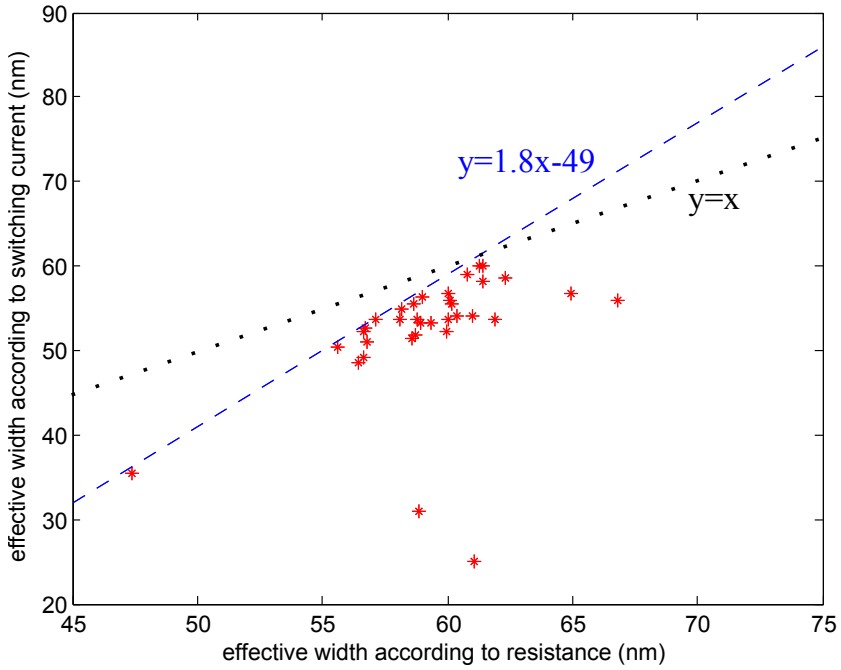

Figure 1.6: Effective width according to switching current ($w_{\text{eff},I_{\text{sw}}}$) versus effective width according to resistance (w_{R}) for devices on SPE223. The dashed line is $y = 1.8x - 49$, which is provided as a guide for the eye. In theory, a line fitting the effective widths of the promising devices should cross the origin, but it does not here in part because the effective widths according to I_{sw} are normalized by assuming that the device with the highest switching current has a value of $w_{\text{eff},I_{\text{sw}}}$ equal to the nominal width. Ideally, the points would fit the equation $y = x$, indicating that the effective widths are equal, which is shown here with a dotted line.

Figure 1.7 gives the device detection efficiency versus the ratio of the effective widths. The trend of the plot shows that devices with a larger value for the ratio of effective widths have a higher DDE. This trend is expected because devices with fewer constrictions (or less severe constrictions) should have both a higher DDE and a higher ratio.

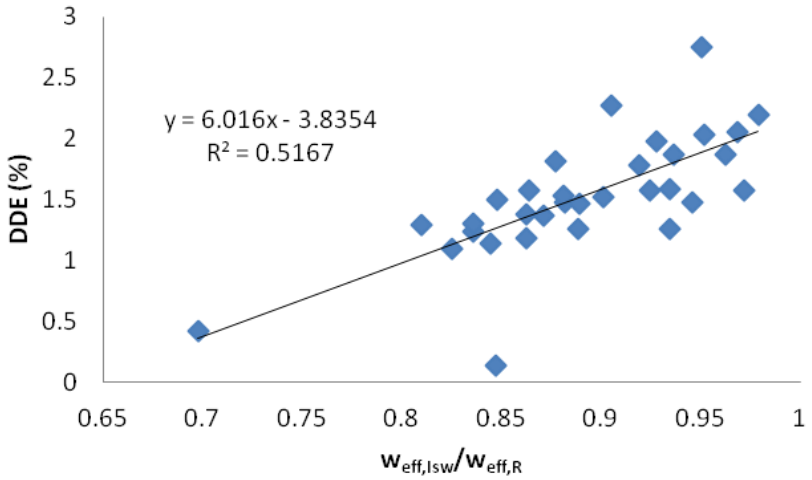

Figure 1.7: Device detection efficiency (DDE) versus the ratio of the effective widths for devices on SPE223. The trend indicates that the DDE increases with the effective width ratio, which suggests that the effective width ratio can be used to screen for promising devices before measuring the DDE.

Except in a few cases with very poor fabrication, the "constricted" devices do not look different than the unconstricted ones under SEM. That is, the narrow regions or defects that lead to low switching current are not visible under SEM along the nanowires. It is possible that the so-called "constrictions" arise due to defects between the substrate and NbN film that are not visible in a top-down SEM view, that they are material defects that do not affect resistance but do affect the flow of Cooper pairs, or that the design of the turns in the meander are not ideal and lead to vortex entry[36].

1.4 Superconducting Nanowire Avalanche Photodetectors (SNAPs)

Some of the results reported use superconducting nanowire single photon detectors[47] (SNAPs) rather than SNSPDs. SNAPs consist of two or more nanowires connected in parallel, rather than a single nanowire, as in the typical SNSPD meander pattern. The main advantage of this geometry is the increase in the single to noise ratio of the output of the detector by a factor of approximately the number of nanowires in parallel, N[47]. A higher SNR allows thinner nanowires that are more sensitive to IR photons to be used[23].

Figure 1.8 shows the structure of a series SNAP[48] with three parallel nanowires (N=3). The current is split between the three parallel branches equally. When a photon triggers the formation of a hotspot in one branch, current is diverted into the other two branches. The critical current is then exceeded in the other branches, and a voltage difference can be detected across the entire device. The geometry of the turns in the structure that are in series with the section that switches to normal is designed such that their kinetic inductance is sufficient to keep the device from latching, which can be a problem if there is no inductance in series with the SNAP[49].

1.4.1 Condensed Series SNAPs

An improvement in the design of series SNAPs can be achieved by increasing the fill factor of the devices, which in turn increases the device detection efficiency. In SNSPDs, both corners of a turn in the meander pattern must be curved with the ideal shape[36] to prevent current crowding. In series SNAP devices, however, there is an opportunity to condense the design and increase the fill factor, as demonstrated in Figure 1.9. In Figure 1.9a, a current is run through one turn of a conducting 3-SNAP structure. Because the current from the leftmost three branches does not immediately flow into a nanowire running in the opposite direction, there is no current flow in some of the curved sections, for example, the area indicated by the arrow. Figure 1.9b shows the current density when

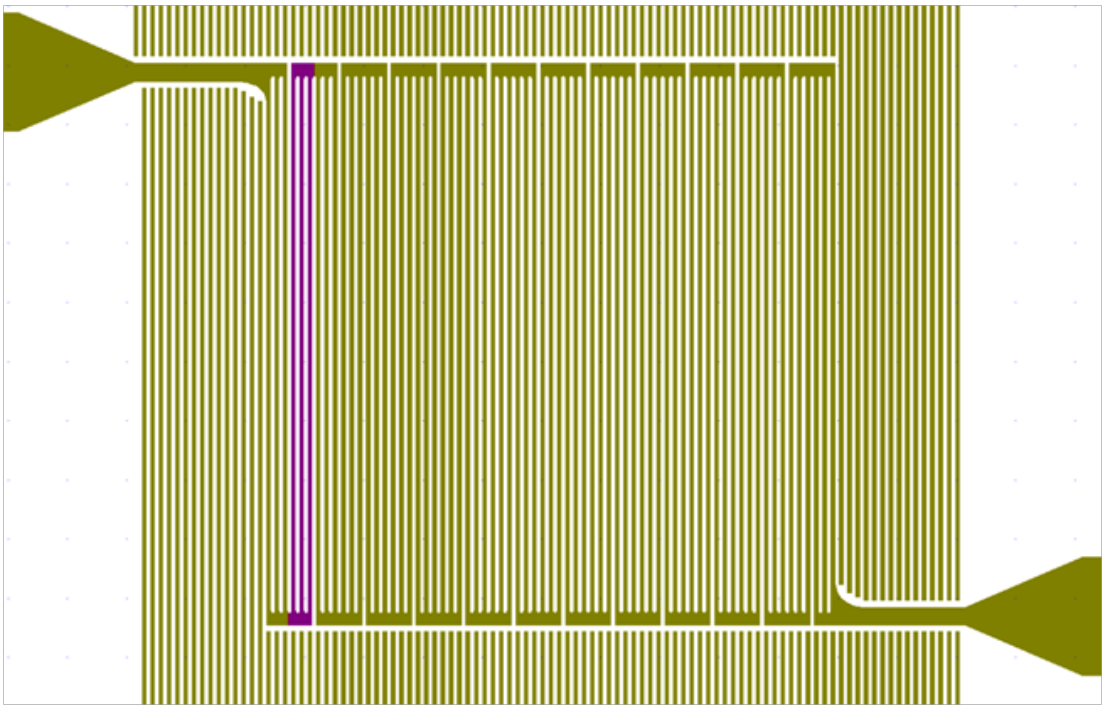

Figure 1.8: Schematic of a "series 3-SNAP", a series SNAP with three nanowires in parallel. The highlighted segment shows the three nanowires in parallel. The benefit of a series SNAP is that a separate inductor need not be fabricated in series with the device if the size and number of segments is correctly designed.

the 3-SNAP geometry is condensed by eliminating the unnecessary curved sections. In this way, a 3-SNAP composed of 60 nm nanowires with a 140 nm pitch, which has a fill factor of 42.9%, can be condensed into a pattern with a fill factor of 52.8%, and a similar 4-SNAP can be similarly condensed to a fill factor of 54.5%. A larger fill factor means a larger absorptance, which in turn can lead to a higher device detection efficiency. The maximum possible fill factor for an SNSPD meander pattern that has ideal turns to prevent current crowding is only 33%[36].

Figure 1.10 shows an SEM image of a condensed 4-SNAP (c4-SNAP). These structures are somewhat more challenging to fabricate than other SNSPD and SNAP structures because the density of the pattern at the turns is higher, as is the overall pattern density, which leads to more complicated proximity corrections. However, sufficient proximity effect correction is provided by writing these

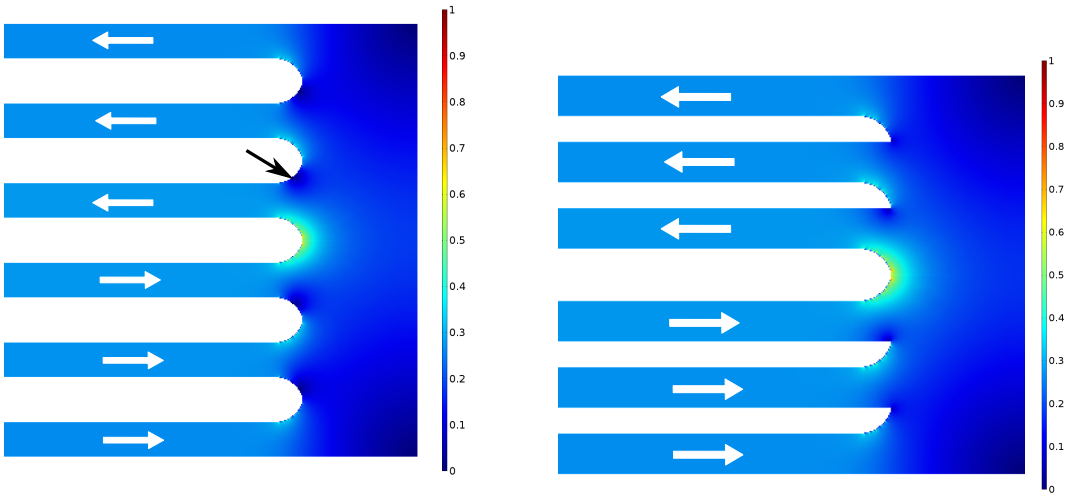

(a) 4-SNAP **(b)** c4-SNAP

Figure 1.9: (a) Normalized current density in one turn of a 3-SNAP pattern. The black arrow indicates an area where the current density is zero. The current flow is as indicated by the white arrows. The bright area in the middle of the turn is due to current crowding because the turn is slightly tighter than optimal. The somewhat bright areas along the edges of the other turns are an artifact of the size of the steps in the model. (b) Normalized current density in one turn of condensed 3-SNAP pattern, where the areas of the curve with no current in (a) have been eliminated. The current crowding seen in the middle of the turn is as in the case of the 3-SNAP.

patterns at a relatively low dose and using the same grating structure that is used for the 4-SNAP pattern.

Another possible advantage of the condensed 4-SNAP design besides the higher fill factor is the smaller area of the loop formed by adjacent nanowires, which could lead to fewer trapped vortices that tunnel out during device operation and decrease the switching current, thus limiting device operation. Figure 1.11 shows the device detection efficiency for high-efficiency c4SNAP and 4SNAP devices written on the same chip. The nominal widths of the nanowires in both devices was the same, though the c4SNAP nanowires were narrower due to the lower dose used to write them. The DDE values for the 4-SNAPs and c4SNAPs on this chip are given in Table 1.1 and Figure 1.12. The average DDE for a c4SNAP was 6.89%, while the average for the 4-SNAPs was 4.69%. This differ-

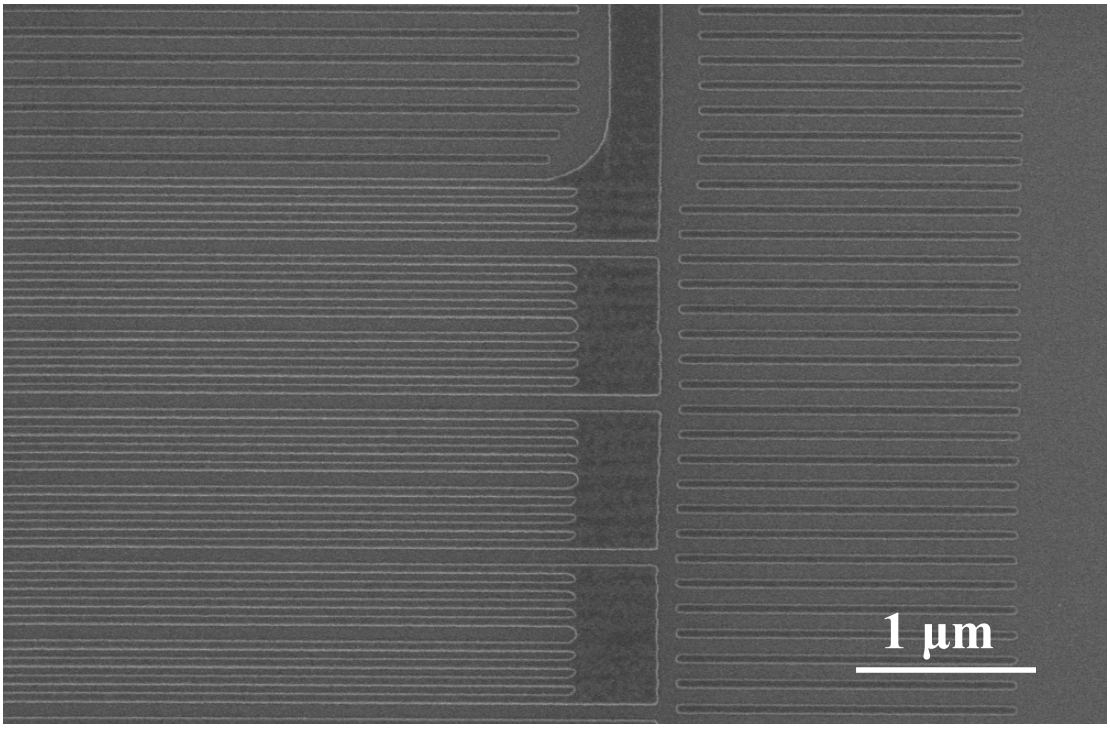

Figure 1.10: SEM image of three turns of the meander pattern of a condensed 4-SNAP that was successfully fabricated.

ence might be explained by the higher fill factor of the c4SNAPs, which can account for an increase in the DDE of about 25%, assuming equal nanowire widths. However, in addition, five of the six c4SNAP devices tested appeared to be saturated, while none of the 4-SNAP devices were saturated, which suggests that the c4SNAPs were generally not constricted, but the 4-SNAPs were.

Figure 1.13 shows the effective width according to the switching current versus the effective width according to the resistance for the 4SNAPs and c4SNAPs on this chip. The effective width according to the switching current was calculated with the same maximum switching current (42.8 µA) for each device, though the widths varied somewhat according to the electron beam dose, and the nominal width of 60 nm was used in the formula for $w_{\mathrm{eff},I_{\mathrm{sw}}}$. Therefore, the effective width according to the switching current is essentially just the switching current multiplied by a constant.

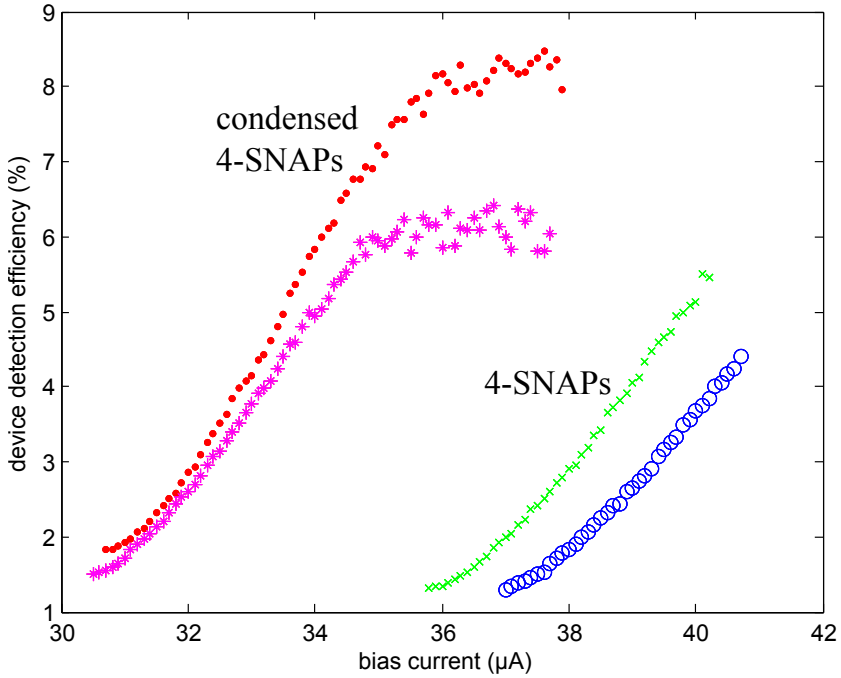

Figure 1.11: Device detection efficiency versus bias current of two c4-SNAPs (red dots and magenta stars) and two 4-SNAP devices (green crosses and blue circles) that were fabricated on the same chip. The DDE curves of the c4-SNAPS "roll over", but those of the 4-SNAPs do not. The difference in the maximum bias currents reached among the devices is likely due to the differences in the widths of the nanowires, which depend on both the nominal design width and the e-beam doses.

The effective width according to resistance was originally calculated with the sheet resistance of the film measured after deposition and before fabrication, but it gave effective widths of approximately 40 nm, which is much narrower than the nominal width of 60 nm. It was adjusted so that the maximum width according to resistance would be approximately 60 nm. In general, the sheet resistance of the films increases during fabrication, as has been measured with wide test devices.

The devices were written with different beam currents, and thus the actual width of the nanowires in the devices varies, which leads to the variation in the resistance between devices and therefore their effective widths. Interestingly, the effective widths for the c4SNAPs and 4SNAPs appear to lie on the same trendline, indicating similar levels of constrictions in both types of devices. Yet, the

Table 1.1: Device detection efficiencies of 4-SNAP and c4-SNAP devices from SPE259.

Device ID and Type	Device Detection Efficiency
H1 (c4-SNAP)	8%
H2 (c4-SNAP)	7.13%
H3 (c4-SNAP)	6.73%
H4 (c4-SNAP)	8.47%
H5 (c4-SNAP)	6.42%
H6 (c4-SNAP)	8.67%
K14 (c4-SNAP)	2.78%
I1 (4-SNAP)	3.78%
I2 (4-SNAP)	4.399%
I3 (4-SNAP)	6.38%
L13 (4-SNAP)	3.96%
L14 (4-SNAP)	4.12%
L15 (4-SNAP)	5.49%

DDE values of the c4-SNAPs are generally higher than those of the 4-SNAPs, indicating that there might be another reason for the relatively poor performance of the 4-SNAPs besides constrictions. One major difference between the 4-SNAP and c4-SNAP geometries is the area between adjacent nanowires in the meander pattern, which form loops of supercurrent. The number of vortices that can be trapped by loops of supercurrent depends on the area of the loop, and the low DDE of the 4-SNAPs might be due to vortex tunneling that reduces the switching current. Thus, the switching currents of devices of different size and pitch (and thus area of the supercurrent loops) should be measured to see if the critical current values differ from the expected current given the size and number of nanowires. It is possible that a greater number of devices must be tested to see a clear trend to support the hypothesis that trapped vortices lead the 4-SNAPs to have lower switching currents than c4-SNAPs composed of nanowires with the same actual widths.

The design of condensed 4-SNAPs could lead to higher fill factor devices and thus higher absorptances and higher device detection efficiencies. In addition, c4-SNAPs appear to better quality

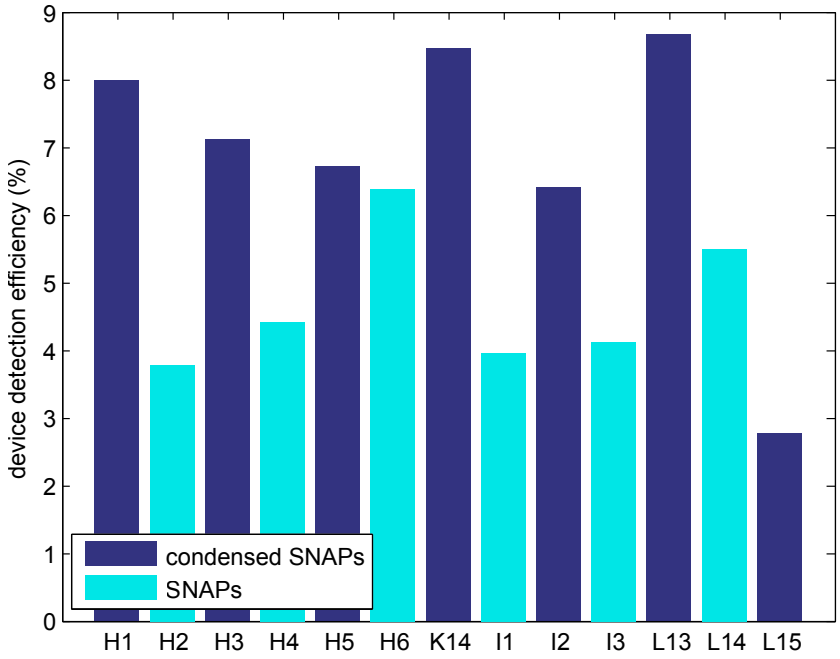

Figure 1.12: Bar plot of the device detection efficiencies given in Table 1.1. The condensed 4-SNAPs are shown in light blue, and the 4-SNAPs are shown in dark blue. In general, the condensed 4-SNAPs have higher device detection efficiencies.

devices than similar, less dense structures both in terms of the higher DDE values achieved and saturation behavior. Optical designs to increase the absorptance of light in NbN nanowires will lead to the highest DDE values if the NbN devices themselves are high quality and respond sensitively to light. Thus, the c4-SNAP pattern is a good candidate for use in device structures with more complicated optical design.

This chapter presented an overview of the fabrication of SNSPD and SNAP devices. It has gathered together some advice for nanofabrication that we have learned in recent years to improve device yield and described a method to quantitatively evaluate device quality using figures of merit derived from the room temperature resistance and the switching current. The selection of promising devices from a chip can in turn lead to more efficient testing. Finally, a new device design, the condensed 4-SNAP, is offered as an improvement on the conventional SNAP design because it has a higher fill

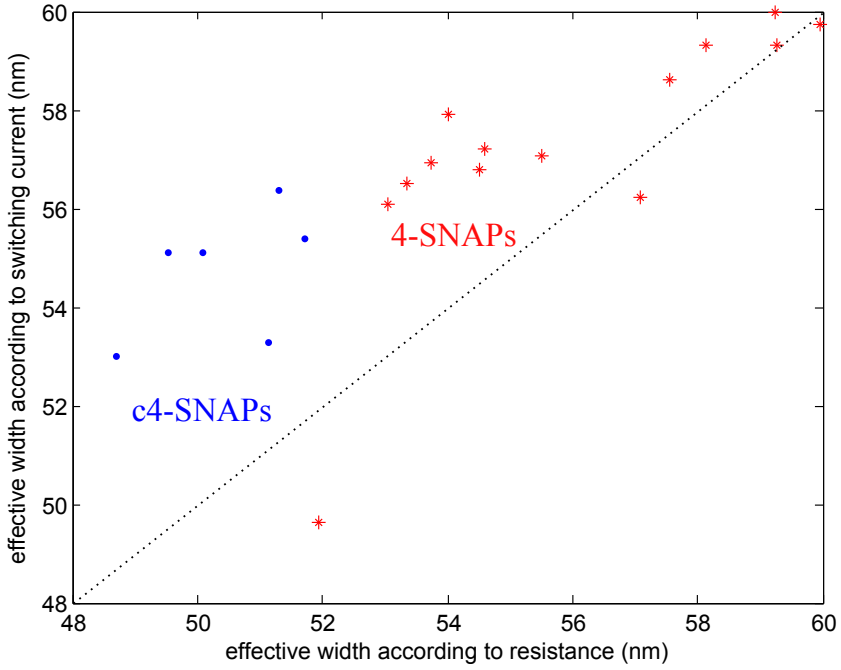

Figure 1.13: Effective width according to switching current versus effective width according to resistance of 4-SNAPs (red stars) and c4-SNAPs (blue dots) on SPE259. The devices all appear to lie on the same trend line, which shows that the ratio of the effective widths for each type of device is similar, and thus the amount or severity of constrictions in each type of device is similar, as explained in the text. In general, the c4-SNAPs were written with lower doses to control overexposure of the HSQ around the tight turns and are therefore narrower than the 4-SNAPs, making it difficult to compare the switching currents of these two types of devices directly.

factor and a higher device detection efficiency. The simulation of current flow through a different type of device can give us a deeper understanding of device performance and lead to incremental improvements in design that are crucial for achieving high-performance devices.

2

Materials For Detector Fabrication

The starting material for our detectors is a thin, 1-cm diameter film of niobium nitride (NbN) on a flat, 1 cm $\times$ 1 cm substrate. Niobium nitride is a type II superconductor that has a critical temperature of up to 17.3 K in the bulk material[50], which is one of the highest values for conventional superconductors. The coherence length of NbN is less than 5 nm, which allows the fabrication of thin (several nanometers) superconducting films with moderately high critical temperatures[51]. NbN is also attractive for devices because it is chemically stable in air and can be cycled from cryogenic

temperatures to room temperature without detectable degradation[51].

This chapter describes some of the material properties of NbN thin films characterized by x-ray diffraction, Auger electron spectroscopy and x-ray photoelectron spectroscopy. These methods give an indication of the stoichiometry and crystalline structure of thin films, and we initially employed them to determine if the starting material itself was responsible for the poor performance of our devices. For example, we used XPS to see whether there was oxygen in the lattice that might be leading to low switching currents. While none of the methods provided definitive evidence of a problem with the starting material, the results did give us information about the structure of our NbN films.

2.1 Deposition of NbN

The deposition of NbN is performed via DC magnetron sputtering with an AJA sputter coating system. The substrates, which are typically MgO, sapphire, or silicon with a nitride or thermal oxide, are mounted on a rotating stage above the niobium target. The chips are heated to 800 °C, and argon and nitrogen are flowed through the chamber. The temperature, deposition time, flow rates of gases and pressure in the chamber must all be optimized to produce high quality films. Typical values for the deposition of our films are approximately one minute.

After deposition, the chips are left in the chamber until it cools to room temperature. The chips are then characterized in terms of sheet resistance, critical temperature (T_c) and thickness. The thickness is determined optically using a reflectometer or transmittometer, as described in the next chapter. In general, the best films have a high critical temperature for their thickness, typically between 10 K and 12 K. It has been found elsewhere that the best films will be deposited under conditions that lead to a lattice parameter of 0.446 nm[52]. The optimal sheet resistance depends on the substrate and is determined in our group by which chips lead to the highest efficiency detectors.

Previous studies have considered the optimal growth conditions of NbN films[52] and have gener-

ally characterized films intended for use in SNSPDs with electrical measurements, such as the sheet resistance[53]. Here we investigated the films intended for SNSPDs using a wider array of methods, some of which are not generally suited for the analysis of such thin films but which nevertheless provided some information on the structure of the films. In particular, the methods described in this chapter give insight into whether the film is epitaxial on the substrate and whether it contains an oxide that might interfere with superconducting properties and lead to constrictions in devices.

2.2 Methods of Characterization

There are several methods to characterize thin films. This section presents some experimental results obtained by x-ray diffraction, Auger electron spectroscopy and x-ray photoelectron spectroscopy, and the next chapter focuses on optical methods of characterization. First, the difficulties of using x-ray diffraction are discussed along with results for an NbN film grown on MgO. Then, results using Auger electron spectrometry and x-ray photoelectron spectroscopy are compared to give insight into the chemical composition of films on MgO.

2.2.1 X-Ray Diffraction of NbN on MgO

X-ray diffraction was used to assess the quality of the NbN film on MgO. Because MgO has a similar lattice constant, it was assumed that the NbN would form a high quality, highly epitaxial film, but the XRD results showed that the NbN film was in fact highly defective, which may explain why devices on MgO did not have the high detection efficiencies previously observed with sapphire[46]. High resolution x-ray diffraction (HRXRD) is a method to study the crystalline structure of solids using an incident x-ray beam at a known wavelength that is then elastically scattered by the planes of atoms in crystals. The scattered beam intensity and angle can be studied to determine the density of electrons within the crystal and thus the locations of atoms and the degree of disorder in the crystal.

A sample with an estimated 5 nm of NbN on MgO was tested using high-resolution x-ray diffraction (HRXRD) on a Bruker D8 High-Resolution XRD. The MgO substrate was obtained from MTI and used without cleaning, and the NbN was deposited at 800 °C for 85 s at a chamber pressure of 1.5 mTorr and argon and nitrogen flow rates of 26.5 and 6 sccm, respectively. The deposition power was 156 W, and the current was 400 mA. Because the MgO substrate was oriented in the <100> direction, the NbN film was assumed to be oriented in this direction as well. The (200) peak of the MgO was very apparent, as shown in Figure 2.1, but it was a double peak, indicating that the MgO substrate was twinned.

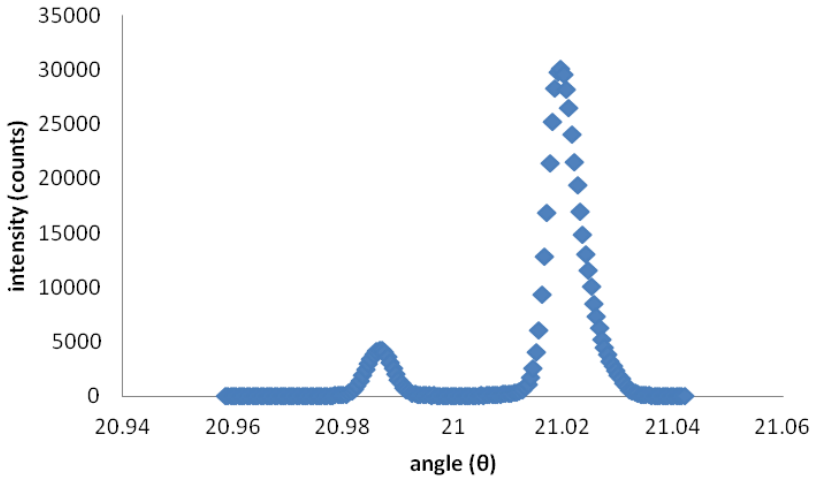

Figure 2.1: Diffraction of the (200) planes of MgO, as measured in a rocking curve, for a sample with a thin film of NbN on MgO. The two peaks indicate the presence of twinning in the MgO crystal structure.

Figure 2.2 shows the NbN(200) peak, which had a very low intensity due to the short exposure time and the thinness of the film. The spot size of the x-ray beam on the sample was less than 1 mm, so the area of the film was much larger than the area sampled by the x-ray beam. The appearance of this peak at all indicates that the film is crystalline and not amorphous or polycrystalline. However, the insertion of an analyzer crystal into the detector to accept a smaller cone of scattered radiation led to the disappearance of the peak, which suggests that the film has a very high defect concentra-

tion and is not epitaxial with the substrate. A reflectivity scan was used to confirm the thickness of the film, which suggested that the NbN film thickness was 5 nm using the NbN(200) peak shown above. The thin film is probably highly strained due to the slight lattice mismatch between MgO and NbN.

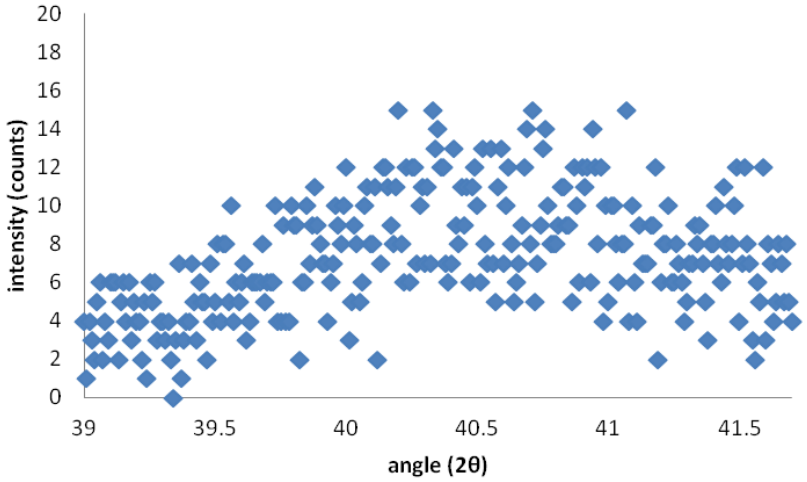

Figure 2.2: The (200) peak of the NbN film on MgO. The peak is very small because the film is very thin and thus the signal from it is weak.

A scan was performed in the range of 68° to 75° to find the asymmetric NbN (311) peak. The (311) peak of the NbN, which was very weak, appeared at roughly 70.7°, which indicates a great amount of strain in the film. This angle indicated a d-spacing of 1.33 Å for these planes. The positions of the (200) and (311) peaks in the 2ϑ scan together yield lattice constants of NbN of 4.46 Å along the direction of growth and 4.25 Å in plane using the following formula:

$$\frac{1}{d^2} = \frac{h^2 + k^2}{a^2} + \frac{l^2}{c^2} \tag{2.1}$$

Here, (*hkl*) refer to either (002) or (113), and the respective d-spacing values are 2.2288 and 1.332 Å, as determined by the position of the peaks in the 2ϑ scan. The values of *a* and *c*, which are the lattice

constants in plane and perpendicular to the surface of the film, respectively, can then be determined. NbN is a cubic crystal, but the values of the lattice constants in plane and out of plane are not equal, which indicates that there is tetragonal distortion. (The actual in plane and out of plane strains can only be calculated only if the relaxed lattice constant for an NbN bulk film grown in these deposition conditions (i.e., the exact stoichiometry) is known.) Despite the preliminary nature of the HRXRD study, it was clear that the NbN films are single crystalline, highly defective and strained.

2.2.2 Auger Electron Spectroscopy (AES) of NbN on MgO

In Auger electron spectroscopy (AES), an incident electron beam is used to induce Auger recombination within a sample, and the Auger electrons emitted from the sample are then characterized. In Auger recombination, an incident electron removes a core electron in an atom. An electron in an outer shell of the atom can then transition into the lower energy position and lose an amount of energy equal to the difference between the shells. Then, this energy can be coupled to an electron in an outer shell, which will be emitted if the energy transferred is larger than the binding energy. The kinetic energies of the Auger electrons detected reflect the orbital energies of atoms in the sample, and so the Auger spectra of samples give unique chemical signatures and can be used to determine the elements present. The depth that AES can investigate is limited to a few nanometers and depends on the mean free path of Auger electrons in the sample, and thus this technique is appropriate for thin films.

AES was initially used to determine the relative stoichiometries of NbN films. Several films were investigated with a PHI 700 Scanning Auger Nanoprobe at 2 kV and 1 μA. Figure 2.3 shows the intensity of the Auger signal from different atomic species with depth (the sample was sputtered in 0.1 min intervals over a 3 mm × 3 mm area) for a typical film on MgO (SPD017). Figure 2.4 shows a similar plot using the calculated atomic concentration for niobium and nitrogen.

All films tested showed evidence of a surface oxide and then a relatively stable composition within

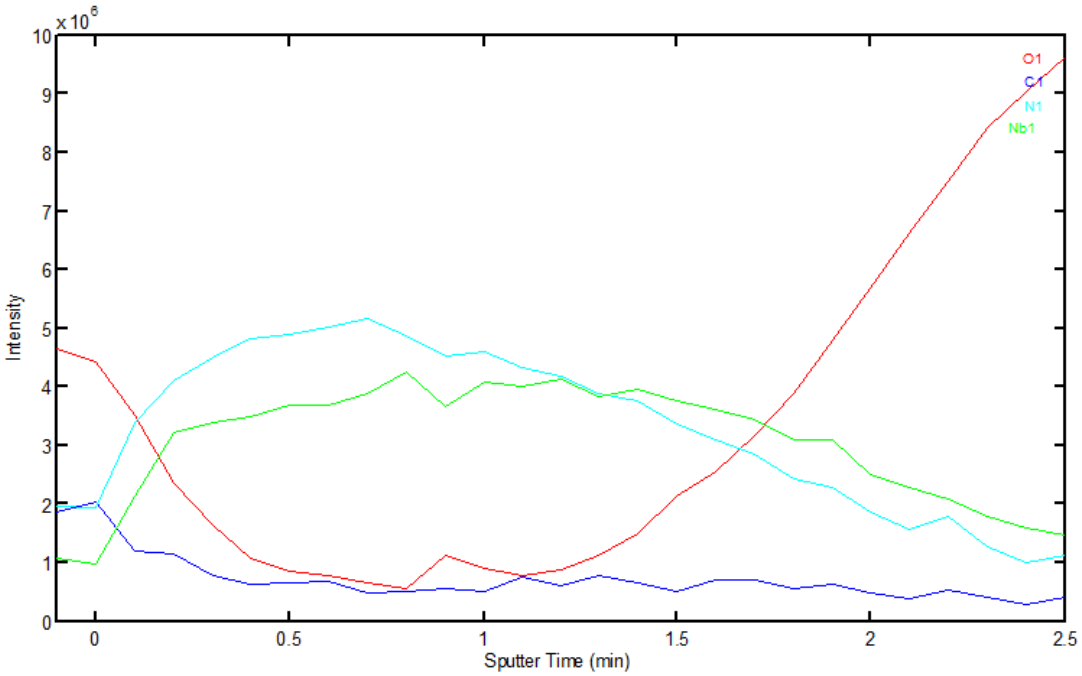

Figure 2.3: Intensity versus sputtering time (which is a proxy for the depth into the sample) of the peaks associated with four atomic species: oxygen (red), carbon (dark blue), nitrogen (cyan) and niobium (green). The carbon signal decreases early on, indicating that it is probably due to adsorbed molecules on the surface. The oxygen signal also disappears near the surface, indicating a surface oxide. It increases with depth, however, as the film is sputtered away and the MgO substrate is revealed.

the film. However, the ratio of the niobium content to the nitrogen content was not the same for all samples and varied from roughly equal to ratios of 70% nitrogen and 30% niobium; in the results shown above, the intensities of the peaks of niobium and nitrogen even vary within the film, leading to a calculated atomic concentration variation. The ratio measured depends on the likelihood of the Auger process in each element and the ease with which electrons with different energies escape the film, and so it does not indicate the actual film composition. However, it was surprising that there was so much variation among the films.

The fact that the composition did not remain constant with depth in SPD017 as the MgO substrate was approached raised the question of whether there was an oxide layer between the NbN film

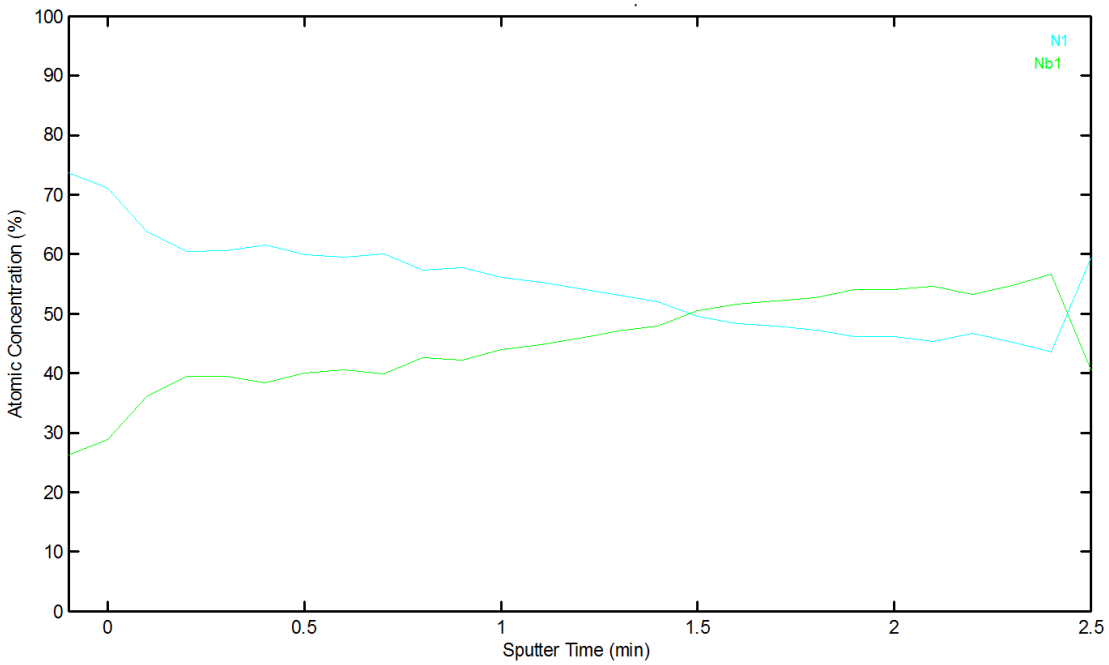

Figure 2.4: Calculated atomic concentration versus sputtering time of the peaks associated with niobium (green) and nitrogen (cyan). The relative concentrations do not appear as constant with depth as they did for other films tested, but not shown here, which had steady concentrations of Nb and N ranging from ratios of 30:70 (Nb:N) to 45:55 (Nb:N).

and the substrate that might have affected the Nb:N ratio. The stack plot in Figure 2.5 shows that there is a small oxygen signal throughout the film, which was found for other films as well, but it is unclear whether it is due to oxygen within the film or just an artifact from the presence of the MgO substrate. Therefore, x-ray photoelectron spectroscopy (XPS), which is more sensitive to not only the presence of different species of atoms but also their chemistry, was used to investigate whether there was an oxide within the films or between the films and the substrate.

2.2.3 X-Ray Photoelectron Spectroscopy (XPS) of NbN on MgO

X-ray photoelectron spectroscopy (XPS) is a quantitative technique to assess surface chemistry (up to a depth of several nanometers) and is thus helpful for characterizing thin films. The sample is irradiated with an x-ray beam with a known wavelength, which can excite electrons in the sample and

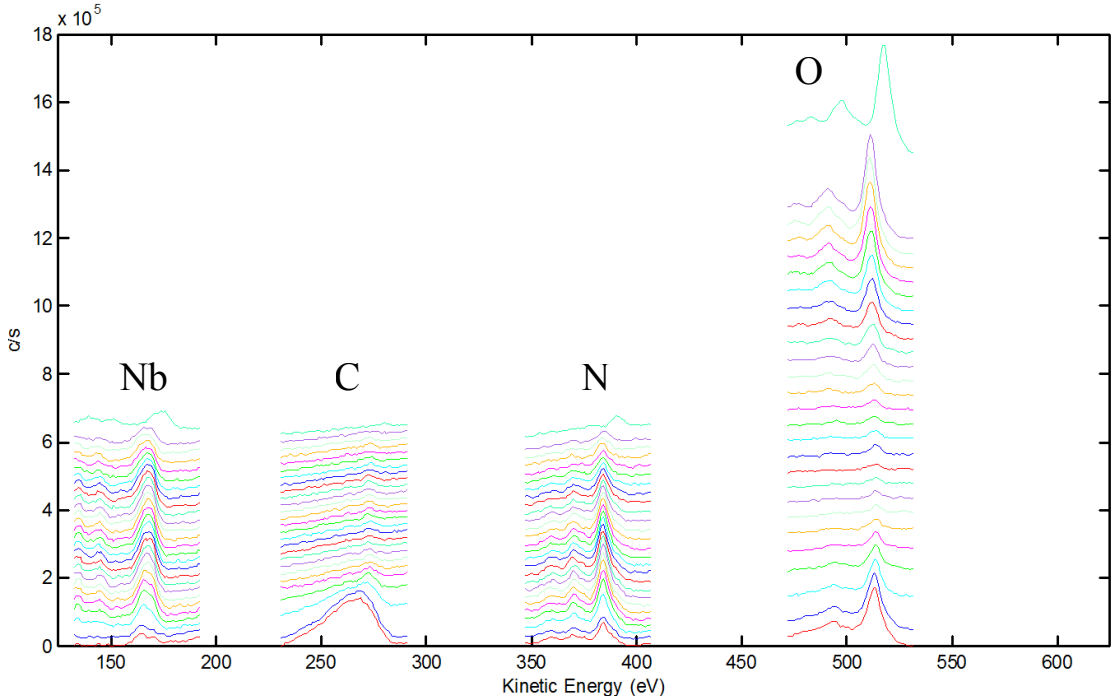

Figure 2.5: Intensity (counts/second) of the peaks associated with four atomic species as measured between 0.1-min sputtering intervals. The depth increases from bottom to top. That is, the red scans at the bottom of the stacks represent the surface scans before sputtering, and the topmost green scans were taken after sputtering and represent the intensities found for the largest depth into the film measured. The carbon peak for the most part disappears within several rounds of sputtering. The oxygen peak is very small throughout the bulk of the thin film and then increases significantly as the substrate is reached.

cause them to be emitted. The kinetic energy of the electrons that escape from the sample can then be measured, and the binding energy of the detected electrons is determined via energy conservation and the given energy of the incident x-ray photons. Electrons have different characteristic binding energies depending on the atomic species and how it is bonded to other atoms.

A PHI VersaProbe II XPS was used to obtain depth profiles of two NbN films on MgO, one that had been grown 5 days before testing (labeled SPD561), and one that had been grown 6 months before testing (labeled SPD073). Previous TEM studies had found an oxide layer on the surface of the NbN film with a thickness of roughly 2 nm[38], but it was unknown whether oxygen migrated into the film over time from the air or the MgO lattice and disrupted the NbN lattice, which could

lead to decreased film quality. The survey spectrum of SPD073 is shown in Figure 2.6, which shows the expected peaks for oxygen, niobium and nitrogen. A peak representing carbon is also present, which is expected for the surface a sample exposed even briefly to the atmosphere, from which carbon species readily adsorb. There was also a concern that Teflon in the sputter coater could have led to fluoride contamination of the newer sample, but, as the survey spectrum in Figure 2.7 shows, no fluorine peak was found for SPD561.

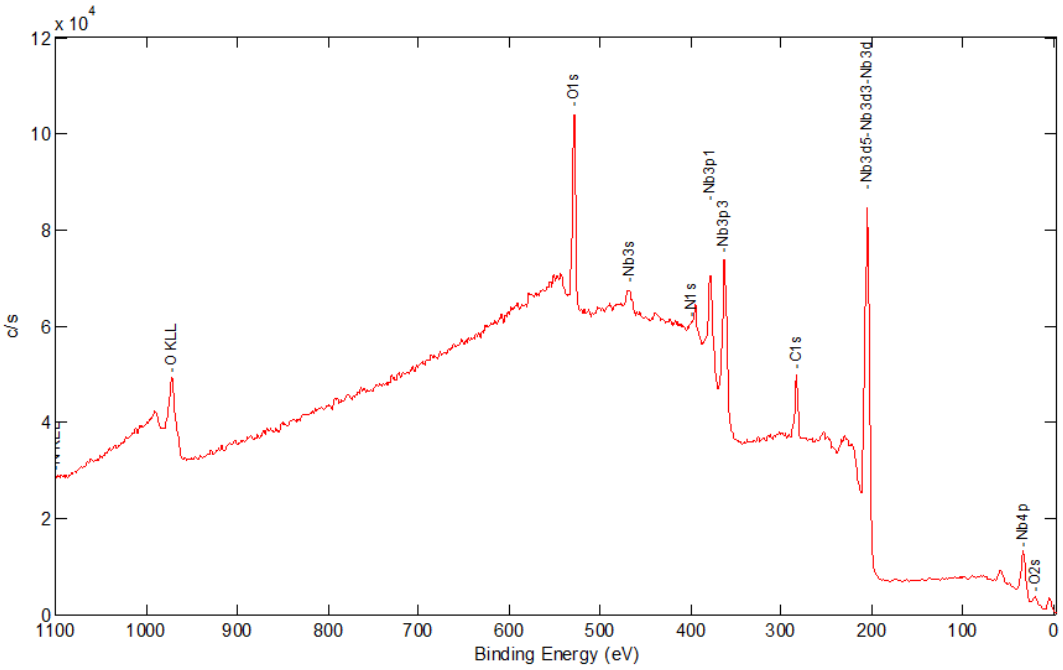

Figure 2.6: XPS survey spectrum of SPD073, which shows peaks indicating the presence of niobium, nitrogen, oxygen and carbon, all of which are typical for the surface of a sample exposed to atmosphere even briefly.

Figure 2.8 shows depth profile of SPD073 after converting the counts into atomic concentrations, which is an operation that the software can do, but it makes some assumptions about the bonding environment of the atoms that might not be correct. However, the plots show the general trends of the relative concentrations of chemical constituents as the NbN is sputtered away with argon ions, which gives a preliminary sense of the concentrations of different atoms with depth. SPD073 shows

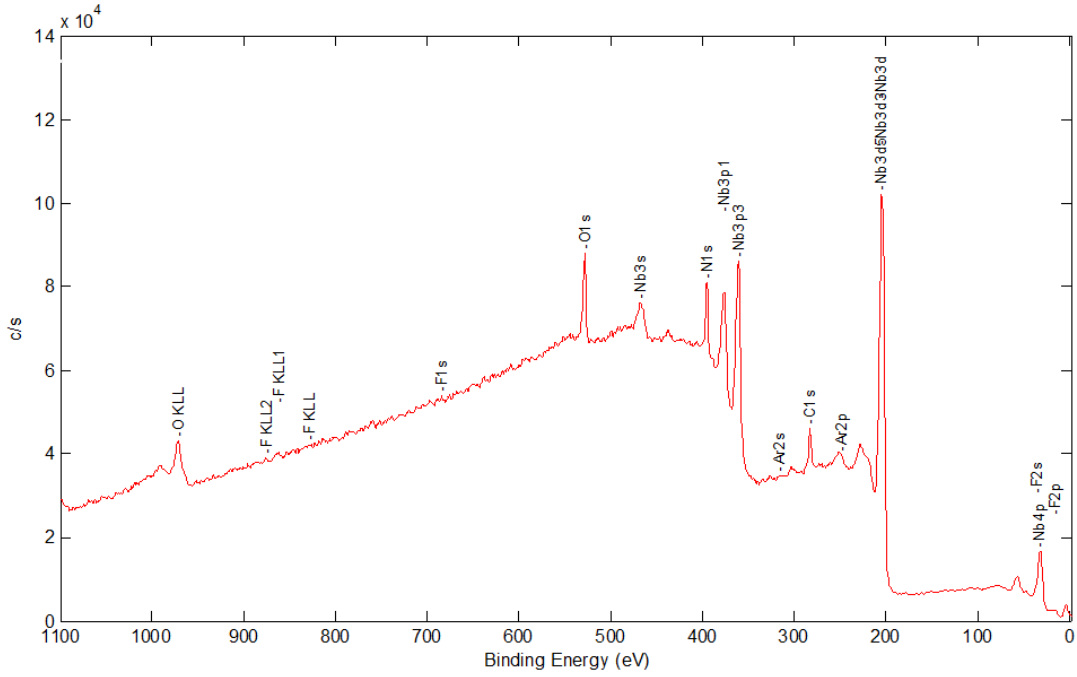

Figure 2.7: XPS survey spectrum of SPD561, which shows peaks indicating the presence of niobium, nitrogen, oxygen and carbon and no peaks for fluorine, which means that this sample likely was not contaminated, as suspected.

a higher concentration of carbon (blue line) on the surface, as determined by the area under the carbon 1s peak, which is probably due to contaminants that immediately adsorb onto the film when it is exposed to atmosphere. The oxygen (green line), which was characterized using the area under the oxygen 1s peak, also shows a higher concentration at the surface that then decreases with depth, albeit more slowly than the carbon, which suggests that there is an oxide layer on the surface. The niobium and nitrogen concentrations (red and orange, respectively), which were determined with the 3d and 1s peaks, respectively, increase with depth and then remain constant. The atomic concentrations calculated suggest that the sample has a higher concentration of nitrogen relative to niobium, but, given the assumptions made by the software, this ratio should not be taken as evidence that the film is in fact nitrogen-rich.

The niobium chemistry of SPD073 was studied by using the nitrogen 1s (N1s) peak for calibra-

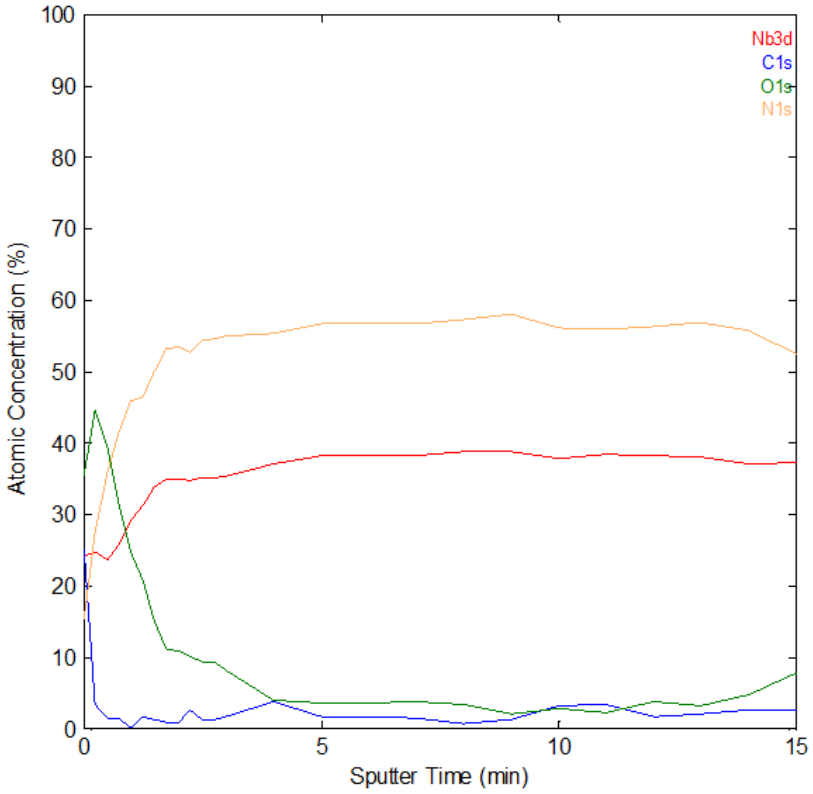

Figure 2.8: XPS depth profile of SPD073. The carbon appears to be present only on the surface, and the oxygen appears to be present as an oxide layer on the surface of the film, where the niobium and nitrogen concentrations are lower.

tion. The depth profile in Figure 2.9 shows the shape of the N1s peak for different depths in the film, from the surface (bottom line, in red) to the maximum depth tested (top line, dark green). The sputtering was performed in 1 minute intervals for a total of 15 minutes on SPD073. The peak on the surface is relatively small, indicating that there was probably a relatively lower concentration of nitrogen on the surface, and then it increases with depth and appears to stabilize in height. There is a shift along the x-axis, which indicates that a lower binding energy was measured. However, this shift is likely an artifact of the charging of the sample and the use of a neutralizer to counteract it, which was necessary because the MgO substrate was not conductive, and not an indication of a change in nitrogen chemistry in the sample. For example, in the XPS results reported in Jouve et al., there is

a small, higher energy peak that indicates oxynitride bonding, which, if present, can make the nitrogen peak of an NbN film appear asymmetric[54]. Our results do not appear asymmetric, and thus there is no indication of oxynitride bonding at the surface or in the bulk.

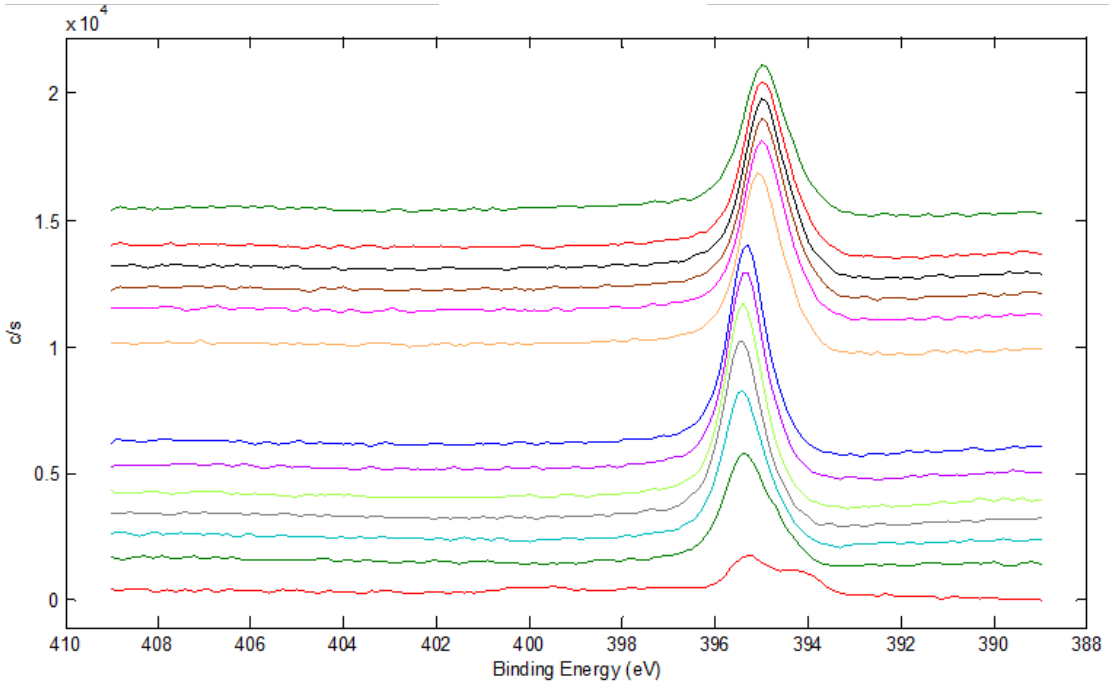

Figure 2.9: XPS results for the nitrogen peak measured between 1-min sputtering intervals. The shift in the peak position is likely an artifact due to the charging of the sample. The peak shape appears to change within the first two rounds of sputtering (bottom two scans), possibly indicating a change in the chemical bonding of nitrogen.

The niobium chemistry–that is, the electronic configuration of the niobium atoms–does appear to change, as shown in Figure 2.10. At the surface (the lower lines), there are three Nb3d peaks, but, within the bulk of the film, there are only two peaks.

The results in Figure 2.10 can be compared to results reported by Jouve et al.[54], who found the Nb3d peaks expected for different niobium chemistries. The higher energy doublet peaks represent niobium pentoxide, and lower doublet is for niobium nitride. There is another doublet between the two that signals an intermediate, oxynitride environment. In Figure 2.10, there are three Nb3d peaks

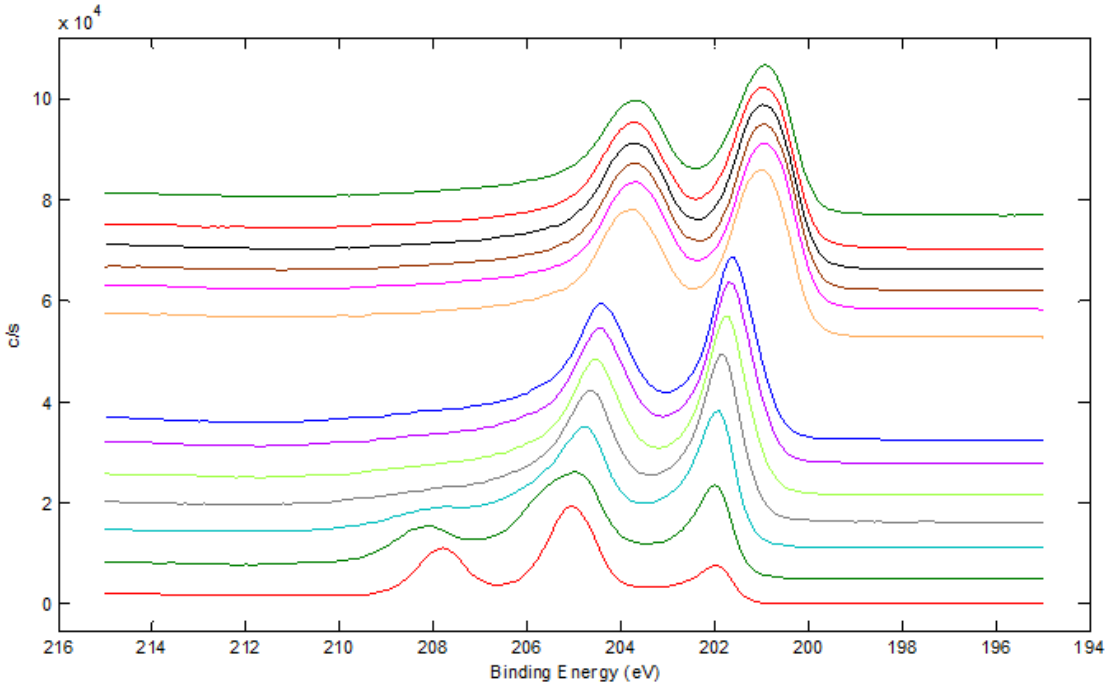

Figure 2.10: XPS results for the niobium peak measured between 1-min sputtering intervals. The shape of the peak changes with depth, indicating a change in the bonding of the niobium atoms.

on the surface, which is likely a mix of pentoxide, oxynitride and niobium nitride. Within the bulk, however, there appears to be only the lower energy doublet, indicating primarily niobium nitride.

Figure 2.11 shows the changes in the Nb3d peaks with depth. The trend in the depth profile for SPD561 was similar to that of SPD073, which suggests that ageing did not affect the composition of the films much. In this case, however, the sputtering appears to have approached the MgO substrate more closely than in SPD073, as indicated by an increase in the oxygen peak with depth. The increase in oxygen could be due to increased oxygen within the NbN lattice as well. However, as shown in Figure 2.11, the niobium chemistry did not change with depth near the substrate despite the increase in the oxygen signal, as shown by the consistent shape of the Nb3d peaks. Thus, it appears that there is no oxynitride or pentoxide layer between the NbN film and the MgO substrate. The oxygen signal at depths near the substrate likely arises solely due to the presence of the substrate

and is not an indication of increased oxygen content within the NbN film. The N1s peak did shift slightly to a higher energy initially in SPD561, which might indicate that there is an oxynitride in the oxide layer on the sample.

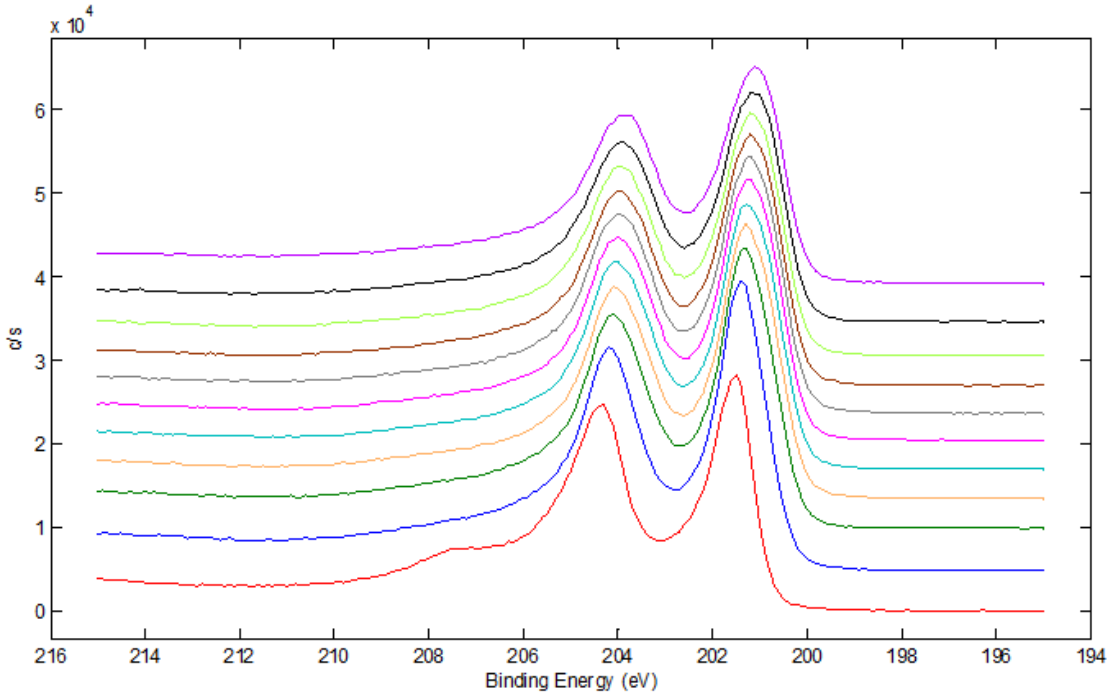

Figure 2.11: XPS results for the niobium peak of SPD561 measured between 1-min sputtering intervals. There is a change in the shape of the peak with depth near the surface, indicating a change in the bonding of the niobium atoms and possibly the presence of more oxynitride than found in SPD073. There is no change in the peak shape near the substrate, however (top lines), which likely means that there is no oxynitride layer between the film and the substrate.

In conclusion, there is good evidence of a surface oxide layer composed of niobium pentoxide on both SPD073 and SPD561. There is no clear evidence of an oxynitride transition below the oxide, and the bulk NbN shows no evidence of peaks associated with niobium bonding to oxygen in either sample. Oxygen is nevertheless present in the bulk of both samples, as evidenced by the persistent oxygen 1s peak in the depth profiles.

The work reported in this chapter is a first step in understanding the microstructure of NbN thin films deposited by sputter coating and how it might affect the properties of devices fabricated

from them. Determining whether there was an oxide layer was also important for the optical modeling presented in a later chapter. If the oxide on NbN were found to be thicker, it would have been necessary to include it in the optical models, but, because it is thinner than the NbN film itself, calculations showed that it had only a very negligible effect on the optical properties of devices.

3

Transmittometry of Thin Films

This chapter describes two optical setups that are used in our group to characterize the thicknesses of thin NbN films in a non-destructive manner to screen samples for fabrication and to better model the performance of the resulting SNSPDs. The transmittometers reported here are easy to use and give results within minutes, so that thickness measurement can be easily integrated into the workflow of growth and characterization. Current reports in the literature often rely on the deposition time[55] or do not report how the film thickness was determined and offer only approximations[56,57];

others have conducted TEM studies on films[58], which are destructive. In our group, we have found that the film thickness does vary consistently with the deposition time, but only as long as the deposition parameters (such as the flow rates of gases) are constant. When the deposition parameters are varied to achieve better quality films, the deposition time should not be used to compare the thicknesses of films. An independent measurement of the film thickness is also useful to see a drift of the growth system parameters over time, where a constant deposition time may produce different film thicknesses.

Currently, there are several instruments to determine the thickness (and sometimes simultaneously the refractive index) of thin films using light, but they are more complicated and time-consuming than the optical setups presented in this chapter. They are based on either ellipsometry or the reflectance/transmittance of samples. Variable angle spectroscopic ellipsometry (VASE) involves scanning a film with a collimated beam over a range of angles of incidence and wavelengths. A model of the film can then be built to fit the resulting reflectance data. The main disadvantage is the cost of a VASE instrument and the amount of time required to scan a single sample, which can be on the order of hours depending on how detailed the analysis has to be and how much is known about the film *a priori*. Thin films must also be on substrates that are not transparent to the wavelengths scanned.

Commercial reflectometers exist on the market, such as the aRTie or the F10-RT from Filmetrics, which measures the reflectance and transmittance of a sample and different wavelengths and includes software to analyze the results to determine the index of refraction and thickness. The minimum thickness that an aRTie is rated to measure is 15 nm and that of the F10-RT is 3 nm, which are too thick for our purposes. The NanoCalc Thin Film Reflectometry System from Ocean Optics, which measures the reflectance of a sample over a range of wavelengths, is advertised as able to determine thickness down to 1 nm. Because the NanoCalc relies on reflectance data, however, it can only be used with a non-transparent substrate, much like a VASE. Companies such as Nanometrics also

manufacture tools that have reflectometry capabilities. The disadvantage of a commercial system is the cost, especially when the instrument will only be used for a limited range of samples, such as sputter coated thin films of NbN, and advanced software for determining the composition of the thin film stack is not necessary.

Other researchers have reported optical setups that can determine the thickness and refractive index of films in a non-destructive manner, but these setups are generally more complicated than ours due to the specific problems investigated. For example, Hirth et al.[59] combine reflectometry and confocal microscopy to determine both film thickness and topography. Jafarfard et al.[60] use dual-wavelength diffraction phase microscopy, which simultaneously acquires phase images at two different wavelengths and requires the use of a laser, a transmission grating and a spatial filter, along with collimating and focusing optics to form an interferometer, to determine not only the refractive index but also the thickness spatial distribution of a sample. Joo et al.[61] consider angle-resolved reflectometry at different wavelengths, similar to a VASE, and Henrie et al.[62] created a spectral reflectometer with a series of LEDs to cover the visible wavelength region. Others have built far ultraviolet (FUV)[63] or extreme ultraviolet (EUV)[64,65,61,66,67] reflectometers, which require a laser or other source that operates at a wavelength of tens of nanometers and in some cases controlling the angle of incidence.

3.1 Transmittometer Setup

The basic idea between both optical setup designs presented below is that it should be possible to determine the thickness of a thin film of NbN on a substrate by determining the transmittance of the film. Figure 3.1 shows some NbN films grown on MgO. The darker films were grown with a longer deposition time and are presumably thicker. Therefore, quantifying the difference in transmitted light should lead to a relative measure of thickness between films.

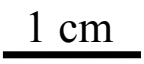

Figure 3.1: Photograph of NbN films on MgO. The darker the NbN film appears, the thicker it is. According to the IR transmittometer measurements, the thicknesses of these films are (left to right) 1.85 nm, 4.09 nm and 9.21 nm.

The concept behind the operation of the transmittometers is shown in Figure 3.2. Light from the LED source is incident on the sample: this figure shows a non-normal angle of incidence for clarity, but in practice, both setups relied on normal incidence. The light that is transmitted through the sample (and, in the case of the visible reflectometer, the light reflected from the sample) is detected to determine the transmittance (T) (and reflectance (R)) of the film. As shown in the schematic, light is both transmitted and reflected at the front and back of the sample, and multiple passes of light contribute to the overall transmittance and reflectance. Some of the light is also absorbed in the NbN layer.

The amount of light transmitted, reflected and absorbed can be calculated using the indexes of refraction of the materials and the transfer matrix method. This method is described in Chapter 4 and is the basis of most of the optical modeling of devices presented in this thesis. Once the expected transmittance versus NbN thickness is plotted for a particular substrate, the thickness of NbN on a sample of that substrate can be read from the plot.

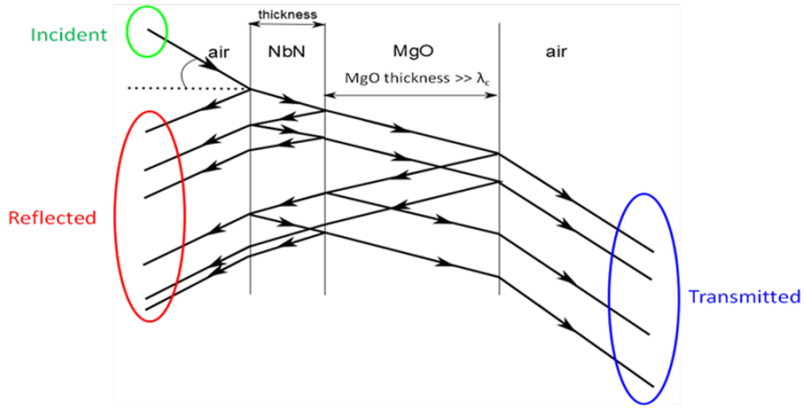

Figure 3.2: Illustration of how the internal reflections within a substrate contribute to the total reflectance and transmittance of a sample that can be measured in an optical setup. The optical setups described in this chapter rely on normal incidence (ϑ=0°).

3.1.1 Infrared Transmittometer

Figure 3.3 shows the basic transmittometer setup for the infrared (1550 nm) transmittometer built in our laboratory and an example of a plot of the transmittance versus NbN thickness expected for an NbN film on 225 nm of silicon nitride on silicon (with 225 nm of silicon nitride on the back of the substrate as well). This wavelength was selected because silicon is transparent in the infrared, and many of our devices are grown on silicon substrates. In addition, our devices are tested at 1550 nm because it is an important wavelength for telecommunication, which is one of the applications of SNSPDs. The same optical constants are used for the transmittometer measurement and the optical models in the next chapter. Thus, even if there is some error in the optical constants of our NbN thin films because the density of thin films is different than that of the thicker films used to determine the index of refraction, the thickness calculated by the reflectometer should reflect an "optical thickness" that might not match the physical thickness but should lead to the correct calculated absorptance in the optical models.

The transmittometer consists of a single column with an LED, a lens to collimate the LED light,

a sample stage and a lens to focus the LED light onto the detector. An LED is used instead of a laser because the coherence length of the LED light is smaller than the thickness of the substrate, and thus there are no etalon effects within the substrate and its thickness does not need to be known.

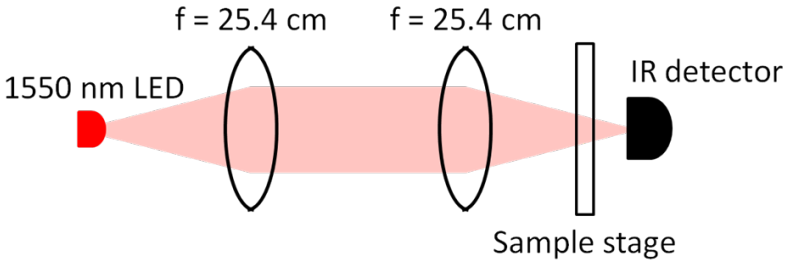

(a) IR transmittometer schematic

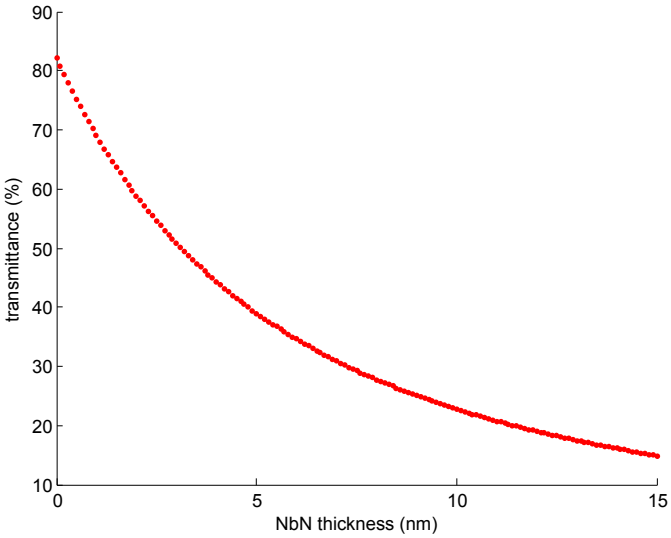

(b) sample transmittance plot

(c) photograph of the IR transmittometer

Figure 3.3: (a) Schematic of the infrared transmittometer showing the basic optical components. (b) Transmittance versus NbN thickness for an NbN film grown on silicon nitride on silicon. In this case, the NbN film is on the side of the chip that is facing the detector. (c) Photograph of the IR reflectometer. The vertical setup is convenient because the sample can be placed on the stage without clips to hold it in place. The sample is typically placed with the film side down to prevent dust settling on it.

To perform a measurement, first, the "dark" signal from the detector when the LED is off is recorded (which is typically around 0.007 V). Then, the detector is read when there is no sample

mounted, when a blank substrate is mounted and when the chip under test is mounted (NbN side facing the detector) at different LED powers. Low powers will sometimes give noisy results, but high powers typically produce precise results. The "dark" signal is subtracted from all recorded data. The measured signal with the blank substrate mounted divided by the signal with no substrate mounted (after subtracting the dark signal from both) gives the transmittance through the blank substrate. This value can be used to determine whether the optical constants of the substrate used in the calculation are accurate. For a double-sided polished silicon substrate composed of 225 nm of silicon nitride on both sides, the transmittance should be approximately 56.4%. The detector signal with the NbN sample mounted divided by the signal with no sample is the transmittance through the sample, which can be used to determine the thickness of the NbN, given the plot of the transmittance versus NbN thickness.

3.1.2 Visible Reflectometer

A visible light reflectometer was built initially, and its more complicated design is shown in Figure 3.4. In practice, because of the multiple optical surfaces between the sample and the reflection detector and the generally weak reflection from thin films, the reflectance signal was much noisier than the transmittance signal, and the transmittance was used to characterize film thickness. This "visible reflectometer" has several disadvantages in terms of design. First, because of the multiple optical surfaces and reflections, the system must be calibrated before every measurement by getting readings of the detectors, especially the reflection detector, when no sample is mounted. These values are then subtracted from the measured reflection signal with a blank substrate and with the thin film chip being tested. The detectors are also responsible for reflecting some light back into the system, and so between measurements, the detectors that are not being used have to be blanked with an absorbing surface. An automated system was built to blank the detectors and to read the unblanked detector signal by an undergraduate research assistant, Christopher Lang, which helped to

reduce the time required for measurements. In addition, if many substrates are being measured, the calibration procedure need only be done at the beginning. The values did change from day to day, however.

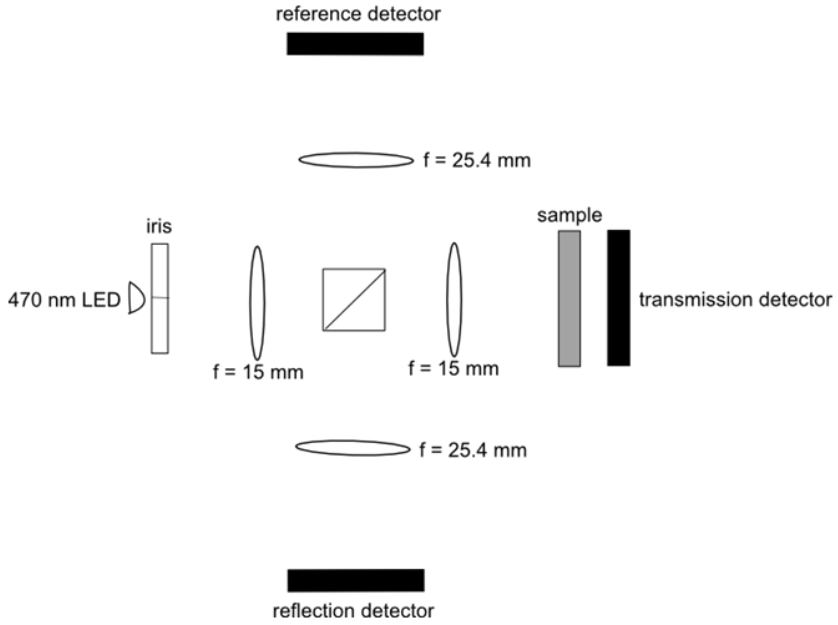

Figure 3.4: Schematic of the visible reflectometer, which operates at 470 nm. It measures a reference signal, the transmitted signal and the reflected signal, in theory giving both R and T of a film at the same time. In practice, the weak reflected signal and internal reflections within the setup made the transmitted signal more reliable than the reflected signal for determining film thickness.

Once the values have been recorded from the detectors, a MATLAB script is used to determine the transmittance (and reflectance and absorptance for the visible reflectometer), which is compared to a plot of the transmittance versus NbN film thickness for the substrate (the next section shows an example of such plots). The thickness of NbN can then be read off of the plot.

3.1.3 Comparison of Different Wavelength LEDs

The two instruments built rely on different wavelength LEDs, which each have advantages and disadvantages. The LED in the simpler, IR (1550 nm) transmittometer can also be replaced with an

LED at another wavelength if necessary for some samples. Silicon is not transparent in the visible, and thus the 470-nm LED cannot be used to determine the thickness of NbN films grown on silicon, while the 1550-nm LED can be. However, bright, high-power LEDs are available in the visible but not the infrared, so the measurements at 1550 nm are more susceptible to noise. In addition, photodetectors in the IR are more expensive. In practice, however, the room lights do not contribute any noise at 1550 nm, but they do at 470 nm, so the IR setup does not need to be shielded, but the visible one does.

The slope of the transmittance versus thickness for NbN on MgO is steeper at 1550 nm for small thicknesses, which implies that a higher precision is possible, as shown in Figure 3.5. However, for larger NbN thicknesses, the transmittance at 1550 nm changes more slowly with thickness and is lower in magnitude for greater thickness than that at 470 nm, and thus visible light can more accurately determine the thickness of films thicker than 10 nm. Thus, each transmittometer is better suited for some samples than others.

Figure 3.5 relies on a model that does not include an anti-reflection coating (ARC), which would typically be spun on at the end of the fabrication process and not immediately after film growth, which is when the films are characterized. The model also neglects an oxide layer on the NbN. Niobium does oxidize in air, though the samples are characterized soon after growth and stored in a nitrogen box to limit oxidation. In addition, the oxide layer, which can be 2 nm thick according to previous TEM results[38], does not change the transmission characteristics much, as shown in Figure 3.6, and thus the plots used to determine the NbN thickness do not consider the presence of an oxide layer.

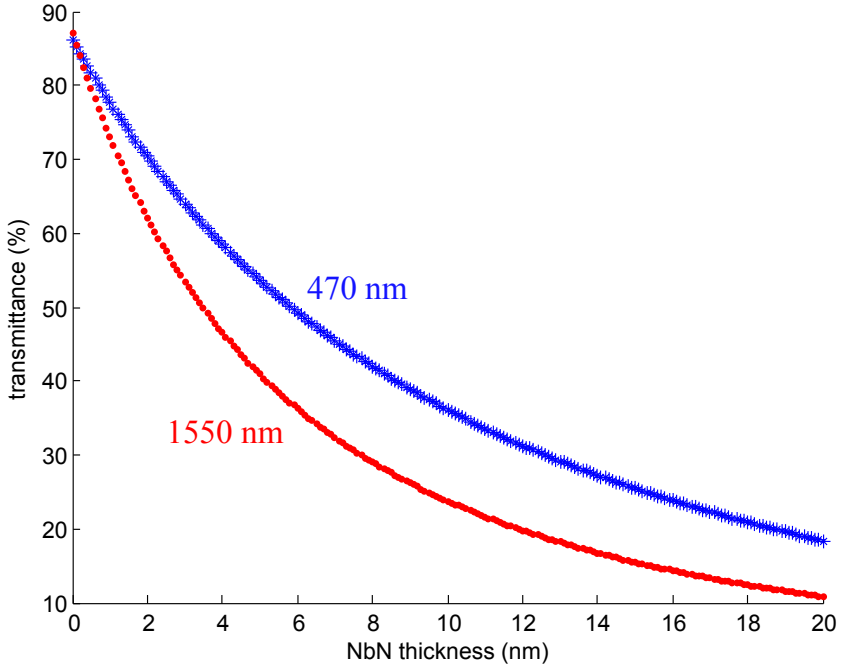

Figure 3.5: Transmittance versus NbN thickness of an NbN film on MgO for 470-nm light (blue asterisks) and for 1550-nm light (red dots). The steeper slope of the 1550-nm line at small thicknesses suggests that it should be more sensitive to differences in thickness of very thin films.

3.2 Experimental Results

The experimental results on the optical setups show that the transmittometers give repeatable values for the thickness and offer a quick, non-destructive method to ascertain the relative thicknesses of films. The measurements using the visible reflectometer and IR transmittometer were compared to the sheet resistance of films, transmission electron microscopy (TEM) results and VASE measurements.

3.2.1 Film Thickness Versus Sheet Resistance

The sheet resistance should vary inversely with the thickness of the films, and the correlation between the sheet resistance and a measurement of the thickness should therefore be high. Figure 3.7

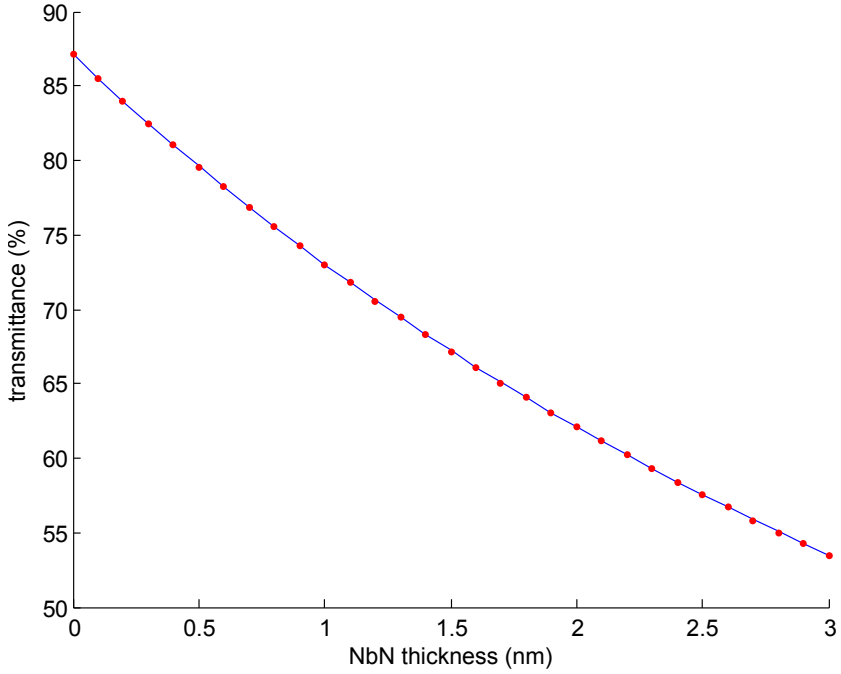

Figure 3.6: Transmittance versus NbN thickness of an NbN film on MgO for 1550-nm light with a 2-nm-thick oxide layer on the NbN ($n = 2.28$[38]) (blue solid line) and without an oxide layer (red dotted line). The oxide layer does not affect the measurement much, and so it is neglected in the calculations of the NbN film thickness.

shows the sheet resistance versus deposition time and the sheet resistance versus film thickness determined with the transmittance measured by the visible reflectometer. The inverse of the sheet resistance correlates much better with the thickness than the deposition time, with R^2 values of the linear fit of 0.65 and 0.06, respectively.

3.2.2 Repeatability of Thickness Measurements

Figure 3.8 shows the results of thirty measurements of a film on MgO taken in succession. This "ironman" trial shows that the measurements are repeatable, without short-term drift. The thickness values for these transmittance values range from 4.875 nm to 5.075 nm, and so the thirty trials are within 0.2 nm of each other.

Figure 3.9 shows the film thicknesses of eight NbN films on MgO as measured with the IR trans-

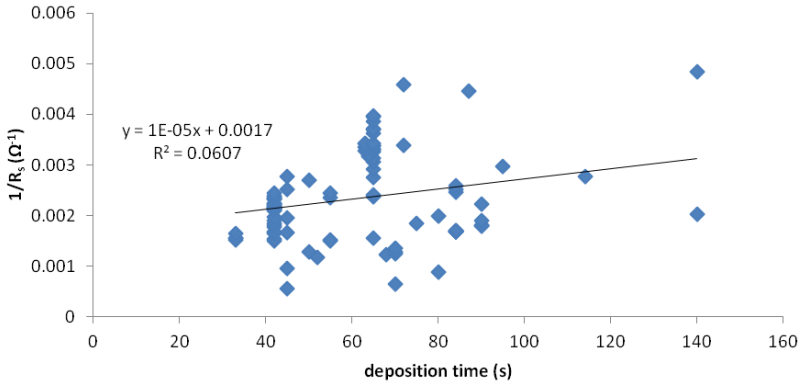

(a) sheet resistance vs. deposition time

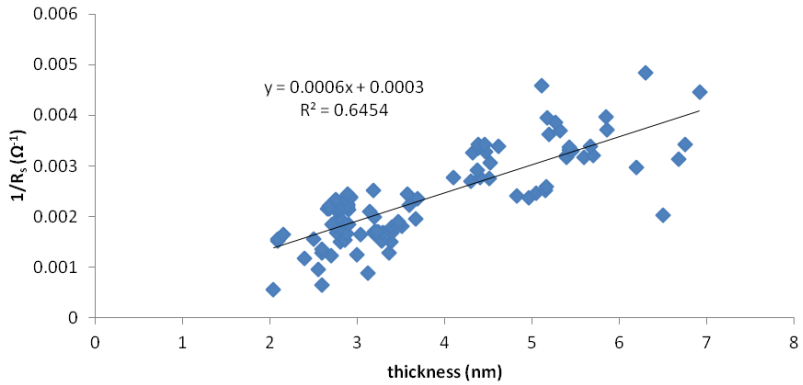

(b) sheet resistance vs. film thickness

Figure 3.7: (a) Sheet resistance versus deposition time with a linear fit to the data. (b) Sheet resistance versus film thickness determined from transmittance measurements in the visible reflectometer. Data were taken by Andrew Dane, who also grew most of these films and prepared these plots.

mittometer, and Table 3.2 gives the thicknesses and the percent increase in thickness. The second set of measurements were taken four weeks after the first set to demonstrate that the IR transmittometer gives repeatable results over time. Each of the films appears to have decreased in thickness, which is likely due to oxidation over time. The greatest variation was still less than 0.2 nm.

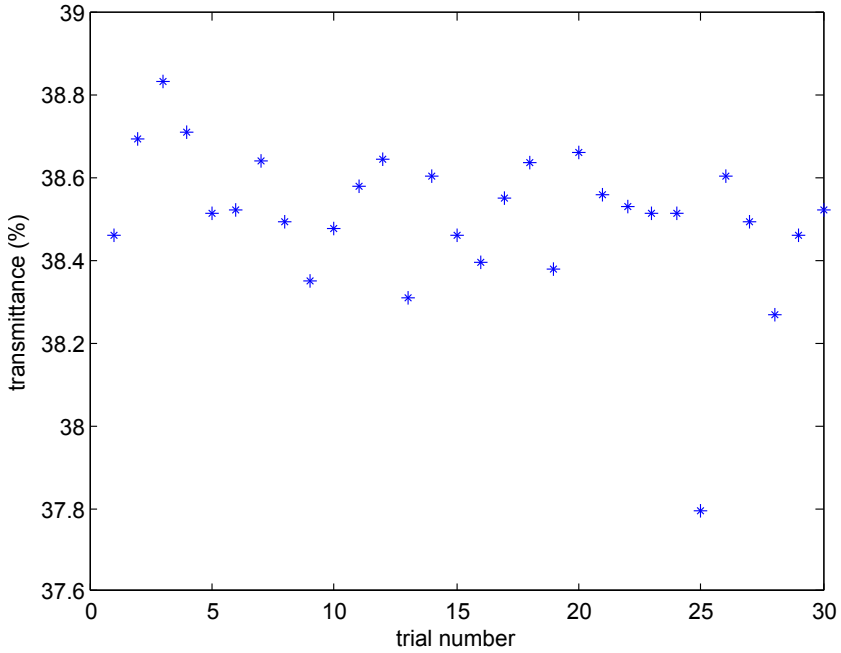

Figure 3.8: Transmittance values measured with the IR transmittometer of an NbN film on MgO. Thirty measurements were performed in succession to demonstrate the repeatability of the measurements.

3.2.3 Comparison of the Results of the Different Optical Setups

Andrew Dane measured the thickness of films he grew in the visible and infrared optical setups to determine whether the setups gave equally consistent results, and the results are shown in Figure 3.10. Figure 3.10a shows the film thicknesses versus deposition time for different substrates measured in both the visible and infrared setups. The IR transmittometer results are consistently thicker than the visible transmittometry results for NbN on MgO, but all films show the expected linear increase in thickness with deposition time. In addition, the thicknesses of NbN films on different substrates are consistent for similar deposition times. It is interesting that the thicknesses of NbN on MgO as measured in the IR transmittometer are consistently thicker than NbN films on silicon for the same deposition time. This difference could be due to an uncertainty in the optical constants of the materials, but it might also be due to a different microstructure in the NbN when grown on a

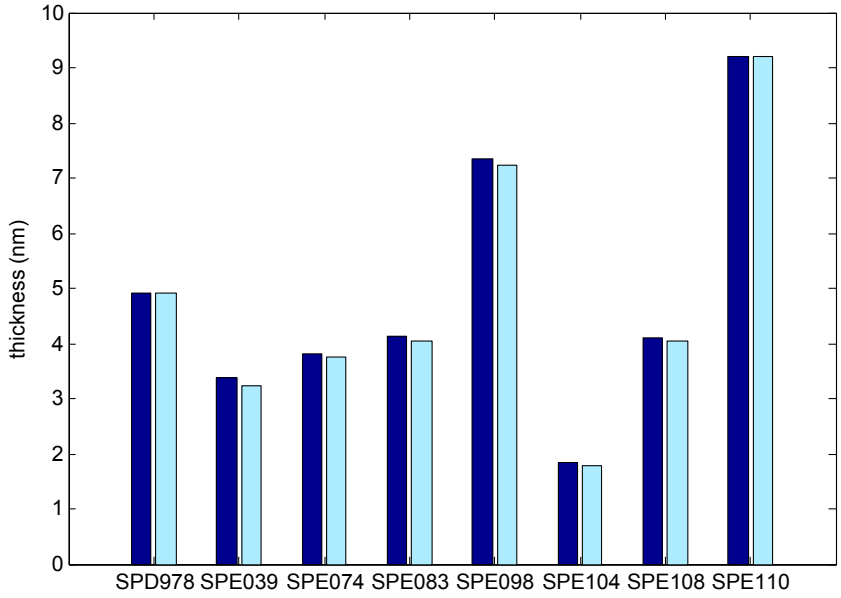

Figure 3.9: Thicknesses of several NbN films grown on MgO. The first set of measurements is given in dark blue, and the second set, 28 days later, is given in light blue. The films are slightly thinner in the later measurements, likely indicating oxidation over time.

crystalline substrate (such as MgO) compared to films grown on amorphous substrates (such as silicon nitride or silicon oxide on silicon), which might lead to either a different thickness or different optical constants of the NbN.

Figure 3.10b shows the thickness data points for the samples of NbN on MgO as determined in the IR transmittometer and the visible reflectometer. A linear fit of the data suggests that the thickness measurements are consistent between the two optical setups, although one gives consistently larger film thicknesses. The deviation of the thickness measurements between the optical setups is likely due to the uncertainty in the index of refraction of NbN thin films at either wavelength, but the close comparison between the setups indicates that either can be used for relative thickness measurements.

Table 3.1: Thicknesses of several NbN films grown on MgO. The films were measured again 28 days later, and the percentage decrease in the film thickness is given.

Sample ID	Thickness (nm)	Thickness 28 Days Later (nm)	Percent Decrease in Thickness (%)
SPD978	4.90	4.91	0.204
SPE039	3.24	3.39	4.42
SPE074	3.75	3.82	1.83
SPE083	4.03	4.12	2.18
SPE098	7.24	7.35	1.50
SPE104	1.79	1.85	3.24
SPE108	4.04	4.09	1.22
SPE110	9.20	9.21	0.109

3.2.4 X-ray Reflectometry of a Thin Film

X-ray reflectometry (XRR) can be used to determine the thickness of films such as NbN[68]. In this subsection, some XRR results are reported, which verify the results of the visible reflectometer but have some important limitations. A sample on silicon nitride on silicon was 4.1 nm thick according to x-ray reflectometry measurements conducted by Andrew Dane and Scott Speakman, and a sister chip from the same growth run on MgO had 4 nm of NbN and 0.1 nm of oxide. The film on MgO was 4.1 nm thick according to the transmittance found by the visible reflectometer[69].

Figure 3.11 shows the XRR interference fringes found when the reflectivity is plotted versus angle, which were used to determine the thickness. The signal is somewhat weak and there are not many fringes, especially for the NbN film on silicon nitride, so fitting the XRR data might not yield very clear results. A future XRR study could investigate a large number of samples to determine whether the agreement seen here is consistent across different samples.

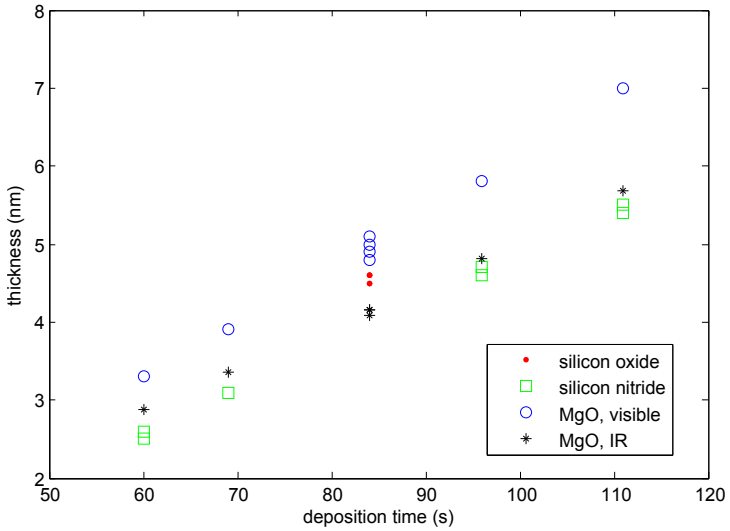

(a) thickness versus deposition time

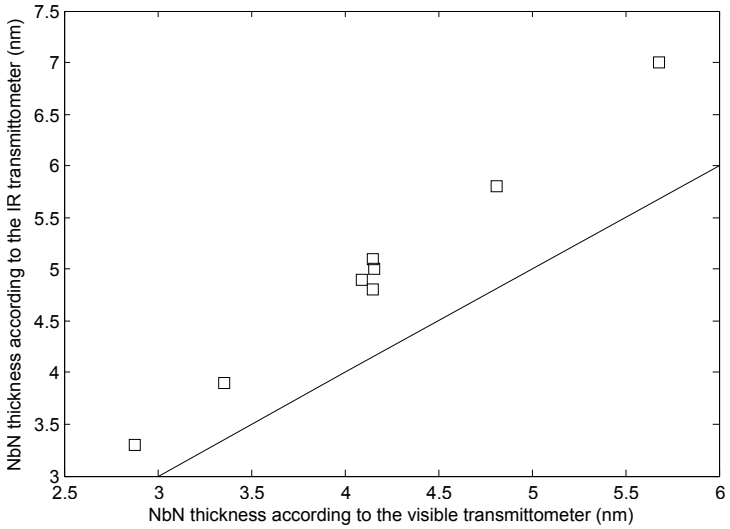

(b) IR versus visible transmittometer results

Figure 3.10: (a) Film thickness versus deposition time for different substrates: silicon oxide/silicon (red dots), silicon nitride/silicon (green squares) and MgO (blue circles) measured with the IR transmittometer, and MgO (black asterisks) measured with the visible transmittometer. (b) Thickness according to the IR transmittometer versus thickness according to the visible reflectometer for NbN films grown on MgO. The black line is the equality line. The measurements were performed by Andrew Dane.

3.2.5 TEM Comparison

The thicknesses of four samples were measured using transmission electron microscopy (TEM), as shown in Table 3.2. There are two possible sources of error in the TEM measurements. First, the

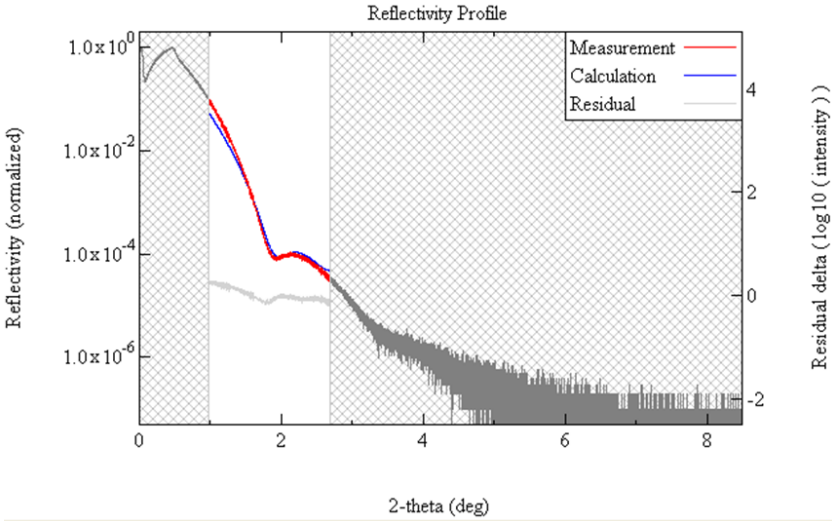

(a) NbN on silicon nitride/silicon

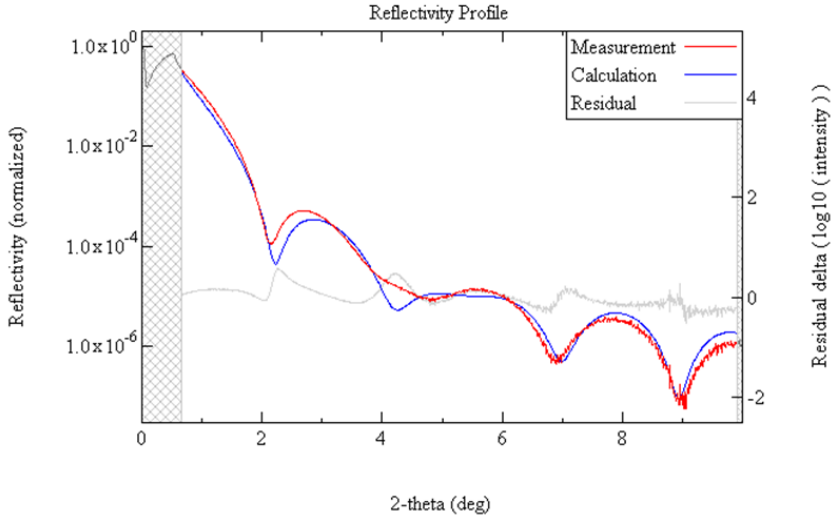

(b) NbN on MgO

Figure 3.11: X-ray reflectometry results for two NbN films that were grown in the same run, as measured by Andrew Dane and Scott Speakman. The red line is the measured signal and the blue line is the fit performed using a model of the materials, which gives the thickness of the films. The fit is only performed for the region of the plot that is not shaded out. (a) NbN on silicon nitride/silicon and (b) NbN on MgO.

samples may be tilted, though that would not produce a large error for small angles of tilt. Second, and more importantly, the images were taken with a large defocus to increase the contrast. The film

Table 3.2: Thicknesses of several NbN films on different substrates as measured by TEM and transmittance using the visible reflectometer. The TEM thicknesses were measured by Chung-Soo Kim and Yachin Ivry, and the reflectometer thicknesses were measured by Jonathan Surick and Yachin Ivry. Most thicknesses agree within the error expected for the optical setups due to uncertainty in the index of refraction of NbN, but some of the discrepancies might be due to charging in the TEM and the tilt of the sample.

Sample ID	Substrate Material	TEM Thickness (nm)	Transmittance Thickness (nm)
SPE159	silicon oxide on silicon	4.5	5.4
SPE184	MgO	14.6	14.2
SPE200	MgO	4.6	2.5
SPE203	sapphire	4.46	3.6

on sapphire and silicon oxide required less defocus than the MgO samples. The results overall suggest that the visible optical setup provides relatively accurate values of the thickness, within one or two nanometers, which is a typical difference between measurement setups. One sample showed a larger difference of 2.1 nm, but it is possible that there were charging effects due to the use of a non-conducting substrate as well.

3.2.6 VASE Results

A variable angle spectroscopic ellipsometer (VASE) was used to characterize a thin film of NbN on silicon nitride on silicon, which could give both the thickness and the optical constants of NbN in the visible. The results for a sample on silicon nitride/silicon are described below; a sister chip of MgO that was sputtered in the same deposition run was measured to have a film thickness of 4.6 nm according to the visible reflectometer, which compares to a thickness of approximately 8 nm found for the film on silicon nitride. One cause of this discrepancy is probably due to the difference between the optical constants found for NbN using the VASE and those used to calculate the thickness according to the transmittance found by the reflectometer. This discrepancy is discussed further in Section 3.3.

Table 3.3: Cauchy constants for the silicon nitride films shown in Figure 3.12.

Constant	value for 255-nm silicon nitride	value for 391-nm silicon nitride
A_n	2.212	2.2182
B_n	0.016751	0.015175
C_n	0.0063829	0.0066628
k amplitude	0.026359	0.078978
exponent	1.0396	2.5462
band edge	400 nm	400 nm

First, bare silicon nitride films on silicon were characterized. The fitting of an optical model to the data, which was performed by Tom Tiwald, an engineer at JA Woollam, is given in Figure 3.12 for a 255-nm-thick silicon nitride layer with 3 nm of roughness (which was modeled as 50% silicon nitride and 50% void) and a 391-nm-thick silicon nitride layer with 5 nm of roughness. The silicon nitride was modeled as "Cauchy" layer, and thus the parameters for the Cauchy equation to describe the index of refraction were found during fitting. The silicon was modeled using parameters in the literature[70]. Although both films were grown using the same CVD system, the Cauchy parameters were not identical, as shown in Table 3.3.

Next, an NbN film grown on a silicon nitride/silicon chip was measured, and the resulting data were fit using the results for silicon nitride above (using a thickness of 388 nm) and a point-by-point fit and then a Drude model fit for the NbN layer that started with the values for n and k found by the point-by-point fit. Figure 3.13 shows the two plots. The two fits gave NbN thickness of 8.12 nm and 8.083 nm, respectively. The mean squared error of the point-by-point fit was 0.767, and that of the Drude model was 3.46. As mentioned above, a sister chip of MgO had a deposited NbN thickness of 4.6 nm according to the visible reflectometer, which is over 3 nm thinner. This difference is large, but the cause is not clear. It is possible that the index of refraction used to calculate the thickness according to the visible reflectometer is not accurate. It is also possible that films grown on

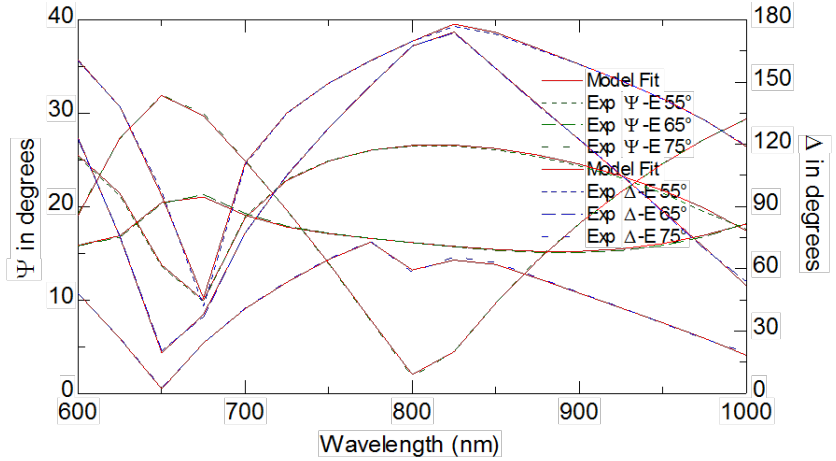

(a) 255-nm-thick silicon nitride

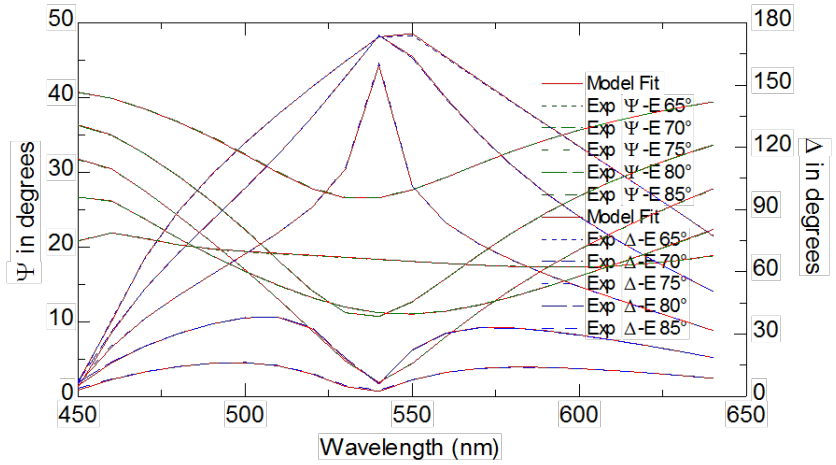

(b) 391-nm-thick silicon nitride

Figure 3.12: VASE results for two silicon nitride samples on silicon, including the fitting results. The VASE results include 200 data points gathered for 3 angles with a wavelength range of 600 nm to 1000 nm. (a) 255-nm-thick silicon nitride layer on silicon, with a mean squared error of the fitting of 13.7. (b) 391-nm-thick silicon nitride layer on silicon, with a mean squared error of the fitting of 4.22.

amorphous substrates, such as silicon nitride, have a different crystalline structure than those grown on nearly lattice matched substrates such as MgO, leading to either a different thickness or different optical constants. Techniques to address these possibilities are discussed below.

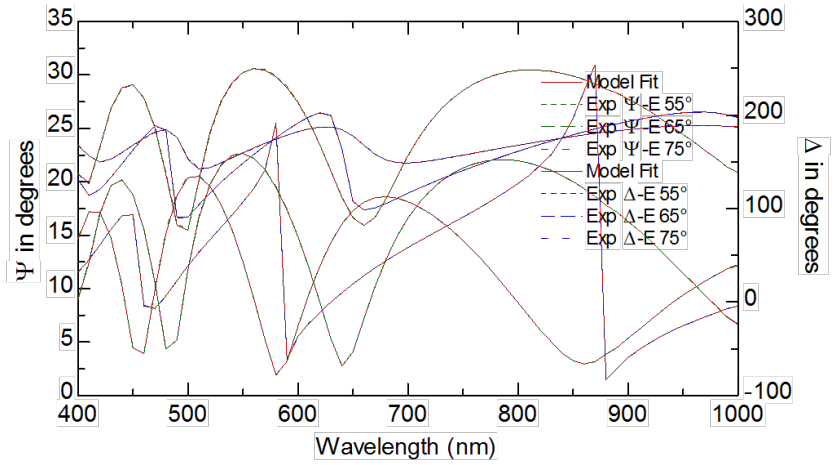

(a) 255-nm-thick silicon nitride

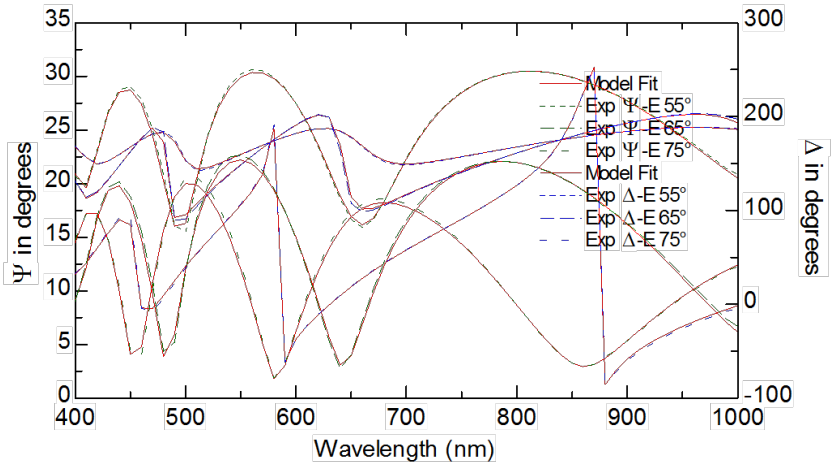

(b) 391-nm-thick silicon nitride

Figure 3.13: (a) VASE results for a thin film of NbN on silicon nitride/silicon and a point-by-point fit of the resutls. (b) VASE results for a different film of NbN on silicon nitride/silicon and Drude model fit of the results.

3.3 Future Improvements

The precision of the results according to the optical setups described in this chapter is high, as shown by the iron man results and the comparison between the optical setups. However, the accuracy of our optical measurements is unknown because of the uncertainty in the optical constants. In addi-

tion, two other improvements to the setup are discussed below, involving the spot size and the angle of incidence.

Figure 3.14 shows the transmittance versus NbN thickness curves for the visible reflectometer for various optical constants of NbN estimated from figures in the dissertation of Moushab Benkahoul[71] for three different NbN phases: the hexagonal δ'-NbN phase, the cubic δ-NbN phase, which has a NaCl structure composed of FCC sublattices of niobium and nitrogen, and the hexagonal β-Nb_2N phase[68]. Figure 3.14 also gives the expected results using the values found by JA Woollam on a thick film grown by our group[38], which are used in the optical simulations in our group, the values found by Gale Petrich at MIT and those found by me and Tom Tiwald using the VASE at Harvard. The variation illustrated in this figure is likely similar to what would be found for optical constants measured at other wavelengths as well. It is encouraging that the results using the indexes of refraction measured for our films (by JA Woollam, Gale Petrich, and me) are all relatively close. The data for our recent films (as characterized by Gale Petrich and me) seems to indicate that we have β-Nb_2N phase films.

In addition, thin films often have somewhat different structure than the surface of thick films or bulk samples due to the growth of columnar grains and other mesoscale structures[72,73], which could lead to variations in the optical constants themselves with film thickness. There might also be a difference between the microstructures, and thus optical constants, of NbN films grown on crystalline substrates (e.g., MgO or sapphire) and those grown on amorphous substrates (silicon nitride or silicon oxide on silicon). A further study to characterize the optical constants of NbN films of varying thicknesses on different substrates using the VASE could give a more accurate value for the optical constants to be used in the model.

Another improvement might be to add angles and polarization to generate more data points and possibly determine the indexes of refraction. Figure 3.15 shows the expected transmittance versus reflectance of a 5-nm-thick NbN film on MgO for the S and P polarizations and three angles (10°, 20°

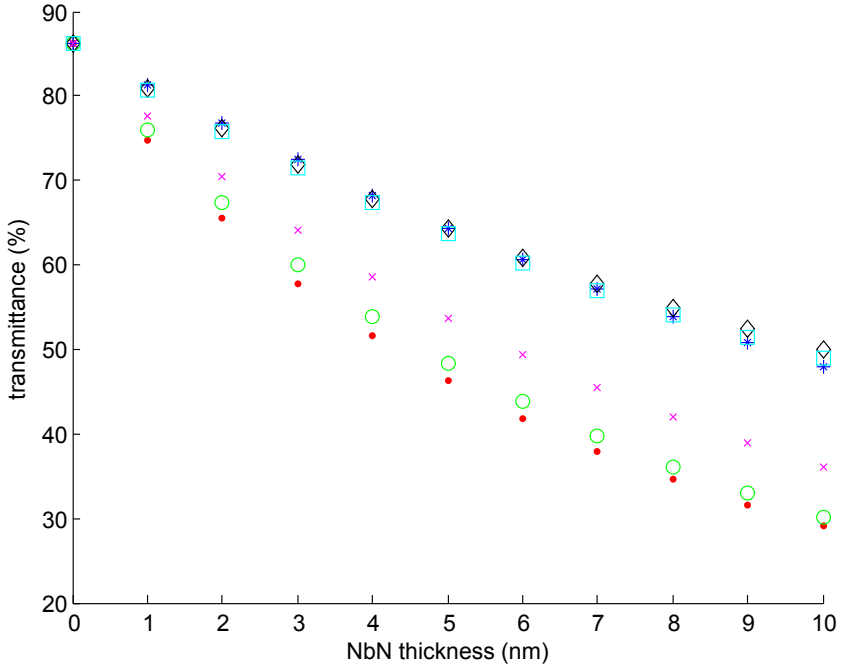

Figure 3.14: Transmittance versus thickness of NbN on MgO for different optical constants of NbN at 470 nm, showing how much the transmittance and therefore the thickness measured by the transmittometer can vary for different optical constants found in the literature and experimentally in our group: δ'-NbN: $n = 3.1 - 2.4i$ (red dots), δ-NbN: $n = 2.1 - 3.1i$ (green circles), β-Nb_2N: $n = 1.1 - 2.6i$ (blue asterisks), $n = 2.09 - 2.55i$ (value used in our simulations, magenta crosses), $n = 2.2954 - 1.3955i$ (value found by Dr. Gale Petrich, black diamonds), $n = 1.9533 - 1.6933i$ (value found by me, cyan boxes).

and 30°). This figure shows the results for different phases of NbN as well: the points are relatively well separated according to transmittance, varying by approximately 4 percentage points for each combination of thickness and polarization. The difference would be even greater for larger angles.

The spot size for the visible reflectometer was measured to be approximately 0.81 to 0.92 millimeters, depending on the size of the iris in front of the LED. In the future, it might be possible to map the thickness of the NbN films over the substrate to check for local variations or defects on the order of 1 mm. In addition, the optical design of the transmittometer could be adjusted to focus the spot to a smaller size, possibly with a microscope objective, to create a more detailed map of the spatial variation of the thickness of the NbN film.

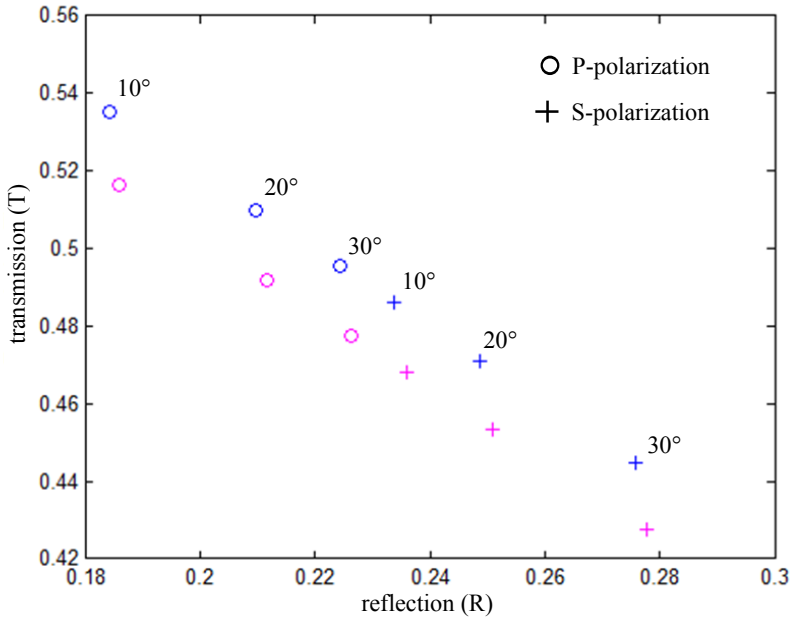

Figure 3.15: Transmittance versus reflectance of a 5-nm-thick NbN film on MgO for 635-nm light. The S-polarization points are represented by crosses, and the P-polarization points are represented by circles. The blue data points are for δ-NbN, and the magenta data points are for β-Nb_2N. The angle is varied from 30° to 10° as labeled, with the points representing greater angles closer to the top left of the figure for each combination of polarization and material.

The optical setups currently give good relative results, which can be used to provide feedback on the stability of the film deposition process and can be correlated with high-efficiency devices to select the best deposition conditions. An accurate, and not merely precise, measurement of the thickness requires additional information, in particular an accurate knowledge of the optical constants of NbN. The optical setups do not give the same thicknesses, but do give the same relative thicknesses between samples, because the optical constants of NbN used in the calculations are taken from VASE results of a thick film grown several years ago under different deposition conditions than we now use. A thick film was necessary so that transmission into the substrate was negligible and thus the measurement did not require a substrate that was opaque over the entire measurement range; however, the optical constants of thin and thick films can differ considerably[74].

The thickness as measured by the optical setups clearly correlates better with the sheet resistance

than the deposition time does, which makes sense given the amount of control over the deposition parameters affecting each individual chip in a run. The XRR and TEM comparisons also corroborate the thickness measurements, though there are some issues with charging of samples and tilt with the TEM measurements. The VASE results seem the most accurate for the individual film tested, though the method has several drawbacks, one of which is the inability to take data at wavelengths at which the substrate is transparent, such as $\lambda = 1550$ nm. Thus, several films from different runs would have to be tested to see whether the relative thicknesses as measured by VASE matched the relative thicknesses measured using the optical setups, perhaps leading to a reliable correlation factor that could be used to calibrate the thickness measurements of the optical setups.

This chapter presented two optical setups to non-destructively measure the film thickness of NbN thin films. The optical measurements correlate better with the sheet resistance than the deposition time, which implies that the deposition time is not as reliable an indicator of the film thickness as the results of the optical measurements. The optical measurements are also simple and relatively quick to perform. However, several assumptions in the optical model used to correlate the measured transmittance with a film thickness lead to discrepancies in the thicknesses measured by the two optical setups and by different methods such as TEM and VASE. The model assumes that the optical constants of NbN are constant throughout the film, which might not be the case if the microstructure of NbN changes near the substrate. In addition, the optical constants of our NbN thin films are not known, and the literature and VASE measurements on other films suggest that they might vary significantly depending on the phase of NbN and the deposition parameters. The optical results are consistent over time and give a good measure of the relative thickness of films, which is adequate for device development.

4

Optical Modeling of Devices

This chapter gives extensive optical modeling of SNSPD devices using an analytical approach based on the transfer matrix method. Previous published reports have not designed optimized optical structures numerically or analytically; instead, they have assumed, for instance, that integrated quarter-wavelength optical cavities are optimal for increasing the strength of the electric field in the NbN device layer[15]. As shown below, the optimal cavity size in fact varies slightly with the thickness and fill factor of the NbN layer. It is also possible to optimize the membrane thickness for SNSPDs

on SiNx membranes and other novel geometries that can be described as a stack of thin films, and the transfer matrix method is modified here to take into account a substrate thickness that is longer than the coherence length of the incident radiation, thus increasing the range of device geometries that can be explored. In addition, the analytical results here show the importance of using incoherent rather than coherent illumination when an integrated cavity is included in the device structure and the insignificant effect of an anti-reflection coating in most cases. Thus, exploring the optical properties of devices analytically gives direction for device design.

4.1 Transfer Matrix Method For Thin Films

The transfer matrix method produces an analytical description of the optical properties of a thin film or a stack of thin films and was first formulated by F. Abeles in 1948[75]. Previous work on modeling the properties of SNSPDs has relied on finite element analysis[38] rather than an analytical solution, though a numerical solution has occasionally been included for comparison with FEA results[76]. As shown below, the electric field intensity within a "cut plane" through a simulated device layer is a valid approximation of the electric field throughout the thickness of a thin layer. However, an exact solution is possible by treating the device layer as an effective medium, similar to what has been done for metamaterials[77]. In the effective medium approximation, the permittivity of a patterned layer is the weighted average of the permittivities of the material components, assuming that the electric field is constant within the plane of the layer. For gratings, this assumption is valid for TE polarization but not TM polarization. It has been found that the incident light must be polarized parallel to the NbN nanowires for maximum absorptance (TE polarization)[38], and thus the device layer can be treated as an effective medium as long as it is assumed that the device will be measured experimentally with TE polarized light. FEA analysis is attractive if both TM and TE polarizations will be investigated, which is perhaps why the transfer matrix method has not been

more widely used. The transfer matrix method also cannot consider complicated, three-dimensional structures such as antennas[20].

Previous work on patterned films has also used rigorous coupled-wave analysis[78], which can handle both the parallel (TE) and perpendicular (TM) cases[79], but here the simpler transfer matrix method is used because TE polarization is almost always used experimentally. The transfer matrix method determines the reflected and transmitted intensity of light through a film or a stack of layers with different indexes of refraction, given the incident intensity on one side and the assumption that there is no incident back-propagating wave[80]. (See Figure 4.1.) It can also give the intensity of the electric field versus depth into the optical stack, which is necessary for finding the absorptance of a single layer in the structure.

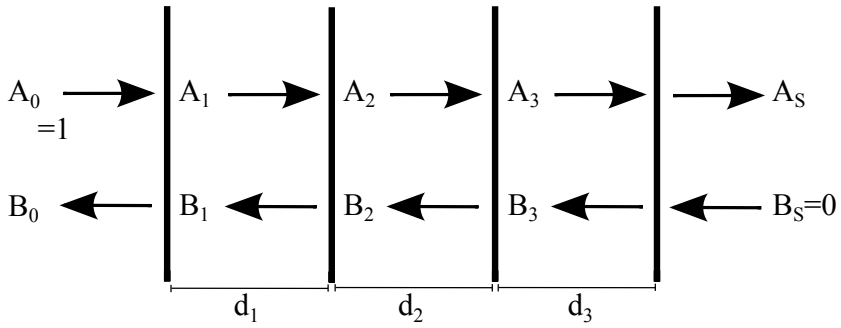

Figure 4.1: Transfer matrix parameters and unknowns. $\mathcal{A}_x$ refers to the forward propagating wave in medium x, and B_x refers to the back propagating wave. For the cavity geometry, the subscript S refers to air, and the subscript 0 refers to the substrate. Figure adapted from Yeh[80].

The transfer matrix is built by considering the relationship between the forward and backward propagating waves across each interface and from one side of a layer to the other. Across each interface, a matrix can be used to describe the Fresnel relations that relate the amplitudes of the forward and backward propagating waves. As a wave travels across a layer, the phases change, and thus another matrix can be used to relate the phases of the waves on each side of the layer. The total transfer matrix is built by multiplying the matrices associated with each interface (denoted as $D_{\text{layer1,layer2}}$)

and each layer in the stack (denoted as P_{layer1}), which gives

$$M = D_{\text{layer0,layer1}} \times P_{\text{layer1}} \times D_{\text{layer1,layer2}} \times P_{\text{layer2}} \cdots \times D_{\text{layer}n-1,\text{layer}n} \tag{4.1}$$

Once the total matrix is determined, the reflected and transmitted amplitudes of the electric field outside the stack can be found because there are two known values and two unknown values. The known values are the incident wave amplitudes in the forward (A_0) and backward directions (B_S, which is assumed to be zero), and the two unknowns are the reflected and transmitted waves, B_0 and A_S.

To determine the amplitudes of the forward and backward propagating waves in a specific layer (A_x and B_x), a submatrix describing the stack of films between the layer of interest (x) and the final medium (S) is found. Because the total transmitted wave (A_S) was found using the total transfer matrix and the incident backward propagating wave (B_S) is assumed to be zero, the submatrix can be multiplied by the vector describing the waves in the final medium to obtain the forward and backward propagating waves in the layer of interest.

Here, the intensities of the electric field in the NbN layer are important in determining the absorptance of light in the NbN. When NbN is the only absorbing medium in the stack, the absorptance in NbN can be found by subtracting the reflectance (R) and the transmittance (T) from the incident intensity, which is usually computed in terms of percentages (i.e., $A = 100\% - R - T$). However, in devices that include a gold layer, which is also absorbing, the total absorptance includes the light absorbed in gold, and thus the electric field intensities of the backward and forward propagating waves in NbN must be found to determine the absorptance in NbN.

The total electric field in a layer is described by

$$E(z) = A_x e^{ik(z-d_x)} + B_x e^{-ik(z-d_x)} \tag{4.2}$$

where A_x is the amplitude of the forward propagating wave in layer x and B_x is the amplitude of the backward propagating wave in layer x, as found using the submatrix and the amplitudes in the final medium. The thickness of layer x is d_x, and the wavevector in layer x is k, which is $2\pi nx/\lambda$. To determine the absorption in layer x, the formula for the resistive losses is[38]

$$Q(z) = \frac{1}{2}\omega \mathrm{Im}(\varepsilon)|E(z)|^2 \tag{4.3}$$

where ω is the angular frequency of the incident light and $\mathrm{Im}(\varepsilon)$ is the imaginary part of the permittivity of the layer. This equation must be integrated over the thickness of the layer to determine the total absorption in the layer. In Anant et al.[38], the absorption was assumed to be constant across the NbN layer because it is relatively thin, and thus the absorption in a cut plane was used as representative of the absorption across the layer.

The assumption that the absorption is relatively constant throughout the thickness of the NbN layer is valid for typical device geometries that are composed of films that are thinner than the skin depth of NbN. Figure 4.2 shows the absorption over distance in a thin, 10-nm-thick film of NbN on sapphire, illuminated through the substrate. The plot shows the exponential decrease with distance into the film, but the absorptance actually varies by less than one percentage point.

Here, though the assumption of constant absorptance with film thickness is generally valid, the total absorptance was determined by integrating the absorptance across the film rather than using a representative cut plane. The integration was carried out using the numerical integration method `trapz` in MATLAB. In Deparis[81] and Pettersson et al.[82], similar work was performed to determine the absorption profile in an optical stack, but the total absorption in a layer was not reported (although it would not be difficult to numerically integrate the absorption profiles reported).

To calculate the absorptance of the NbN layer of a device, which is composed of nanowires and not a continuous film, the effective index of refraction of the layer must be used, which depends

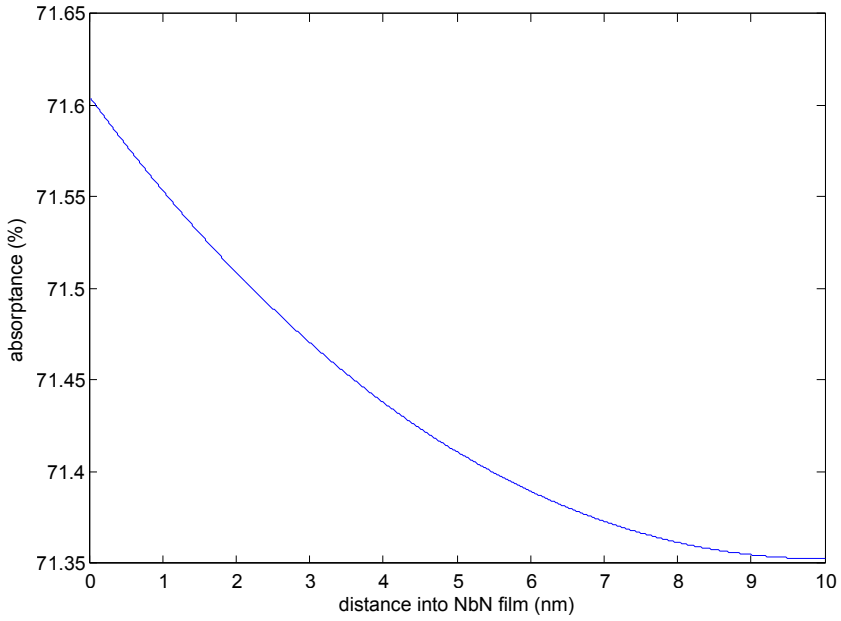

Figure 4.2: Absorptance versus distance into a 10-nm-thick NbN film on sapphire, illuminated through the sapphire substrate. Although there is a decrease in the absorptance with distance as expected, the decrease is small enough that the absortpance can be assumed to be constant with thickness in calculations of the total absorptance.

on the fill factor. A weighted average (weighted by the fill factor) of the permittivity of NbN and the permittivity of either air or HSQ (depending on the material that is between the nanowires) is found, and then the square root is used as the effective index of refraction. The thickness is simply the thickness of the nanowires. An example of a MATLAB script used to produce the plots here is given in Appendix B.

4.2 Coherent and Incoherent Light Sources

In experimental practice, lasers are often used to test the detection efficiency of devices. If the laser is continuous as in Anant et al.[38] and Maingault et al.[83], then the substrate acts as an etalon. However, because the substrate thickness is not precisely known within a factor of the wavelength, it could either help or hinder the absorptance in the NbN layer. In previous work, the etalon effect did not

offer much of an advantage or disadvantage, and the effects of ignoring it might appear to be noise in the data collected on devices, because the boundary between the substrate and air was not highly reflective. For example, if the substrate is sapphire, the reflectance at the interface between sapphire and air is only 7.4%. However, once an optical cavity is introduced, which has a gold mirror with a high reflectance, the etalon effect in the substrate can be significant and must be taken into account in the measurement setup, as shown below. Other groups who use pulsed sources on the order of picoseconds might also see substrate effects due to the partial coherence of the light in this case. A 1-ps pulse has a coherence length on the order of the pulse width, which is 300 μm in vacuum and 175 μm in MgO, which could be close to the thickness of the substrate.

The transfer matrix method assumes that the incident light has a coherence length that is longer than the thickness of the optical stack. In the case of a thick layer, for example, a substrate with a thickness much larger than the coherence length of the light, the transfer matrix method is not applicable. As illustrated in Figure 4.3, the transfer matrix method is used on the initial layers of the device (e.g., the antireflection coating (ARC)) on the "first side" of the substrate to find the transmitted light intensity into the substrate. Then, this intensity is used as the input to the transfer matrix representing the layers on the second side of the substrate. The light reflected from the second side back into the substrate is then used as input to the transfer matrix for the layers on the first side of the substrate. The light reflected initially from the first side is added to the light later transmitted from the substrate into air to give the total reflectance of the device. The light transmitted through the second side on each pass is added to give the total transmittance of the device. The absorptance in a layer must be calculated in every pass and added to give the total absorptance. The totals are calculated for 100 loops in the substrate in the MATLAB code given in Appendix A, but in practice, the reflectance, transmittance and absorptance of the device are relatively stable after three passes.

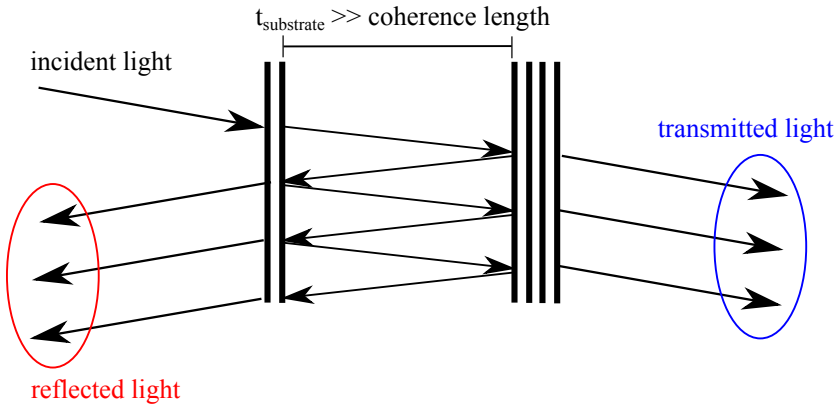

Figure 4.3: Schematic representation of the multiple passes that light makes through a substrate. Light is incident on the left side of the substrate. The reflectance includes contributions from the light that is first reflected from the left side as well as the light that is transmitted through the left side after multiple passes within the substrate. The transmittance is the total of the contributions from light transmitted through the layers on the right side of the substrate after a single or multiple passes through the substrate.

4.2.1 Absorptance in NbN Device Without an Optical Cavity

A typical device geometry is a 4-nm-thick NbN device with a 40% fill factor on sapphire. When the device is back-illuminated (i.e., the light is incident on the side of the substrate that does not have the device), it is typical to include an anti-reflection coating (ARC) composed of a quarter wavelength layer of hydrosesquisiloxane (HSQ, a type of spin-on glass) (n=1.38, d=281 nm). A perfect ARC would have an index of refraction that is the geometric mean between the refractive index of air and that of the sapphire substrate (n=1.75), which is approximately 1.32, and its thickness for 1550 nm light is approximately 293 nm.

Figure 4.4 shows the effects of back illumination with coherent light with a perfect ARC, with an imperfect ARC and with no ARC. The substrate acts as an etalon, and there are interference effects within the substrate. However, the perfect ARC eliminates the effect of the substrate thickness on the absorptance because the ARC guarantees that no light is reflected back into the cavity once it is reflected from the device layer: there is no standing wave in the substrate. The imperfect ARC,

though, can increase the absorptance of the film above that with a perfect ARC or decrease it, depending on the thickness of the substrate. The greatest absorptance with an imperfect ARC is 13.2%, and the lowest is 12.7%, which is an improvement of 7% over absorptance with the perfect ARC when the substrate thickness is optimal. Without an ARC, however, the absorptance in the film varies widely from 10.8% to 13.5%. Thus, a difference of approximately 200 nm in substrate thickness can lead to a decrease in the coupling into the device of 17% from the value with a perfect ARC. The difference in either case is only a few percentage points of absorptance, which is a typical level of variation between devices on a chip due to other factors, such as fabrication quality.

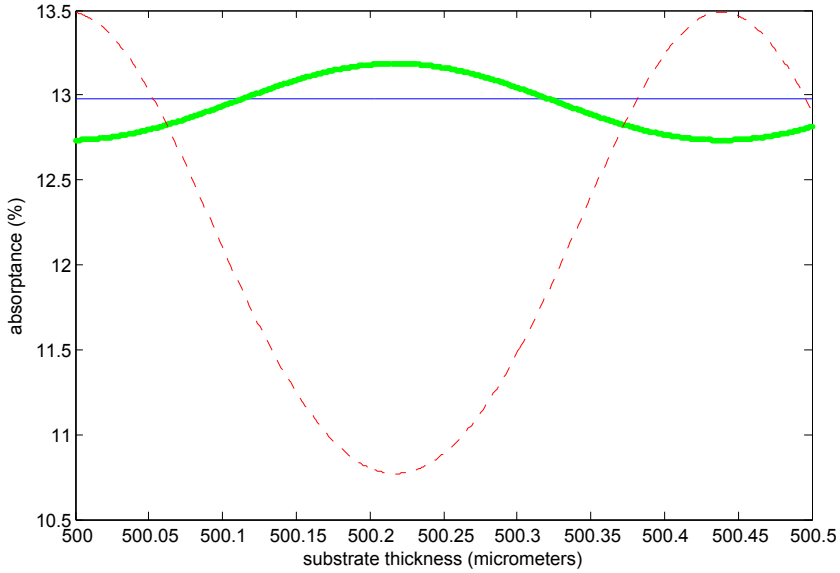

Figure 4.4: Absorptance in NbN versus substrate thickness with a perfect ARC (thin blue line), an imperfect ARC (thick green line) and no ARC (dashed red line). The substrate is sapphire (n=1.75), and the fill factor of the 4-nm-thick NbN layer is 40%. Although the absorptance varies with the substrate thickness with an imperfect ARC or no ARC, the variation is only at most 17%.

4.2.2 Absorptance in NbN Device With an Integrated Optical Cavity

The effect of substrate thickness is more dramatic when an optical cavity is added to the device. Here, a quarter-wavelength HSQ layer is added on top of the NbN layer, with a gold layer on top

of the HSQ to act as a mirror, to form an optical cavity on top of the device. With an optical cavity, most of the light that is transmitted through the detector initially is reflected back, which increases the absorptance dramatically. Figure 4.5 shows the absorptance in a 4-nm-thick, 40% fill factor NbN device with an optical cavity and a perfect ARC, an imperfect ARC and no ARC. As above, an imperfect ARC can help or hinder the performance of the device when the substrate thickness is taken into account, with a range of absorptance of 27.8% to 32%. Without an ARC, however, the variation in absorptance in NbN is from 18.4% to 46.2%, which is a difference of a factor of 2.5, over a range of substrate thickness of only approximately 200 nm, which is several orders of magnitude smaller than the typical thickness tolerance of silicon wafers of 20 μm. This effect is much larger than what occurs with either incoherent light or coherent light without an optical cavity.

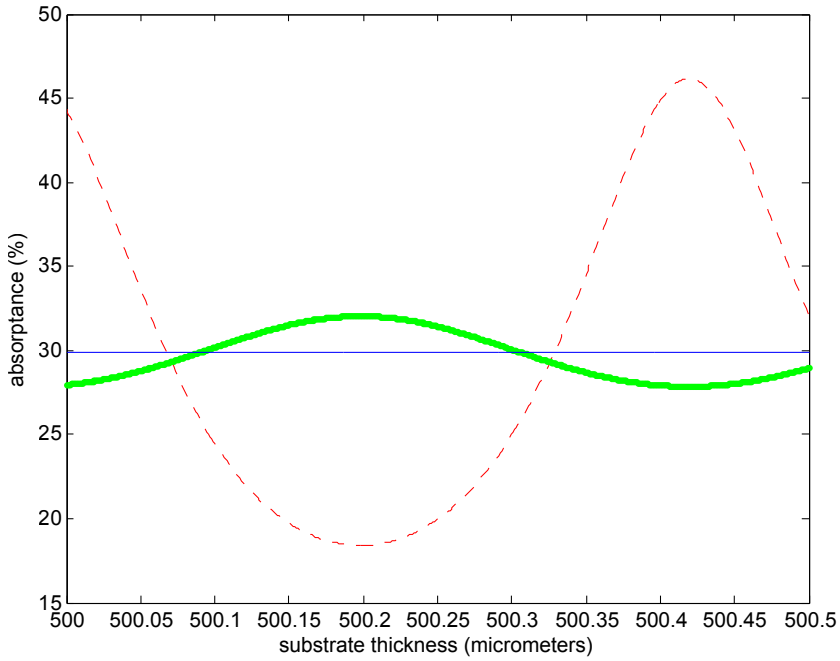

Figure 4.5: Absorptance in NbN versus substrate thickness with a perfect ARC (thin blue line), an imperfect ARC (thick green line) and no ARC (dashed red line). The substrate is sapphire (n=1.75), and the fill factor of the 4-nm-thick NbN layer is 40%. The optical cavity on top of the NbN device is composed of a quarter-wavelength layer of HSQ and gold. Here the variation with an imperfect ARC or no ARC is significant, up to a factor of 2.5.

4.2.3 Use of an Anti-Reflection Coating (ARC)

The effect of the substrate when coherent illumination is used does not appear to be significant without an optical cavity and can thus be neglected in optical models without a great loss in accuracy. It also would not be especially worthwhile to attempt to fabricate on the areas of the substrate that are close to the ideal thickness given in the models above if no optical cavity is used because the increase in absorptance would only be several percentage points. By this line of reasoning, though, fabrication of the ARC can also be neglected for most applications. Figure 4.6 shows the variation in the absorptance versus NbN device thickness with and without a perfect or imperfect ARC coating on the sapphire substrate for incoherent illumination at 1550 nm. The absorptance with a perfect ARC is 27.94% compared to 27.89% with an imperfect, HSQ ARC and 25.89% without an ARC for a device thickness of 4 nm. The improvement with the perfect ARC is relatively small (only 7.3% greater for a 4-nm-thick device with an ARC compared to the case with no ARC), which compares to the effect found above for the use of coherent illumination without an ARC. In practice, if extra processing steps are necessary to fabricate an ARC, especially steps that could damage the NbN layer with heat or solvents, it is probably not worthwhile to include an ARC unless the application demands the highest level of quantum efficiency possible. The calculations in this chapter also neglect the niobium oxide layer on the NbN, which can be several nanometers thick in practice[38], because calculations showed that including it made very little difference.

4.3 Results For Various Device Geometries

In this section, analytical results are presented for devices with integrated optical cavities and devices on free-floating membranes to guide the fabrication of high-efficiency devices. Table 4.1 gives the indexes of refraction of the materials used in the calculations unless otherwise specified. In all simulations presented below, a perfect ARC is assumed unless otherwise specified, and the source of

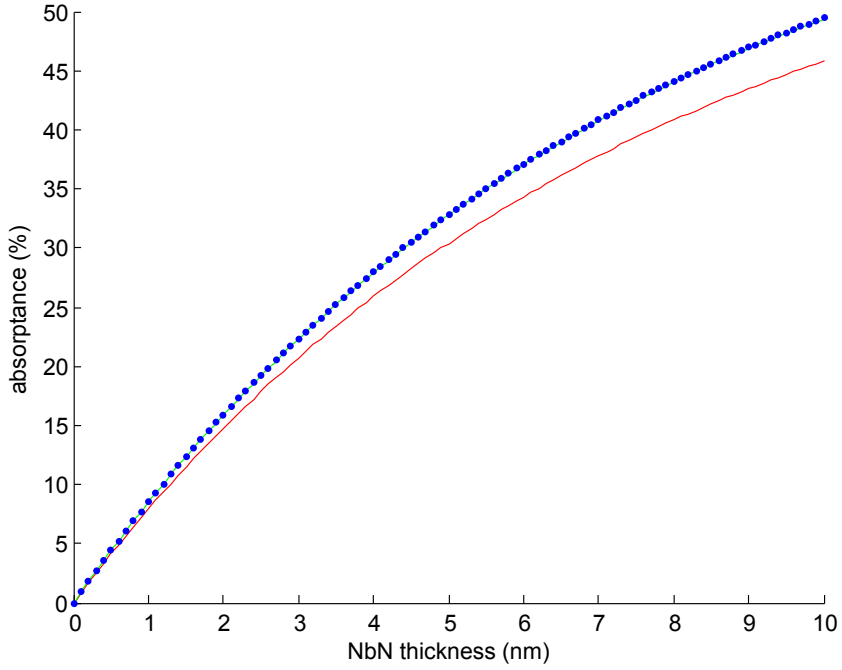

Figure 4.6: Absorptance in a 40%-fill-factor NbN layer versus NbN layer thickess with a perfect ARC (blue dotted line), imperfect HSQ ARC (green solid line, which is almost coincident with the blue dotted line) and no ARC (red solid line) on the back of the sapphire substrate. The difference between using a perfect ARC (n=1.32) and an "imperfect" one composed of HSQ (n=1.38) is vanishingly small, and the difference between a perfect ARC and no ARC at all is also very small, suggesting that an ARC in this geometry is not necessary.

illumination is assumed to have a coherence length that is much shorter than the thickness of the substrate.

4.3.1 Integrated Optical Cavities on Sapphire

An integrated optical cavity fabricated on top of the NbN using HSQ and a gold mirror can enhance the absorptance of light in the NbN layer. The thickness of the HSQ cavity is such that there is constructive interference at the NbN layer, which increases the local electric field intensity and thus the amount of resistive losses in the NbN. Figure 4.7 shows the electric field intensity as determined using COMSOL MultiPhysics 4.3 for a two-dimensional model of a device on sapphire, which shows the high intensity within the NbN. In general, the HSQ cavity thickness is approxi-

Table 4.1: Indexes of refraction of materials used in the calculations for a wavelength of 1550 nm. The value given in the literature for HSQ is 1.39, but the value used in the calculations was mistakenly entered as 1.38.

Material	Index of refraction
silicon	3.47772 [84]
silicon dioxide	1.54 [85]
silicon nitride	2.217 [86]
HSQ	1.38 [87]
sapphire	1.75 [38]
NbN	$5.23 - 5.82i$ [38]
gold	$0.55 - 11.5i$ [88]

mately a quarter wavelength thick, which is 281 nm for HSQ at a wavelength of 1550 nm. Here, the HSQ thickness is 267 nm, which is the optimal HSQ thickness according to the transfer matrix calculation for a cavity on silicon with a 4-nm-thick, 40% fill factor NbN layer.

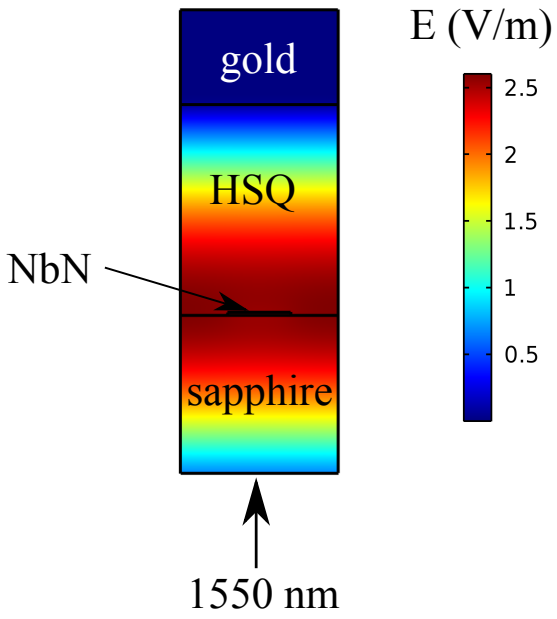

Figure 4.7: Two-dimensional FEA simulation using COMSOL MultiPhysics 4.3 to show the high intensity of the electric field within the NbN layer when the cavity thickness is optimal. Light is incident from below and linearly polarized with the polarization direciton out of the page.

An integrated optical cavity on a sapphire substrate was explored by Rosfjord et al.[46], who achieved a device detection efficiency of 57% with a 195-nm-thick HSQ cavity and an ARC composed of HSQ on the other side of the substrate, through which the device was illuminated. Figure 4.8 shows the absorptance of NbN versus the HSQ thickness of the cavity for a device with the same approximate thickness, fill factor and values for the indexes of refraction as that reported by Rosfjord et al. (where n_{HSQ} is estimated to be 1.4). The HSQ cavity fabricated in that study was slightly thinner than intended due to thinning of the HSQ layer during processing, and Figure 4.8 shows that the ideal cavity thickness, 268 nm, was in fact much higher than what was fabricated. This plot shows that the absorptance of the NbN for a 195-nm-thick cavity is 63.8%, which is roughly the maximum value that was found experimentally (57%). The maximum absorptance, however, could reach 68% for the optimal cavity thickness. The absorptance is not very sensitive to the thickness of the HSQ cavity, as this plot shows. A cavity that is 100 nm too thin (168-nm-thick) would lead to an absorptance of 59.7%, which is still 88% of the maximum absorptance.

4.3.2 Silicon Oxide or Nitride Layer on Silicon Substrate

Figure 4.11 shows a schematic of a device with a thermal oxide layer between the silicon substrate and the NbN device layer as well as a plot of the absorptance in NbN versus the thickness of either a thermal oxide layer or a nitride layer for a variety of thicknesses of NbN with a fill factor of 40%. Figure 4.9b assumes that the other side of the device has a perfect ARC.

The quarter wave thickness of silicon dioxide (252 nm) is close to the ideal thickness for 1 nm of NbN with a 40% fill factor, but it is increasingly far from the ideal values for thicker NbN thicknesses (or higher fill factors). The ideal SiO_2 thicknesses are given in Table 4.2 for thicknesses from 1 nm to 6 nm for a fill factor of 40%, which shows that it is difficult to select an appropriate thickness for a device if we do not already know what the thickness and fill factor of the device will be. In previous papers that use a silicon dioxide layer between the silicon substrate and the NbN[15], a

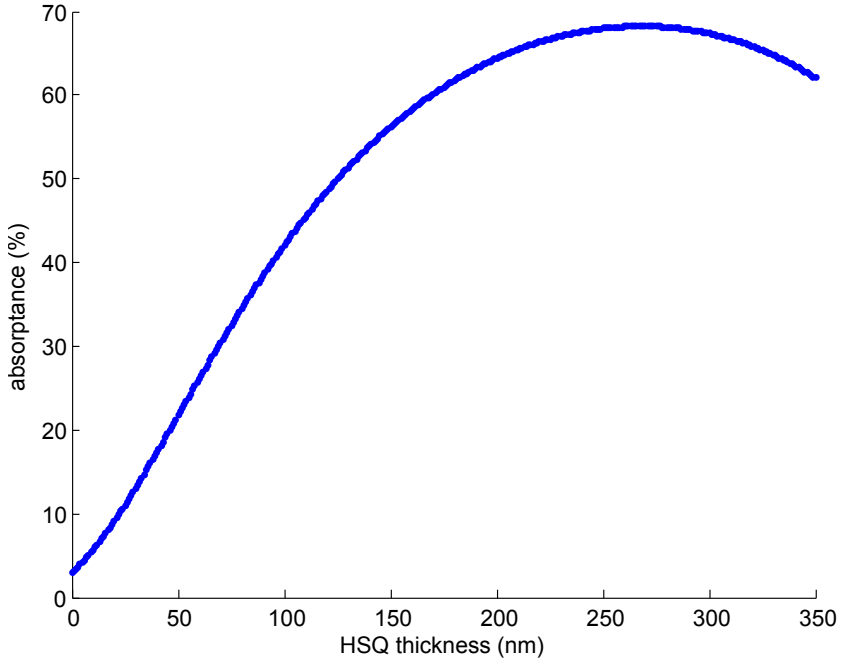

Figure 4.8: Absorptance in NbN for a 4-nm-thick, 50% fill factor device on sapphire versus HSQ cavity thickness. The values for the indexes of refraction are those reported in Rosfjord et al.[46]. This plot shows that a non-optimal cavity thickness can decrease the absorptance to a value less than that without a cavity, but for thicknesses near the optimal HSQ thickness, the absorptance is still close to the maximum. It also shows that no HSQ thickness can give an absorptance of over 90%.

quarter-wavelength layer is used in conjunction with an integrated cavity, but these results show that it might be worthwhile to optimize the thicknesses of the oxide and HSQ cavity layers depending on the device thickness and fill factor if an integrated cavity is not going to be used. The results for silicon nitride, which is more optically dense than the oxide, are less sensitive to the changing thickness of the NbN layer: the optimal thickness varies from 176 nm to 188 nm for NbN thicknesses of 1 nm and 7 nm, respectively.

Once an integrated cavity is added, however, the thickness of the HSQ layer can be optimized to produce the highest absorptance for a given thickness of thermal oxide, as shown in the next section.

One concern with using silicon nitride is the index of refraction, which varies with density and thus is sensitive to the growth conditions when it is grown via chemical vapor deposition. Fig-

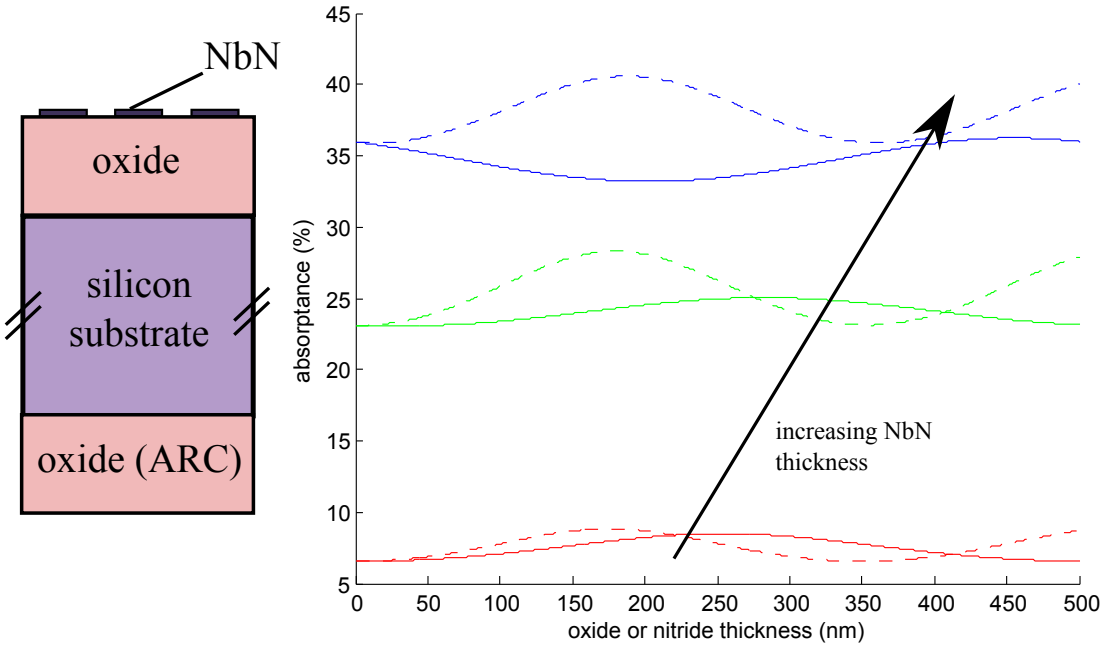

(a) Schematic **(b)** Transfer matrix method results

Figure 4.9: (a) Schematic of an NbN device on a silicon substrate with thermal oxide layers. The oxide layer on the bottom acts as an ARC. (b) Absorptance in NbN versus thermal oxide (solid lines) or nitride (dotted lines) thickness between the silicon substrate and the NbN layer for a 40% fill factor NbN device for NbN thicknesses of 1 nm (red, bottom two lines), 4 nm (green, middle two lines) and 7 nm (blue, top two lines). The optimal oxide layer thickness is sensitive to the thickness of the NbN, with an optimal value for 1 nm of 250 nm being very close to the least optimal value for 7 nm of approximately 200 nm.

ure 4.10 shows the absorptance in NbN for a 4-nm-thick, 40% fill factor NbN device on a silicon nitride/silicon substrate with a perfect ARC versus the silicon nitride thickness for a range of values for n_{SiN_x}. As shown, the optimal cavity thickness increases from 181 nm to 226 nm when the index of refraction decreases from 2.2 to 1.8.

4.3.3 Integrated Optical Cavities With SiO_2/Si Substrates

Integrated optical cavities fabricated with HSQ have been used with NbN devices on silicon dioxide/silicon substrates[15], and this section shows the results of detailed calculations of this geometry to expand our knowledge of the fabrication tolerance of the cavities and how they affect device per-

Table 4.2: Optimized thermal oxide layer thickness for different NbN thicknesses and a fill factor of 40%.

NbN film thickness (nm)	Optimized thermal oxide thickness (nm)
1	255
2	260
3	267
4	284
5	336
6	423

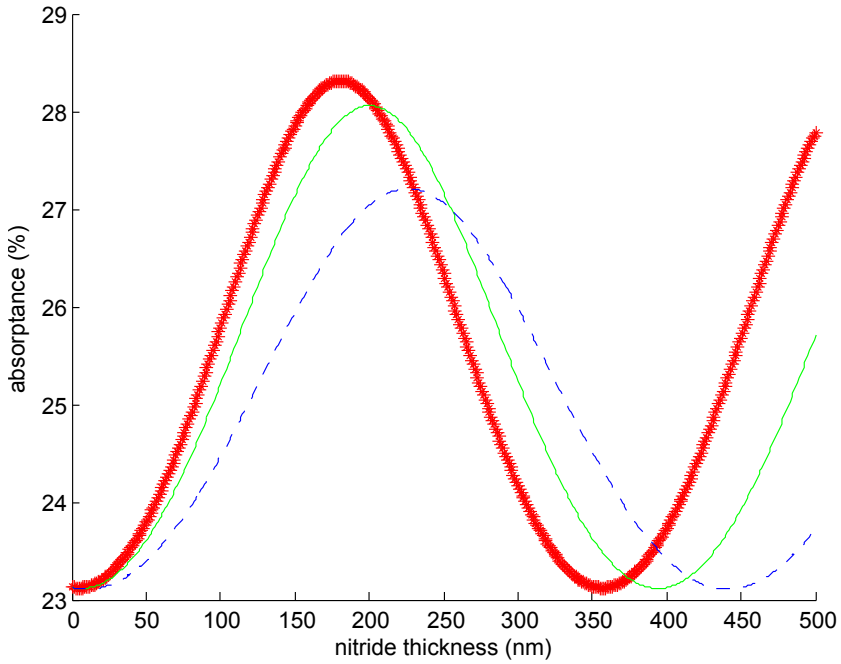

Figure 4.10: Absorptance in NbN for a 4-nm-thick, 40% fill factor device on silicon nitride on silicon versus silicon nitride thickness. The index of refraction of silicon nitride is 2.2 (thick red line), 2.0 (thin green line) and 1.8 (dashed blue line). The index of refraction of silicon nitride can vary within this range depending on the deposition parameters.

formance at different wavelengths. Figure 4.11a shows the geometry of this type of device, and Figure 4.11b shows the absorptance in NbN versus the thickness of the HSQ layer for different thermal oxide layers ranging from 235 nm to 325 nm for a 4-nm-thick, 40% fill factor NbN device. The highest absorptance, 91.5%, is achieved with a thermal oxide layer thickness of 255 nm, which is approxi-

mately the quarter wavelength thickness for oxide (252 nm), and an HSQ cavity thickness of 261 nm. However, high absorptance values can be achieved for other thermal oxide thicknesses as long as a suitable HSQ thickness is chosen for the optical cavity. This figure also shows that the absorptance in NbN does not decrease significantly over a range of HSQ cavity thicknesses of approximately 40 nm, which indicates that the fabrication tolerance is quite high.

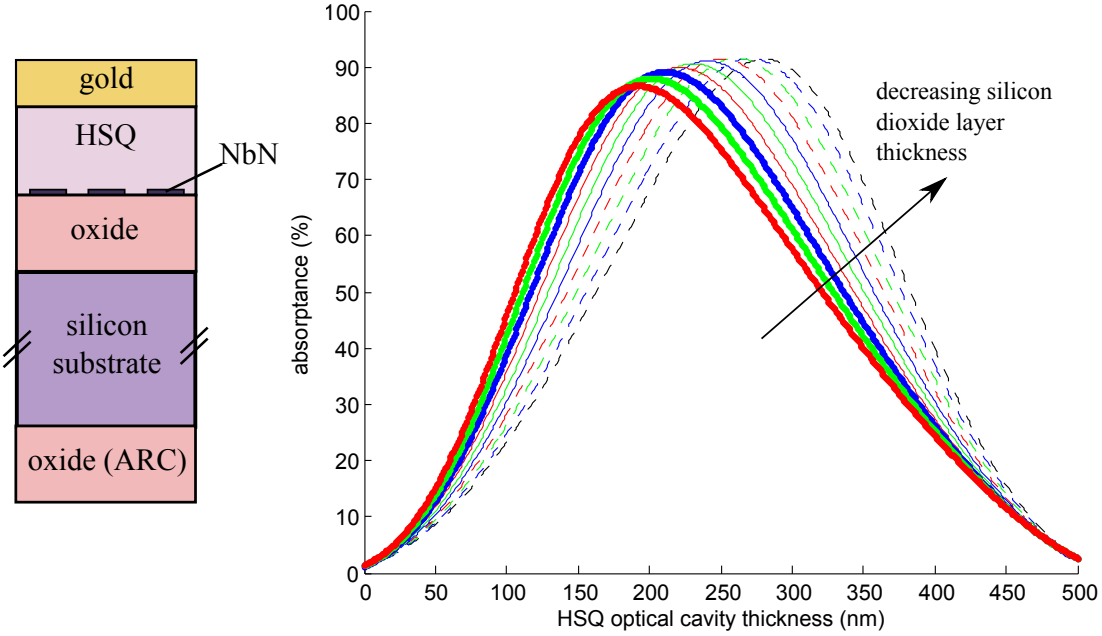

(a) Schematic **(b)** Transfer matrix method results

Figure 4.11: (a) Schematic of a device on silicon oxide on silicon and an integrated optical cavity composed of HSQ and a gold mirror. The oxide layer on the bottom acts as an ARC. (b) Absorptance in NbN versus HSQ integrated cavity thickness for various thermal oxide layer thicknesses ranging from 235 nm to 325 nm for a 40% fill factor, 4-nm-thick NbN device. The peak value does not decrease significantly, but the optimal HSQ thickness does change.

Figure 4.12 shows the absorptance in the NbN versus the wavelength of the incident light with and without an optical cavity and shows both the broadband nature of the optical cavity and the enhancement in the absorptance compared to the device without a cavity. The full width at half maximum of the cavity is approximately 900 nm, and thus the optical cavity does not select a narrow bandwidth of incident light in the infrared. In fact, the presence of the optical cavity does not

decrease the absorptance for long wavelengths of light significantly. The gold mirror, however, may block stray photons in the testing setup and thus reduce dark counts.

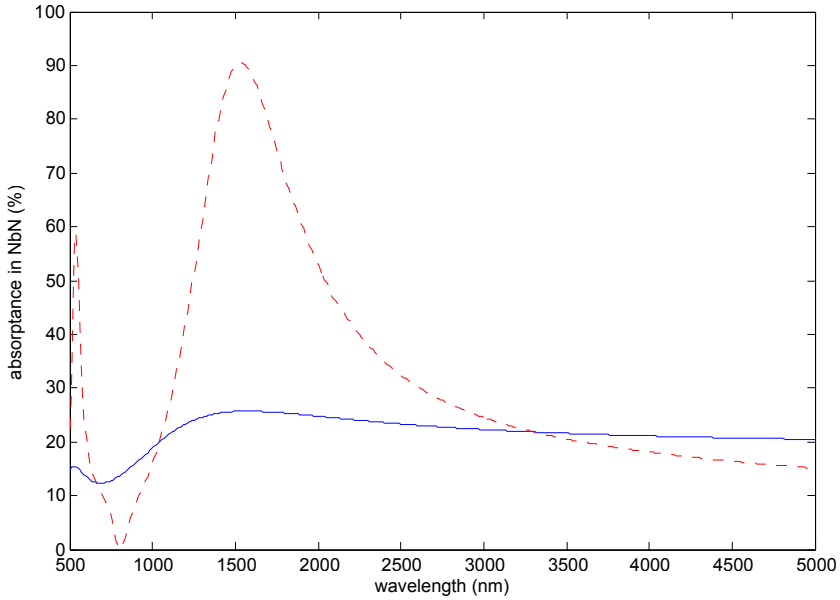

Figure 4.12: Absorptance in 4-nm-thick, 40% fill factor NbN device on silicon with a 252-nm layer of silicon dioxide under the device and on the back of the substrate to act as an ARC. The solid blue line is the absorptance without an integrated optical cavity, and the dashed red line is the absorptance with a 264-nm-thick HSQ cavity. The absorptance is enhanced up to approximately 2.5 μm with an HSQ cavity.

Another possible method to integrate an optical cavity is to bury a gold mirror beneath the silicon oxide or nitride and then use front illumination of the the device, as shown in Figure 4.13. This geometry is similar to that investigated for a transition-edge sensor in Lita et al.[89] and the optical stack for an SNSPD based on amorphous WSi^{14}, but it has not been explored for NbN SNSPDs. As Figure 4.13 shows, the absorption of a 4-nm-thick, 40% fill factor NbN layer is only 80% at an optimized oxide layer thickness of 234 nm. Fabricating a buried cavity has several advantages. First, the NbN nanowires are the last part of the structure to be fabricated, which minimizes the amount of potential damage to them due to exposure to heat and solvents during the cavity fabrication process. Second, the thickness of the substrate would not affect the optical performance of this device be-

cause it is top illuminated, so it could be used to detect coherent light sources without etalon effects in the substrate.

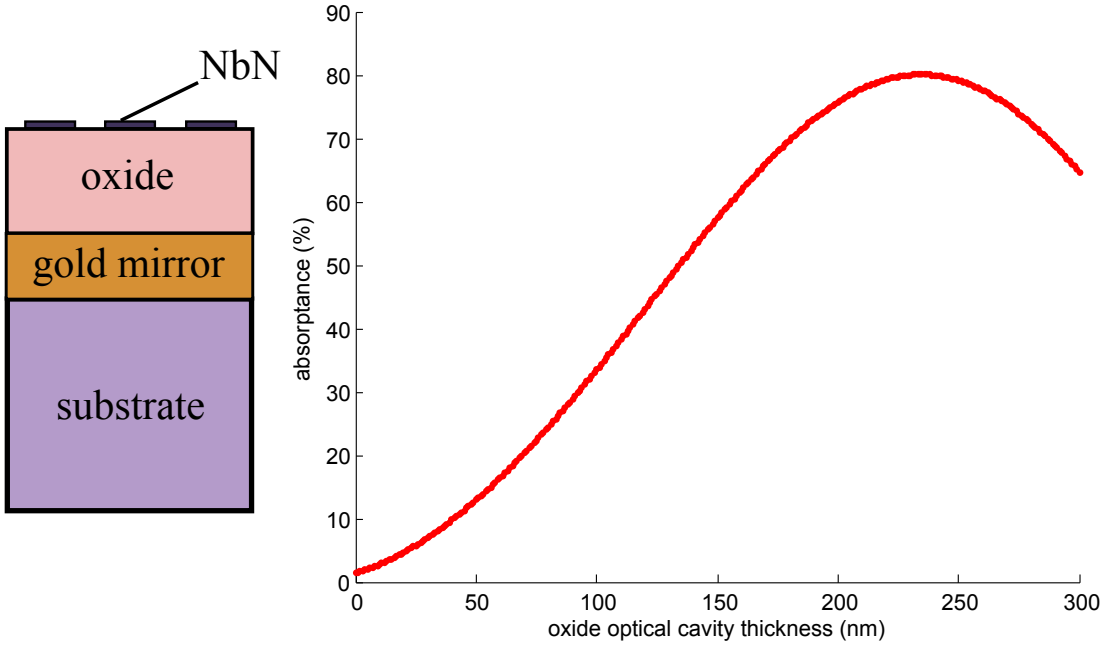

(a) Schematic **(b)** Transfer matrix method results

Figure 4.13: (a) Schematic of a device on an oxide layer grown on a buried gold mirror layer. The oxide and gold mirror act as an optical cavity, and the device is illuminated from the top. (b) Absorptance versus oxide optical cavity thickness for the device shown in (a), which reaches up to 80%.

The fabrication of a buried cavity structure does present some challenges. The gold layer on which the silicon nitride is deposited must be flat. Template stripping[90] could be used to produce a very flat gold surface (with less than 1 nm of roughness), and then an oxide or a nitride could be deposited. The NbN would have to be sputtered at room temperature to prevent the gold from melting or cracking due to the mismatch in thermal expansion of the layers, but room temperature deposition of NbN has been done in the past by our group and others[91,92].

4.3.4 Optimizing the Thickness and Fill Factor With an Optical Cavity

The optimized HSQ thickness depends on the thickness and fill factor of the device and the nature of the substrate, which has not been previously explored in the literature. This subsection gives detailed results on the absorptance that can be achieved with an optimized cavity for various fill factors and thicknesses of the NbN and shows that NbN on silicon dioxide/silicon substrates has the highest absorptance for typical SNSPD device thicknesses and fill factors. The following calculations assume a perfect ARC and illumination through the substrate.

The optimal thickness of the HSQ layer in the optical cavity depends on the nature of the substrate, as shown in Figure 4.14, and the optical density (thickness and fill factor) of the NbN (see Figure 4.15). The higher the index of refraction of a monolithic (non-layered) substrate, the lower the absorptance in NbN due to mismatch of the indexes of refraction. However, the use of a layered substrate with a well-chosen thickness for the oxide or nitride layer can lead to higher absorptances when a silicon substrate is used. The optimal HSQ thicknesses vary from 264 nm for the oxide on silicon substrate to 275 nm for the solid silicon substrate. There is also a difference in the full width at half maximum of the curves plotted.

The differences in optimal HSQ thickness shown in Figure 4.15 are not as large as the effect reported above in Subsection 4.2.2 and can generally be neglected. Here, a monolithic sapphire substrate with a perfect ARC is assumed. The optimal HSQ thickness for the optical cavity varies from 260 nm for a 1-nm-thick, 10% fill factor device to 270 nm for a 5-nm-thick, 50% fill factor device. In general, the greater the optical density of the NbN layer (i.e., the greater the thickness and/or the fill factor), the greater the optimal cavity thickness will be.

Figure 4.16 shows the absorptance versus the thickness and fill factor of the NbN layer for a device on a silicon substrate and on a sapphire substrate. The maximum absorptance possible for the silicon substrate is almost 97% for a 10-nm-thick, continuous (100% fill factor) film and 37%

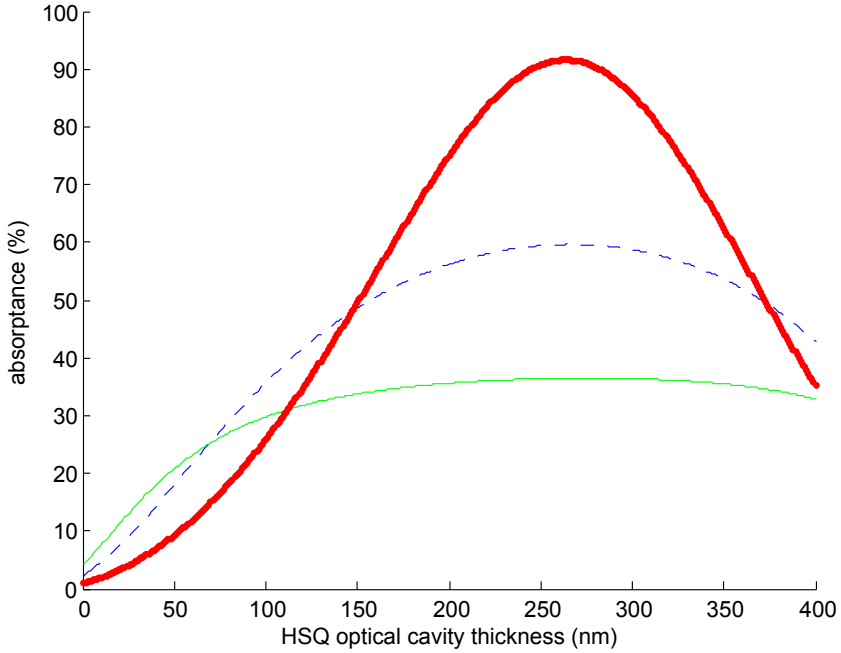

Figure 4.14: Absorptance in 4-nm-thick, 40% fill factor NbN device versus the HSQ cavity thickness for a substrate composed of sapphire (dashed blue line), silicon (thin green line) and a quarter wavelength of thermal oxide on silicon (thick red line). Sapphire can only reach approximately 60%, but silicon dioxide/silicon can reach over 90%.

for a 40% fill factor, 4-nm-thick device with an optimal cavity thickness of 315 nm and 276 nm, respectively. The maximum absorptance on sapphire is over 97% for a range of high-fill-factor, high-thickness devices and almost 60% for a 40% fill factor, 4-nm-thick device with an optimal cavity thickness of 267 nm. A sapphire substrate is more promising for high efficiency devices than a silicon substrate.

The maximum absorptance possible for NbN on both of these substrates is found in a region at or near the upper right corner of the plot, with high fill factor and high thickness. Unfortunately, the NbN thickness and fill factor in this region are impractical: if the cross section of a nanowire is too thick, the device will not be sensitive to low-energy infrared photons[29], and thus nanowires with thicknesses of 8-10 nm would not produce sensitive devices unless they were very narrow, which would present fabrication challenges[23]. The fill factor of a meander pattern is also limited by the

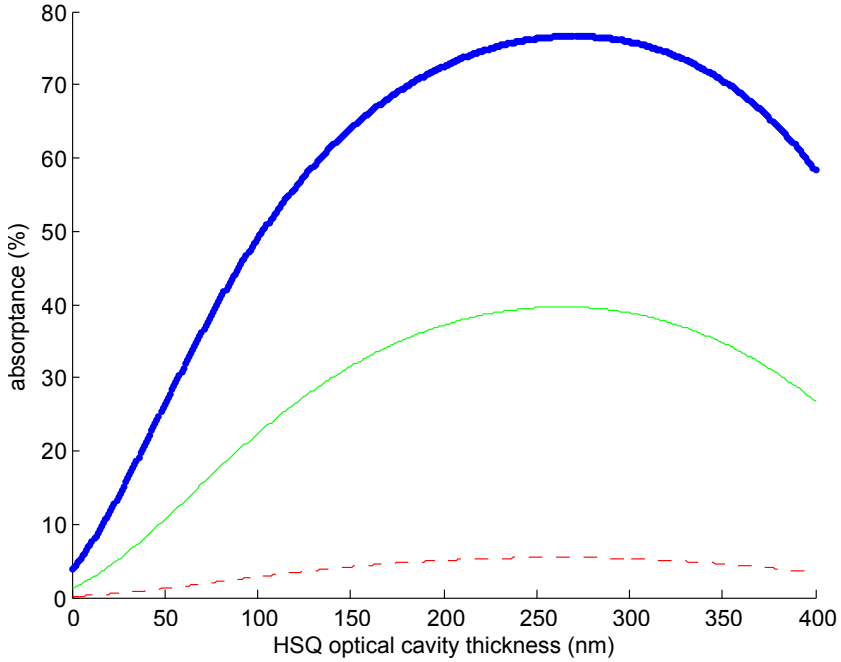

Figure 4.15: Absorptance in a 1-nm-thick, 10% fill factor NbN device (dashed red line), a 3-nm-thick, 30% fill factor NbN device (thin green line) and a 5-nm-thick, 50% fill factor NbN device (thick blue line) versus the HSQ cavity thickness on a sapphire substrate with an ARC. The optimal HSQ thickness varies with the optical density of the NbN layer.

current crowding at the turns, and fill factors of greater than 1/3 lead to current crowding and thus reduction of I_{sw}[36].

The challenge, then, is to find a substrate where the maximum absorptance is greater than 90% for practical thicknesses and fill factors. Figure 4.17 gives the "heat maps" of NbN devices on a quarter wavelength layer of silicon nitride and silicon dioxide and an optimal HSQ cavity. This figure shows that even typical devices on silicon dioxide/silicon substrates are capable of reaching high absorptances of over 90%. For example, a 4-nm-thick, 40% fill factor device has an absorptance of 91.6% with a cavity thickness of 264 nm.The thicknesses and fill factors to reach greater than 90% with silicon nitride on silicon are not as low–a 4-nm-thick, 40% fill factor device on silicon nitride with an optimal cavity has an absorptance of only 67.7%–so the best substrate for high-efficiency

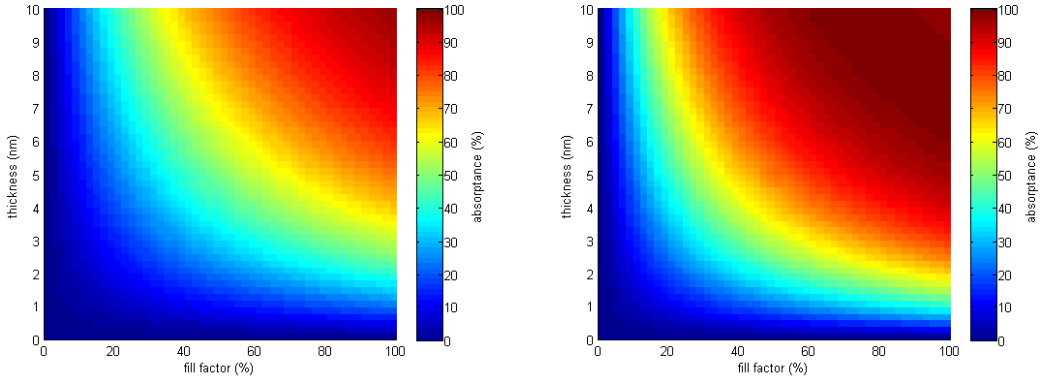

(a) silicon substrate **(b)** sapphire substrate

Figure 4.16: (a) Absorptance in NbN versus thickness and fill factor on a silicon substrate with no oxide or nitride layer. (b) Absorptance in NbN versus thickness and fill factor on a sapphire substrate. Both simulations assume back illumination through a perfect ARC. The sapphire substrate gives greater absorptance in NbN for typical device designs.

devices is silicon dioxide/silicon.

More "heat maps" and two-dimensional line plots are given in Appendix C for common substrate geometries.

4.3.5 Free-standing Silicon Nitride Membranes

SNSPDs have been fabricated on free-standing silicon nitride membranes [48], which offers the advantage of being able to transfer them onto chips using a flipchip technology and enabling integration with on-chip waveguides. SNSPDs on free-standing membranes could also be attached to the end of optical fibers, so it is important to choose the membrane thickness to maximize the absorptance of light in the NbN. Figure 4.18 shows the absorptance versus membrane thickness for a 4-nm-thick, 40% fill factor NbN device on silicon nitride in air and on an optical fiber facet ($n_{\text{fiber}} = 1.5$), where the device is illuminated either from the air or fiber or through the membrane. In every case, the optimal silicon nitride membrane thickness is approximately a half wavelength layer (350 nm). The best absorptance at this thickness is offered by the geometries that include the optical fiber because it

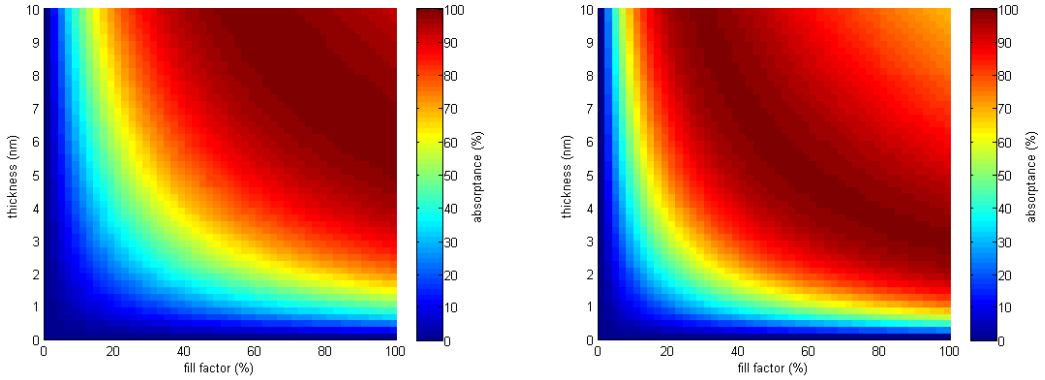

(a) silicon nitride/silicon substrate

(b) silicon dioxide/silicon substrate

Figure 4.17: (a) Absorptance in NbN versus thickness and fill factor on a silicon substrate with a quarter-wavelength nitride layer. (b) Absorptance in NbN versus thickness and fill factor on a silicon substrate with a quarter-wavelength oxide layer. Both simulations assume back illumination through a perfect ARC and an optimized HSQ optical cavity on top. The silicon dioxide/silicon substrate shows the greatest absorptance in NbN for typical device designs.

has a smaller mismatch in refractive index with the membrane.

Figure 4.19 shows the results for a free-standing membrane illuminated from the NbN side with a gold layer evaporated on the other side of the membrane, forming an optical cavity. This figure shows the results for the device illuminated in air and on an optical fiber facet. The case in air is similar to the results above for a mirror buried beneath an oxide layer in Figure 4.13. In this case, the optimal membrane thickness is approximately a quarter wavelength in thickness, similar to the results for other optical cavity structures. The highest absorptance is found for the membrane in air, which is almost 80%.

Optical fibers can be cleaved at an angle, and thus a model was built to represent the case of a non-normal angle of incidence, as shown in Figure 4.20. For non-normal incidence, there are two polarizations to consider—*s*-polarization, where the electric field is perpendicular to the plane of incidence, and *p*-polarization, where the electric field is within the plane of incidence. In the simulations, it was assumed that the nanowires would be oriented parallel to the electric field for both polarizations.

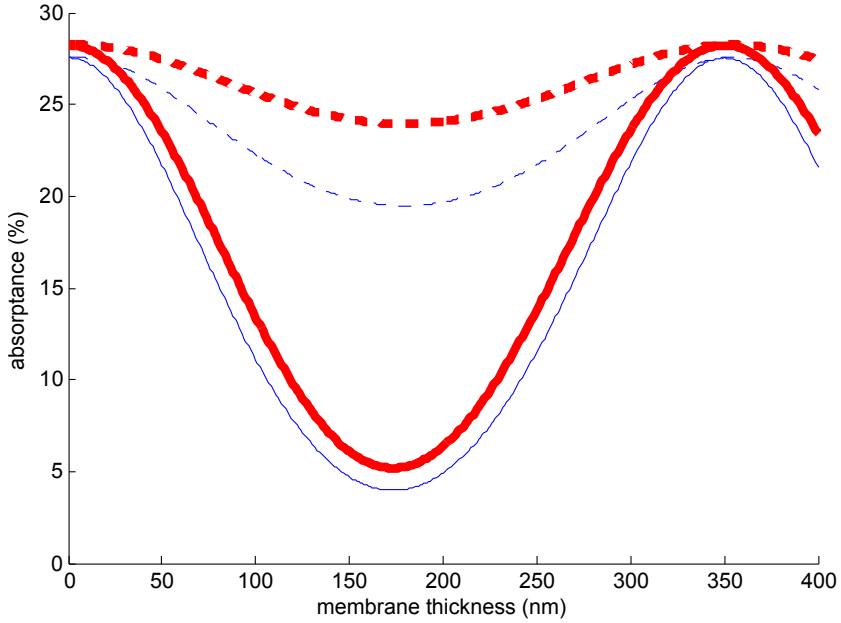

Figure 4.18: Absorptance in a 4-nm-thick, 40% fill factor NbN device on a silicon nitride membrane in air (thin blue lines) or on an optical fiber (thick red lines). The device is either illuminated from above (or from the fiber) and not through the membrane (solid lines) or illuminated through the membrane (dashed lines). In all cases, the best design would be to have the NbN device on the optical fiber with no membrane behind it, but a thick membrane of approximately 350 nm also gives the same absorptance values in NbN.

Figure 4.21 shows the absorptance in NbN for a 40% fill factor, 4-nm-thick NbN device versus the angle of incidence for several silicon nitride membrane thicknesses for *s*-polarized and *p*-polarized light. The results are similar in that the highest absorptance is found for normal incidence with a 158-nm-thick membrane for both polarizations. The optical fiber is assumed to have an index of refraction of 1.5 and to be infinite in extent, which is a reasonable approximation for a small area device. The highest absorptance, 64.7%, is found for normal incidence with a membrane thickness of 158 nm. The shape of the curves for the absorptance versus angle change for thinner and thicker membranes, with a thickness of 50 nm, for example, leading to a low dependence on angle for *p*-polarized light, though unfortunately also a very low absorptance of approximately 12.5%-13.5%. In an optical model of *p*-polarized light transmitted through a boundary from a region with

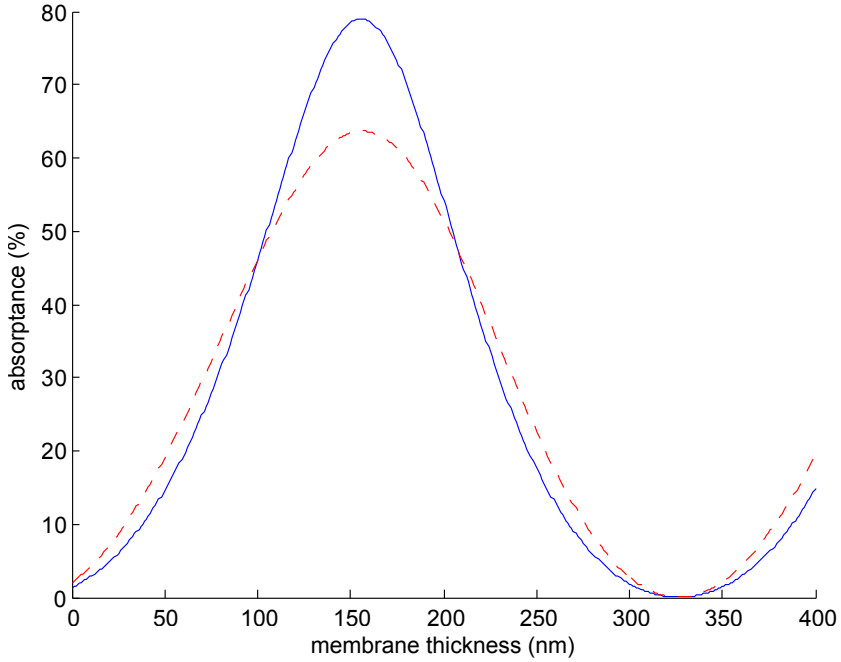

Figure 4.19: Absorptance in a 4-nm-thick, 40% fill factor NbN device on a silicon nitride membrane with gold on the other side in air (blue solid line) or on an optical fiber (red dashed line). The optimal membrane thickness in this case is approximately 150 nm and leads to an absorptance in NbN of almost 80% for the device in air and over 60% for the device on an optical fiber.

a lower index of refraction into a region with a higher index of refraction, there is an angle where no light is reflected and all is transmitted, known as Brewster's angle. There does not appear to be a Brewster's angle here due in part to the complex indexes of refraction of NbN and gold, though, for some membrane thicknesses, there is a local peak in the absorptance at high angles, which can also be observed as a local minima in the reflectance. For some membrane thicknesses, the peak in the absorptance at higher angles is significant compared to that at normal incidence, particularly for *p*-polarization. However, none of these peaks are as high as the absorptance for normal incidence with the optimal membrane thickness.

In summary, the effects of several SNSPD design parameters on the absorptance in NbN were explored in depth through analytical calculations in this chapter. The results show that the use of

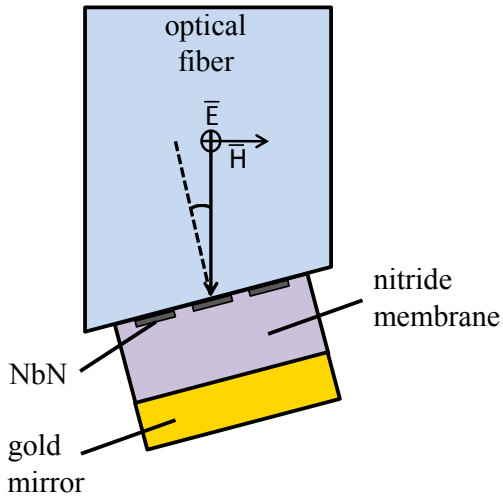

Figure 4.20: Schematic of a device on a nitride membrane that is placed on an optical fiber that has been cleaved at an angle. In this case, the electric field polarization is perpendicular to the plane of incidence, which is *s*-polarization. The light could also be polarized with the electric field within the plane of incidence, and the NbN nanowires would be oriented such that they were also parallel to the plane of incidence.

coherent light for testing leads to significant changes in the performance of the device with the thickness of the substrate if the device has an integrated optical cavity, that an anti-reflection coating is not necessary for most applications, and that the fill factor and thickness of the NbN layer influence the optimal HSQ thickness. The results also show that adding an optimal HSQ cavity can enhance the absorptance to over 90% with a silicon dioxide/silicon substrate but cannot increase the absorptance above 60% for typical device designs on sapphire, and thus fabrication of high-efficiency NbN devices cannot be done on sapphire.

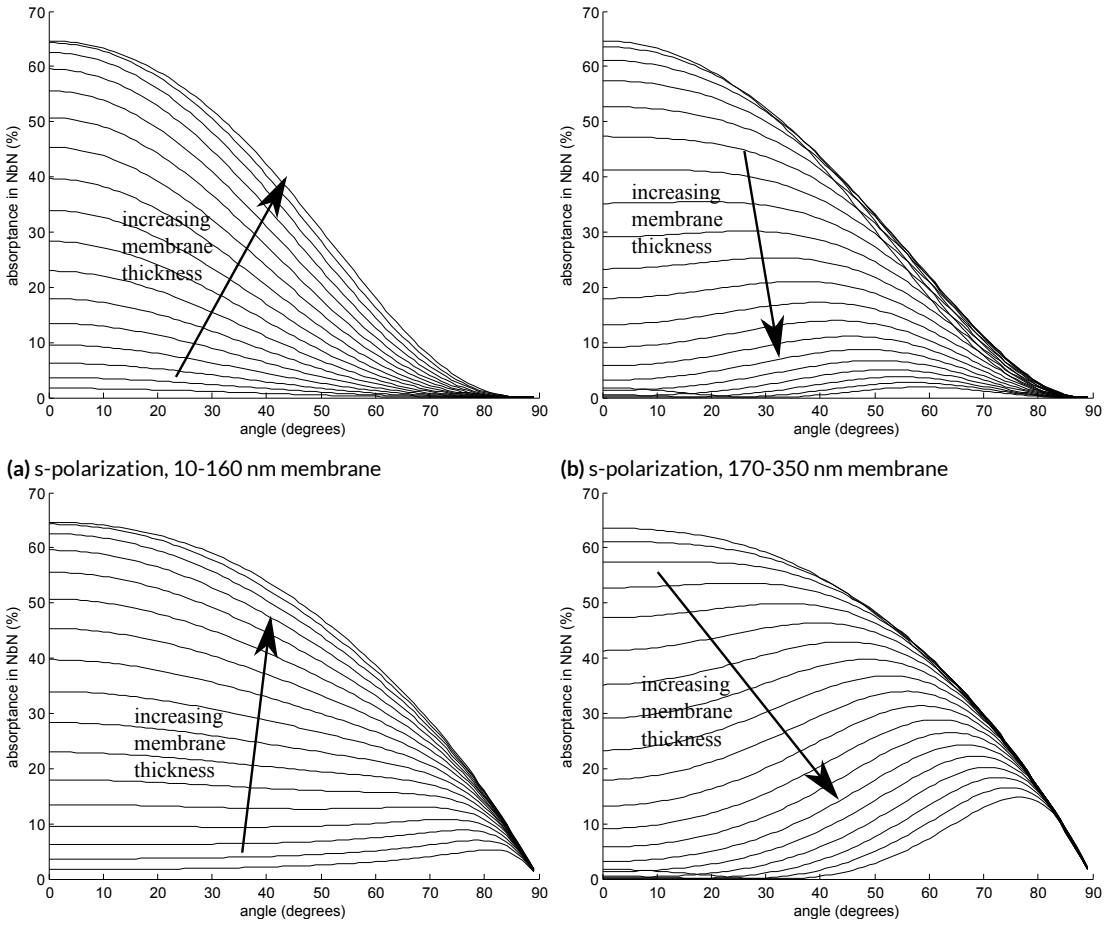

(a) s-polarization, 10-160 nm membrane

(b) s-polarization, 170-350 nm membrane

(c) p-polarization, 10-160 nm membrane

(d) p-polarization, 170-350 nm membrane

Figure 4.21: Absorptance in NbN of a 4-nm-thick, 40% fill factor device versus angle for *s*-polarized light with membrane thicknesses in the range of (a) 0 nm to 160 nm and (b) 170 nm to 350 nm. Absorptance in NbN of the same device versus angle for *p*-polarized light with membrane thicknesses in the range of (c) 0 nm to 160 nm and (d) 170 nm to 350 nm. The highest absorptance is achieved with normal incidence with a membrane that is approximately 160 nm thick for both polarizations.

5

Experimental Validation of Optical Models

5.1 Fabrication Process For Optical Cavities

Once the devices have been fabricated and screened, an optical cavity can be fabricated on the high-performance detectors to increase the absorptance and thus the device detection efficiency, as shown in the previous chapter. This chapter describes some experimental results on devices that demonstrates the close agreement between the experimental and theoretical results.

The HSQ used for cavity fabrication was FOx-16 from Dow Corning, which is 16% HSQ, that was diluted with methyl isobutyl ketone (MIBK) down to an HSQ concentration of 14.5%. A spin curve was determined for this formulation by spinning the HSQ on silicon chips that were roughly 1 cm x 1 cm. As Figure 5.1 shows, the ellipsometry data for the HSQ films on silicon matches the theoretical curve for an oxide with an index of refraction of 1.38 very well, which made it possible to determine the thicknesses easily. A plot of the spin speed versus film thickness is shown in Figure 5.2. A cavity with a thickness of 230 nm, for example, requires a spin speed of 2.1 krpm.

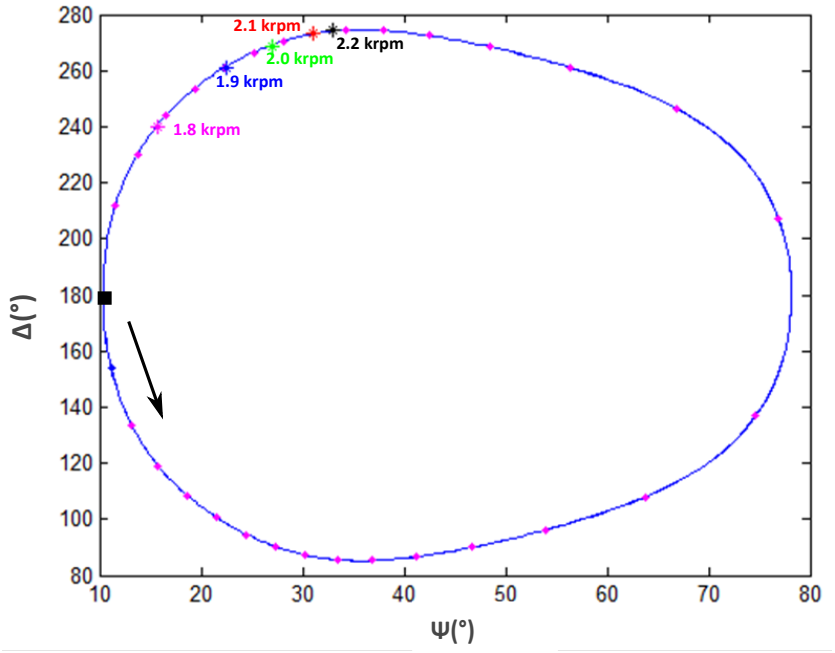

Figure 5.1: Plot of the $\Psi - \Delta$ curve for a n=1.38 layer on silicon. The point representing zero thickness is at (10°, 180°), and the arrow indicates the direction of increasing thickness. The magenta diamonds are spaced at 10 nm intervals along the curve. The experimental points are shown as stars and labeled with the spin speed used to produce them. These results only give the thickness of the as-spun HSQ, however, not the thickness of features written with the e-beam.

However, the HSQ thickness changes during electron beam exposure, as illustrated in Figure 5.3 for FOx-14 HSQ (which is 14% HSQ in MIBK). With lower doses, the HSQ is not fully crosslinked, and some thickness is lost during development as uncrosslinked HSQ is washed away. It appears

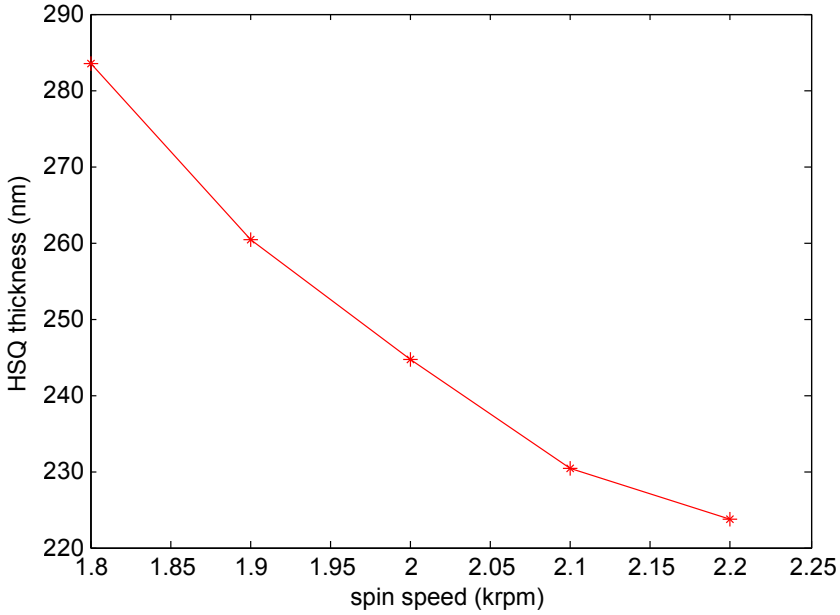

Figure 5.2: Thickness of HSQ versus spin speed for 14.5% HSQ in MIBK, as measured by ellipsometry.

that higher doses induce an increase in density of the HSQ, and the thickness decreases. The index of refraction change was not measured to determine if the optical density changed, though.

It is important to measure the thicknesses of test cavities that are fabricated with varying doses to determine the correct spin speed for a given cavity thickness. Then, once the appropriate thickness of HSQ is spin coated onto the chip, the cavity is written using an electron beam of the appropriate dose according to the test cavities. The area of the cavity must be large enough to cover the devices and, more importantly, extend beyond the gold mirror evaporated on top of it so as to prevent the gold from contacting the device and shorting it or proximitizing it. Cavities of at least 40 μm by 40 μm are practical, given the mask alignment step below. The beam current can be increased and the dose time decreased to decrease the total write time required. Beam currents of up to 10 nA have been used with no apparent degradation of the NbN devices.

The HSQ is then developed in TMAH at room temperature for 3 min and rinsed in deionized water. To fabricate the mirror, Shipley S1813 photoresist is spin coated at 5.5 krpm and baked at

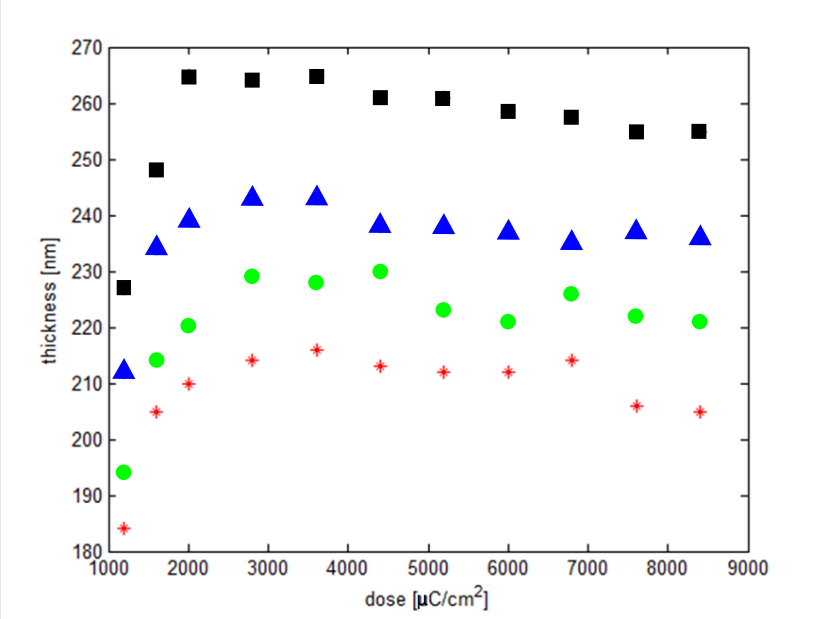

Figure 5.3: Thickness of FOx-14 HSQ cavities versus electron beam dose for spin speeds of 3.0 krpm (black squares), 3.5 krpm (blue triangles), 4.0 krpm (green dots) and 4.5 krpm (red asterisks). It is important to select an e-beam dose in the plateau region to produce cavities of controlled thickness.

110 °C for 90 s. The photoresist is exposed using a mask aligner to align the mirrors with the cavities with a dose of approximately 60 mJ/cm². Then, the photoresist is developed in CD-26 for 15 s and rinsed in deionized water. A 120-nm-thick gold mirror is evaporated with an electron beam evaporator onto the chip with a 1-nm-thick titanium sticking layer, and the photoresist is lifted off in acetone. Figure 5.4 shows an optical micrograph of the optical cavity on a device.

5.2 Experimental Results For Device on MgO

A 40%-fill-factor, 2-nm-thick NbN device on MgO was used to test the enhancement that could be obtained with an HSQ optical cavity. The MgO substrate had no anti-reflection coating, and the NbN layer was assumed to have no oxide. The residual HSQ mask from patterning the nanowires was also neglected in the model. According to the model, this device was expected to have an ab-

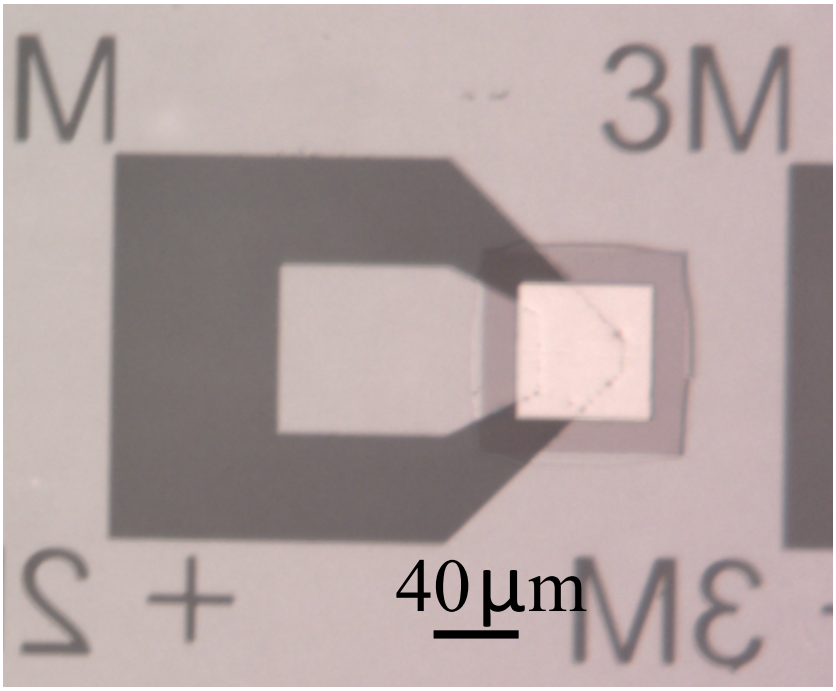

Figure 5.4: Optical micrograph of a device with an HSQ cavity and a gold mirror. This design was later modified so that the mirror was smaller because it was found that poor liftoff of the gold pads could lead to "rabbit ears" that poked up through the HSQ cavity, and then the mirror could short the device if it were large enough to span the gold leads, as it does here.

sorptance of 8.7%. An actual device tested on this chip had a device detection efficiency of only 3.8%, though it is unclear what limited the device detection efficiency (e.g., constrictions, damage to the material during fabrication, etc.).

According to the numerical model, an optical cavity can increase the absorption of a device with this geometry to 20.83% when the HSQ thickness is 260 nm, which is an improvement by a factor of 2.4. An HSQ optical cavity was fabricated on the test device, but it was probably only 240 nm thick, as estimated based on the HSQ thickness from previous tests. This thickness corresponds to an absorptance of 20.7% based on the model, and an enhancement of a factor of 2.38. When this device was tested again, the device detection efficiency was found to be 9.1%, which is an improvement over the initial DDE by a factor of 2.38, as predicted by the model.

5.3 Experimental Results For Device on Silicon Substrate

The optical model can also give us an indication of expected enhancement due to cavity integration on silicon substrates. However, the thickness of the NbN before fabrication was not generally known; the need to know NbN thickness on substrates that were not transparent to visible light was the motivation for creating the IR transmittometer described in Chapter 3. However, the thickness can be backed out of the experimental results on the DDE to see if the thickness according to the optical model is similar to what would be expected given the growth conditions for the NbN film.

Figure 5.5 shows the device detection efficiency of a 3-SNAP device on a chip labeled SPD952 before and after cavity integration. The absorptance at a bias current of 19 μA was 22% before cavity integration and 70% after cavity integration. The nominal design of this device had a fill factor of 42.9% (60-nm nanowires with a 140-nm pitch) with an integrated optical cavity of approximately 290 nm in thickness. The thermal oxide ARC and buried oxide cavity underneath the NbN layer were both 224 nm in thickness. The indexes of refraction for the silicon, thermal oxide, HSQ gold and NbN at 1550 nm were those given in Table 4.1 (in Chapter 4).

The absorptance according to the optical model for this device is shown in Figure 5.6. An absorptance of approximately 22% before cavity integration fits the model for an NbN thickness of 3.3 nm. An absorptance of 70% after cavity integration fits the model for an NbN thickness of 2.4 nm. Both of these values are reasonable for the thickness of NbN because the thickness of the NbN of a sister chip of MgO that was sputtered alongside SPD952 was measured in the visible reflectometer to have an NbN thickness of 4.3 nm. The slight discrepancy in the thickness values before and after cavity fabrication could be because several values used in the optical model are only estimates (for example, the HSQ thickness, which was measured for other cavities fabricated on a different chip, and the HSQ refractive index, which varies with the density of HSQ and thus depends on the electron beam dose) and because of possible degradation of the device during cavity fabrication due to the baking

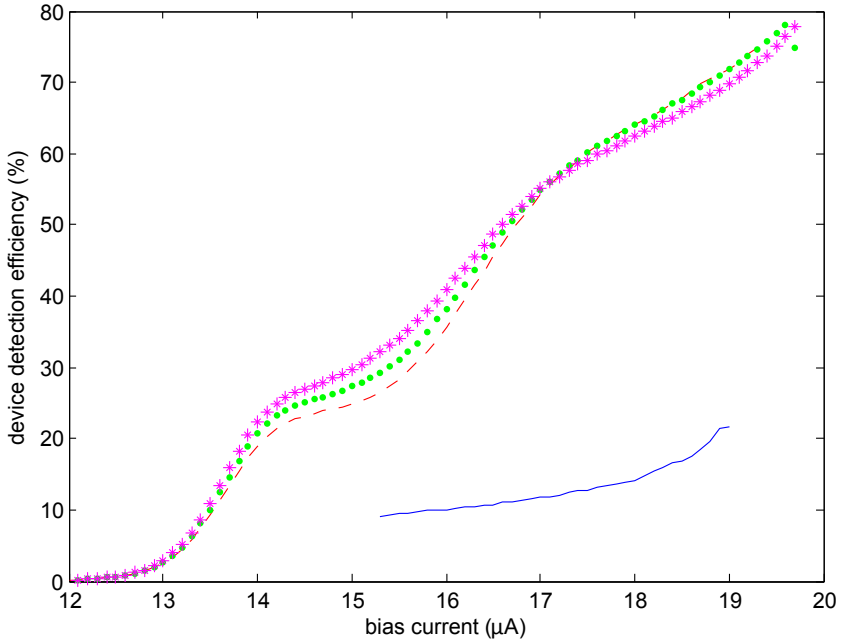

Figure 5.5: Device detection efficiency (%) versus bias current (μA) for SPD952. The blue solid line is the measured DDE before the HSQ cavity was fabricated (data were not collected for low bias currents). The other lines are the data taken after cavity integration at three photon fluxes: 0.04234 photons/pulse (magenta asterisks), 0.0737 photons/pulse (green dotted line) and 0.134 photons/pulse (red dashed line). The similar DDE values found at different photon fluxes shows that the device was operating in the single photon regime.

steps. The NbN thickness on the MgO sister chip is similar to the thickness on SPD952, though again the discrepancy could be due to degradation of the NbN during fabrication or differences in the structures of the NbN thin films grown on amorphous (e.g., silicon dioxide) versus crystalline (MgO) substrates.

The experimental results reported in this chapter confirm the results of the optical modeling using the transfer matrix method, as described in Chapter 4. The measurements on actual devices also extend the work on the reflectometer and transmittometer demonstrated in Chapter 3. While the reflectometer and transmittometer can only measure the thickness of a large area of film, the experimental results here show that the same optical modeling can be used to determine the thickness of much smaller area devices. The experimental confirmation of the analytical results in Chapter 4

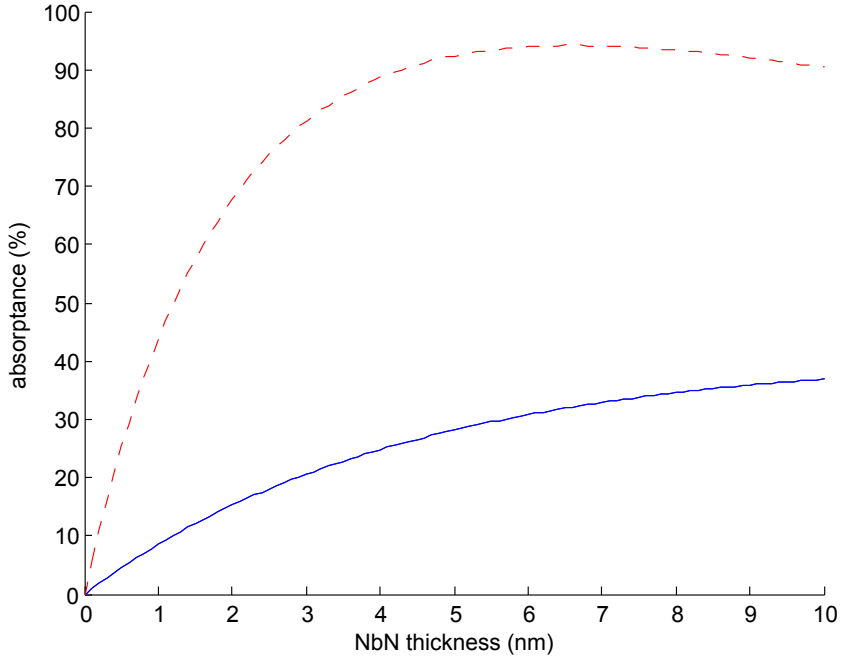

Figure 5.6: Absorptance versus NbN thickness for a device with the approximate layer thicknesses and fill factor as SPD952. The blue solid line is the absorptance without the HSQ cavity, and the red dashed line is the absorptance with the HSQ cavity.

shows that optical modeling can be used to optimize the design of devices before fabrication and testing, which enables us to produce high-performance devices faster. We can also now explore modifications to device designs theoretically, such as the addition of more dielectric layers, to select the best designs for fabrication and testing.

6

Simulations of Optical Antennas

This chapter describes the simulation of several antenna designs to improve the performance of SNSPD detectors using finite element analysis, which was original formulated for structural analysis but has been used for electromagnetic problems since 1968[93]. Optical antennas can manipulate light at the nanometer scale, which makes them useful components for systems such as detectors[94]. Arrays of nanoantennas, for example, bowtie nanoantennas[95], can harvest light from a large area and focus it into a nanoscale region, though some of the incident energy is also dissipated as heat in

metallic nanoantennas[96].

All of the antennas discussed here increase the amount of incident radiation that is ultimately absorbed by the nanowire, but they either require that the fill factor of the SNSPD be lower to accommodate the presence of the nanowires or that the active area of the SNSPD be lowered to fit it into the antenna design. Therefore, when the antenna is fabricated in the same layer as the SNSPD, there is a tradeoff between the active area or fill factor of the SNSPD and the detection efficiency with the integration of these antennas, which is captured in a figure of merit given below. Other non-coplanar antenna designs, such as the one proposed by Chen et al.[97] that uses a metal-insulator-metal concentric ring grating above the SNSPD active area, can achieve both high fill factor and large active area, but the fabrication of such a device has not yet been demonstrated.

The dipole, bowtie and log-periodic designs have been previously used to increase the collection efficiency of bolometers for infrared imaging systems[98], light harvesting for solar cells[99] and coupling to emission from single molecules[100,101], but they have not yet been applied to SNSPDs or SNAPs or other detectors with a meandering pattern for use in the near infrared wavelength range. Plasmonic nanoantennas have been proposed[102] and demonstrated[103] to couple broadband light into dieletric slot waveguides or to modulate light in waveguides[104], but similar antennas have not yet been used to direct light to SNSPDS. The dual Vivaldi antenna, which the most promising antenna design for near-IR SNSPD applications, has only previously been studied for its high radiation efficiency in the IR[105]. Here, integration with a detection device is proposed for the first time, and the simulations of a modified dual Vivaldi design show that it can compete favorably with optical designs based on cavities[46] and other antenna designs for SNSPDs[87]. This chapter will also present the unique fabrication challenges for metallic antennas coupled to superconducting nanowires and demonstrate that gaps between the antennas and the NbN nanowire can be made very small, down to several nanometers.

6.1 Numerical Modeling of Antennas With FEA

The optical modeling performed in Chapter 4 cannot describe the three-dimensional geometries necessary to model antennas. Therefore, COMSOL MultiPhysics 4.3, a finite element analysis (FEA) program, was used to model the absorption of incident light in niobium nanowires with and without the presence of gold nanoantennas and to optimize the geometry of the gold nanoantennas to maximize the coupling of incident light into the NbN nanowire. The nanowire was modeled as a thin strip of NbN (4.5 nm in thickness, 40 nm in width) on a sapphire substrate for the dipole, bowtie and dual Vivaldi antennas. The absorption in the niobium nitride nanowire was measured as the Joule heating in the nanowire, which was the method used in previous simulations of cavity structures to characterize the absorption of light[38].

The thickness of the gold antennas was fixed at 20 nm, which is approximately twice the skin depth of gold at 1550 nm. Increasing the thickness of the antenna led to increased losses in the antenna, but thinner antenna would be difficult to fabricate due to the roughness of very thin evaporated gold films.

The incident light was modeled as a plane wave. The mesh size of the simulations was optimized by decreasing the size of the largest mesh element and refining the volume containing the antenna until the difference in the measured resistive losses in the nanowire between simulations was less than 1%. The area simulated was limited by the amount of memory required to run the simulations, which in turn determined the period of the nanowire meander and the spacing of the antennas for each design. The boundary conditions were either scattering boundary conditions (for the top and bottom boundaries) that described the incident plane wave or perfect electric conductor and perfect magnetic conductor boundaries to form "mirrors" of the simulated area. Thus, the simulations were all actually of an infinite grating of NbN rather than a finite meander pattern, but this method has been used in the past with previous COMSOL simulations because the device detection efficiency

calculated as the ratio of the absorptance in the nanowire to the incident power over the simulation area, and thus the size of the simulation area cancels out[38,87].

The ratio of the Joule heating in NbN with the gold nanoantenna to the Joule heating without the antenna is called the enhancement factor. The enhancement factor was used in the optimization of the nanoantenna dimensions. The figure of merit that was used in Hu et al.[87] is also used here to compare devices with antennas to typical devices that do not incorporate antennas and thus have a smaller active area and a higher fill factor. The kinetic inductance, L_K, of a device scales with the length of the nanowire and determines the reset time of the device as

$$t = \frac{L_K}{R} \tag{6.1}$$

where R is the input impedance of the transmission line and amplifier network, which is 50 Ω. To build large-active-area detectors that still have a fast reset time, it is necessary to limit the kinetic inductance by limiting the overall length of the nanowire. The following figure of merit considers the area ($\mathcal{A}$), the device detection efficiency (DDE) and the reset time (τ):

$$\text{figure of merit} = \frac{\mathcal{A} \times DDE}{\tau} \tag{6.2}$$

For example, in Hu et al.[87], a device with an active area of $9 \times 9\,\mu m^2$, a reset time of 5 ns and a device detection efficiency of 47% was reported, which had a figure of merit of $7.6\,\mu m^2/ns$. The device in Rosfjord et al.[46], with a smaller active area of $3 \times 3.3\,\mu m^2$, a reset time of 3.4 ns and a detection efficiency of 57%, had a figure of merit of $1.7\,\mu m^2/ns$. These figures were determined experimentally on fabricated devices.

The figures of merit reported for the antenna designs below assume that all of the radiation that is coupled into the nanowire results in a count–that is, the absorptance in NbN, as measured by

the Joule heating, divided by the incident power is the device detection efficiency. The reset time is calculated by assuming that the kinetic inductance of the nanowire is 80 pH/square[106]. The number of squares can be determined by the geometry of the nanowire simulated as the length of the nanowire divided by its width. Thus, the reset time is

$$\tau = \frac{80[\text{pH}] \times (l/w)}{R} \tag{6.3}$$

The reset time scales with the length of the nanowire, and the length of the nanowire scales with the simulated area. The detection efficiency is the same for any simulated area of the device because it is calculated by dividing the Joule heating in the nanowire by the power incident on the area of simulation. Therefore, the figure of merit is independent of the specific area of the simulation.

6.1.1 Dipole Antennas

The simplest antenna structure is a dipole antenna. Figure 6.1 shows two designs of the dipole antenna to couple light to the NbN nanowire: the single-threaded meander pattern with dipoles on either side of the nanowire and the double-threaded version.

In these geometries, the nanowire rests within a gap between two dipole antennas. Previous research has shown that the field in the gap of a plasmonic nanoantenna is enhanced as well as the field at the end points of the antenna[107,108,109,110,111]. However, in our case, the distance of the gap to accommodate a nanowire is too large for the two arms to be considered part of one dipole antenna. Instead, the resonant condition occurs when each of the arms of the antenna has a length L_{dipole} of roughly $\lambda_{\text{effective}}/2$, indicating that each arm of the antenna is acting as a dipole antenna.

At sufficiently small wavelengths (in the visible and near IR), the plasmonic properties of the antenna must be considered, and the design of a nanoantenna is not merely a scaled design of a microwave antenna[112]. The presence of a substrate and the plasmonic properties of the antenna mate-

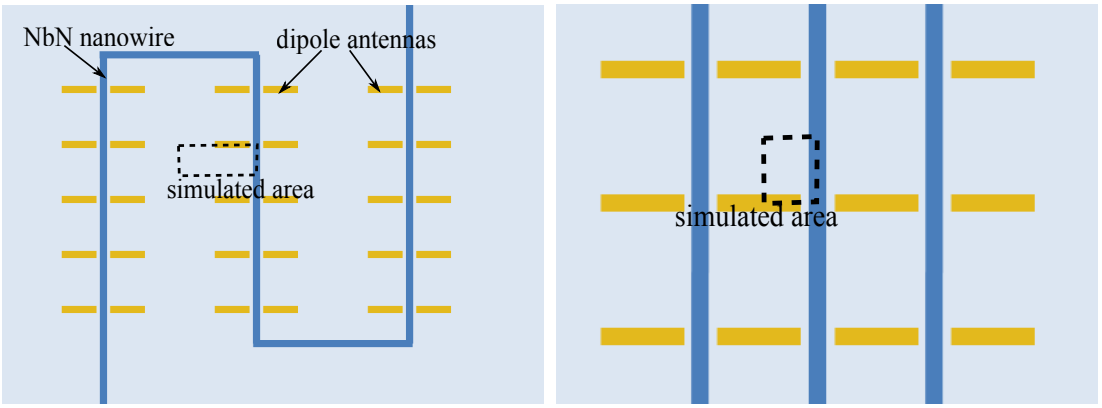

(a) single-threaded dipole antenna **(b)** double-threaded dipole antenna

Figure 6.1: Dipole antenna coupling to NbN nanowires: (a) full design for a meander pattern NbN nanowire with a "single-threaded" dipole antenna layout. The dotted line shows the simulated area, which was the minimum area necessary given the symmetries of the design. (b) "Double-threaded" dipole antenna layout to increase the fill factor of the detector.

rial both redshift the resonant wavelength.

In the first set of simulations, the width of the detector and the width of the antenna were set to 40 nm, the gap between the dipoles was set to 80 nm, and the length of the dipole was varied. Figure 6.2a shows the enhancement in the absorption (resistive losses or Joule heating) of the nanowire versus the length of the dipole for $\lambda = 1550$ nm light polarized along the length of the antenna (perpendicular to the nanowire). The optimized length of the dipole is L_{dipole} is approximately 400 nm and gives an enhancement factor of 19.2. Figure 6.2b shows the total electric field intensity for the optimized length of the dipole in Figure 6.2a. The field intensity is particularly high between the end of the dipole antenna and the NbN nanowire.

The dipole antenna responds to light that is polarized parallel to its length only. If the electric field is polarized along the length of the nanowire and perpendicular to the antenna, the enhancement factor is only 1.003 for the optimized design above. There is also a difference in the amount of absorption in the nanowire without the antenna for the different directions of polarization. When the polarization is parallel to the nanowire, the absorption is a factor of almost 400 times greater

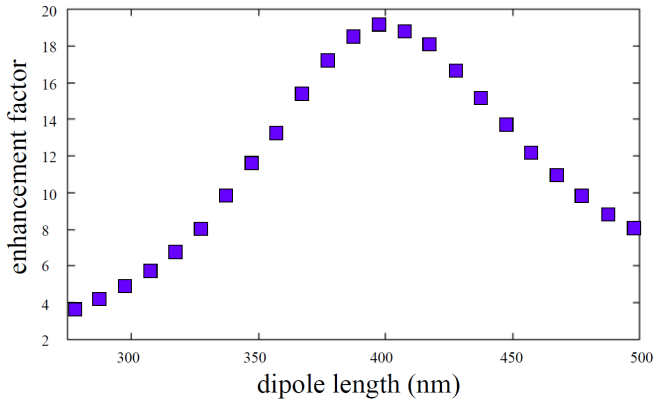

(a) enhancement factor versus dipole length

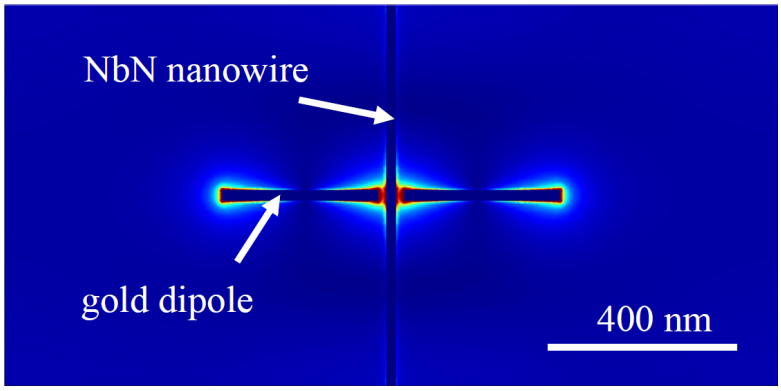

(b) electric field intensity for $L_{\text{dipole}} = 400$ nm

Figure 6.2: (a) Enhancement factor versus length of the dipole, showing an optimal length. (b) Electric field concentration (scale from 0 to 20 V/m) for the optimized design.

than the absorption when the polarization is perpendicular to the nanowire, which is qualitatively similar to the results found experimentally for SNSPDs[38]. Therefore, the absorptance of light is highest when the light is polarized parallel to the nanowire, whether or not the dipole antenna is present.

The enhancement factor for the dipole design is 19.2, but the actual detection efficiency calculated by considering the Joule heating of the NbN and the incident power gives a figure of merit of only 0.108 $\mu m^2/ns$ due to the low fill factor of the design; in addition, the polarization direction is not optimal for the nanowire. Thus, the "double-threaded" design in Figure 6.1b was con-

sidered to increase the fill factor of the NbN nanowire. The enhancement factor at the optimized dipole length for the "double-threaded" design led to a figure of merit that was more than doubled to 0.25 $\mu m^2/ns$; however, the actual device detection efficiency was still only approximately 0.2%.

6.1.2 Bowtie Antennas

Bowtie antennas offer a broader frequency response band than dipole antennas. Figure 6.3a shows the geometry of the simulated bowtie antennas. The flare angle was 60° for all simulations, and the optimized length, L_{bowtie} was 410 nm for 1550 nm light, similar to the case for dipole antennas above.

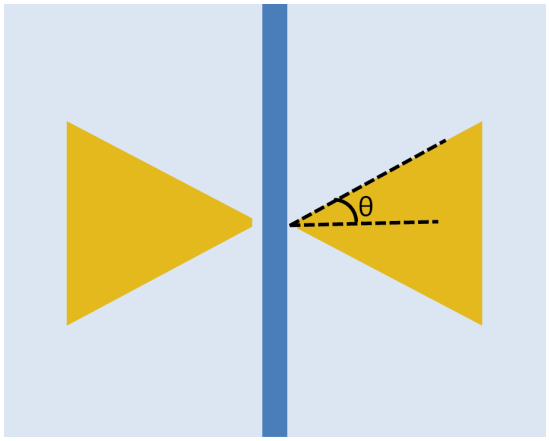

(a) bowtie antenna design

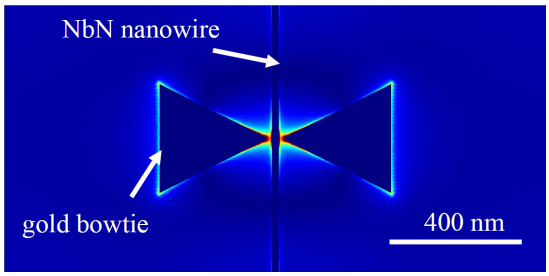

(b) enhancement factor vs. L_{bowtie}

Figure 6.3: (a) Design of the bowtie antenna integrated with a meander pattern. (b) Enhancement factor versus length of the bowtie antenna, L_{bowtie}, showing an optimal length.

Figure 6.3b shows the enhancement factor versus the length of the bowtie antenna, which shows

that the variation in the enhancement factor with the length of the bowtie for a fixed incident wavelength is less dramatic than in the case of a dipole antenna. In the case of the dipole antenna, decreasing the length of the optimized antenna by 40 nm led to a reduction in the enhancement factor of 30.7%. For the bowtie antenna, decreasing the length by 40 nm led to a reduction in the enhancement factor of only 17.2%. In theory, a bowtie antenna of infinite length with an infinitessimal gap between the arms should have a flat response versus wavelength[98].

The optimized thickness of the bowtie antenna was also explored. Figure 6.4a shows the Joule losses in the NbN nanowire versus the thickness of the gold bowtie antenna. There is an optimal thickness for the gold antenna where the antenna is sufficiently thick to interact with the incident light but sufficiently thin that the electric field enhancement at both the top and bottom of the sharp point interact with the nanowire.

The figure of merit for the bowtie antenna design, however, was only 0.121 $\mu m^2/ns$ for the optimized design with $L_{bowtie} = 400$ nm and a thickness of 40 nm, which was similar to the case for the dipole antenna with a similarly low fill factor. The enhancement versus wavelength was also not much wider, as shown in Figure 6.4b. The bowtie antenna design also has the same polarization dependence issues as the dipole design: the optimal polarization for the bowtie antennas is perpendicular to the optimal polarization for the NbN nanowire.

6.1.3 Dual Vivaldi Antennas

The dual Vivaldi nano-antenna was first explored by Iluz et al.[105] for its high radiation efficiency in the infrared. Figure 6.5a shows the dual Vivaldi antenna geometry, which is similar to the design of multiple bowtie antennas. However, in this case, the antenna is optimized for radiation polarized parallel to the nanowire and not perpendicular to it, as in the case of dipole or bowtie antennas. The nanowires absorb far more radiation when the light is polarized parallel to them, so the enhancement in absorption due to the antennas will increase the maximum absorptance of the nanowires.

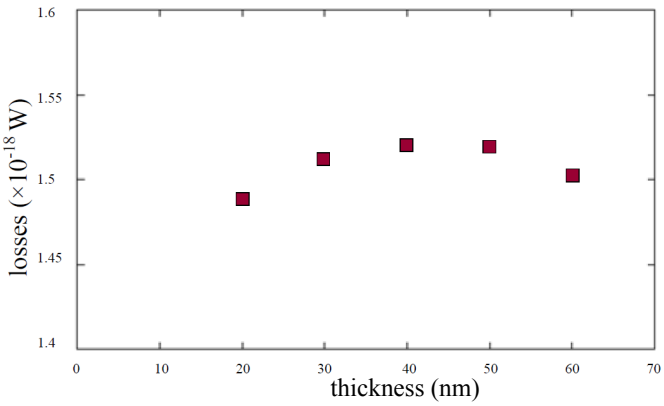

(a) Joule losses in NbN versus antenna thickness

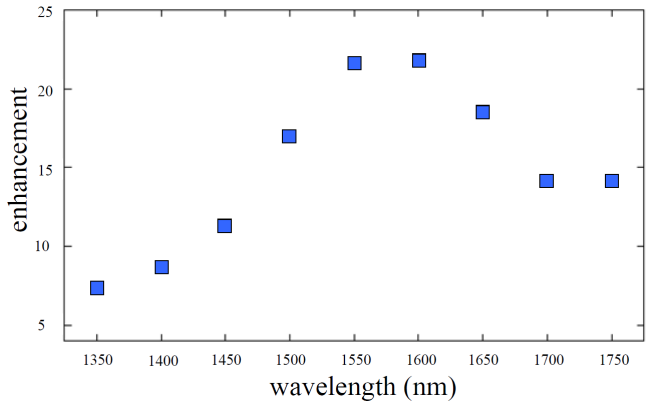

(b) enhancement factor versus wavelength

Figure 6.4: (a) Joule losses in the NbN nanowire versus bowtie antenna thickness, where the optimal thickness is 40 nm and probably due to a tradeoff between the need for a thick antenna to interact with the incident light and the need for a sufficiently thin antenna to couple to the thinner NbN nanowire. (b) Enhancement factor versus wavelength of the incident radiation for the optimized bowtie antenna design.

Figure 6.5b shows the enhancement in the absorptance in the NbN nanowire as a function of the length of the dual Vivaldi antenna. There are lengths of the antenna where the enhancement factor is actually less than one; that is, the dual Vivaldi antennas can decrease the amount of light absorbed at non optimized wavelengths, which might be useful for controlling the detection of radiation at wavelengths other than those required for the signal.

The figure of merit for the dual Vivaldi geometry with a fill factor of 1.96% (40-nm-wide nanowires

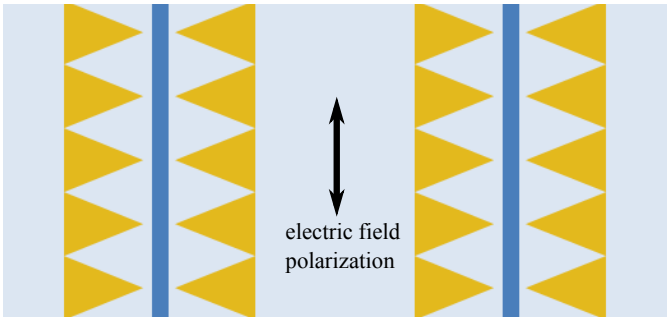

(a) Dual Vivaldi antenna design

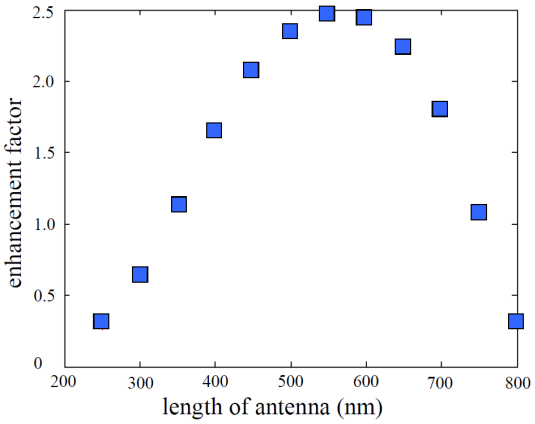

(b) enhancement factor versus L_{Vivaldi}

Figure 6.5: (a) Dual Vivaldi antenna design. The optimal polarization for both the nanowire and the antenna is parallel to the nanowire. (b) Enhancement factor versus the length of the dual Vivaldi antenna, given the optimized antenna length.

with a pitch of 2040 nm) is 4.054 $\mu m^2/ns$. The detection efficiency of the SNSPD without the antenna is approximately 4% and the detection efficiency with the antenna is nearly 10%, corresponding to an enhancement factor of 2.47.

It should be noted that the figure of merit for this SNSPD geometry without the antenna is 1.642 $\mu m^2/ns$, which is close to that achieved experimentally by Rosfjord et al.[46] of 1.7 $\mu m^2/ns$. The reason that this figure of merit even without the antenna is so much higher than the values above for the dipole and bowtie antennas is that the polarization of the incident light is parallel to the nanowire, not perpendicular to it, and the device detection efficiency even without the antenna

is thus much higher. These devices have a larger area per reset time because they are low fill factor devices, which makes up for their low detection efficiency due to the sparseness of the NbN lines, which is why the figure of merit is so close to that of the small-active-area detectors in Rosfjord et al.[46].

The dual Vivaldi geometry can be improved by increasing the fill factor of the device by creating a "double threaded" geometry, as shown in Figure 6.6a. This geometry was investigated by varying the length of the antenna, as shown in Figure 6.6b with a plot of the enhancement factor and the figure of merit versus length of the dual Vivaldi antenna geometry. (The figure of merit is more appropriate to plot because the size of the simulation area decreases as the antenna length decreases.) The optimal length appears to be approximately 500 nm, which corresponds to a device detection efficiency of 17.7% and an enhancement factor of 3.62. The detection efficiency reaches a maximum for a slightly lower antenna length, but this is where the detection efficiency of the device without the antenna is higher due to the higher fill factor, and so the antenna does not help as much.

6.1.4 Log-Periodic Antennas

The sensitivity of SNSPDs decreases as the wavelength of incident light increases and the energy of incident photons decreases[29], with negligible absorption beyond 5 μm. One hypothesis is that low energy photons do not create a large enough hotspot to lead to the current crowding necessary to switch the cross section of the nanowire normal and trigger a voltage pulse. Narrower nanowires have been fabricated with the aim of increasing IR sensitivity, but there is a limit to how narrow nanowires can be reproducibly fabricated[17]. Another problem, though, is that higher wavelength light cannot be focused to a small spot size due to the diffraction limit, so the small, possibly sub-wavelength, active area of SNSPDs also limits the amount of light that can be collected. In this section, log-periodic antennas are used to increase the area over which light is collected and to harness mid-infrared wavelength radiation.

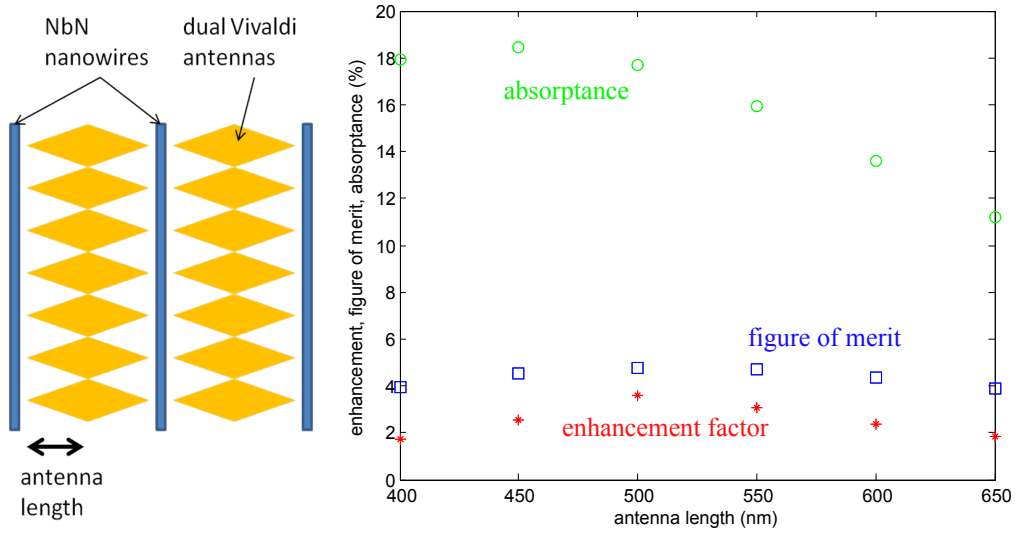

(a) double-threaded design **(b)** enhancement factor, FOM and DDE vs. $L_{\text{double Vivaldi}}$

Figure 6.6: (a) Geometry for the "double-threaded" dual Vivaldi antenna to increase the fill factor over the "single-threaded" design. (b) Enhancement factor, figure of merit and device detection efficiency versus length of the double-threaded dual Vivaldi antenna, which give different values for the optimized antenna length.

Log-periodic antennas are broadband antennas composed of multiple elements that couple radiation between them. Log-periodic antennas for operation at radio frequencies are composed of dipoles that are spaced according to a logarithmic function; the elements in mid-infrared log-periodic antenna designs are circular arcs[98] or trapezoidal patches[113] that differ in size according to a logarithmic function. Log-periodic antennas designed for detection of terahertz radiation (wavelengths down to 100 μm) have previously been integrated with a high electron mobility transistor[114] and a semiconductor nanowire field effect transistor[115].

The design explored here is based on Gonzalez and Boreman[98]. Log-periodic antennas funnel the incident radiation to the center of the structure, where an SNSPD can be placed to absorb it. Log-periodic antennas are most appropriate for mid-infrared applications rather than near infrared (e.g., $\lambda = 1550$ nm) applications due to fabrication constraints; for example, the design optimized for 10.6 μm light by Gonzalez and Boreman has a smallest arc of five that is 200 nm in width[98]. It would

thus be extremely difficult to fabricate a design scaled for light with a wavelength ten times as small. A number of design parameters can be optimized to vary the wavelength response of the antenna, as shown in Figure 6.7a. The smaller the ratio between the radii of success arcs, τ, the closer together the peaks of the antenna response are in both frequency and wavelength. The number of arcs determines the number of peaks in the antenna response, and the lengths of the longest and shortest arcs set the wavelength range of the antenna response.

Figure 6.7b shows the simulated structure of the log-periodic antenna coupled to a small-area SNSPD, which is modeled as a $0.5\,\mu\text{m} \times 0.5\,\mu\text{m} \times 5$ nm patch of NbN.

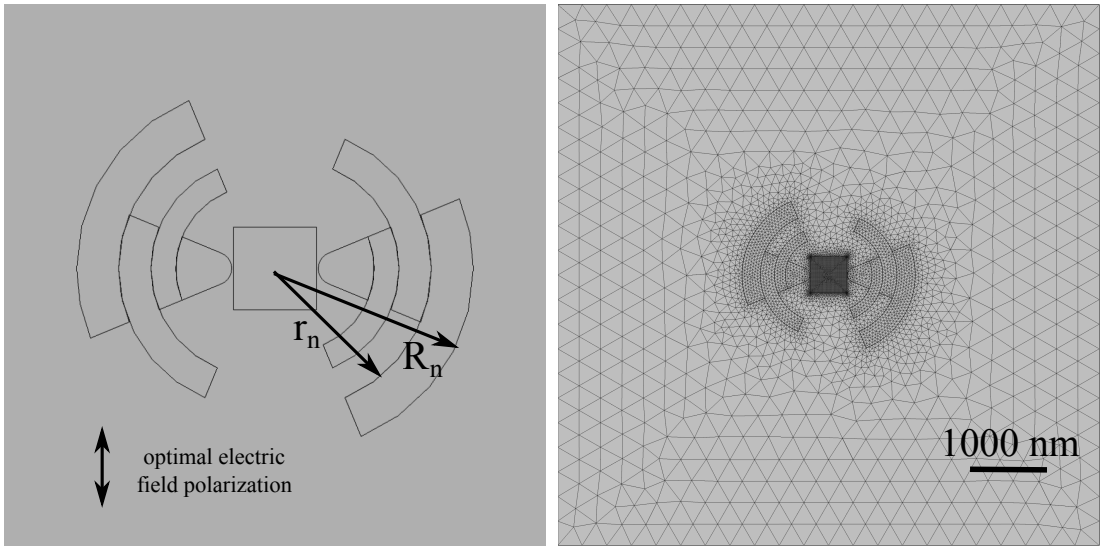

(a) log-periodic antenna parameters **(b)** simulation area and mesh

Figure 6.7: (a) Parameters for the log-periodic antenna design. The arcs are characterized by an inner (r_n) and outer radius (R_n), and the ratio between successive radii in the design is τ. The optimal polarization for coupling to the antenna is indicated with an arrow, and thus an actual fabricated device would have nanowires parallel to this line for the most efficient coupling to incoming radiation. (b) Log-periodic antenna and NbN patch with the FEA mesh. The NbN SNSPD is modeled as a thin NbN patch that is $0.5\,\mu\text{m}$ on each side and 5 nm thick. The simulated area is $7.5\,\mu\text{m} \times 7.5\,\mu\text{m}$. The antenna and patch are on a sapphire substrate that is $5\,\mu\text{m}$ deep, and the vacuum above the antenna plane is also $5\,\mu\text{m}$ thick.

In the simulation here, τ was set to 1.3, the inner radius of the smallest arc was 500 nm, and the outer radius of the largest arc was 1098.5 nm. The fillet radius at the center of the design was 100 nm

in these simulations, but a sharper radius would lead to a higher field concentration at the point, and the effect of varying the fillet radius on the coupling between the antenna and the NbN patch was not explored. The thickness can also be varied, but here the thickness was set to 40 nm.

Figure 6.8a gives the enhancement of the absorption in the NbN patch versus incident wavelength for this antenna design, and Figure 6.9 shows the electric field intensity surrounding the antenna and NbN patch at two different wavelengths. Here the enhancement factor is the ratio of the Joule heating in the NbN patch with the antenna to the Joule heating in the NbN patch when there is no antenna. There is some enhancement even at low wavelengths, but the antenna has a large enhancement factor of over 5 for light at 5 μm. The upper limit of the bandwidth of this antenna could not be simulated because of a lack of data for the index of refraction of NbN beyond 5 μm. Figure 6.8b gives the Joule losses in the gold antenna itself versus wavelength, as well as the losses in the NbN patch when the gold antenna is present for comparison. Further optimization of the antenna design, particularly the thickness, might decrease the losses in the antenna.

The log-periodic antenna is somewhat less sensitive to the polarization of the incident light than, for example, a dipole antenna because it can act as a bowtie antenna when the polarization is perpendicular to the direction shown in Figure 6.7a. In this case, the enhancement factor at $\lambda = 4\,\mu\text{m}$ is still approximately 1.6, though it is much less than the enhancement with the other polarization, which is 4.7. The Joule losses in the antenna are 3.6×10^{-16} W for the non-optimal polarization and 1.1×10^{-15} W for the optimal one.

6.2 Fabrication of Antennas

Gold antennas were fabricated to demonstrate that the alignment of features with very small gaps is possible. Unlike the fabrication of gold antennas for use with semiconductor detectors[108], it is crucial that the gold not contact the superconducting nanowire due to the proximity effect; that is, a

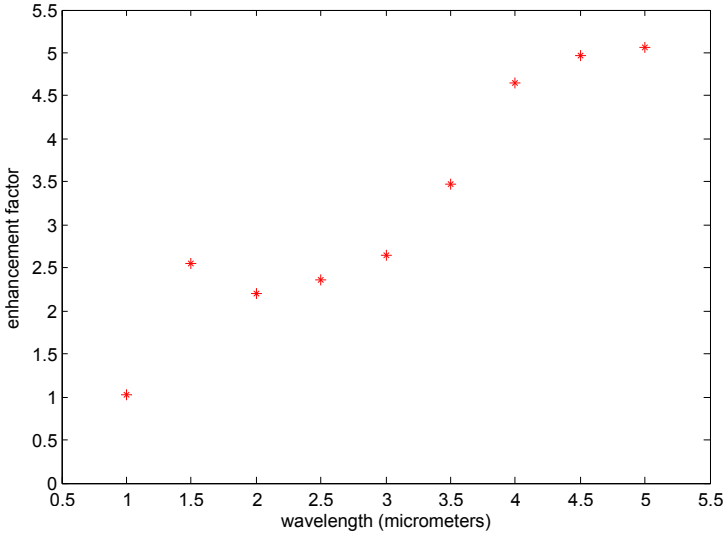

(a) enhancement factor versus wavelength

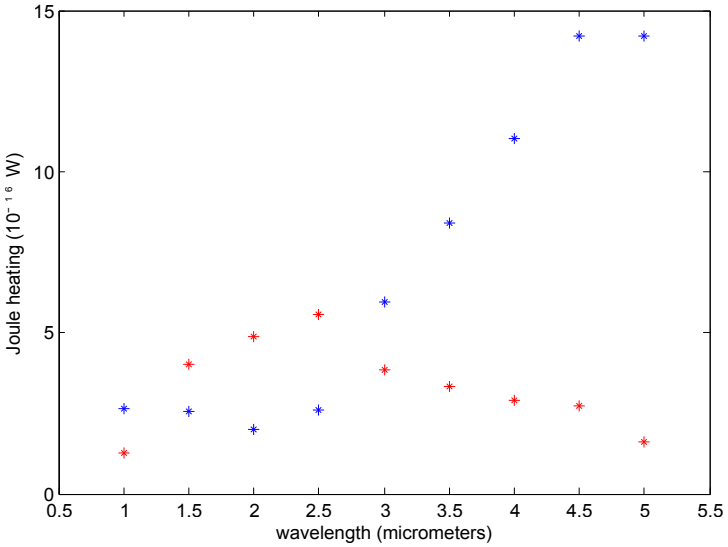

(b) absorptance in antenna versus wavelength

Figure 6.8: (a) Enhancement factor versus wavelength for the log-periodic antenna design shown in Figure 6.7b, which shows the increase in absorptance in NbN with the antenna starting at a wavelength of approximately $3.5\,\mu\text{m}$. (b) Incident radiation absorbed by the antenna (blue) and by the NbN patch (red) versus wavelength of incident light. Further optimization might decrease the radiation losses in the antenna.

gold nanoantenna that overlaps the superconducting nanowire will "proximitize" the superconductor and cause a region of normal metal to form[116]. Arrays of optical antennas have been fabricated

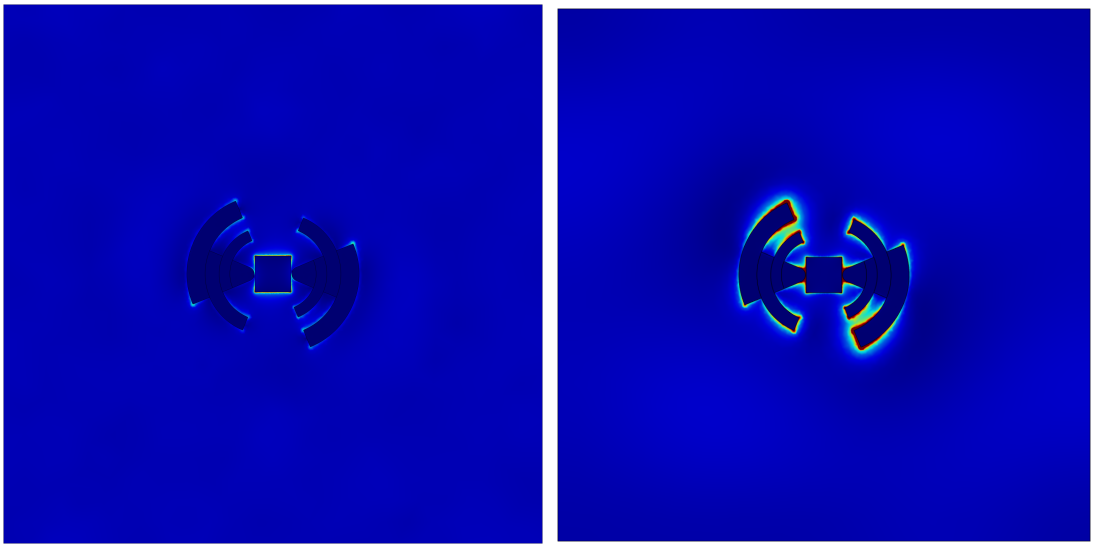

(a) $\lambda = 2\,\mu\text{m}$ **(b)** $\lambda = 2\,\mu\text{m}$

Figure 6.9: Electric field intensity surrounding the gold log-periodic antenna and NbN patch for incident light at a wavelength of (a) 2 μm, for which the antenna does not show much enhancement, and (b) 5 μm, for which the antenna does lead to enhancement of the absorptance in NbN. The color range is from 0 (dark blue) to 10 V/m (red).

and studied previously (e.g., by Silva-Lopez et al.[117] and Trevino et al.[95]) but not closely aligned with a superconductor.

SNSPD devices designed with the optimized simulation structures were fabricated first. The widths of the nanowires were 80 nm and 100 nm for the dipole and bowtie antennas, respectively, and the pitches of the SNSPDs were 520 nm and 2 μm, respectively. Small-active area (1 μm^2) SNSPDs composed of 80 nm nanowires with a 160-nm pitch were also fabricated for integration with log-periodic antennas.

To fabricate the gold antennas, 4% PMMA 950 dissolved in anisol was spin coated on the chip at a spin speed of 5 krpm after the SNSPDs were fabricated. The chip was then baked at 180 °C for one minute before electron beam writing. The antennas were written using the Elionix electron beam writer with a current of 200 pA and dose times of 0.1 μs for the dipoles and 0.16 μs for the bowties, which correspond to doses of 1280 and 2048 $\mu\text{C}/\text{cm}^2$, respectively. Log-periodic antennas were also

written with doses between 0.06 and 0.22 μs, which correspond to doses of 768 and 2816 $\mu C/cm^2$, respectively, and, because they are larger area than the dipoles, they were somewhat less sensitive to differences in dose. To ensure alignment with the SNSPDs, four registration marks were used, and the tolerance was 0.02 mrad and 20 nm.

The dipole antennas were 40 nm in width, and the length was varied from 380 nm to 420 nm to vary the gap between the antenna and the nanowire from 10 nm up to 30 nm (see Figure 6.10). The bowtie antennas were composed of equilateral triangles with a side length of 460 nm and a height of 400 nm, and the gap between the tip of the bowtie and the nanowire was varied from 5 nm to 55 nm.

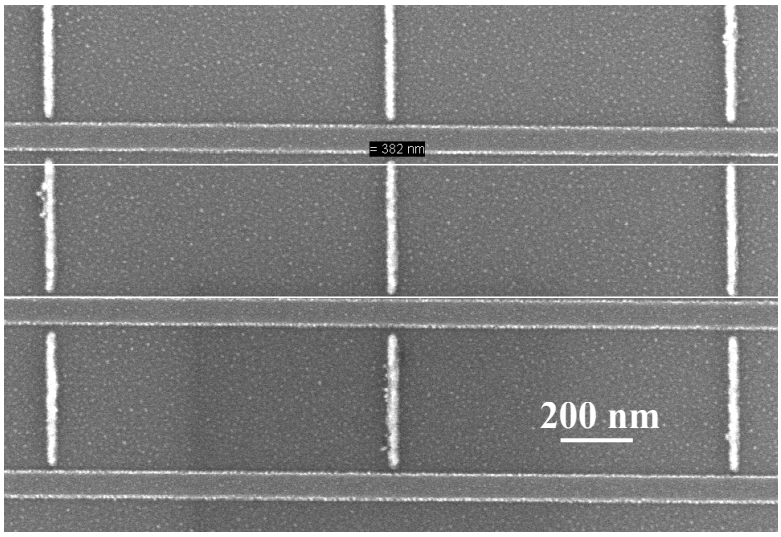

Figure 6.10: SEM image of dipole antennas integrated with a meander pattern. The two horizontal white lines are 382 nm apart and measure the length of the dipole antenna.

The PMMA was developed for 90 s in IPA:MIBK (2:1) at 21 °C and rinsed with IPA. Then, 5 nm of titanium and 35 nm of gold were evaporated using an electron beam evaporator. As shown in Figure 6.11a, the alignment of some of the dipoles was very good; the alignment decreased over the course of the write, but using four registration marks when writing the SNSPDs instead of the typi-

cal two registration marks improved the yield. The alignment of the bowtie antennas (Figure 6.11b) was similar to that of the dipoles, and the alignment of the log-periodic antennas (Figure 6.11c) was generally better because the designed gap was larger (80 nm). A misalignment that produces a slightly larger gap is not ideal, but a misalignment that leads to physical overlap between the SNSPD and the antenna is likely to be fatal to device operation as the metal from the antenna proximitizes the superconducting nanowire, leading to a normal region and thus a constriction. Therefore, designs with larger gaps are likely to be more reproducible.

6.3 Future Directions

The finite element simulation results show that several of the antenna designs studied above could find use in applications with SNSPDs, and the designs that are less promising might still be improved upon for specific applications. For example, the figure of merit shows that the dipole and bowtie designs are only practical for very large active area devices or for devices where sensitivity to a certain wavelength is important. The optimal polarization for both dipoles and bowties is perpendicular to that necessary for the SNSPD, which is a further disadvantage. The bowtie antenna has a somewhat broader band response, but its bandwidth is still limited by the finite size of the antenna. However, it might be possible to further optimize the dipole antenna design by varying the width of the antenna to reduce losses in the gold or the spacing between the dipole and the nanowire to increase coupling. The gap distance in the simulations was 20 nm, which is a reasonable number for electron beam fabrication, but a smaller gap is possible, as shown in the fabrication results. The polarization dependence could be addressed by using an asterisk of several nanoantennas centered around a nanowire. There is also the possibility of using disk-shaped antennas, as in Casadei et al.[118], where gold disks were used to couple light into GaAs nanowires.

The dual Vivaldi design is in many ways an improvement over the bowtie antenna design because

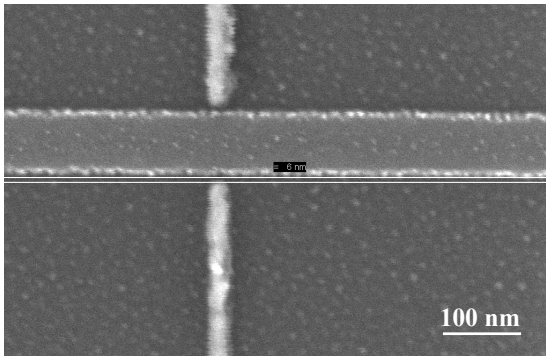

(a) dipole antenna alignment

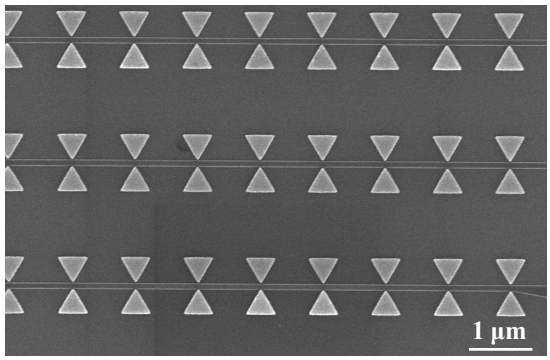

(b) bowtie antenna alignment

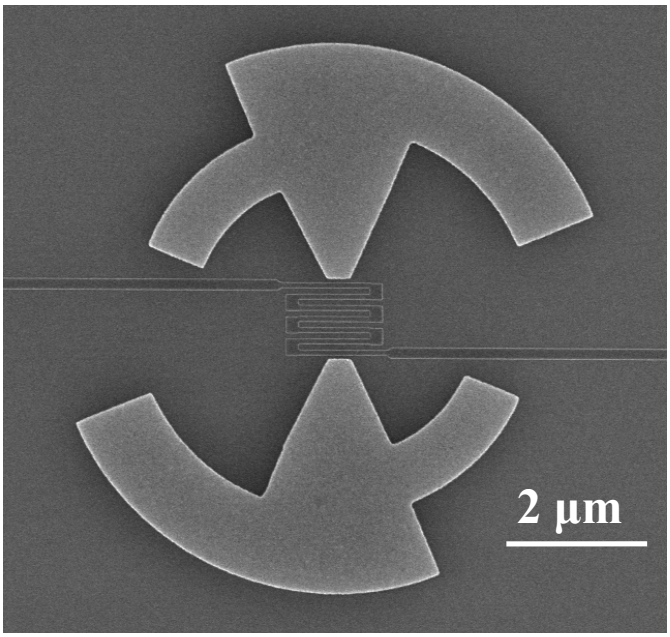

(c) log-periodic antenna alignment

Figure 6.11: (a) Alignment of dipole antennas: the gap between the antenna and the nanowire is only approximately 6 nm. (b) Alignment of bowtie antennas. There is a slight overlap with the NbN nanowires because the PMMA was slightly overdosed and the antennas are larger than the nominal size. (c) Alignment of log-periodic antennas, with a relatively large gap of 80 nm.

it offers the benefits of enhanced light absorption while the optimal polarization of the incident light is the same for both the antenna and the nanowire. The figure of merit indicates that even a relatively sparse, "single-threaded" dual Vivaldi geometry is competitive with small active area, high

efficiency devices. That is, the dual Vivaldi antenna could be a good choice in applications where the absolute detection efficiency is less important, but the active area and the reset time are important, e.g., when light cannot be focused to a small spot. The double-threaded dual Vivaldi design is the most promising because of the high detection efficiencies achievable with even a low-fill-factor design. The losses due to heating in the gold antennas might be mitigated by optimizing the design further, by considering, for example, thinner antennas or perhaps a dielectric material[119].

The log-periodic antenna would find applications further in the mid-infrared. In particular, it is the largest area detector and would increase the effective active area of the device. It is also the easiest antenna to integrate with a detector in terms of fabrication because of the relatively large gap between the antenna and the device. Other log-periodic designs, such as the trapezoidal design in Aouani et al.[113], could be explored as well. Due to the size of the log-periodic antenna, it might be possible to incorporate the antenna itself into the device as part of the electrodes, similar to what has been demonstrated for a nanowire photodetector with gold leads[120]. The electrodes could also be patterned as a spiral antenna, which would offer polarization independence[121].

This chapter describes the simulations of several proposed antenna structures to increase the detection efficiency of low fill factor or small area detectors, which could lead to detectors that can both collect light from a large area and have a low kinetic inductance. While most of the designs cannot compete with existing detectors, the double-threaded dual Vivaldi antenna is very promising, and the log-periodic antenna can collect mid-infrared light better than the detectors on their own. Because of the proximity effect, it is imperative that the metallic antennas do not contact the superconducting nanowires, and preliminary fabrication trials have demonstrated that it is possible to fabricate antennas that are within nanometers of nanowires without touching them.

7

Conclusion

This thesis has covered a broad range of topics surrounding the optical modeling of SNSPDs to design higher efficiency devices. Although concluding remarks were included within the chapters, here I present a summary of the entire work and provide some promising directions for future work.

This work began with the fabrication of high-quality detectors, without which no optical design can significantly improve the state of the art. Once detectors are fabricated, they must be tested, and this work provides a quantitative measure of the quality of a device given its resistance and switching

current, which are more easily and quickly measured than other properties, such as the device detection efficiency. Future work in this area could focus on identifying the physical mechanism behind constrictions, which seem not to be visible under scanning electron microscopy. They are perhaps due to a physical thinning of the nanowire due to some property of the NbN/substrate interface, but they might also arise from some microscopic property of the NbN nanowire itself that we have not yet identified. Determining the physical origins of constrictions and eliminating them would lead to a higher yield of high-quality devices.

Some work on identifying the cause of highly constricted devices has been performed in the past by Clem et al.[36,37], who considered the current crowding in SNSPD device design and explained the poor performance of high-fill-factor device[35]. A new design for a 4-SNAP that has a high fill factor without introducing more current crowding was presented based on modeling the current flow through a device with finite element analysis. Increasing the fill factor of devices to increase the density of NbN in the active area will increase the absorptance and thus should also increase the device detection efficiency. In fact, the device detection efficiency of condensed 4-SNAPs over conventional series 4-SNAPs was enhanced by a factor of almost 1.5 on average. The Berggren group is currently exploring other optimized turns for SNAP devices with the goal of preventing current crowding while increasing the fill factor of the device above the 33% maximum predicted for a meander pattern of a single nanowire with ideally-shaped curves.

This thesis also investigated the starting material for physical causes of poor performance, especially oxide within the NbN lattice. Auger electron spectroscopy and especially x-ray photoelectron spectroscopy did not show any evidence for oxygen that is bonded to niobium within the lattice, though oxygen atoms were present, and neither could give the stoichiometry of the NbN. It might be the case that a stoichiometry that differs from 1:1 leads to microscopic physical defects that introduce normal regions in the lattice. X-ray diffraction could give some insight into the quality of the film, but future work should explore XRD in more depth. For example, the XRD results presented

here were for NbN on MgO, but the better performance device reported in Chapter 5 was on silicon dioxide. XRD should be used to explore the defect concentration and strain of NbN films grown on amorphous substrates such as silicion dioxide and silicon nitride because these substrates are currently being used in the field for SNSPD and SNAP fabrication.

The optical properties of NbN thin films are another area for future work. The transmittometry setups described in Chapter 3 provide a fast, convenient and non-destructive way to measure the thickness of films, and the results are precise and do not vary over short time scales. However, the thickness values calculated rely on the assumption that the index of refraction of NbN is known and constant throughout the thickness of the film, and thus the results are not necessarily accurate. Variable angle spectroscopic ellipsometry (VASE) could be used to obtain the index of refraction of thin films of NbN deposited under slightly different conditions to obtain a realistic range of values as input into the thickness calculation, but these data cannot be obtained if the substrate is transparent. It is also not clear whether the NbN thin films deposited on different substrates have different optical properties, so VASE data cannot be taken for non-transparent substrates and used to model NbN films on transparent substrates.

One optical method to determine the index of refraction of a thin film is a graphical method first described by Malé[74]. The transmittance through the film on a substrate and the reflectance from both directions (illuminated through the film and through the substrate) are measured and compared to plots using several input values to find the unknown optical constants of the film. This method would require the capability to measure the reflectance of films, preferably at a wavelength of 1550 nm because the simulations of devices rely on this wavelength, and thus the IR transmittometer would need to be adjusted to include more optics, perhaps similar to the visible reflectometer, but with fewer optical elements so that the reflected light is not too attenuated before reaching the detector. This method assumes that the index of refraction is constant throughout the film thickness, which can be checked by seeing whether the transmittance with the film side facing the

detector and with the film side facing away from the detector give the same calculated thickness.

The optical modeling work in Chapter 4 can also be extended to consider more device geometries. For example, tthe angular dependence of the absorptance both with and without the gold layer on the back should be calculated for the devices on cleaved optical fibers to select an optimal silicon nitride thickness and angle, and the angular dependence of other geometries can also be investigated. The work in Chapter 4 also relies on materials that are currently used in fabrication, but future work could attempt to determine the ideal properties of a substrate and then find out whether a similar material is available.

The best performance detector reported in Chapter 5 has a device detection efficiency of over 77%, but higher absorptances were calculated for this device geometry. The difference is partly due to a value of P_R of less than one, which means that not all photons that are absorbed lead to a counting event. However, improvements in the reliability of the fabrication process, such as better control over the cavity thickness and index of refraction, and the probe station testing setup could lead to higher performance devices.

There is a great amount of work yet to be done on the integration of coplanar nanoantennas with SNSPDs. The designs with the antennas interleaved between nanowires, such as the double-threaded dual Vivaldi design, offer a way to increase the active area of the devices without increasing the kinetic inductance and thus sacrificing speed. According to finite element simulations, this design had a figure of merit comparable to other published devices. It might be improved further with an integrated optical cavity to reflect otherwise transmitted light back into the active layer. In addition, other design parameters, such as the thickness of the nanowires and the angle of the antenna point near the detector, should also be optimized.

The most important next step in the integration of antennas with SNSPDs is the fabrication and testing of a device with an antenna. Chapter 6 shows that it is possible to fabricate antennas very close to nanowires without touching them, with gaps on the order of several nanometers. I am

currently attempting to fabricate working devices and to measure the actual enhancement in the device detection efficiency. The major challenge will be reproducibility and yield, however, because the alignment of the e-beam writer drifts over the course of a write. However, alignment of the log-periodic antenna is less difficult. In this case, the major challenge will be testing the detector with a single-photon source that extends into the mid-infrared range. Simulations of the device detection efficiency to higher wavelengths will be possible once the index of refraction of NbN to wavelengths beyond 5 μm is determined. The log-periodic antenna opens up a much wide wavelength range for the operation of SNSPDs, which could lead to applications in fields such as chemical sensing in low-light environments, such as astronomy.

Overall, this thesis demonstrates the power of predicting SNSPD device performance using optical models, whether analytical models relying on the transfer matrix method or simulations using finite element analysis. The optical model of a thin film of NbN on various substrates is also the basis of the optical setups to measure film thickness quickly without destroying the film, which will be useful for other groups who deposit thin films on thick substrates. It shows how device detection efficiency can be optimized using models before fabrication, and it includes the fabrication of devices and antennas, which has opened up an area of future research to increase the performance of large area detectors and detectors for the mid-infrared.

A

MATLAB Scripts For the Elionix

The scripts in this appendix were written by Qingyuan Zhao. The first script reorders the write order of a pattern to eliminate write fracture if the pattern is composed of multiple shapes, and the second adjusts the height of the stage based on a plane fit to three input points when the height sensor cannot be used during a write on a transparent substrate.

A.1 Reordering the Write Order

This script will adjust the write order such that the pattern is written either left to right or bottom to top. Copy the .cc7 files associated with a particular .con file, and place them in a folder (the .cc7 files are generated by Layout Beamer when the .con file is exported). In the code below, the location of the folder, the number of .cc7 files and the .cc7 file name must be entered, as indicated. If there are more than ten .cc7 files, the `for` loop must be modified for the correct number of zeros in the input file name.

The output of the program are modified .cc7 files that must the original .cc7 files in the same folder as the schedule file that uses them. The modified .cc7 files can be found in the folders with the original .cc7 files, labeled `'Re_order_lr'` or `'Re_order_bt'` for the files modified for a left-to-right writing sequence (which is appropriate for vertical nanowires) or for a bottom-to-top writing sequence (appropriate for horizontal nanowires), respectively.

```
clc;clear all;


fn_old_fd = 'F:'; % Enter folder in which the .cc7 files are stored.


fn_new_bt_fd = [fn_old_fd 'Re_order_bt\'] ;
fn_new_lr_fd = [fn_old_fd 'Re_order_lr\'] ;


mkdir(fn_new_bt_fd);
mkdir(fn_new_lr_fd);


for i = 1:10 % Replace the "10" with the total number of .cc7 files.
```

```
% Replace the file name 'test000' with the .cc7 file name.
filename = ['test000' num2str(i-1) '.cc7'];
fn_old =[fn_old_fd filename];
fn_new_bt = [fn_new_bt_fd filename];
fn_new_lr = [fn_new_lr_fd filename];

x_left = 0;
y_bottom = 0;
line_index  = 1;

fid_old=fopen(fn_old,'rt');
arr_lines = cell(1,1);
a = fgets(fid_old);
while ~feof(fid_old)
    a = fgets(fid_old);
    find_end = strfind(a,'END');
    if isempty(find_end)
        arr_lines{line_index,1} = a;
        find_com = strfind(a,',');
        find_bra = strfind(a,'(');
        x_left(line_index) = str2num(a(find_bra(1)+1:find_com(1)-1));
        y_bottom(line_index) = str2num(a(find_com(1)+1:find_com(2)-1));
        line_index = line_index+1;
    end
end
```

```
fclose(fid_old);


str = 'PATTERN';
%follow the sequence from bottom to up, left to right
y_bottom2up = 1;
if y_bottom2up == 1
    [x_order,x_ix] = sort(x_left);
    arr_lines_left2right = arr_lines(x_ix);
    y_bottom_left2right = y_bottom(x_ix);
    [y_order,y_ix] = sort(y_bottom_left2right);
    arr_new_bot2top = arr_lines_left2right(y_ix);
end

%follow the sequence from left to right,bottom to up
x_left2right = 1;
if x_left2right == 1
    [y_order,y_ix] = sort(y_bottom);
    arr_lines_bot2top = arr_lines(y_ix);
    x_left_bot2top = x_left(y_ix);
    [x_order,x_ix] = sort(x_left_bot2top);
    arr_new_left2right = arr_lines_bot2top(x_ix);
end


fid_new_lr=fopen(fn_new_lr,'w');
fid_new_bt=fopen(fn_new_bt,'w');
```

```
    fprintf(fid_new_lr,'%s\n','PATTERN');
    fprintf(fid_new_bt,'%s\n','PATTERN');
    for j = 1:1:length(arr_lines)
        fprintf(fid_new_lr,'%s',arr_new_left2right{j});
        fprintf(fid_new_bt,'%s',arr_new_bot2top{j});
    end
    fprintf(fid_new_lr,'%s','END');
    fprintf(fid_new_bt,'%s','END');

    fclose(fid_new_lr);
    fclose(fid_new_bt);

end
```

A.2 Manually Adjusting the Stage Height During a Write

The script given here is specifically to modify the height of the sample stage when a transparent substrate is used. Use of this script is not necessary for, e.g., silicon substrates or very thick layers of NbN. To use this script, export the .csv file from the Elionix software WECAS and save it. Enter the location and name of the old .csv file and a location and name for this script to save the new .csv file where indicated below. Once the new .csv file is written, it can be imported into the WECAS software.

The Elionix allows you to move the stage and adjust its height manually to zero the height sensor using WECAS. Move the stage to three non-colinear locations on the chip that are not transparent, e.g., where there is a gold layer, and record the location and height of the stage when the height sen-

sor reads zero. Enter these points where indicated. Further down, the names of the .con files must also be entered. Here they are 'detectors', 'leads', 'lines' and 'dosetest'. The `if` statements that follow must be modified to fit the pattern being written. Here, as an illustrative example, 'detectors' and 'leads' are written with the same write field locations, but 'lines' and 'dosetest' are not.

```
clc;

%Enter the location and name of the old .csv file
%and a location and name for the new .csv file.
fn_old = 'location\old.csv';
fn_new = 'location\new.csv';

fid_old=fopen(fn_old,'rt');
fid_new=fopen(fn_new,'w');
i =1;
% read and write the tilte
a = fgets(fid_old);
fprintf(fid_new,'%s',a);
% read the mark information
a = fgets(fid_old);
fprintf(fid_new,'%s',a);

%Enter the three-location focuses
px1 = 95.94893911;py1 = 120.15406432;pz1 = 5.4291;
px2 = 104.23209019;py2 = 122.93458710;pz2 = 5.4369;
```

```
px3 = 100.98778193;py3 = 116.14797598;pz3 = 5.4326;
%the position of the sample in the gds file
%SSPD, leads
dx1 = 3.3;
dy1 = 3.2;
%line
dx2= 6.1;
dy2= 8.8;
%squares
dx3 = 5.8;
dy3 = 9.6;

pxlist = [px1 px2 px3];
pylist = [py1 py2 py3];
pzlist = [pz1 pz2 pz3];

px12 = [px1-px2 py1-py2 pz1-pz2];
px13 = [px1-px3 py1-py3 pz1-pz3];
nv = cross(px12,px13);
nvx = nv(1);nvy = nv(2);nvz = nv(3);
figure(1)
plot3(px1,py1,pz1,'b*');
set(gca,'FontSize',14)
xlabel('Las X (mm)','FontSize',24)
ylabel('Las Y (mm)','FontSize',24)
```

```
zlabel('Height Value (mm)','FontSize',24);
hold on;
plot3(px2,py2,pz2,'b*'); hold on;
plot3(px3,py3,pz3,'b*'); hold on;

while ~feof(fid_old)
    a = fgets(fid_old);
    gg = strfind(a,',');
    ff = strfind(a,'*B');
    if gg(1)~=1
        % Enter the names of the .con files here,
        %and modify the if-statements below according
        %to whether the .con files share the same write field.
        fsmall_SSPD = strfind(a,'detectors');
        flarge_SSPD = strfind(a,'leads');
        fline = strfind(a,'lines');
        f_squares = strfind(a,'dosetest');
        if ~isempty(fsmall_SSPD)|~isempty(flarge_SSPD)
            px = str2num(a(gg(1)+1:gg(2)-1))+dx1;
            py = str2num(a(gg(2)+1:gg(3)-1))+dy1;
        end
        if ~isempty(fline)
            px = str2num(a(gg(1)+1:gg(2)-1))+dx2;
            py = str2num(a(gg(2)+1:gg(3)-1))+dy2;
        end
```

```
        if ~isempty(f_squares)
            px = str2num(a(gg(1)+1:gg(2)-1))+dx3;
            py = str2num(a(gg(2)+1:gg(3)-1))+dy3;
        end
    end
    % skip the meta commond
    if isempty(ff)
        pz = -((px-px1)*nvx+(py-py1)*nvy)/nvz+pz1;
        fprintf(fid_new,'*Z,0,0,%5.4f,1,0,0\n',pz);
        plot3(px,py,pz,'ro');
    end
    fprintf(fid_new,'%s',a);
    %Use the line position to end the scanning
    if ~isempty(fline)
        break
    end
end
hold off;
fclose(fid_old);
fclose(fid_new);
```

B

MATLAB Code For Optical Simulations

The following MATLAB script creates a plot of the transmittance, reflectance and absorptance of a 40%-fill-factor NbN device on a silicon oxide (thickness = 224 nm)/silicon substrate with a perfect ARC on the back and an optical cavity versus the NbN thickness. The code assumes back illumination and can easily be modified to plot, e.g., the absorptance versus HSQ thickness. The first section of the code gives the indexes of refraction and thicknesses of the layers. To remove a layer from the simulation, enter a thickness of 0; e.g., if the simulation should not include the oxide layer on the

NbN, then enter `d_NbO = 0`, as demonstrated below. The fill factor entered should be a value from 0 to 1 as indicated, not a percentage. The effective index of refraction must be used for both the NbN and the oxide layer, which is calculated based on the fill factor given. The effective permittivity of the NbN device is simply a weighted sum of the permittivity of NbN and that of air (or HSQ, if there is an HSQ cavity on the NbN), and then the effective index of refraction is the square root of the effective permittivity.

Within the outer `for` loop, the thickness of NbN is set, and the amount of light transmitted into the substrate and reflected from it is calculated initially. Then there is a `for` loop that gives the contributions to the total reflectance (`R_plot`), the total transmittance (`T_plot`), the absorptance in NbN (`A_NbN_plot`) and the total absorptance (`A_plot`) for each cycle of reflections within the substrate. The matrices calculated by this script give the transmittance, reflectance and absorptance as fractions, not percentages. The total values for each NbN thickness are then gathered into matrices that can be plotted, as shown in Figure B.1.

```
clear all
%%
%Values and constants: all distances are in nanometers unless otherwise
%specified.
lambda0 = 1550;
k = 2*pi/lambda0;


n_substrate = 3.47772;
k_substrate = n_substrate*k;


n_air = 1;
```

```
k_air = n_air*k;


n_ARC = sqrt(n_air*n_substrate);

k_ARC = n_ARC*k;

d_ARC = lambda0/(4*n_ARC);


n_HSQ = 1.38;

k_HSQ = n_HSQ*k;

d_HSQ = 290;


n_NbN_given = 5.23-5.82*1i;

n_NbO_given = 2.28;

fill_factor = 0.4; %A value of 1 indicates a continuous film


%This calculation depends on the material between the nanowires, which

%could be air or HSQ.

epsilon_weighted_NbN = fill_factor*(n_NbN_given^2)

+(1-fill_factor)*(n_HSQ^2);

n_NbN = sqrt(epsilon_weighted_NbN);

epsilon_weighted_NbO = fill_factor*(n_NbO_given^2)

+(1-fill_factor)*(n_HSQ^2);

n_NbO = sqrt(epsilon_weighted_NbO);

k_NbN = n_NbN*k;

k_NbO = n_NbO*k;

d_NbO = 0;
```

```
%These values are used to calculate the absorptance in NbN.
c = 3*10^8; %c in m/s
omega = 2*pi*c/(lambda0*10^-9);
imeps = (8.85418782*10^-12)*imag(n_NbN^2);
k_NbNm = k_NbN*10^9; %k_NbN in meters, not nm

n_SiNx= 1.54;
k_SiNx = n_SiNx*k;
d_SiNx = 224;

n_gold = 0.55-11.5*1i;
k_gold = n_gold*k;
d_gold = 120;
%%
%Initialize values for result matrices
max=100;
T_plot = zeros(max+1,1);
R_plot = zeros(max+1,1);
A_plot = zeros(max+1,1);%total absorption
A_NbN_plot = zeros(max+1,1);%absorption in only the NbN layer
thickness = zeros(max+1,1);
%%
for count=0:1:max
    d_NbN = count/10;
```

```
    T_total = 0;
    R_total = 0;
    A_total = 0;
    A_NbN_total = 0;
    inc = 1; %fraction of incident power

    %At the first interface (back of the sample)
    D_air_ARC = 0.5*[1+(k_ARC/k_air) 1-(k_ARC/k_air);
1-(k_ARC/k_air) 1+(k_ARC/k_air)];
    P_ARC = [exp(1i*k_ARC*d_ARC) 0; 0 exp(-1i*k_ARC*d_ARC)];
    D_ARC_substrate = 0.5*[1+(k_substrate/k_ARC) 1-(k_substrate/k_ARC);
1-(k_substrate/k_ARC) 1+(k_substrate/k_ARC)];
    M_ARC = D_air_ARC*P_ARC*D_ARC_substrate;

    R_ARC = abs(M_ARC(2,1)/M_ARC(1,1))^2;
    R_total = R_total+inc*R_ARC;
    T_ARC = (n_substrate/n_air)*abs(1/M_ARC(1,1))^2;
    inc = inc*T_ARC;

    %These equations are used in the loop below for the second interface.
    D_substrate_SiNx = 0.5*[1+(k_SiNx/k_substrate) 1-(k_SiNx/k_substrate);
1-(k_SiNx/k_substrate) 1+(k_SiNx/k_substrate)];
    P_SiNx = [exp(1i*k_SiNx*d_SiNx) 0; 0 exp(-1i*k_SiNx*d_SiNx)];
    D_SiNx_NbN = 0.5*[1+(k_NbN/k_SiNx) 1-(k_NbN/k_SiNx);
```

```
1-(k_NbN/k_SiNx) 1+(k_NbN/k_SiNx)];
    P_NbN = [exp(1i*k_NbN*d_NbN) 0; 0 exp(-1i*k_NbN*d_NbN)];
    D_NbN_NbO = 0.5*[1+(k_NbO/k_NbN) 1-(k_NbO/k_NbN);
1-(k_NbO/k_NbN) 1+(k_NbO/k_NbN)];
    P_NbO = [exp(1i*k_NbO*d_NbO) 0; 0 exp(-1i*k_NbO*d_NbO)];
    D_NbO_HSQ = 0.5*[1+(k_HSQ/k_NbO) 1-(k_HSQ/k_NbO);
1-(k_HSQ/k_NbO) 1+(k_HSQ/k_NbO)];
    P_HSQ = [exp(1i*k_HSQ*d_HSQ) 0; 0 exp(-1i*k_HSQ*d_HSQ)];
    D_HSQ_gold = 0.5*[1+(k_gold/k_HSQ) 1-(k_gold/k_HSQ);
1-(k_gold/k_HSQ) 1+(k_gold/k_HSQ)];
    P_gold = [exp(1i*k_gold*d_gold) 0; 0 exp(-1i*k_gold*d_gold)];
    D_gold_air = 0.5*[1+(k_air/k_gold) 1-(k_air/k_gold);
1-(k_air/k_gold) 1+(k_air/k_gold)];
    M_second_interface = D_substrate_SiNx*P_SiNx*D_SiNx_NbN*P_NbN
*D_NbN_NbO*P_NbO*D_NbO_HSQ*P_HSQ
*D_HSQ_gold*P_gold*D_gold_air;
    R_second_interface = abs(M_second_interface(2,1)
/M_second_interface(1,1))^2;
    T_second_interface = (n_air/n_substrate)
*abs(1/M_second_interface(1,1))^2;

    %These equations are used in the loop below to calculate the
    %absorptance in NbN.
    irradiance = n_substrate*(3*10^8)*(8.85418782*10^-12)*0.5;
    matrix = D_NbN_NbO*P_NbO*D_NbO_HSQ*P_HSQ*D_HSQ_gold*P_gold*D_gold_air;
```

```
    %AB is the constants for the electric field in NbN:
    AB = matrix*[1/M_second_interface(1,1) 0]';
    d = d_NbN*10^-9; %d is in meters
    X = 0:d/1000:d;
    Y = abs(AB(1)*exp(-1i*k_NbNm*(X-d))+AB(2)*exp(1i*k_NbNm*(X-d))).^2;

    %These matrices are used in the loop below for the first interface,
    %from the substrate, through the ARC, into air.
    D_substrate_ARC = 0.5*[1+(k_ARC/k_substrate) 1-(k_ARC/k_substrate);
1-(k_ARC/k_substrate) 1+(k_ARC/k_substrate)];
    D_ARC_air = 0.5*[1+(k_air/k_ARC) 1-(k_air/k_ARC);
1-(k_air/k_ARC) 1+(k_air/k_ARC)];
    M_first_interface = D_substrate_ARC*P_ARC*D_ARC_air;
    R_first_interface = abs(M_first_interface(2,1)
/M_first_interface(1,1))^2;
    T_first_interface = (n_air/n_substrate)
*abs(1/M_first_interface(1,1))^2;

    %Start for loop for muliple passes within the substrate. Generally,
    %three passes is an adequate number of internal reflections, but the
    %calculation is fast.
    for pass=1:1:100

        %At the second interface
        T_total = T_total+inc*T_second_interface;
```

```
        A_total = A_total+inc*(1-T_second_interface-R_second_interface);

        %Absorption in NbN
        Z = inc*trapz(X,Y);
        Q = 0.5*omega*imeps*Z/irradiance;
        A_NbN_total = A_NbN_total - Q;
        inc = inc*R_second_interface;

        %At the first interface
        R_total = R_total + inc*T_first_interface;
        inc = inc*R_first_interface;
    end

    %These values are in fractions, not percentages.
    T_plot(count+1)=T_total;
    R_plot(count+1) = R_total;
    A_plot(count+1) = A_total;
    A_NbN_plot(count+1) = A_NbN_total;
    thickness(count+1)=d_NbN;
end



%%
hold on
plot(thickness, T_plot*100, 'b--')
```

```
plot(thickness, R_plot*100, 'r--')

plot(thickness, A_NbN_plot*100, 'g--')


xlabel('NbN thickness (nm)')

ylabel('transmittance, reflectance and absorptance (%)')
```

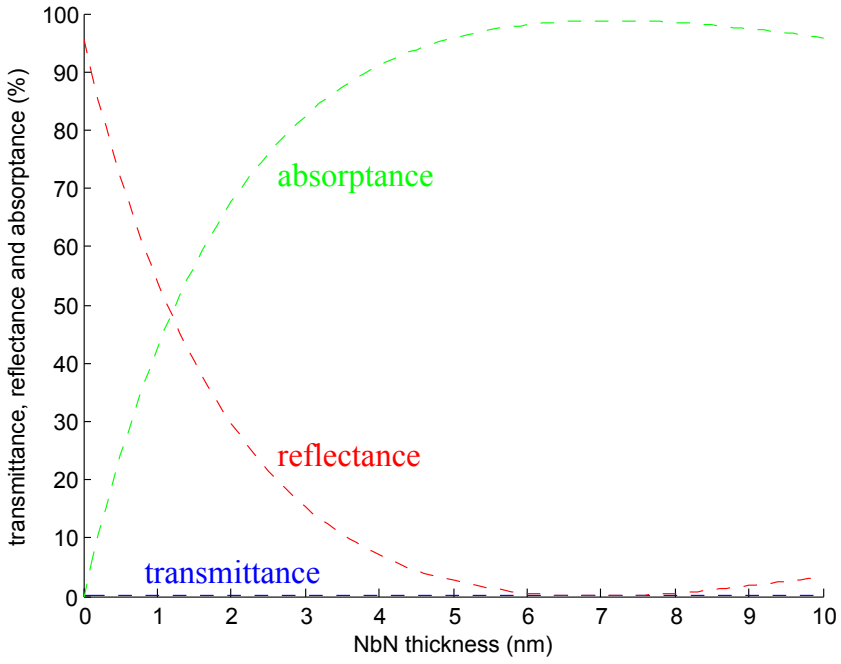

Figure B.1: Transmittance (blue), reflectance (red) and absorptance in NbN (green) versus NbN thickness, as output by the MATLAB script given here.

C

Heat Maps and Two-Dimensional Plots For Various Device Substrates

This appendix gives "heat maps" and two-dimensional graphs of the absorptance in NbN for common substrates with and without an optimized integrated optical cavity. "Heat maps" of the optimal HSQ thicknesses are also included. The simulations assume a perfect anti-reflection coating and back illumination of the device through the substrate.

C.1 NbN on Sapphire

Sapphire and MgO have similar refractive index values, and thus the results reported in this section are also relevant for fabrication on MgO.

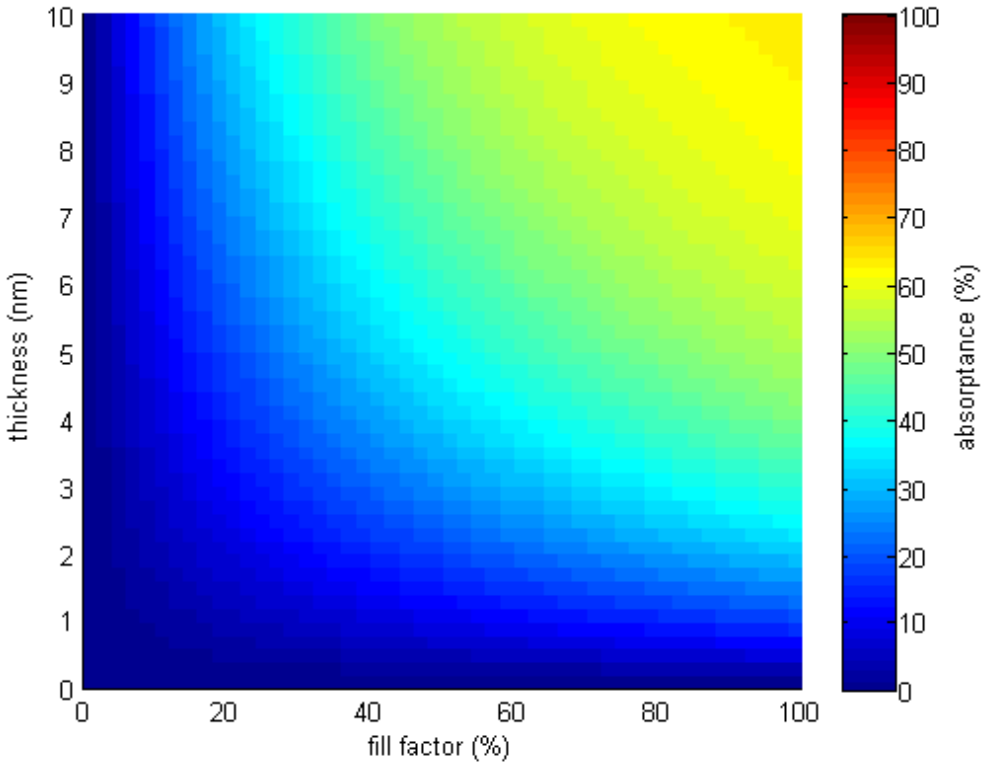

Figure C.1: Heat map of the absorptance versus fill factor and thickness for NbN on sapphire without an optical cavity.

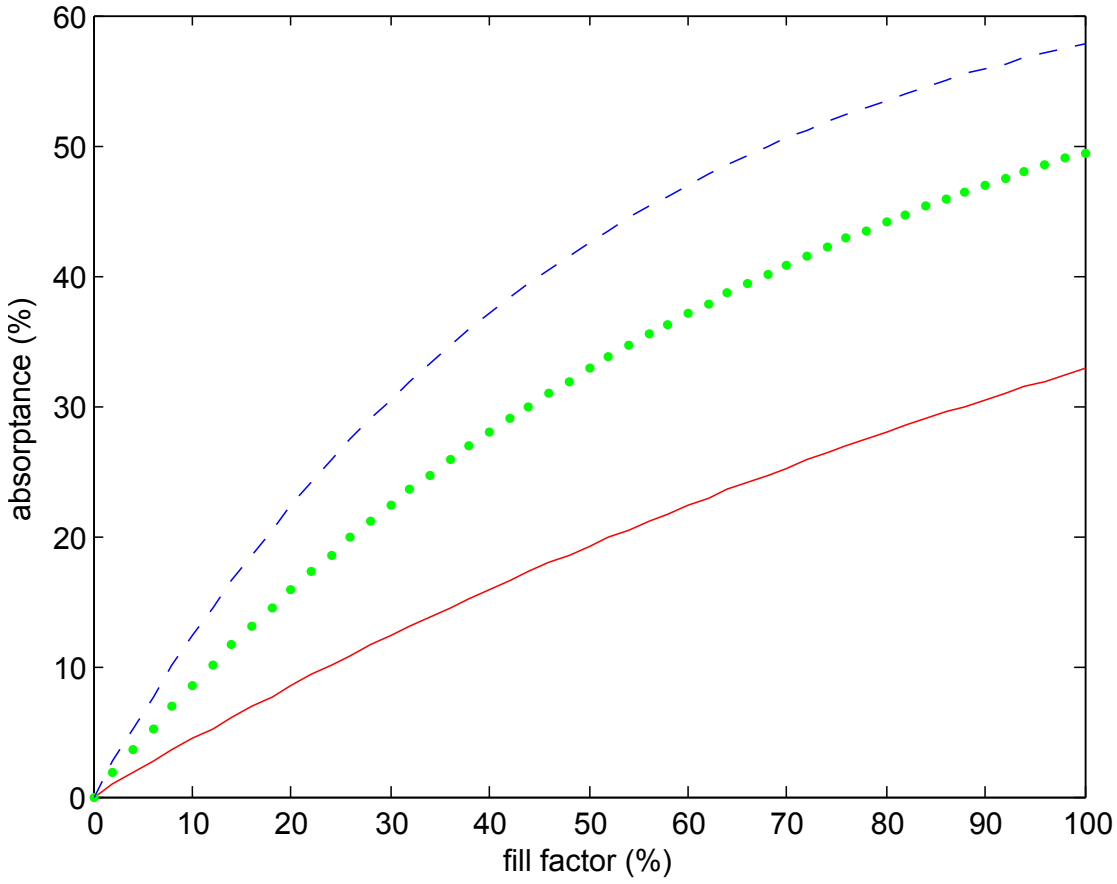

Figure C.2: Line plots of the absorptance versus fill factor of NbN on sapphire without an optical cavity for thicknesses of 2 nm (red solid line), 4 nm (green dotted line) and 6 nm (blue dashed line).

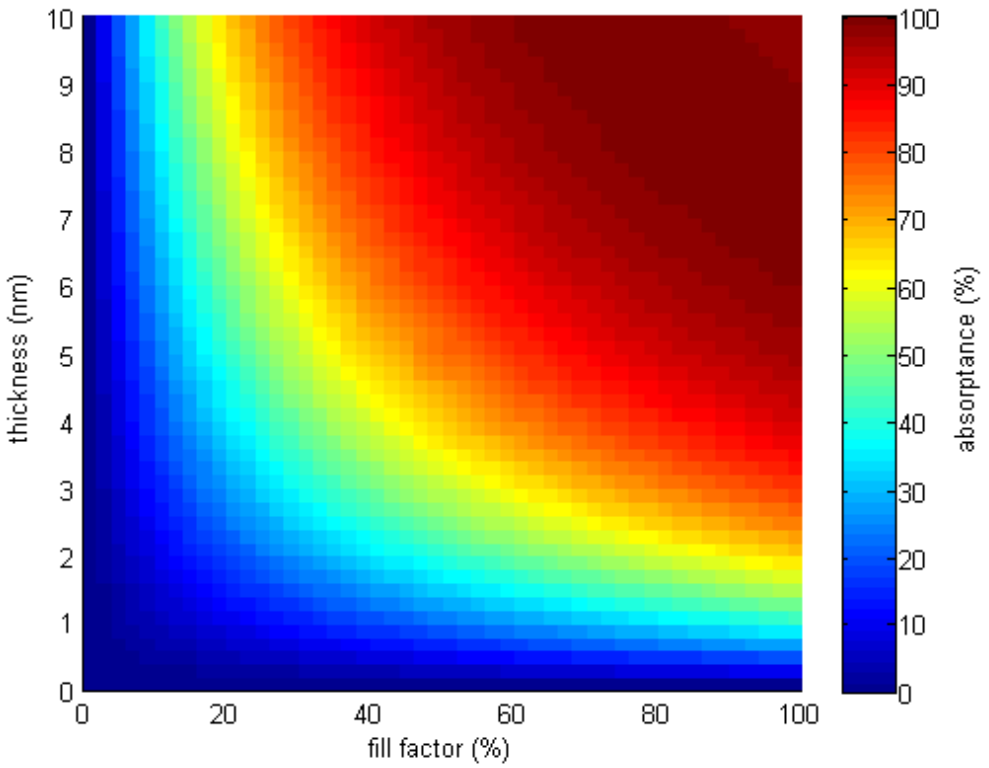

Figure C.3: Heat map of the absorptance versus fill factor and thickness for NbN on sapphire with an optical cavity.

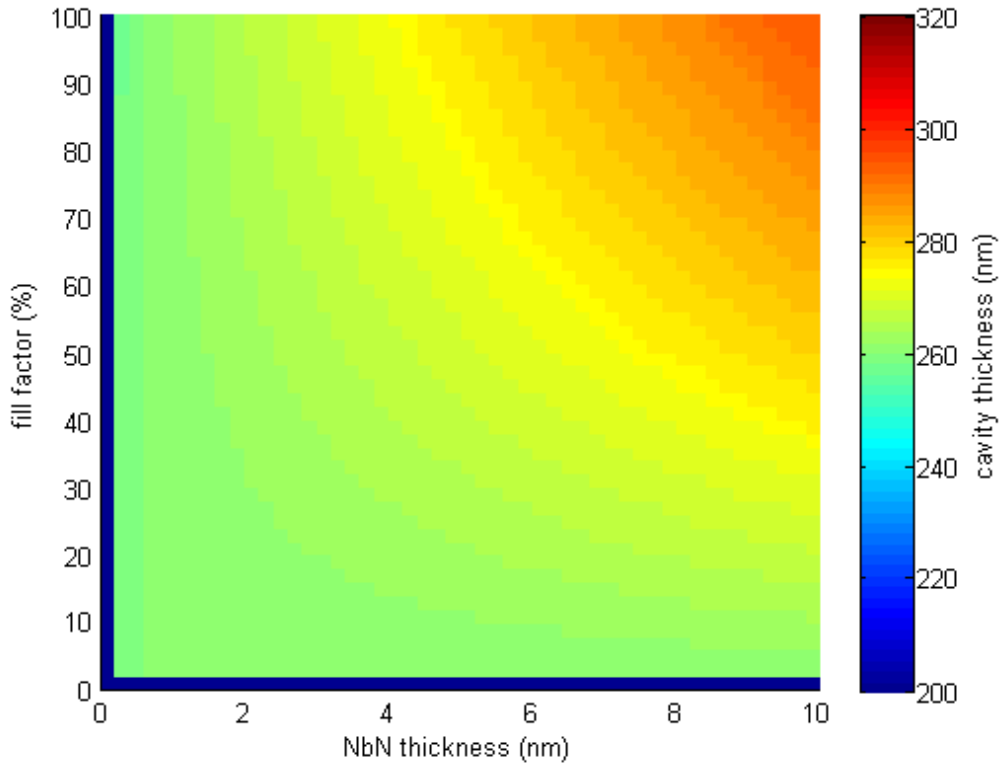

Figure C.4: Heat map of the thickness of the optimal HSQ optical cavity versus fill factor and thickness for NbN on sapphire.

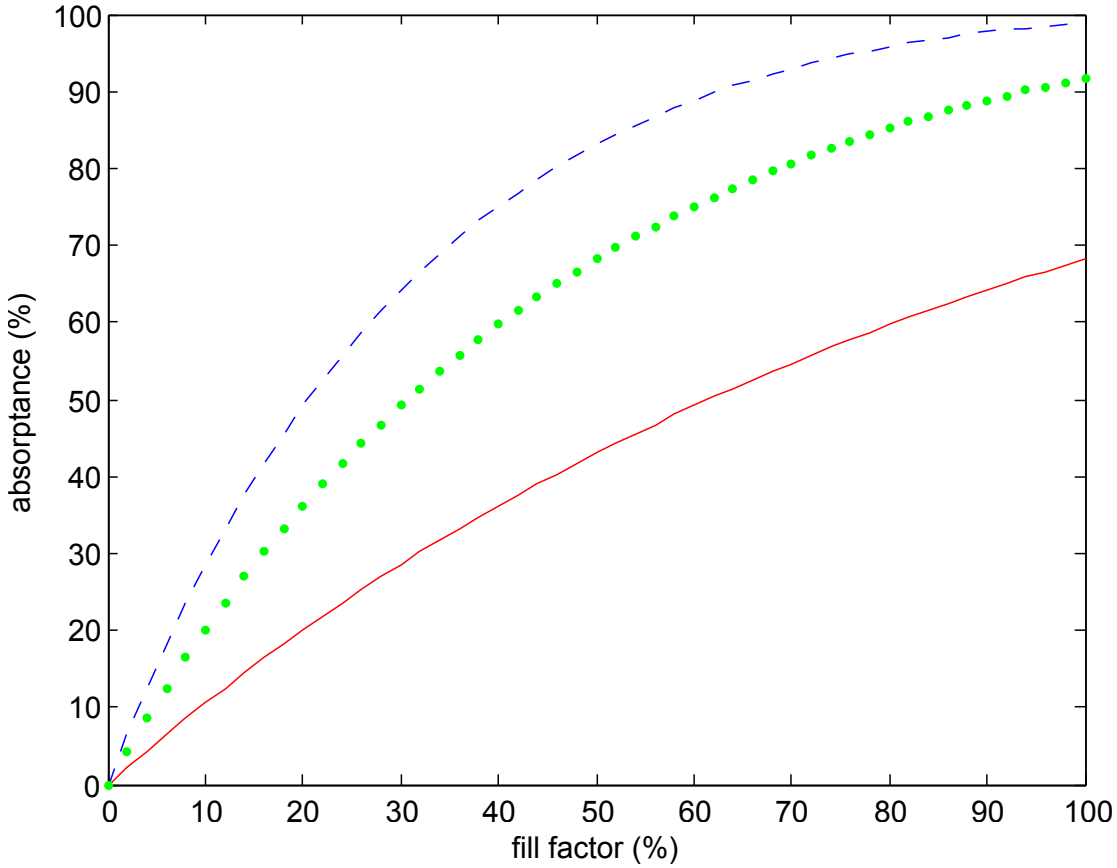

Figure C.5: Line plots of the absorptance versus fill factor for thicknesses of 2 nm (red solid line), 4 nm (green dotted line) and 6 nm (blue dashed line) for NbN on sapphire with an optimal HSQ optical cavity.

C.2 NbN on Silicon

SNSPDs are typically not fabricated directly on silicon with no oxide or nitride, but these results are included for comparison with the results on sapphire, which as a much lower index of refraction. Without an optical cavity, the results for silicon and sapphire are quite similar. However, with an optical cavity, sapphire can achieve absorptances of greater than 90% at lower fill factors and thicknesses.

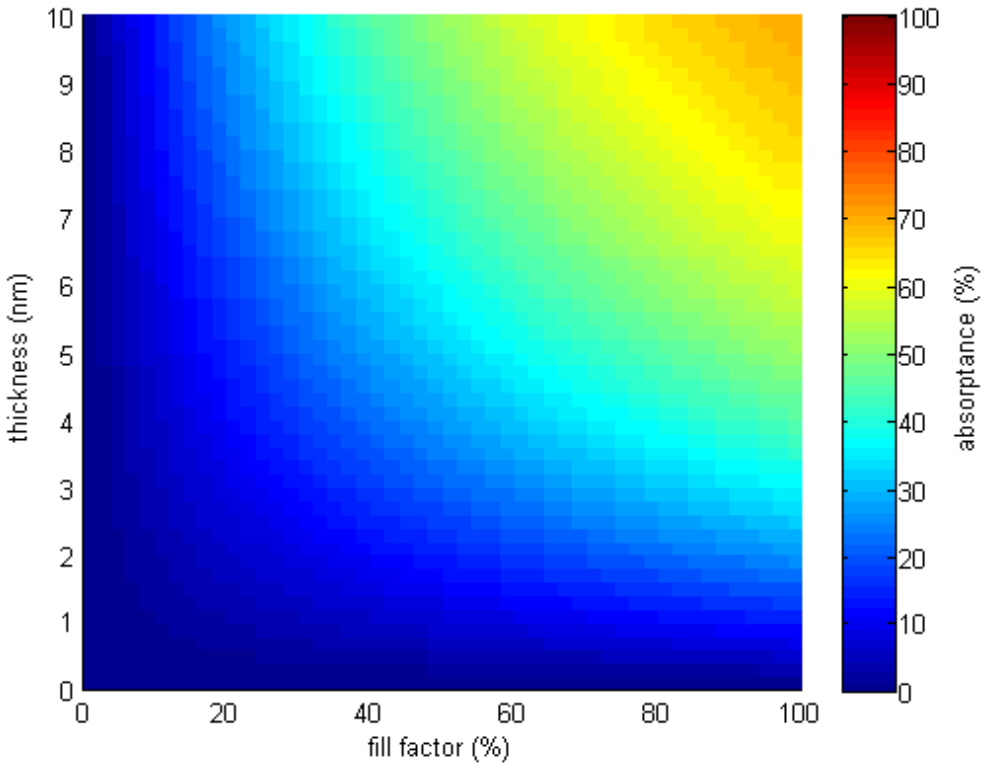

Figure C.6: Heat map of the absorptance versus fill factor and thickness for NbN on silicon without an optical cavity.

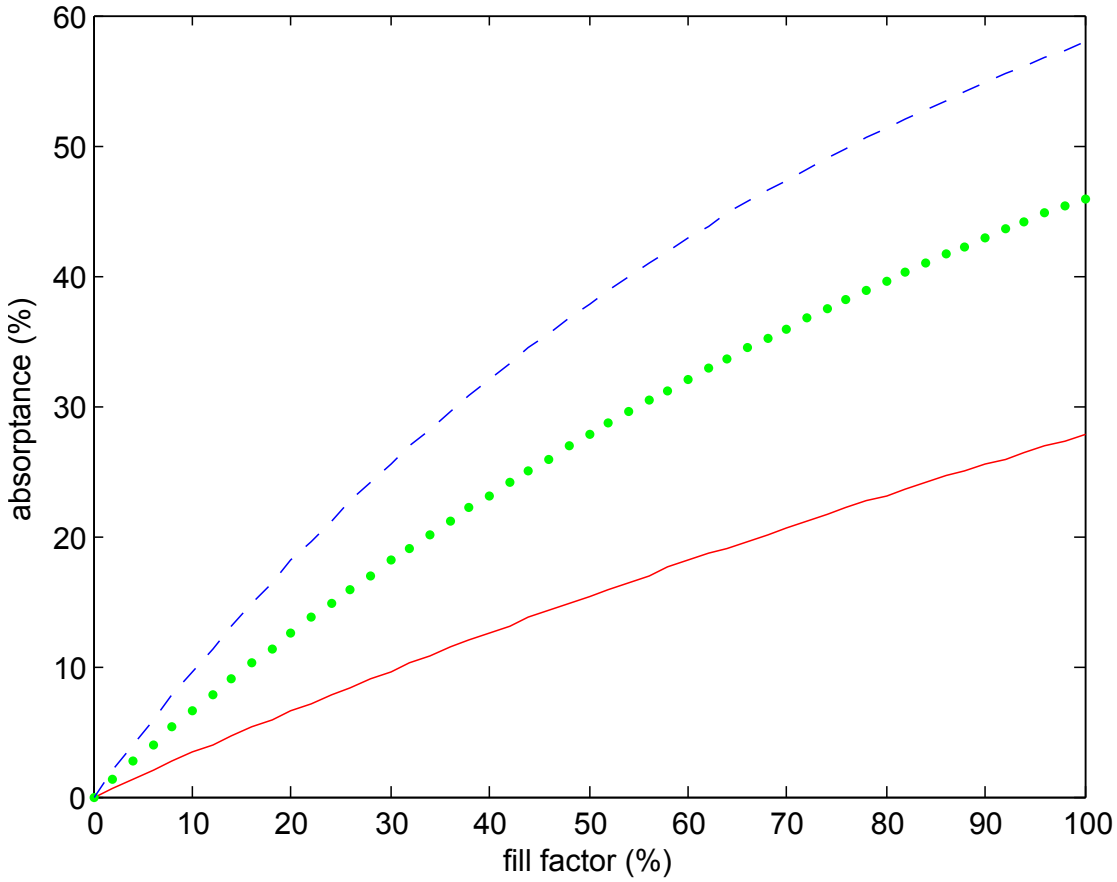

Figure C.7: Line plots of the absorptance versus fill factor of NbN on silicon without an optical cavity for thicknesses of 2 nm (red solid line), 4 nm (green dotted line) and 6 nm (blue dashed line).

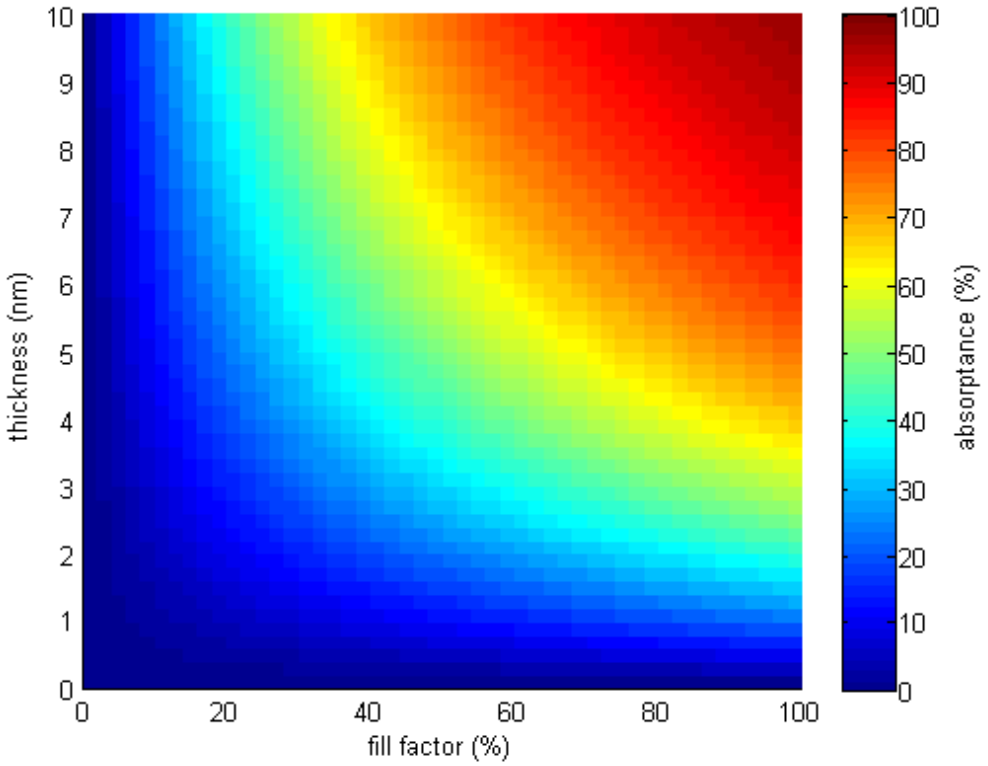

Figure C.8: Heat map of the absorptance versus fill factor and thickness for NbN on silicon with an optical cavity.

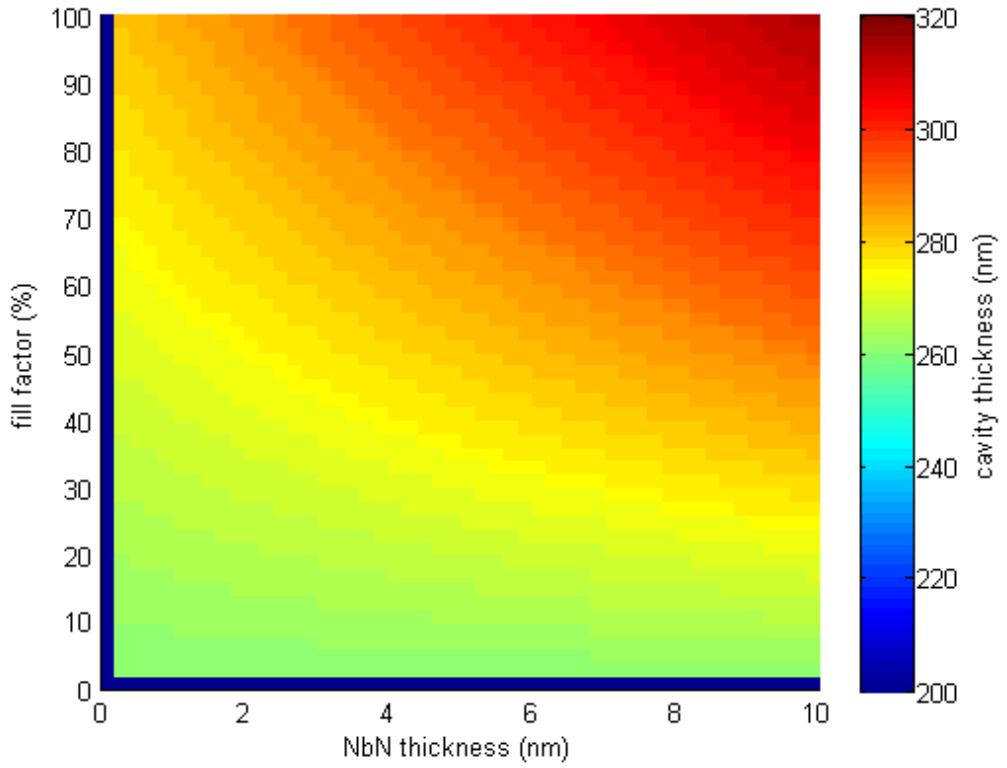

Figure C.9: Heat map of the thickness of the optimal HSQ optical cavity versus fill factor and thickness for NbN on silicon.

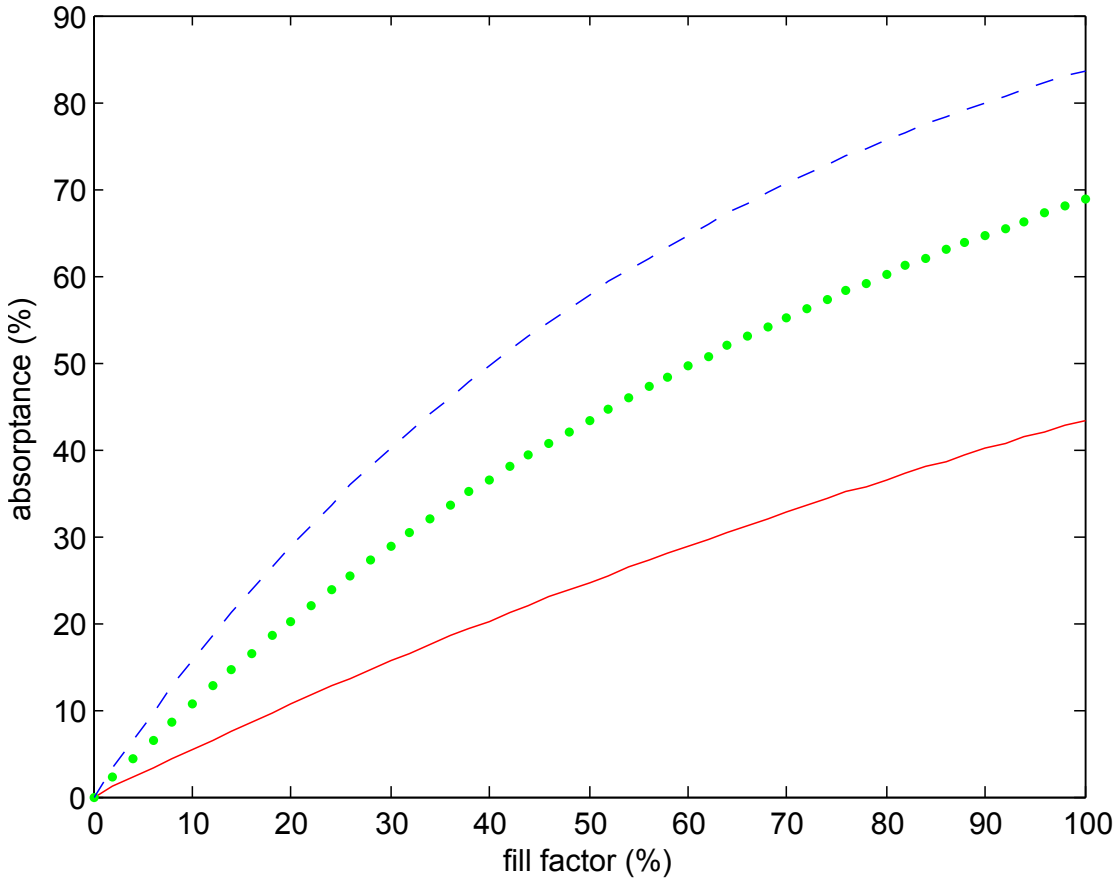

Figure C.10: Line plots of the absorptance versus fill factor for thicknesses of 2 nm (red solid line), 4 nm (green dotted line) and 6 nm (blue dashed line) for NbN on silicon with an optimal HSQ optical cavity.

C.3 NbN on Silicon Nitride on Silicon

The absorptance in NbN devices fabricated on silicon substrates changes when a quarter wave layer of silicon nitride or dioxide between the silicon and the NbN is included to act as an additional optical cavity. Without an HSQ cavity on top of the device, the quarter wave layer actually decreases the absorptance if it is composed of silicon dioxide and does not change the absorptance much if it is silicon nitride. However, when an HSQ cavity on top of the device is included, much higher absorptances with lower fill factors and thicknesses of NbN can be obtained with the quarter wave layers of silicon dioxide or silicon nitride.

The results in this section were obtained with a quarter wave silicon nitride layer (thickness 175 nm). The absorptance with an HSQ optical cavity in addition is over 60% for a typical device of 4 nm in thickness and 40% fill factor.

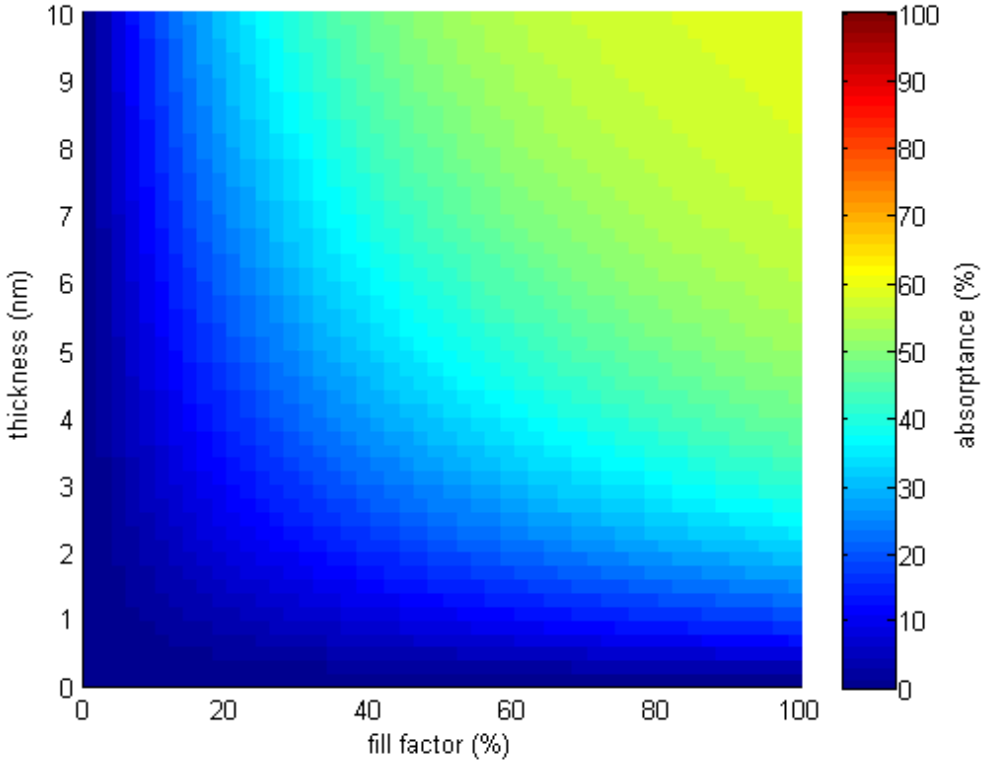

Figure C.11: Heat map of the absorptance versus fill factor and thickness for NbN on silicon nitride/silicon without an optical cavity.

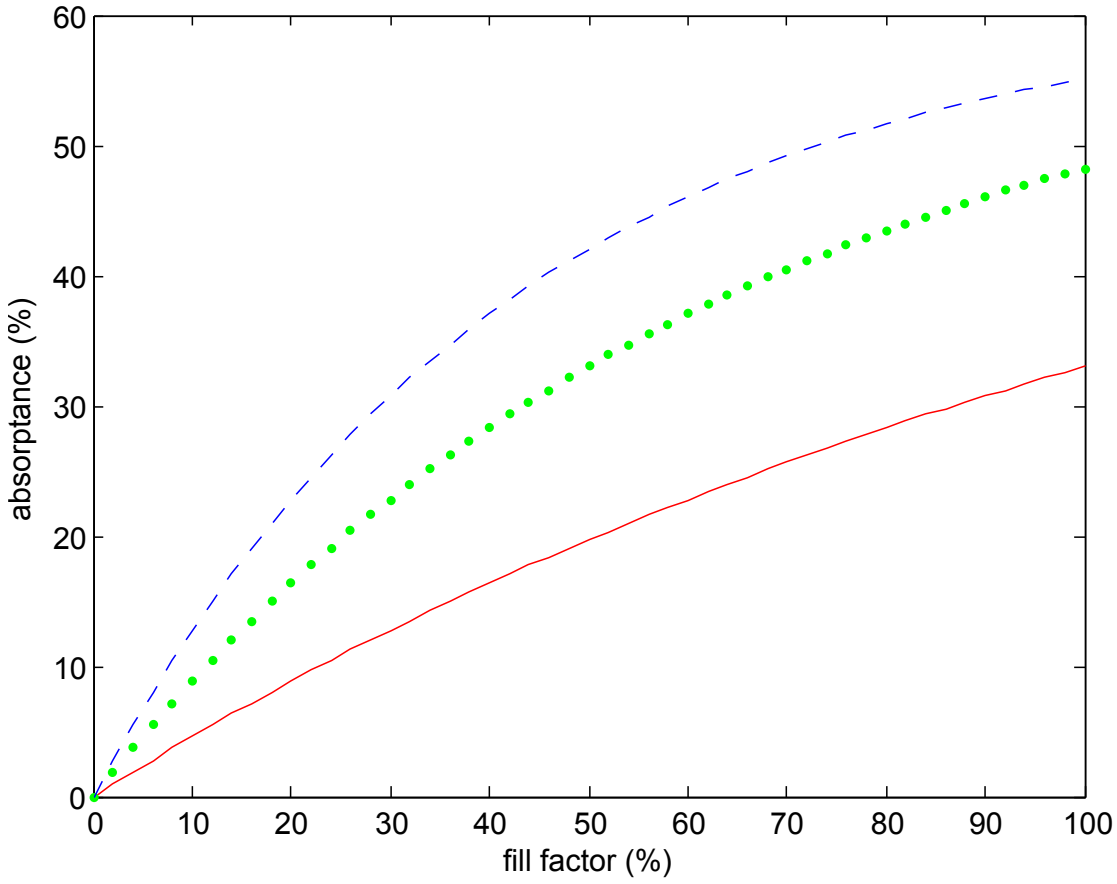

Figure C.12: Line plots of the absorptance versus fill factor of NbN on silicon nitride/silicon without an optical cavity for thicknesses of 2 nm (red solid line), 4 nm (green dotted line) and 6 nm (blue dashed line).

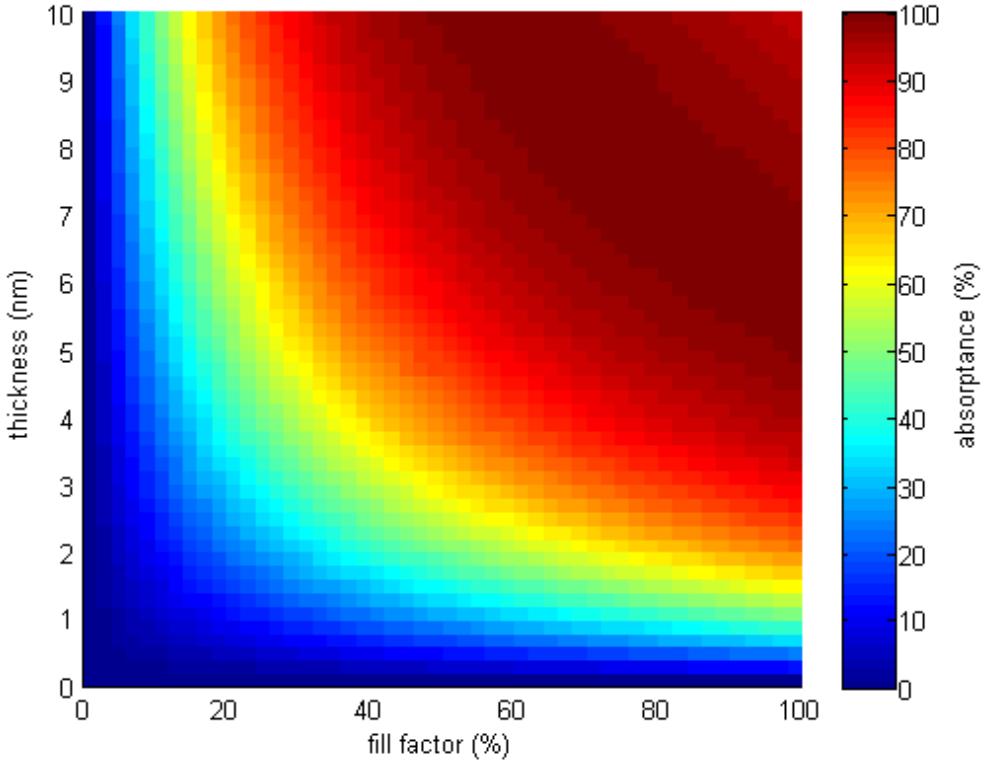

Figure C.13: Heat map of the absorptance versus fill factor and thickness for NbN on silicon nitride/silicon with an optical cavity.

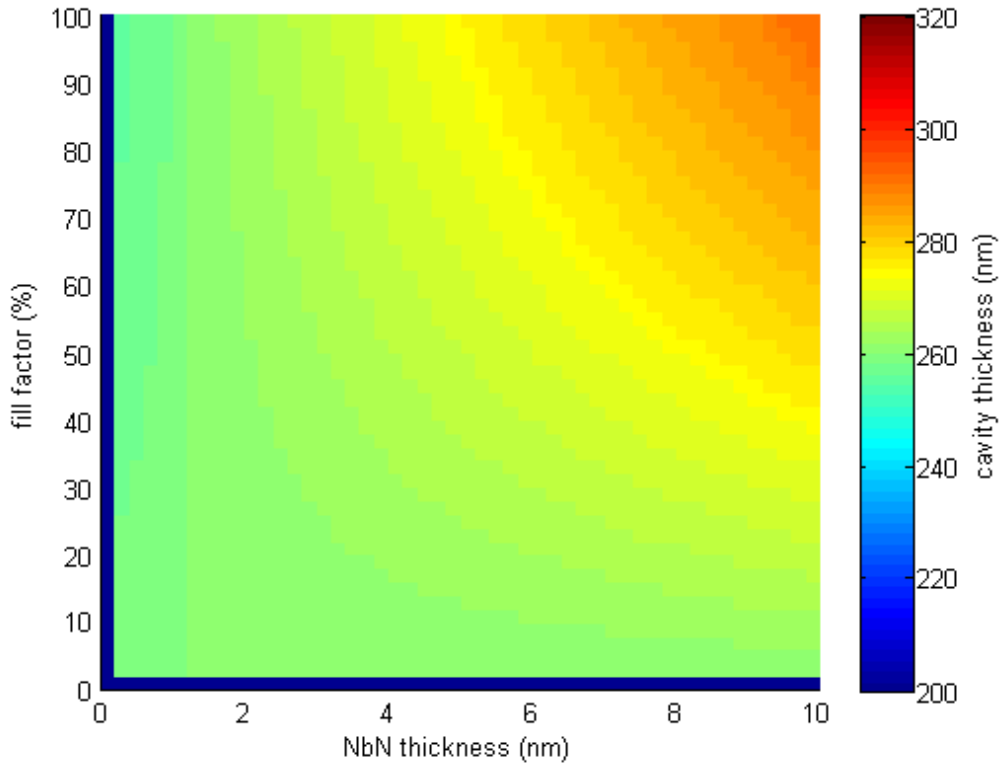

Figure C.14: Heat map of the thickness of the optimal HSQ optical cavity versus fill factor and thickness for NbN on silicon nitride/silicon.

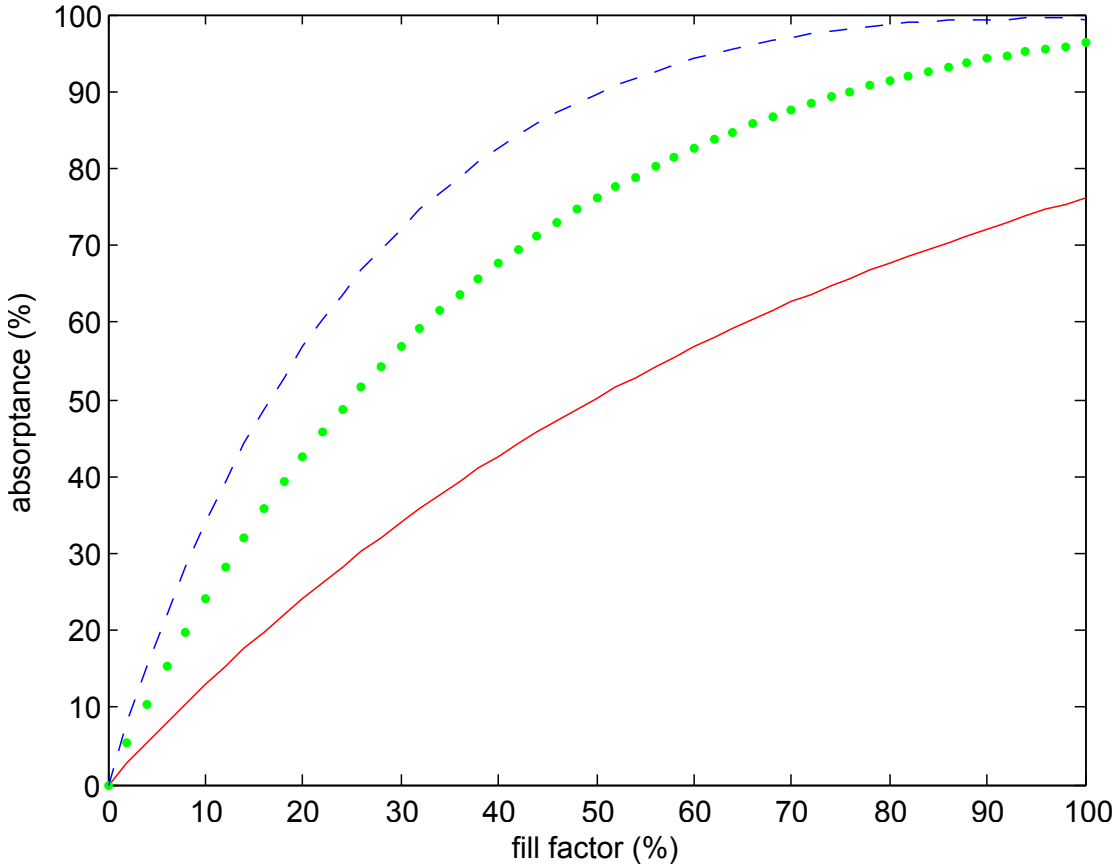

Figure C.15: Line plots of the absorptance versus fill factor for thicknesses of 2 nm (red solid line), 4 nm (green dotted line) and 6 nm (blue dashed line) for NbN on silicon nitride/silicon with an optimal HSQ optical cavity.

C.4 NbN on Silicon Oxide on Silicon

The most promising results are for NbN devices on silicon dioxide on silicon, where a typical NbN meander pattern of 4 nm in thickness and 40

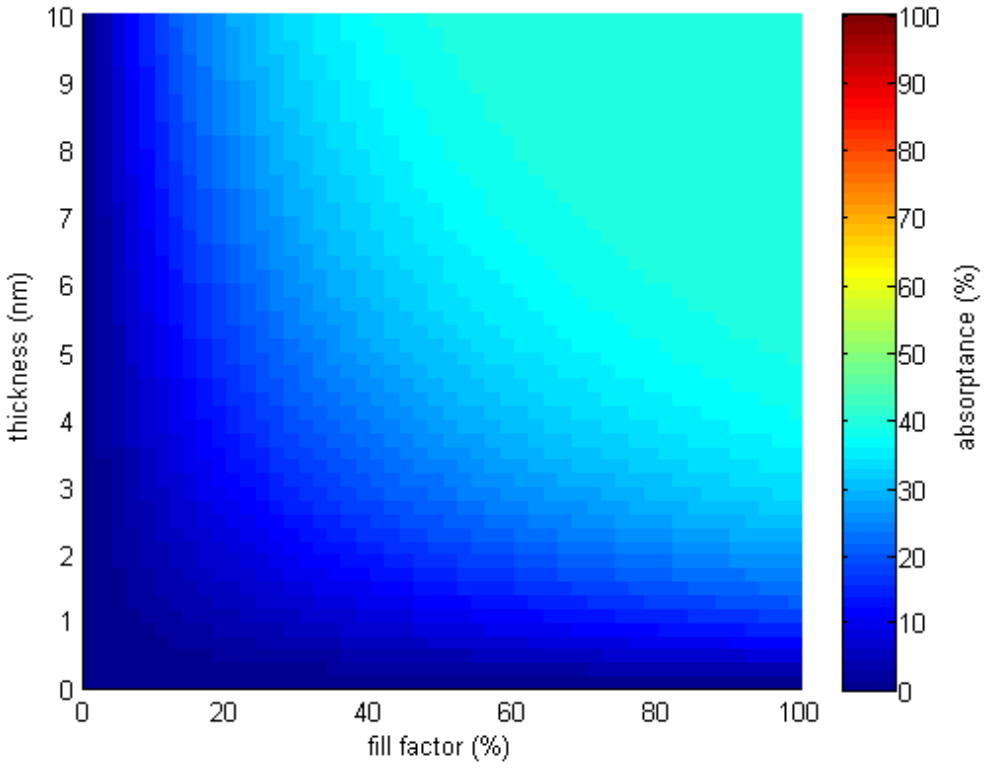

Figure C.16: Heat map of the absorptance versus fill factor and thickness for NbN on silicon dioxide/silicon without an optical cavity.

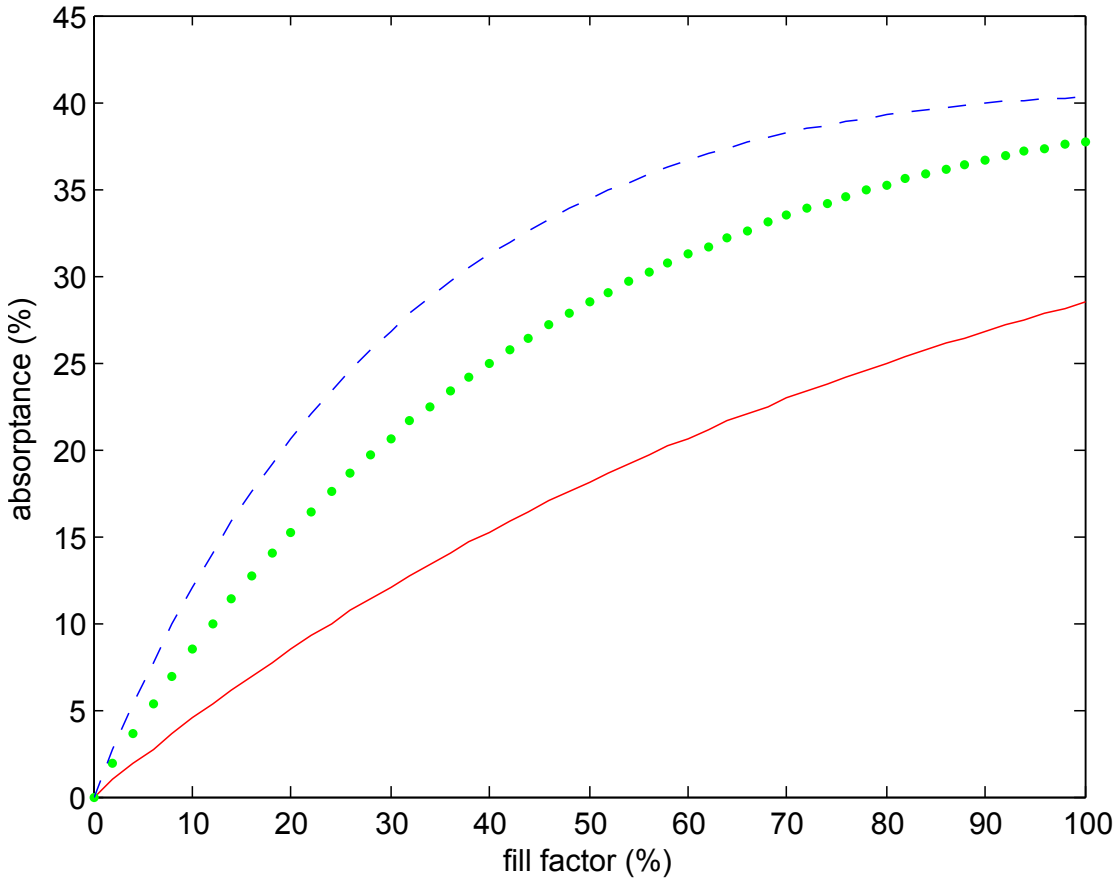

Figure C.17: Line plots of the absorptance versus fill factor of NbN on silicon dioxide/silicon without an optical cavity for thicknesses of 2 nm (red solid line), 4 nm (green dotted line) and 6 nm (blue dashed line).

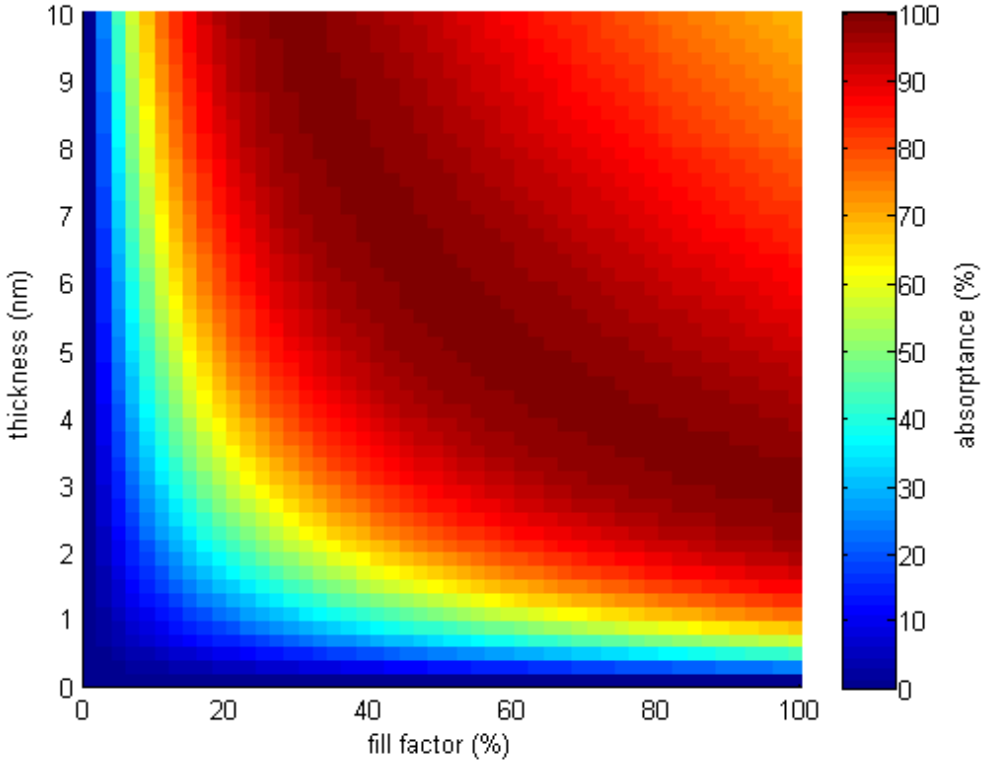

Figure C.18: Heat map of the absorptance versus fill factor and thickness for NbN on silicon dioxide/silicon with an optical cavity.

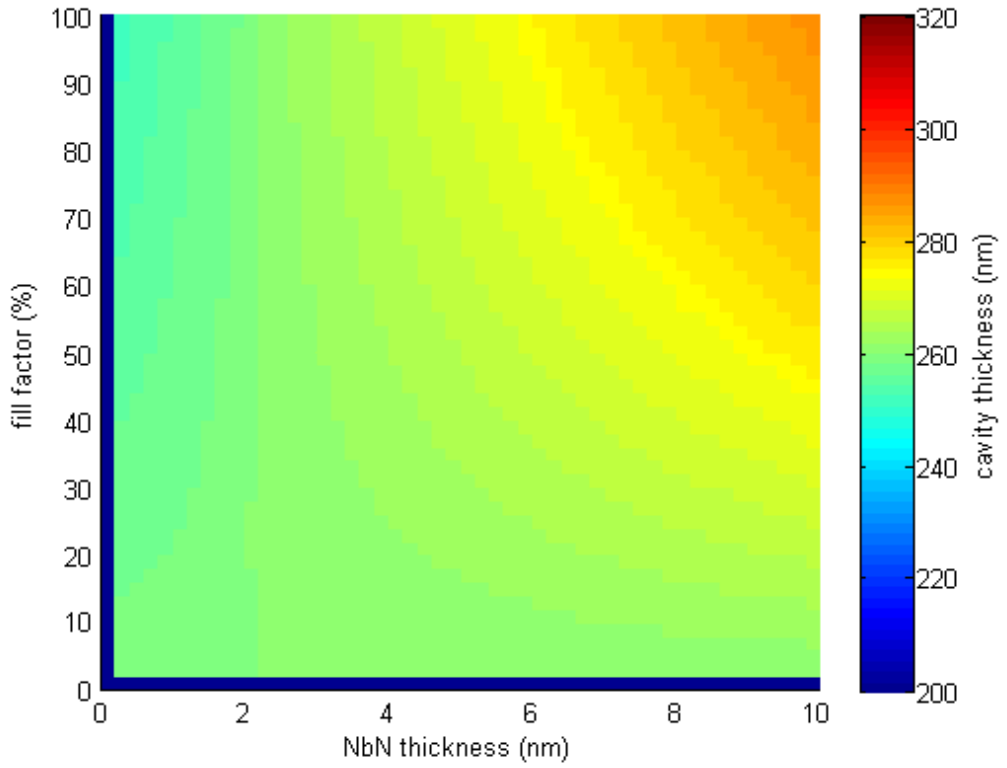

Figure C.19: Heat map of the thickness of the optimal HSQ optical cavity versus fill factor and thickness for NbN on silicon dioxide/silicon.

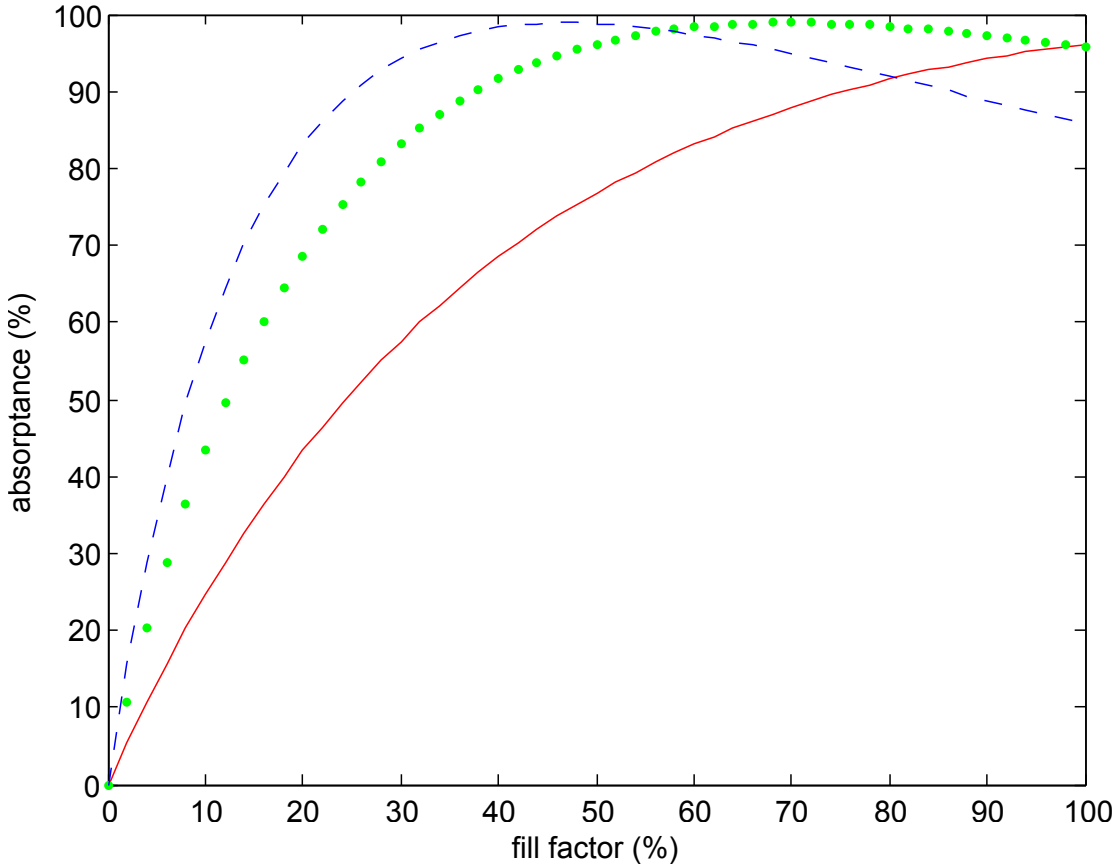

Figure C.20: Line plots of the absorptance versus fill factor for thicknesses of 2 nm (red solid line), 4 nm (green dotted line) and 6 nm (blue dashed line) for NbN on silicon dioxide/silicon with an optimal HSQ optical cavity.

References

[1] F. Stellari, A. Tosi, and P. Song, "Switching time extraction of CMOS gates using time-resolved emission (TRE)," in *IEEE 44th Annual International Reliability Physics Symposium*, vol. 06CH37728, (San Jose, CA), 2006.

[2] F. Stellari, P. Song, and A. J. Weger, "Single photon detectors for ultra low voltage time resolved emission measurements," *IEEE Journal on Quantum Electronics*, vol. 47, no. 6, pp. 841–848, 2011.

[3] R. H. Hadfield, J. L. Habif, J. Schlafer, R. E. Schwall, and S. W. Nam, "Quantum key distribution at 1550 nm with twin superconducting single-photon detectors," *Applied Physics Letters*, vol. 89, no. 241129, 2006.

[4] H. Takesue, S. W. Nam, Q. Zhang, R. H. Hadfield, T. Honjo, K. Tamaki, and Y. Yamamoto, "Quantum key distribution over a 40-dB channel loss using superconducting single-photon detectors," *Nature Photonics*, vol. 1, pp. 343–348, 2007.

[5] D. Rosenberg, C. G. Peterson, J. W. Harrington, P. R. Rice, N. Dallmann, K. T. Tyagi, K. P. McCabe, S. W. Nam, B. Baek, R. H. Hadfield, R. J. Hughes, and J. E. Nordholt, "Practical long-distance quantum key distribution system using decoy levels," *New Journal of Physics*, vol. 11, no. 045009, 2009.

[6] D. Stucki, N. Walenta, F. Vannel, R. T. Thew, N. Gisin, H. Zbinden, S. Gray, C. R. Towery, and S. Ten, "High rate, long-distance quantum key distribution over 250 km of ultra low loss fibres," *New Journal of Physics*, vol. 11, no. 075003, 2009.

[7] C. M. Natarajan, L. Zhang, H. Coldenstrodt-Ronge, G. Donati, S. N. Dorebos, V. Zwiller, I. A. Walmsley, and R. H. Hadfield, "Quantum detector tomography of a time-multiplexed superconducting nanowire single-photon detector at telecom wavelengths," *Optics Express*, vol. 21, no. 1, pp. 893–902, 2013.

[8] M. D. Shaw, K. Birnbaum, M. Cheng, M. Srinivasan, K. Quirk, J. Kovalik, A. Biswas, A. Beyer, F. Marsili, V. B. Verma, S. W. Nam, J. A. Stern, and W. H. Farr, "A receiver for the lunar laser communication demonstration using the optical communications telescope laboratory," in *CLEO: Science and Innovations*, vol. SM4J, (San Jose, CA), 2014.

[9] H. Shibata, K. Shimizu, H. Takesue, and Y. Tokura, "Superconducting nanowire single-photon detector with ultralow dark count rate using cold optical filters," *Applied Physics Express*, vol. 6, no. 7, p. 072801, 2013.

[10] E. A. Dauler, A. J. Kerman, B. S. Robinson, J. K. W. Yang, B. Voronov, G. Goltsman, S. A. Hamilton, and K. K. Berggren, "Photon-number-resolution with sub-30-ps timing using multi-element superconducting nanowire single photon detectors," *Journal of Modern Optics*, vol. 56, no. 2–3, pp. 364–373, 2008.

[11] Q. Zhao, L. Zhang, T. Jia, L. Kang, W. Xu, J. Chen, and P. Wu, "Intrinisc timing jitter of superconducting nanowire single-photon detectors," *Applied Physics B*, vol. 104, pp. 673–678, 2011.

[12] L. You, X. Yang, Y. He, W. Zhang, D. Liu, W. Zhang, L. Zhang, L. Zhang, X. Liu, S. Chen, Z. Wang, and X. Xie, "Jitter analysis of a superconducting nanowire single photon detector," *AIP Advances*, vol. 3, no. 7, p. 072135, 2013.

[13] A. J. Kerman, E. A. Dauler, W. E. Keicher, J. K. W. Yang, K. K. Berggren, G. Gol'tsman, and B. Voronov, "Kinetic-inductance-limited reset time of superconducting nanowire photon counters," *Applied Physics Letters*, vol. 88, no. 111116, 2006.

[14] F. Marsili, V. Verma, J. Stern, S. Harrington, A. Lita, T. Gerrits, I. Vayshenker, B. Baek, M. Shaw, R. Mirin, and S. W. Nam, "Detecting single infrared photons with 90% system efficiency," *Nature Photonics*, vol. 7.

[15] T. Yamashita, S. Miki, H. Terai, and Z. Wang, "Low-filling-factor superconducting single photon detector with high system detection efficiency," *Optics Express*, vol. 21, no. 22, pp. 27177–27184, 2013.

[16] R. Cheng, H. Yin, J. Liu, T. Li, H. Cai, Z. Xu, and W. Chen, "Photon-number-resolving detector based on superconducting serial nanowires," *IEEE Transactions on Applied Superconductivity*, vol. 23, no. 1, p. 2200309, 2013.

[17] F. Najafi, F. Marsili, E. Dauler, R. J. Molnar, and K. K. Berggren, "Timing performance of 30-nm-wide superconducting nanowire avalanche photodetectors," *Applied Physics Letters*, vol. 100, no. 15, p. 152602, 2012.

[18] R. H. Hadfield, "Single-photon detectors for optical quantum information applications," *Nature Photonics*, vol. 3, no. 12, pp. 696–705, 2009.

[19] M. D. Eisaman, J. Fan, A. Migdall, and S. V. Polyakov, "Invited review article: Single-photon sources and detectors," *Review of Scientific Instruments*, vol. 82, no. 071101, 2011.

[20] X. Hu, C. W. Holzwarth, D. Masciarelli, E. A. Dauler, and K. K. Berggren, "Efficiently coupling light to superconducting nanowire single-photon detectors," *IEEE Transactions on Applied Superconductivity*, vol. 19, no. 3, pp. 336–340, 2009.

[21] X. Hu, T. Zhong, J. E. White, E. A. Dauler, F. Najafi, C. H. Herder, F. N. C. Wong, and K. K. Berggren, "Fiber-coupled nanowire photon coutner at 1550 nm with 24% system detection efficiency," *Optics Letters*, vol. 34, no. 23, pp. 3607–3609, 2009.

[22] S. N. Dorenbos, R. W. Heeres, E. F. C. Driessen, and V. Zwiller, ""efficient and robust fiber coupling of superconducting single-photon detectors," *arXiv*, vol. 1109.5809, 2011.

[23] F. Marsili, F. Najafi, E. Dauler, F. Bellei, X. Hu, M. Csete, R. J. Molnar, and K. K. Berggren, "Single-photon detectors based on ultranarrow superconducting nanowires," *Nano Letters*, vol. 11, no. 5, pp. 2048–2053, 2011.

[24] C. M. Natarajan, M. G. Tanner, and R. H. Hadfield, "Superconducting nanowire single-photon detectors: physics and applications," *Superconductor Science and Technology*, vol. 25, no. 6, p. 063001, 2012.

[25] G. N. Gol'tsman, O. Okunev, G. Chulkova, A. Lipatov, A. Semenov, K. Smirnov, B. Voronov, A. Dzardanov, C. Williams, and R. Sobolewski, "Picosecond superconducting single-photon detector," *Applied Physics Letters*, vol. 79, no. 6, pp. 705–707, 2001.

[26] J. K. W. Yang, A. J. Kerman, E. A. Dauler, V. Anant, K. M. Rosfjord, and K. K. Berggren, "Modeling the electrical and thermal response of superconducting nanowire single-photon detectors," *IEEE Transactions on Applied Superconductivity*, vol. 17, no. 2, pp. 581–585, 2007.

[27] A. Engel and A. Schilling, "Numerical analysis of detection-mechanism models of superconducting nanowire single-photon detector," *Journal of Applied Physics*, vol. 114, no. 21, p. 214501, 2013.

[28] J. J. Renema, R. Gaudio, Q. Wang, Z. Zhou, A. Gaggero, F. Mattioli, R. Leoni, D. Sahin, M. J. A. de Dood, A. Fiore, and M. P. van Exter, "Experimental test of theories of the detection mechanism in a nanowire superconducting single photon detector," *Physical Review Letters*, vol. 112, no. 11, p. 117604.

[29] F. Marsili, F. Bellei, F. Najafi, A. E. Dane, E. A. Dauler, R. J. Molnar, and K. K. Berggren, "Efficient single photon detection from 500 nm to 5 micrometer wavelength," *Nano Letters*, vol. 12, no. 9, pp. 4799–4804, 2012.

[30] A. Semenov, A. Engel, H.-W. Huebers, K. Il'in, and M. Siegel, "Spectral cut-off in the efficiency of the resistive state formation caused by absorption of a single-photon in current-carrying superconducting nano-strips," *The European Physical Journal B*, vol. 47, no. 4, pp. 495–501, 2005.

[31] A. Engel, A. Semenov, H.-W. Huebers, K. Il'in, and M. Siegel, "Fluctuations and dark count rates in superconducting NbN single-photon detectors," *Physica Status Solidi (C)*, vol. 2, no. 5, pp. 1668–1673, 2005.

[32] L. N. Bulaevskii, M. J. Graf, and V. G. Kogan, "Vortex-assisted photon counts and their magnetic field dependence in single-photon superconducting detectors," *Physical Review B*, vol. 85, no. 1, p. 014505, 2012.

[33] H. Bartolf, A. Engel, A. Schilling, K. Il'in, M. Siegel, H.-W. Huebers, and A. Semenov, "Current-assisted thermally activated flux liberation in ultrathin nanopatterned NbN superconducting meander structures," *Physical Review B*, vol. 81, no. 2, p. 024502, 2010.

[34] L. N. Bulaevskii, M. J. Graf, C. D. Batista, and V. G. Kogan, "Vortex-induced dissipation in narrow current-biased thin-film superconducting strips," *Physical Review B*, vol. 83, no. 14, p. 144526, 2011.

[35] J. K. W. Yang, A. J. Kerman, E. A. Dauler, B. Cord, V. Anant, R. J. Molnar, and K. K. Berggren, "Suppressed critical current in superconducting nanowire single-photon detectors with high fill-factors," *IEEE Transactions on Applied Superconductivity*, vol. 19, no. 3, pp. 318–322, 2009.

[36] J. R. Clem and K. K. Berggren, "Geometry-dependent critical currents in superconducting nanocircuits," *Physical Review B*, vol. 84, no. 174510, 2011.

[37] H. L. Hortensiu, E. F. C. Driessen, T. M. Klapwijk, K. K. Berggren, and J. R. Clem, "Critical-current reduction in thin superconducting wires due to current crowding," *Applied Physics Letters*, vol. 100, no. 18, p. 182602, 2012.

[38] V. Anant, A. J. Kerman, E. A. Dauler, J. K. W. Yang, K. M. Rosfjord, and K. K. Berggren, "Optical properties of superconducting nanowire single-photon detectors," *Optics Express*, vol. 16, no. 14, pp. 10750–10761, 2008.

[39] P. T. Lin, V. Singh, L. Kimerling, and A. M. Agarwal, "Planar silicon nitride mid-infrared devices," *Applied Physics Letters*, vol. 102, no. 25, p. 251121, 2013.

[40] "LOR and PMGI resists." Accessed on the web on July 25, 2014 from microchem.com.

[41] S. Choi, N. Jin, V. Kumar, I. Adesida, and M. Shannon, "Effects of developer temperature on electron-beam-exposed hydrogen silsesquioxane resist for ultradense silicon nanowire fabrication," *Journal of Vacuum Science and Technology B*, vol. 25, no. 6, pp. 2085–2088, 2007.

[42] J. K. W. Yang, V. Anant, and K. K. Berggren, "Enhancing etch resistance of hydrogen silsesquioxane via postdevelop electron curing," *Journal of Vacuum Science and Technology*, vol. 24, no. 6, pp. 3157–3161, 2006.

[43] A. J. Kerman, E. A. Dauler, J. K. W. Yang, K. M. Rosfjord, V. Anant, K. K. Berggren, G. N. Gol'tsman, and B. M. Voronov, "Constriction-limited detection efficiency of superconducting nanowire single-photon detectors," *Applied Physics Letters*, vol. 90, no. 10, p. 101110, 2007.

[44] R. G. Hobbs, M. Schmidt, C. T. Bolger, Y. M. Georgiev, P. Fleming, M. A. Morris, N. Petkov, J. D. Holmes, F. Xiu, K. L. Wang, V. Djara, R. Yu, and J.-P. Colinge, "Resist-substrate interface tailoring for generating high-density arrays of Ge and Bi_2Se_3 nanowires by electron beam lithography," *Journal of Vacuum Science and Technology B*, vol. 30, no. 4, p. 041602, 2012.

[45] C. Peiffert, C. Nguyen-Trung, D. A. Palmer, J. P. Laval, and E. Giffaut, "Solubility of B-Nb_2O_5 and the hydrolysis of niobium(V) in aqueous solution as a function of temperature and ionic strength," *Journal of Solution Chemistry*, vol. 39, pp. 197–218, 2010.

[46] K. M. Rosfjord, J. K. W. Yang, E. A. Dauler, A. J. Kerman, V. Anant, B. M. Voronov, G. N. Gol'tsman, and K. K. Berggren, "Nanowire single-photon detector with an integrated optical cavity and anti-reflection coating," *Optics Express*, vol. 14, no. 2, pp. 527–534, 2006.

[47] M. Ejrnaes, R. Cristiano, O. Quaranta, S. Pagano, A. Gaggero, F. Mattioli, R. Leoni, B. Voronov, and G. Gol'tsman, "A cascade switching superconducting single photon detector," *Applied Physics Letters*, vol. 91, no. 26, p. 262509, 2007.

[48] F. Najafi, J. Mower, N. Harris, F. Bellei, A. Dane, C. Lee, P. Kharel, F. Marsili, S. Assefa, K. K. Berggren, and D. Englund, "On-chip detection of entangled photons by scalable integration of single-photon detectors," *arXiv*, 2014.

[49] F. Marsili, F. Najafi, E. Dauler, R. J. Molnar, and K. K. Berggren, "Afterpulsing and instability in superconducting nanowire avalanche photodetectors," *Applied Physics Letters*, vol. 100, no. 11, p. 112601, 2012.

[50] L. E. Toth, *Transition Metal Carbides and Nitrides*. Academic Press, Inc., 1971.

[51] S. P. Chockalingam, M. Chand, J. Jesudasan, V. Tripathi, and P. Raychaudhuri, "Superconducting properties and Hall effect of epitaxial NbN thin films," *Physical Review B*, vol. 77, no. 21, p. 214503, 2008.

[52] Z. Wang, A. Kawakami, Y. Uzawa, and B. Komiyama, "Superconducting properties and crystal structures of single-crystal niobium nitride thin films deposited at ambient substrate temperature," *Journal of Applied Physics*, vol. 79, no. 10, pp. 7837–7842, 1996.

[53] F. Marsili, *Single-Photon and Photon-Number-Resolving Detectors Based on Superconducting Nanowires*. PhD thesis, Ecole Polytechnique Federale de Lausanne, 2009.

[54] G. Jouve, C. Severac, and S. Cantacuzene, "XPS study of NbN and (NbTi)N superconducting coatings," *Thin Solid Films*, vol. 287, no. 1–2, pp. 146–153, 1996.

[55] X. Q. Jia, L. Kang, M. Gu, X. Z. Yang, C. Chen, X. C. Tu, B. B. Jin, W. W. Xu, J. Chen, and P. H. Wu, "Fabrication of a strain-induced high performance NbN ultrathin film by a Nb_5N_6 buffer layer on Si substrate," *Semiconductor Science and Technology*, vol. 27, no. 035010, 2014.

[56] L. Zhang, Q. Zhao, Y. Zhong, J. Chen, C. Cao, W. Xu, L. Kang, P. Wu, and W. Shi, "Single photon detectors based on superconducting nanowires over large active areas," *Applied Physics B*, vol. 97, pp. 187–191, 2009.

[57] M. Hofherr, D. Rall, K. Il'in, A. Semenov, H.-W. Huebers, and M. Siegel, "Dark count suppression in superconducting nanowire single photon detectors," *Journal of Low Temperature Physics*, vol. 167, pp. 822–826, 2012.

[58] Y. Ufuktepe, A. H. Farha, S. I. Kimura, T. Hajiri, K. Imura, M. A. Mamun, F. Karadag, A. A. Elmustafa, and H. E. Elsayad-Ali, "Superconducting niobium nitride thin films by reactive pulsed laser deposition," *Thin Solid Films*, vol. 545, pp. 601–607, 2013.

[59] F. Hirth, T. C. Buck, A. P. Grassi, and A. W. Koch, "Depth-sensitive thin film reflectometer," *Measurement Science and Technology*, vol. 21, no. 12, p. 125301, 2010.

[60] M. R. Jafarfard, S. Moon, B. Tayebi, and D. Y. Kim, "Dual-wavelength diffraction phase microscopy for simultaneous measurement of refractive index and thickness," *Optics Letters*, vol. 39, no. 10, pp. 2908–2911, 2014.

[61] W.-D. Joo, J. You, and Y.-S. Ghim, "Angle-resolved reflectometer for thickness measurement of multi-layered thin-film structures," in *Conference on Interferometry XIV - Techniques and Analysis*, vol. 7063, (San Diego, CA), 2008.

[62] J. Henrie, E. Parsons, A. R. Hawkins, and S. M. Schultz, "Spectrum sampling reflectometer," *Surface and Interface Analysis*, vol. 37, pp. 568–572, 2005.

[63] J. A. Aznarez, J. I. Larruquert, and J. A. Mendez, "Far-ultraviolet absolute reflectometer for optical constant determination of ultrahigh vacuum prepared thin films," *Review of Scientific Instruments*, vol. 67, no. 2, pp. 497–502, 1996.

[64] S. Doring, F. Hertlein, A. Bayer, and K. Mann, "EUV reflectometry for thickness and density determination of thin film coatings," *Applied Physics A*, vol. 107, no. 4, pp. 795–800, 2012.

[65] G. H. Ho, F.-H. Kang, and H.-W. Fu, "Absorption and loss of film thickness in photoresists and underlayer materials upon irradiation at 13.5 nm," in *Conference On Extreme Ultraviolet (EUV) Lithography*, vol. 7636, (San Jose, CA), 2010.

[66] M. Benyay and L. Juschkin, "Table-top reflectometer in the extreme ultraviolet for surface sensitive analysis," *Applied Physics Letters*, vol. 94, no. 063507, 2009.

[67] S. Schroeder, T. Feigl, and A. Duparre, "Euv reflectance and scattering of mo/si multilayers on differently polished substrates," *Optics Express*, vol. 15, no. 21, pp. 13997–14012, 2007.

[68] M. Torche, G. Schmerber, M. Guemmaz, A. Mosser, and J. C. Parlebas, "Non-stoichiometric niobium nitrides: structure and properties," *Thin Solid Films*, vol. 436, pp. 208–212, 2003.

[69] A. E. Dane, "Ultrathin superconducting niobium nitride films for applications," Master's thesis, Massachusetts Institute of Technology, 2014.

[70] C. M. Herzinger, B. Johs, W. A. McGahan, J. A. Woollam, and W. Paulson, "Ellipsometric determination of optical constants for silicon and thermally grown silicon dioxide via a multi-sample, multi-wavelength, multi-angle investigation," *Journal of Applied Physics*, vol. 83, no. 6, pp. 3323–3336, 1998.

[71] M. Benkahoul, *Niobium nitride based thin films deposited by DC reactive magnetron sputtering: NbN, NbSiN and NbAlN*. PhD thesis, Ecole Polytechnique Federale de Lausanne, 2005.

[72] J. A. Thornton, "High rate thick film growth," *Annual Review of Materials Science*, vol. 7, pp. 239–260, 1977.

[73] R. Messier, A. P. Giri, and R. A. Roy, "Revised structure zone model for thin film physical structure," *Journal of Vacuum Science and Techology*, vol. 2, no. 2, pp. 500–503, 1984.

[74] O. S. Heavens, *Optical Properties of Thin Solid Films*. Courier Dover Publications, 1991.

[75] F. Abeles, "Sur la propagation des ondes electromagnetiques dans les milieux stratifies," *Annales de Physique (Paris)*, vol. 3, pp. 504–520, 1948.

[76] M. Csete, A. Sipos, F. Najafi, X. Hu, and K. K. Berggren, "Numerical method to optimize the polar-azimuthal orientation of infrared superconducting-nanowire single-photon detectors," *Applied Optics*, vol. 50, no. 31, pp. 5949–5956, 2011.

[77] D. R. Smith, S. Schultz, P. Markos, and C. M. Soukoulis, "Determination of effective permittivity and permeability of metamaterials from reflection and transmission coefficients," *Physical Review B*, vol. 65, p. 195104, 2002.

[78] E. F. C. Driessen and M. J. A. de Dood, "The perfect absorber," *Applied Physics Letters*, vol. 94, p. 171109, 2009.

[79] M. G. Moharam, E. B. Grann, D. A. Pommet, and T. K. Gaylord, "Formulation for stable and efficient implementation of the rigorous couple-wave analysis of binary gratings," *Journal of the Optical Society of America A*, vol. 12, no. 5, pp. 1068–1076, 1995.

[80] A. Yariv and P. Yeh, *Optical Waves in Layered Media*. New York, NY: Wiley, 1988.

[81] O. Deparis, "Poynting vecotr in a transfer-matrix formalism for the calculation of light absorption profile in stratified isotropic optical media," *Optics Letters*, vol. 36, no. 20, pp. 3960–3962, 2011.

[82] L. A. A. Pettersson, L. S. Roman, and O. Inganas, "Modeling photocurrent action spectra of photovoltaic devices based on organic thin films," *Journal of Applied Physics*, vol. 86, no. 1, pp. 487–496, 1999.

[83] L. Maingault, M. Tarkhov, I. Florya, A. Semenov, R. Espiau de Lamaestre, P. Cavalier, G. Gol'tsman, J.-P. Poizat, and J.-C. Villegier, "Spectral dependency of superconducting single photon detectors," *Journal of Applied Physics*, vol. 107, no. 11, p. 116103, 2010.

[84] B. Tatian, "Fitting refractive-index data with the sellmeier dispersion formula," *Applied Optics*, vol. 23, no. 24, pp. 4477–4485, 1984.

[85] G. Ghosh, "Dispersion-equation coefficients for the refractive index and birefringence of calcite and quartz crystals," *Optics Communications*, vol. 163, no. 1–3, pp. 95–102, 1999.

[86] M. R. Watts, *Polarization Independent Microphotonic Circuits*. PhD thesis, Massachusetts Institute of Technology, 2005.

[87] X. Hu, E. A. Dauler, R. J. Molnar, and K. K. Berggren, "Superconducting nanowire single-photon detectors integrated with optical nano-antennae," *Optics Express*, vol. 19, no. 1, pp. 17–31, 2011.

[88] E. Palik, *Handbook of Optical Constants of Solids*. Academic Press, Inc., 1998.

[89] A. E. Lita, B. Calkins, L. A. Pellouchoud, A. J. Miller, and S. Nam, "Superconducting transition-edge sensors optimized for high-efficiency photon-number resolving detectors," *Proceedings of SPIE 7681, Advanced Photon Counting Techniques IV*, vol. 7681, no. 76810D, 2010.

[90] P. Nagpal, N. C. Lindquist, S.-H. Oh, and D. J. Norris, "Ultrasmooth patterned metals for plasmonics and metamaterials," *Science*, vol. 325, no. 5940, pp. 594–597, 2009.

[91] S. Thakoor, J. L. Lamb, A. P. Thakoor, and S. K. Khanna, "High T_c superconducting NbN films deposited at room temperature," *Journal of Applied Physics*, vol. 58, no. 12, pp. 4643–4648, 1985.

[92] S. Thakoor, H. G. LeDuc, A. P. Thakoor, J. Lambe, and S. K. Khanna, "Room temperature deposition of superconducting NbN for superconductor-insulator-superconductor junctions," *Journal of Vacuum Science and Technology A*, vol. 4, no. 3, pp. 528–531, 1986.

[93] M. N. O. Sadiku, "A simple introduction to finite element analysis of electromagnetic problems," *IEEE Transactions on Education*, vol. 32, no. 2, pp. 85–93, 1989.

[94] L. Novotny and N. van Hulst, "Antennas for light," *Nature Photonics*, vol. 5, pp. 83–90, 2011.

[95] J. Trevino, G. F. Walsh, E. F. Pecora, S. V. Boriskina, and L. Dal Negro, "Photonic-plasmonic coupled nanoantennas for polarization-controlled multispectral nanofocusing," *Optics Letters*, vol. 38, no. 22, pp. 4861–4863, 2013.

[96] M. Husnik, S. Linden, R. Diehl, J. Niegemann, K. Busch, and M. Wegener, "Quantitative experimental determination of scattering and absorption cross-section spectra of individual optical metallic nanoantennas," *Physical Review Letters*, vol. 109, no. 23, p. 233902, 2012.

[97] F. Chen, S.-W. Wang, Y. Zhang, Q. Li, X. Sun, X. Chen, and W. Lu, "Simulation of superconducting single photon detector coupled with metal-insulator-metal concentric ring grating," *Optical and Quantum Electronics*, vol. published online, 2013.

[98] F. J. Gonzalez and G. D. Boreman, "Comparison of dipole, bowtie, spiral and log-periodic IR antennas," *Infrared Physics and Technology*, vol. 46, no. 5, pp. 418–428, 2005.

[99] M. W. Knight, H. Sobhani, P. Nordlander, and N. J. Halas, "Photodetection with active optical antennas," *Science*, vol. 332, no. 6030, pp. 702–704, 2011.

[100] T. H. Taminiau, F. D. Stefani, F. B. Segerink, and N. F. van Hulst, "Optical antennas direct single-molecule emission," *Nature Photonics*, vol. 2, pp. 234–237, 2008.

[101] T. H. Taminiau, F. D. Stefani, and N. F. van Hulst, "Single emitters coupled to plasmonic nano-antennas: angular emission and collection efficiency," *New Journal of Physics*, vol. 10, p. 105005, 2008.

[102] F. Obelleiro, J. M. Taboada, D. M. Solis, and L. Bote, "Directive antenna nanocoupler to plasmonic gap waveguides," *Optics Letters*, vol. 38, no. 10, pp. 1630–1632, 2013.

[103] I. S. Makymov and Y. S. Kivshar, "Broadband light coupling to dielectric slot waveguides with tapered plasmonic nanoantennas," *Optics Letters*, vol. 38, no. 22, pp. 4853–4863, 2013.

[104] R. Bruck and O. L. Muskens, "Plasmonic nanoantennas as integrated coherent perfect absorbers on SOI waveguides for modulators and all-optical switches," *Optics Express*, vol. 21, pp. 27662–27671, 2013.

[105] Z. Iluz and A. Boag, "Dual-Vivaldi wideband nanoantenna with high radiation efficiency over the infrared frequency band," *Optics Letters*, vol. 36, no. 15, pp. 2773–2775, 2011.

[106] F. Marsili, F. Najafi, C. Herder, and K. K. Berggren, "Electrothermal simulation of superconducting nanowire avalanche photodetectors," *Applied Physics Letters*, vol. 98, no. 9, p. 093507, 2011.

[107] O. L. Muskens, V. Giannini, J. A. Sanchez-Gil, and J. Gomez Rivas, "Optical scattering resonances of single and coupled dimer plasmonic nanoantennas," *Optics Express*, vol. 15, no. 26, pp. 17736–17746, 2007.

[108] L. Tang, S. E. Kocabas, S. Latif, A. K. Okyay, D.-S. Ly-Gagnon, K. C. Saraswat, and D. A. B. Miller, "Nanometre-scale germanium photodetector enhanced by a near-infrared dipole antenna," *Nature Photonics*, vol. 2, pp. 226–229, 2008.

[109] H. Fischer and O. J. F. Martin, "Engineering the optical response of plasmonic nanoantennas," *Optics Express*, vol. 16, no. 12, pp. 1944–1954, 2008.

[110] A. Alu and N. Engheta, "Input impedance, nanocircuit loading, and radiation tuning of optical nanoantennas," *Physical Review Letters*, vol. 101, no. 4, p. 043901, 2008.

[111] J. A. Schuller, E. S. Barnard, W. Cai, Y. C. Jun, J. S. White, and M. L. Brongersma, "Plasmonics for extreme light concentration and manipulation," *Nature Materials*, vol. 9, pp. 193–204, 2010.

[112] P. Bharadwaj, B. Deutsch, and L. Novotny, "Optical antennas," *Advances in Optics and Photonics*, vol. 1, pp. 438–483, 2009.

[113] H. Aouani, M. Navarro-Cia, M. Rahmani, T. P. H. Sidiropoulos, M. Hong, R. F. Oulton, and S. A. Maier, "Multiresonant broadband optical antennas as efficient tunable nanosources of second harmonic light," *Nano Letters*, vol. 12, no. 9, pp. 4997–5002, 2012.

[114] G. C. Dyer, N. Q. Vinh, S. J. Allen, G. R. Aizin, J. Mikalopas, J. L. Reno, and E. A. Shaner, "A terahertz plasmon cavity detector," *Applied Physics Letters*, vol. 97, no. 19, p. 193507, 2010.

[115] M. S. Vitiello, D. Coquillat, L. Viti, D. Ercolani, F. Teppe, A. Pitanti, F. Beltram, L. Sorba, W. Knap, and A. Tredicucci, "Room-temperature terahertz detectors based on semiconductor nanowire field-effect transistors," *Nano Letters*, vol. 12, no. 1, pp. 96–101, 2012.

[116] P. G. de Gennes, *Superconductivity of Metals and Alloys*. Westview Press, 1999.

[117] M. Silva-Lopez, A. Cuadrado, N. Llombart, and J. Alda, "Antenna array connections for efficient performance of distributed microbolometers in the IR," *Optics Express*, vol. 21, no. 9, pp. 10867–10877, 2013.

[118] A. Casadei, E. F. Pecora, J. Trevino, C. Forestiere, D. Rueffer, E. Russo-Averchi, F. Matteini, G. Tutuncuoglu, M. Heiss, A. Foncuberta i Morral, and L. Dal Negro, "Photonic-plasmonic coupling of GaAs single nanowires to optical nanoantennas," *Nano Letters*, vol. 14, no. 5, pp. 2271–2278, 2014.

[119] L. Zou, W. Withayachumnankul, C. M. Shah, A. Mitchell, M. Bhaskaran, S. Sriram, and C. Fumeaux, "Dielectric resonator nanoantennas at visible frequencies," *Optics Express*, vol. 21, no. 1, pp. 1344–1352, 2013.

[120] P. Fan, C. Y. Huang, L. Cao, and M. L. Brongersma, "Redesigning photodetector electrodes as an optical antenna," *Nano Letters*, vol. 13, no. 2, pp. 392–396, 2013.

[121] E. N. Grossman, J. E. Sauvageau, and D. G. McDonald, "Lithographic spiral antennas at short wavelengths," *Applied Physics Letters*, vol. 59, no. 25, pp. 3225–3227, 1991.

This thesis was typeset using LaTeX, originally developed by Leslie Lamport and based on Donald Knuth's TeX. The body text is set in 11 point Egenolff-Berner Garamond, a revival of Claude Garamont's humanist typeface. The above illustration, "Science Experiment 02", was created by Ben Schlitter and released under CC BY-NC-ND 3.0. A template that can be used to format a PhD thesis with this look and feel has been released under the permissive MIT (X11) license, and can be found online at github.com/suchow/Dissertate or from its author, Jordan Suchow, at suchow@post.harvard.edu.